Synchronization of a Spin Transfer oscillator to a RF current : mechanisms and room-temperature characterization.

Christophe Dieudonné

UNIVERSITÉ DE GRENOBLE

THÈSE

Pour obtenir le grade de

DOCTEUR DE L'UNIVERSITÉ DE GRENOBLE

Spécialité : **Nanophysique**

Arrêté ministériel :

Présentée par

Christophe Dieudonné

Thèse dirigée par **Ursula Ebels**
et codirigée par **Marie-Claire Cyrille**

préparée au sein **CEA LETI** / **Spintec**
et de **Ecole doctorale de physique de Grenoble**

Synchronisation d'un oscillateur à transfert de spin à une source de courant RF :
Mécanismes et caractérisation à température ambiante.

Thèse soutenue publiquement le **6 juillet 2015**,
devant le jury composé de :

M., Alain Marty
DR, SP2M, INAC, Président
M., Vincent Cros
HDR, CNRS/Thales, Rapporteur
M., Nicolas Vukadinovic
HDR, Dassault Aviation, Rapporteur
M., Joo-Von Kim
DR, IEF/CNRS, Examinateur
Mme., Ursula Ebels
HDR, Spintec(CEA), Examinateur
Mme., Marie-Claire Cyrille
DR, LETI(CEA), Examinateur
Mme., Liliana Buda-Prejbeanu
DR, Spintec(CEA), Invité

Contents

Aknowledgement

Here I want to give my best thanks to all the people, coworkers and friends that supported me and but also kept inspiring me to go on during these 3 years of thesis. Being here in Spintec marked at the same time the last years of studentship and the first years of me being an active worker. With it comes a number of difficult but often enriching experiences, that I was glad to share with all my friends there.

I will first my thanks my family, my parents and my two sisters for bringing me here to the PhD, the constant support and care during the 3 years, providing me with a shelter during tired times, but also with very unwise scientific input.

Of course I would like to thank my two thesis supervisors Ursula Ebels and Marie-Claire Cyrille for all the help, the scientific guidance and the necessary will to walk me through the thesis. Ursula I want to say that you have shown me how to keep working hard and not giving up even when the wind blows against you. I can understand now that it requires a lot of resolve and energy to keep a group like the RF group in Spintec running, but you still found the time (even in moments where we openly disagreed) to listen and make me progress, and I really appreciated it.

In the RF group, I think about Liliana too, you became my unofficial supervisor during the last year and provided all the necessary help for the backup simulations. I remember of course the other members of the group, Elmer the unstoppable stimulant, Michael the specialist of noisy dynamics that was always there to answer my questions on the subject, Felipe, Jiafeng, Alex, Juan, Marina, Karla, but also the promising new wave of students with Matthieu, Jerome, Anicke, Tititshka and Iteshika, whom I wish the best and also keep confident.

I do not forget about my colleagues and friends in Spintec - the senior scientists, Daria, Mihail, Olivier Klein and Boulle, Mair, Gilles, Stephane, Vincent, Christophe for their scientific input and morning / late evening discussions - but also the postdocs and people I shared the office with, Giovanni, Nicolai, Andrey, Eldar, Ali, Hongxin, Lara...

There is the group of Spintec PhD students with whom I shared the experience of the PhD thesis and their up and downs, we became close friends and grew up together, this is something that cannot and will not be forgotten - Alexandre, we started from the same office to writing the thesis at the campus towards the end, and whatever you say, it was great moments, you kept my motivation running from the beginning to the end, thank you. All my friends, Pierre-Yves, Marc, Thomas, Alexandru, Pablo, Giovanni, Alex too, Kamil and the freedom 11 A.M. cigarettes under the sun, and the PhDs who made Spintec the luckiest exception in a scientific world, Léa, Cécile, Selma, Magali, Claire, Mélissa. You have been the best for me, for these years thank you, I will miss you.

Part A : Introduction

Basic research and applied research usually progress in two different time scales : the basic, core research is primarily motivated by scientific curiosity which produces results on the long term, while applied research focuses on the development of functional devices in a competitive market where short and mid-term objectives matter.

To illustrate, let us suppose that the goal of scientific research is to cross a river from one side to the other : the people doing basic research and the people doing applied research use two different approaches, and work together. The "basic researcher" wants to find out at which places the river can be crossed : he throws out rocks to find out about the depth of the river, evaluates the distance between the two banks, measures the flow of the stream. At some point he concludes : at this location somebody can go to the other bank using this particular method, and eventually tries. If he succeeds he marks on a map the location and writes down the proposed method.

Then he hands out the map to the "applied researcher", gives him his contact information, and continues its walk down the river. The "applied researcher" does not have the opportunity to wander and look for all the possible locations where the river can be crossed. His goal is to build a bridge at the most convenient places so that people can cross the river. He will look for the different possibilities for the construction, depending on the resources readily available, information on the map, and the potential utilization of the bridge : in some cases a sturdy bridge will be designed to allow for cars, in other cases a boardwalk will be sufficient for pedestrians.

The beginning of Spintronics is marked by a particularly swift transfer from basic research to applied research. It started in 1988 when the two teams of Albert Fert and Peter Grünberg discovered independently the magnetoresistance effect in nanometer-thick magnetic multilayers. From there, only ten years later the effect was used by IBM to successfully design and market read heads for magnetic recording in hard drives. Albert Fert and Peter Grünberg were awarded in 2007 the Nobel prize in physics for their discovery, and nowadays magnetoresistive read heads are widely used. While reads head are still based on the magnetoresistive effect, the technology evolved to improve the sensitivity of the device : from AMR (anisotropic magnetoresistance) to GMR (giant magnetoresistance) and TMR (tunnel magnetoresistance).

In 1996 the Spin-Transfer Torque (STT) effect was discovered and enabled not only electrical reading but also electrical writing of the magnetization state. It opened the way for STT-MRAMs, a promising candidate to replace SRAMs and DRAMs in the market of random-access memories.

Here we focus on another type of device using both the STT and the MR effects : the Spin-Torque Oscillator (STO). A STO is a nanoscaled oscillating system which produces a tunable RF signal in the GHz range with an output power in the order of a microwatt : the natural application is tunable frequency synthesis for wireless telecommunications devices. However, in order to compete with the other frequency sources currently used in telecommunications, namely Voltage Controlled Oscillators (VCO), two major blocking points in terms of signal properties of the STO need to be addressed : (i) the output power and (ii) the generation linewidth.

We narrow down to the subject of this thesis : *Synchronization in a Spin-Torque Oscillator*. Speaking of applied research, the motivation is clearly defined : Synchronization of several STOs is a promising way to enhance the signal properties of and, consequently, make the STO competitive for practical applications in frequency synthesis. The pioneering work of Adler *et al.* in 1946 on injection-locking of electronic oscillators (that is,

synchronization to a driving oscillatory current) opened the way for an important number of studies in electronics demonstrating how to use a weak, precise external signal to stabilize an oscillator with stronger but noisier output. It is one of the goals of this thesis : characterization at room-temperature of the stability of the STO signal under the application of a RF current, in the synchronized regime.

This thesis also relates to basic research with the investigation of the synchronization phenomena in a STO. Indeed, STOs are oscillators that rely on the sustained precession of the magnetization : their dynamics are regulated by the Landau-Lifshitz-Gilbert-Slonczewski (LLGS) equation, which is a highly non-linear equation. As a consequence, we observe rich dynamics in a very versatile system, and it makes the investigation of synchronization phenomena in STOs particularly stimulating.

We hope that this thesis contributes to the progress towards (i) the design of a practical, competitive STO device for frequency synthesis in telecommunications and (ii) a useful understanding of the STO dynamics and the related synchronization phenomena.

This manuscript is organized into three parts :

• **Part A**. This part consists of the first chapter, in which we introduce the main concepts and ideas being utilized during this manuscript, and we perform a rapid review of the scientific literature. First we start by familiarizing the reader with the basic concepts of spintronics to those of precessional magnetization dynamics : both of these aspects are needed for the description of the STO, from its static configuration to the dynamical behaviour. Then we examine the notion of self-sustained oscillator and its attributes such as the phase and the amplitude : the KTS formalism for the STO dynamics will be introduced as well. Finally we consider synchronization phenomena. We go from a general picture of synchronization and introduce phase-locking and frequency adjustment, then to the specifics of synchronization to an external source and then we review synchronization in the context of Spin-Torque Oscillators.

• **Part B**. This part presents the results of the investigation of synchronization mechanisms of an in-plane precession STO to a driving current, which contains the most notable findings of this thesis. It is composed of two chapters. Chapter 2 presents the analytical development leading to the phase and amplitude equations for the STO dynamics in synchronized regime. It starts with the LLGS equation and examines the peculiarities of the transformation to the equation of motion in KTS formalism when applied to the IPP trajectory. We also analyze the way the RF current couples with the oscillation, and the differences between synchronization at f and $2f$ with their associated mechanisms. Chapter 3 confronts on a quantitative level the analytical results with macrospin simulations in the synchronized regime at 0 K. The configuration is in-plane precession, where the polarizer orientation allows for both synchronization at f and $2f$. First we evaluate the domain of validity of the KTS model in the autonomous regime, then the frequency and power variations are calculated, and finally the phase-difference and the synchronization regions are analyzed, where we confirm the link between frequency and amplitude adjustment at $2f$.

• **Part C**. This final part of the manuscript reports the characterization of injection-locking at $2f$ of a MTJ-based STO at room temperature with the associated experimental methods. In Chapter 4 we review the experimental techniques utilized during this thesis.

It starts with the engineering of the magnetic stack : we examine the composition and the different layers of a MTJ-based STO, and discuss the required MTJ properties for a STO, low RA and high TMR. We also look at the factors leading to the formation of pinholes in the barrier. The second aspect focuses on the techniques used for microwave frequency measurements and the injection and collection of a RF signal in our setup. The topic of impedance matching, and signal processing will be addressed there. Next, Chapter 5 presents the dynamics of the injection-locked STO. First the dynamics of a MTJ-based STO in autonomous regime are examined, where we look at the evolution of the linewidth and the generated power as a function of the applied field and applied current. Then we add the RF current at $2f$ and analyze the dynamics in the frequency-domain, namely the linewidth reduction and next the behavior of the locking-range when the RF and DC current amplitude are changed. Finally we characterize noise properties in synchronized regime through analysis in the time-domain of the phase-difference and phase and amplitude noise plots.

Chapter I

Magnetization dynamics and synchronization

I.1 Context : Spintronics and magnetization dynamics

In order to introduce spin-torque oscillators and understand how they operate, we must first review some essential physical phenomena in the discipline of spintronics, namely spin-dependent transport with magnetoresistance, and then spin-transfer torque (STT). In particular we will examine some key models that contributed to the swift development of spintronics as a promising topic of both applied and basic research in nanoelectronics.

In contrast with other spintronic devices (MRAM) or areas of research in spintronics (Dowain wall motion, transport, switching etc...), it is necessary that the reader is familiar with precessional magnetization dynamics before studying spin-torque oscillators. We will then examine precessional magnetization dynamics through the analysis of the LLGS equation.

I.1.1 Spintronics : Magnetoresistance and spin-transfer torque

Spintronics is a contraction of two words : *Spin* and *Electronics*. As we know an electron possesses three fundamental properties : its mass, its charge, and its spin. "Classical" electronics is the discipline that relies only on the use of the charge of the electron to design circuits and components, and the vast majority of devices coming out nowadays are the product of conventional electronics technology.

The notion of spin of a particle was first introduced by Pauli in 1928 in the framework of relativistic quantum theory. The idea is to consider that the particle is spinning around an axis, which in turn generates a magnetic angular momentum that is called the *spin* of the particle.

More than fifty years later, the phenomenon of *spin-dependent* transport was experimentally confirmed by the discovery in 1988 of the giant magnetoresistance (GMR) effect by A. Fert in (001)Fe/(001)Cr magnetic multilayers [2].

This discovery has since then opened the way for technological applications using spin-dependent transport, i.e., the use of both the charge and the spin of moving electrons in the same device - leading to the emergence of the field of spintronics. Maybe one of the most inspiring success of spintronics is the invention of the "spin valve" configuration[15]

three years after the discovery of GMR, and its quick marketing in 1998 by IBM as a field sensor for magnetic read heads.

The second, more recent building block of spintronics, is the discovery of the spin-transfer torque (STT) effect in ferromagnetic layers by J.C. Slonczewski and Berger in 1996 [85, 5]. It enabled new ways to control the magnetization of magnetic layers using spin-polarized current only - steady state precession of the magnetization with constant current and magnetization switching with current pulses. Using the STT effect STT-MRAMs are one of the most promising candidates for future RAMs.

I.1.1.1 Giant magnetoresistance (GMR) and tunneling magnetoresistance (TMR)

The giant magnetoresistance effect (GMR) is a direct consequence of spin-polarized transport in magnetic multilayers. The practical manifestation of the GMR effect is roughly as follows : when a current flows through a magnetic multilayer [1] the relative orientation of the magnetization of the layers will induce two distinct resistance states - a high resistance state when the layers magnetization are in anti-parallel (AP) configuration and a low resistance state when the layers magnetization are in the parallel (P) configuration.

The magnetoresistance ratio is defined as follows :

$$MR = \frac{R_{AP} - R_P}{R_P}, \tag{I.1}$$

where R_{AP} is the resistance in the antiparallel state (high resistance) and R_P is the resistance in the parallel state (low resistance) (see Fig. I.1).

Initially the MR effect was experimentally discovered in the "current-in-plane" configuration for a (001)Fe/(001)Cr (x10) multilayer[2], meaning that the current was flowing in plane of the layers. Now the most popular configuration is the "current-out-of-plane" type, where the current flows perpendicular to that plane, allowing for higher MR ratios. It is this configuration that is used as a basis for "spin-valves"(SV) used in the first type of read heads. The term "spin-valve" was coined in Ref. [16] and designates a structure made of two uncoupled ferromagnetic layers with in-plane anisotropy separated by a non-magnetic metal. The magnetic sandwich Co/Cu/Co is an example of SV, yielding a magnetoresistive (MR) ratio of 8.8 % at room temperature [14].

The spin-valve structure corresponds to one type of trilayer (ferromagnetic / non-magnetic / ferromagnetic) composition which gives rise to a noticeable magnetoresistive effect. Another type of magnetic trilayer structure can be used for studies of the STT : the *magnetic tunnel junction* (MTJ). Instead of the metallic spacer used in spin-valves, the spacer in a magnetic tunnel junction is an insulator. The main point of interest of MTJ is a much higher MR ratio called Tunneling Magnetoresistance (TMR) in the order of a hundred %, yielding a better sensitivity than spin-valves. TMR was first evidenced experimentally in 1975 by Jullière [38] at 4K in Fe/Ge/Co junctions giving a 14% MR ratio. Recent developments in materials science now yield TMR ratios at room temperature up to 500% in epitaxial CoFeB/MgO/CoFeB MTJ structures [17, 50].

We will make here a rapid review of the main theoretical models and the corresponding concepts that were proposed to explain the GMR and TMR effects.

1. The thickness of the magnetic layers must be on the nanometer scale

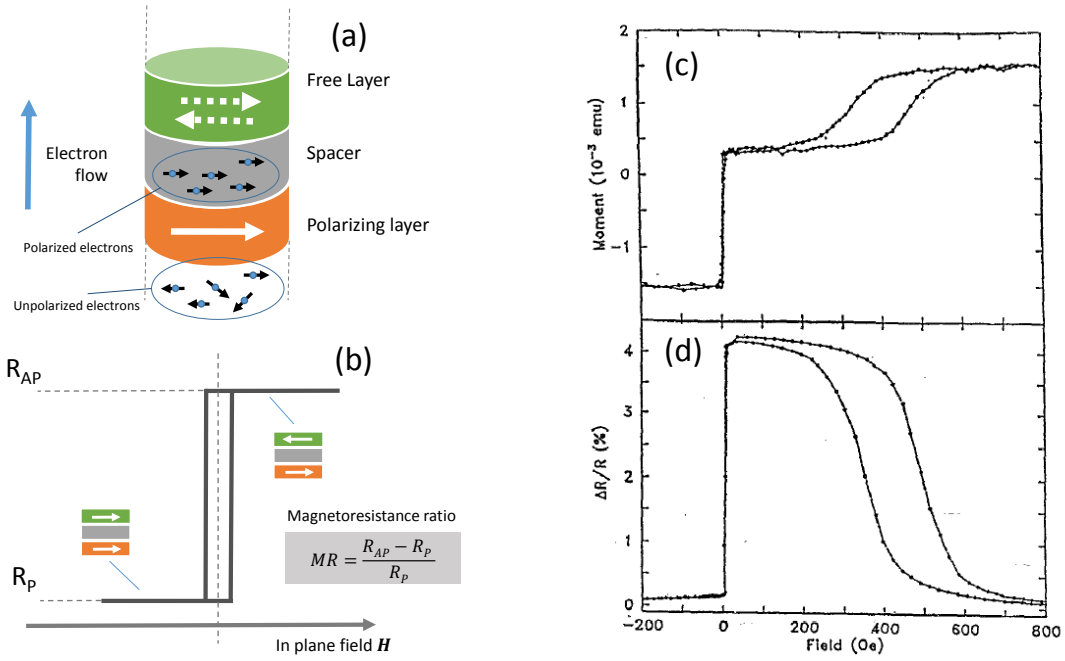

Figure I.1 – (a) Schematic representation of spin-polarized transport in a spin-valve structure. The magnetization of the bottom layer (polarizing layer) is fixed and electrons flowing through it have their spin polarized in that direction, while the direction of magnetization of the top layer (free layer) can be changed. (b) Magnetoresistance curve (schematic) showing the two resistances states : High resistance (AP configuration) and low resistance (P configuration). (c),(d) Experimental room temperature hysteresis loop (c) and magnetoresistive ratio (d) for a sample with a NiFe/Cu/NiFe sandwich structure. Field is applied in plane. From [14].

• **Spin-polarized transport : The two-channel model (Mott 1936)**.

This model relies on the distinction of two types of electrons in the ferromagnet depending on their electronic orbitals : the s orbital electrons (conduction electrons) and the d orbital electrons (localized electrons). It is the interaction between these two types of electrons which gives rise to spin-dependent transport. The s electrons are moving through the structure and will carry the information (spin up or down) from one ferromagnetic electrode to another. The d electrons carry the bulk angular momentum of the ferromagnet - they are at the source of the magnetization in the material.

In addition, both s and d electrons are split into two categories : *majority* and *minority* electrons. Majority electrons have their spin [2] oriented in the direction of the magnetization of the material, minority electrons have their spin oriented in the opposite direction.

The exchange interaction in ferromagnets creates a splitting of the d bands for majority and minority electrons. d bands can be considered like reservoirs for electronic states - due to exchange splitting, the d band for majority electrons is filled with more electronic states that the d band for minority electrons. All the occupied states (at the Fermi level but mostly below the Fermi level) in the d band contribute to the polarization of the material.

If we go back the s conduction electrons, a priori they do not have a preferred orientation (up/down). However through collisions with the lattice, (in particular the diffusion from s to d bands) majority or minority s electrons will end up in two separate ohmic channels. If we consider no spin-flip scattering [3], a minority s electron will diffuse in the minority d band, and a majority s electron will diffuse in the majority d band.

Now, because of exchange splitting, at the Fermi level the available density of states (DOS) in the d band is not the same for minority and majority electrons : typically it is *higher* for the minority d band. As a consequence, according to the Fermi rule, the probability that minority conduction s electrons diffuse is higher than majority conduction s electrons. In the end, minority electrons sense a *higher* resistance (collisions are more likely) and majority electrons sense a *lower* resistance (collisions are less likely), which leads to spin-polarized transport.

Let us now suppose electrons flowing in two identical, successive ferromagnetic layers whose relative orientation (P or AP) can be changed. Crossing one ferromagnetic layer gives a resistance r for a minority electron and R for a majority electron.

– **P orientation**.

Spin up : $R_{up} = R + R$

Spin down : $R_{down} = r + r$

$$R_P = R_{up}//R_{down} = \frac{2rR}{r+R}$$

– **AP orientation**.

Spin up : $R_{up} = R + r$

Spin down : $R_{down} = r + R$

$$R_{AP} = R_{up}//R_{down} = \frac{r+R}{2}$$

Using a phenomenological argument, we finally obtain $R_{AP} > R_P$.

2. In the manuscript, by spin we actually refer to the spin magnetic moment. For an electron, the spin magnetic moment $\boldsymbol{\mu}_s$ is in opposite direction to that of the spin$\boldsymbol{s}$ due to a negative Landé factor g

3. The *spin diffusion length* l_{sf} is the mean distance over which happen collisions affecting the electron spin. In the two conduction channels model, we consider that collisions do not affect the spin of the electron, which is the case when the thickness of the magnetic layers is smaller than l_{sf}.

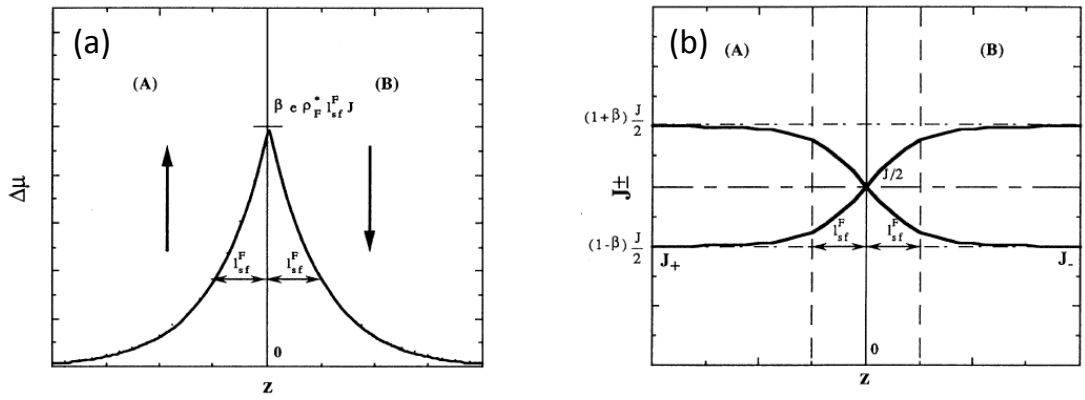

Figure I.2 – Illustration of the spin accumulation effect. Chemical potential $\Delta\mu$ (a) and current densities (b) J_+ and J_- versus z for an isolated interface separating two semi-infite domains with opposite magnetization. Spin-accumulation takes place within a area delimited by the spin-diffusion length l_{sf}. From [94].

- **Spin accumulation (GMR) : Valet-Fert model (1993)** [94] .

The previous model of the two conduction channels is simplistic in the sense that it only takes into account the bulk contributions of the ferromagnet to spin-dependent scattering. In addition, it is not valid when the magnetic layers are thicker that the spin-diffusion length [4]. The Valet-Fert model addresses this issue by introducing both volume and interfacial spin-dependent scattering at the boundary between either two ferromagnets with opposite magnetization direction or at the ferromagnet/non magnetic metal interface.

The notion that is introduced is the *spin accumulation* at the interface [5]. The idea is as follows : similarly to the Mott model, we consider two conduction channels for spin up and spin down electrons. However, we take into account here the possibility for the spin of a conduction electron to switch from one direction to another, which is designated by *spin-flip* process. We take the case of two semi-infinite ferromagnetic materials with anti-parallel orientation F1 and F2 with a current flowing perpendicular to the interface. Far from the interface, the current density for spin *up* electrons is $J_+ = J/2(1+\beta)$ for F1 and $J_+ = J/2(1-\beta)$ for F2 [6]. Likewise (far the interface), the current density for spin *down* electrons is $J_- = J/2(1-\beta)$ for F1 and $J_- J/2(1+\beta)$ for F2.

In the absence of spin-flip, this would create a discontinuity in current density at the interface F1/F2 for each spin channel. In order to avoid the discontinuity, electrons are progressively transferred from one spin channel to the other so that at the interface, the incoming spin *up* current density J_+ in F1 (resp. spin *down* current density J_- in F1) is equal to the outgoing spin *up* current density J_+ in F2 (resp. spin *down* current density J_- in F2). This is illustrated in Fig. I.2(b) [7]. Therefore, as one gets closer to the interface,

4. Considering two spin conduction channels remains valid, but the picture is more complicated since electrons can also scatter in states having opposite spin direction

5. The Valet-Fert model was not the first model using the idea of spin accumulation at the interface. It was initially proposed a few years earlier by Johnson *et al.* [37, 36] and also by Van Son *et al.* [95] in a less general context.

6. β is coefficient for asymmetry in spin-current $\beta = J_+/J_-$.

7. This process takes place within a limited area close to the interface which is given by the spin-flip length l_{sf}.

it is required to move electrons above and below the Fermi level, leading to an *excess* or a *lack* of electrons for spin up and spin down electrons and with respect to the bulk. This process is designated *spin accumulation*. Since this transfer has a certain cost in energy, it creates an additional shift of the chemical potential $\Delta\mu$ at the interface (Fig. I.2(a)). The electric field being proportional to the gradient of the chemical potential, an electric field is established at the interface, which in turn generates an interfacial resistance that contributes to the magnetoresistance of the stack.

- **Spin-Filtering in epitaxial MTJs (TMR) : Butler's model (2001)** [8] .

Following Jullière first observation of the magnetoresistive effect in MTJ, others groups reported later similar results using other materials. In particular, Moodera [61] and Miyazaki [59] obtained TMR ratios at room temperature of $11,8\%$ and 11% respectively. They used in both cases aluminum oxide for the barrier to obtain higher TMR ratios. Those ratios were explained with rather good agreement applying Jullière's model which was introduced at the time [8]. However, Jullière's model fails to describe the results obtained later on *epitaxial* MgO-based MTJ which experimentally yield much higher TMR ratios [50]. In 2001 Butler *et al.* proposed a model explaining why epitaxial MTJ are expected to yield those high TMR ratios. It relies on the conservation of the electron's wave function symmetry through the insulating barrier, which leads to a *spin-filtering* effect.

Let us take the example of two ferromagnetic Fe electrodes separated by an MgO barrier. If the structure is grown epitaxially, then the three layers have the (001) crystalline orientation. In (001)Fe at the Fermi energy, the available Bloch states for majority electrons have either a Δ_1, Δ_5 or a Δ_2' wave function symmetry whereas the available Bloch states for minority electrons have either a Δ_2, Δ_5 or a Δ_2' wave function symmetry [9]. All these states potentially contribute to the propagation of the electrons.

In parallel, the MgO barrier also has a (001) structure, so the electrons wave's function symmetry is preserved and the states mentioned above can be identified in the MgO barrier. However, only decaying evanescent states with $k \neq 0$ are allowed in the barrier : to know which states will contribute most to the conduction in the barrier, one has to pick states with the lowest decay rate. Typically, the state with the highest symmetry has the lowest decay rate.

For the (001) crystallographic orientation the Δ_1 state has the highest symmetry and will contribute most to the conduction in the barrier (see Fig. I.3). The interesting part is that, in the ferromagnetic electrodes, the Δ_1 state is available for majority electrons but *not* for minority electrons.

In the parallel configuration (see Fig. I.3(a)), the up channel (with symmetry Δ_1) carries an important amount of current in *both* electrodes *and* through the barrier, while the down channel electrons (without symmetry Δ_1) cannot pass the barrier. The sum of the two channels gives an overall *high* conduction. In the anti-parallel configuration (see Fig. I.3(b)), the up channel carries the current in the first electrode which passes through the barrier, but does not go through the second electrode because up electrons become now minority electrons (and the Δ_1 state is not available anymore). As before, the down

8. Jullière's phenomenological model relies on the assumption that ferromagnetic electrodes have a certain polarization P whereby the TMR ratio can be calculated

9. Compared to the previous picture of separate conduction s and localized d electrons in ferromagnetic materials, this is a more realistic description of electronic states that takes into account hybridization of the s and d bands.

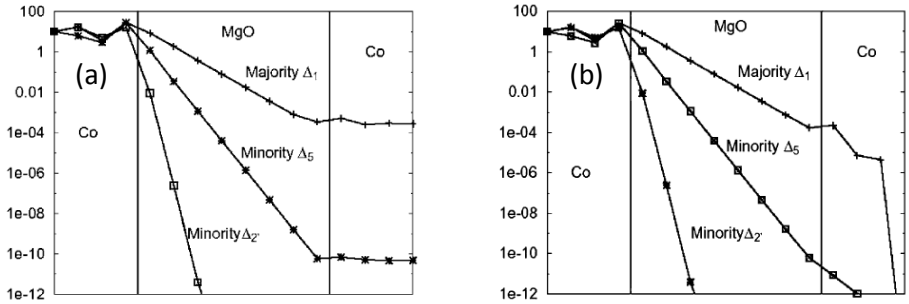

Figure I.3 – Bloch state density for bcc Co electrodes having a MgO barrier in between as a function of atomic layer number for (a) P alignement (b) AP alignement. Incident states come from the left. From [9].

channel electrons cannot pass the barrier. The sum of the two channels gives an overall *low* conduction.

In the end, two resistance states are obtained for P and AP configuration, which gives a magnetoresistive effect. To summarize, the difference in conduction for the two spin channels combined with selective decay rates in the barrier arising from wave function symmetry is at the source of the *spin-filtering* effect.

I.1.1.2 Spin-Transfer Torque

Up to now we have discussed the magnetoresistance effect in both spin-valves (GMR) and magnetic tunnel junctions (TMR). This effect is used for sensing the relative orientation of two ferromagnetic electrodes separated by either a metallic or insulating material. Usually one of the two ferromagnetic layers is pinned and serves as a polarizer while the other is free, meaning that its magnetization orientation can be changed. Before the discovery of spin-transfer torque (STT) and the related spin-current effects (Spin-Hall or Spin-orbit Torque), the means to change the orientation of the FL is to apply an external magnetic field which aligns the magnetization of the FL in the direction of the field.

The STT provides another way of controlling the magnetization of the FL - while the magnetoresistance can be seen as the effect of the magnetization state of the structure on the electron transport, the STT can be considered as the reciprocal effect, i.e. the effect of electron transport on the magnetization state of the structure. STT typically requires current densities in the order of 10^{10} to 10^{12} A/m^2, so that spintronic devices operating with the help of STT typically require lateral dimensions below 200 nm. STT is being used in several spintronic devices - most notably (i) STT-MRAM, which use current *pulses* in order to switch the magnetization of the FL from AP to P state (yielding 0 or 1 binary state) or, the subject of interest in this manuscript (ii) Spin-Transfer Oscillators (STO) which uses a *constant* current in order to induce steady-state precession of the FL.

There are several ways to give a picture of the STT effect. The first way involves a macroscopic approach, which is the level of description we limit ourselves to here, and the second is the microscopic approach which requires the calculation of spin-dependent reflection and transmission coefficient through the structure.

Later on in the manuscript we will use the Landau-Lifshiftz-Gilbert (LLG) equation to characterize the magnetization dynamics, in which a term for the STT will be included.

The macroscopic approach provides an explicative basis for the form of the STT term introduced in the LLG equation.

As usual, we consider two ferromagnetic layers F1 and F2 separated by a thin spacer, this time having their magnetization misaligned by an angle θ (Fig. I.4(a)). An electrical current passes through the structure from left to right.

We look at the system delimited by the two surfaces A and B in Fig. I.4(a) : due to spin-polarization, the electrons flowing in carry an angular momentum $\vec{\mu}_1$ aligned with $\vec{m}_1$ and electrons flowing out carry an angular momentum $\vec{\mu}_2$ aligned with $\vec{m}_2$. Then since the moment of the incoming electrons and of the outgoing electrons is not the same, some magnetic moment from the electrons (a vector $\vec{T}$, the difference of $\vec{\mu}_1$ and $\vec{\mu}_2$ [10]) has been transferred to the magnetization of the layers. The magnetic moment transferred then translates into a temporal change of the magnetization of F1 $d\vec{m}_1/dt$ and F2 $d\vec{m}_2/dt$ whose sum must be equal to it $\vec{T} = d\vec{m}_1/dt + d\vec{m}_2/dt$.

Now the norm of the magnetization of a given layer $\vec{m}$ does not change with time, so that any temporal changes of the magnetization must be perpendicular to the direction of the magnetization (see Eq. I.2). In addition the temporal change of the magnetization of each layer is directly linked with the *torque* $\vec{t}_m$ acting on it by the gyromagnetic ratio γ (Eq. I.3).

$$\frac{d|\vec{m}|^2}{dt} = 2\vec{m}.\frac{d\vec{m}}{dt} = 0, \tag{I.2}$$

$$\frac{d\vec{m}}{dt} = -\gamma\vec{T}'. \tag{I.3}$$

We can then decompose the transferred angular momentum $\vec{T}$ into two components, a torque acting on $\vec{m}_1$ perpendicular to it, $\vec{T}_1$, and another torque acting on $\vec{m}_2$ perpendicular to is as well, $\vec{T}_2$ (Fig. I.4(b)). Due to Eq. I.2, both are in the plane $(\vec{m}_1, \vec{m}_2)$ and the only possible option for the form of the torque $\vec{T}_1$ (resp. $\vec{T}_2$) is of the type $\vec{T}_1 = T_1\vec{m}_1 \times (\vec{m}_1 \times \vec{m}_2)$ (resp. $\vec{T}_2 = T_2\vec{m}_2 \times (\vec{m}_1 \times \vec{m}_2)$). Since we only consider the effect of spin-transfer here (there is no external magnetic field and the damping is not considered), these two torques are called *spin-transfer torques*.

I.1.2 Magnetization dynamics and the LLGS equation

We mentioned earlier that the STT enables the steady-state precession of a ferromagnetic layer using the flow of a constant current through a magnetic heterostructure, which is the basis of STOs. STOs rely on *self-sustained* oscillations of the magnetization : it means that a constant energy source (coming here from the current-induced STT) compensates the intrinsic magnetic damping to sustain magnetization oscillations over time. STOs are the first examples of a self-sustained oscillator based on the precession of magnetization.

However, the field of magnetization dynamics did not start with STOs. First, magnetization dynamics is a very broad topic which also includes non-precessional dynamics, i.e. domain wall motion or magnetization switching, and second self-sustained oscillations are one particular type of precessional dynamics.

10. In spite of the notation $\vec{T}$, $\vec{T}$ is not a torque. We cannot define an overall torque that would act on the same time on the magnetization of both layers T1 and T2

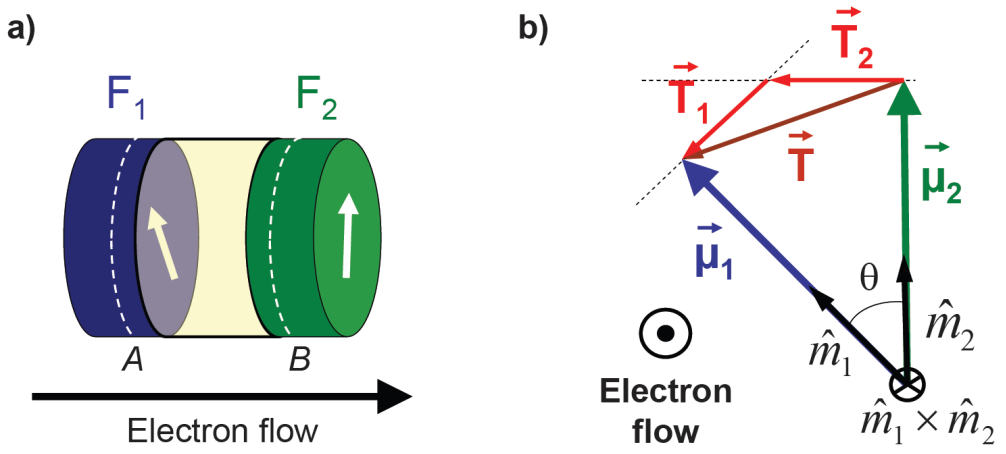

Figure I.4 – (a) Schematic representation of the system composed of two ferromagnetic layers F1 and F2 spaced by a non-magnetic layers. The planes A and B are far enough from the interface to consider that the electrons flowing into A and out of B are perfectly spin-polarized by respectively F1 and F2. (b) In the plane perpendicular to the electrons flow. Electrons flowing in have a magnetic moment $\vec{\mu}_1$ aligned with $\vec{m}_1$ and electrons flowing out have a magnetic moment aligned with $\vec{m}_2$. Transferred magnetic moment $\vec{T}$ to the system and its decomposition into two components, corresponding to spin-transfer torques $\vec{T}_1$ and $\vec{T}_2$. From [3].

The LLGS equation is used in order to model the precessional dynamics of the magnetization in magnetic layers. It is named after its four contributors, L. Landau, E. Lifshitz, T.L. Gilbert and J.C. Slonczewski. It was originally introduced in its elementary form by Landau and Lifshitz in 1935 to predict the motion of a single spin in Hamiltonian formalism. Later on in 1954, Gilbert modified the form of the equation to account for the damping using a phenomenological approach. Finally, after the discovery of the STT by Slonczewski in 1996, another term was added to the equation, accounting for the three aspects of the dynamics of the magnetization under current : *Precession*, *Damping* and *STT*[11].

We will restrict ourselves to the macrospin case, where the system we consider using the LLGS equation is a magnetic layer whose magnetization $\boldsymbol{M}$ [12] can vary in terms of direction but whose magnitude is constant. In other terms, all spins contributing to the magnetization of the layer are held parallel during the motion, which excludes the case of magnons with a wavevector $\boldsymbol{k} \neq 0$.

From a physical standpoint, the dynamics of the LLGS equation consist of the analysis of rotation of the magnetization direction in response to *torques*. Whether it is the precession, damping or anti-damping, all three contributions acting on the magnetization can be put in the form $\boldsymbol{T} = \lambda \boldsymbol{M} \times \boldsymbol{Q}$.

This simple form for the forces acting on the magnetization can actually lead to a variety of phenomena : the LLGS equation turns out to be an all-emcompassing nonlinear dynamical system whose analysis is challenging and must be solved numerically

11. The term added for the STT at the time only contains the one type of contribution, the longitudinal STT (the transverse STT is discussed at the end of the section)

12. From now in the manuscript the notation for vectors is bold symbols $\boldsymbol{M}$ instead of up arrow $\vec{M}$.

in most cases. Mathematically, the LLGS equation will be in our case a system of three non-linear ordinary differential equations for the magnetization coordinates (m_x, m_y, m_z).

To analyze the LLGS equation, we will look at the equation by adding subsequently the precession, the damping and the anti-damping contributions. Here for simplicity we will not look specifically at the types of motion and dynamical behaviour that can obtained using this equation, but in the second chapter a detailed analysis of the in-plane precession (IPP) will be performed.

- **Conservative dynamics**

In contrast to the damping and the anti-damping, the precession term corresponds to a motion of the magnetization along energy equipotentials, meaning that during this motion the system does not gain or lose any energy. Obviously this depicts an ideal case where there are no losses :

$$\frac{d\boldsymbol{M}}{dt} = -\gamma(\boldsymbol{M} \times \boldsymbol{H}_{\text{eff}}) \tag{I.4}$$

Here γ is the gyromagnetic ratio and $\boldsymbol{H}_{\text{eff}}$ is the effective field [13]. The effective field will define the axis around which the magnetization rotates (see Fig. I.5(a)). However, this effective field is usually a function of the direction of the magnetization, which usually makes the magnetization motion more complex than a circular motion.

- **Non-conservative dynamics**

The other two terms in the LLGS equation are the damping and the STT. Usually these terms are much smaller in amplitude than the precession term, and they are also called perturbative terms.

Damping term

$$\frac{d\boldsymbol{M}}{dt} = -\gamma(\boldsymbol{M} \times \boldsymbol{H}_{\text{eff}}) + \gamma\frac{\alpha}{M_s}\boldsymbol{M} \times \frac{d\boldsymbol{M}}{dt}. \tag{I.5}$$

Eq. I.5 shows (second term of the RHS of the equation) the damping term arising from magnetic relaxation in addition to the precession term. Fig. I.5(b) illustrates the effect of the damping on the dynamics : the energy is dissipated and the magnetization relaxes back to the static equilibrium position, i.e., with $\boldsymbol{M}$ and $\boldsymbol{H}_{\text{eff}}$ aligned.

The characteristic quantity that determines the intensity of the damping is the dimensionless Gilbert damping factor, α. A way to analyze α is looking at it as the sum of two contributions : an intrinsic damping and an extrinsic damping. The intrinsic damping depends on the material properties, for example it is not the same for Permalloy, Cobalt, or other magnetic alloys. Typically it is in the range of 0,01. On the other hand the extrinsic damping arises from external factors such as spin-pumping [24, 76] and typically enhances the damping with respect to its intrinsic value. Finally, we mention magnon-magnon interactions, which can lead to changes in both the intrinsic and extrinsic value of the damping factor α.

13. The effective field $\boldsymbol{H}_{\text{eff}}$ is the variational derivative of the magnetic free energy. The magnetic free energy is a sum of several contributions which are detailed in the IPP case in the second chapter.

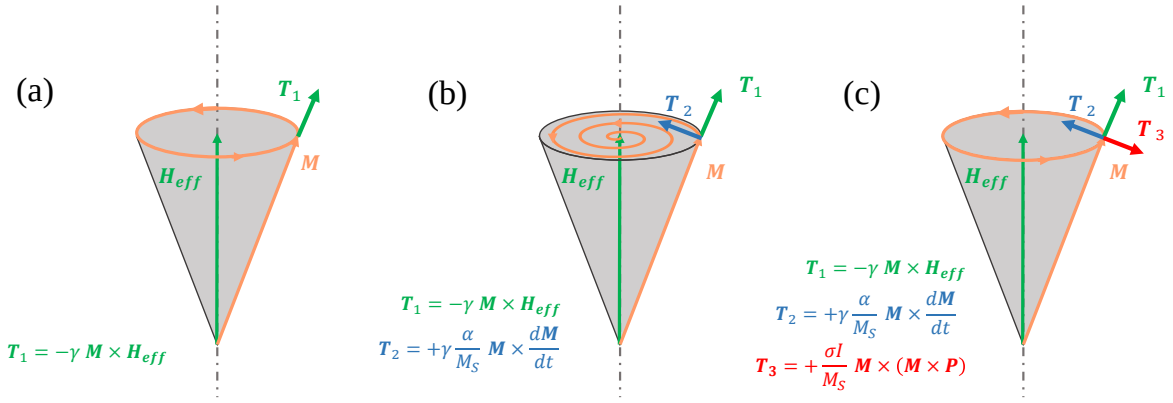

Figure I.5 – Schematic representation of the motion of the magnetization $\boldsymbol{M}$ in light red according the LLGS equation. (a) Precession torque $\boldsymbol{T}_1$ only : the magnetization $\boldsymbol{M}$ precesses around the effective field $\boldsymbol{H}_{eff}$ following a circular trajectory of constant energy. (b) Precession and damping torque $\boldsymbol{T}_2$. The damping causes dissipation of the energy, and as a consequence the magnetization spirals back to the static equilibrium position. (c) Precession, damping and Spin-Transfer Torque $\boldsymbol{T}_3$. Here the STT acts as a source of energy which fully compensates the damping. As a consequence, energy is conserved and the magnetization precesses.

STT term

$$\frac{d\boldsymbol{M}}{dt} = -\gamma(\boldsymbol{M} \times \boldsymbol{H}_{\text{eff}}) + \gamma\frac{\alpha}{M_s}\boldsymbol{M} \times \frac{d\boldsymbol{M}}{dt} - \frac{\sigma I}{M_s}(\boldsymbol{M} \times (\boldsymbol{M} \times \boldsymbol{P})) \tag{I.6}$$

Eq. I.6 is the form of the LLGS equation that we will use to analyze the magnetization dynamics in the rest of the manuscript, which takes into account the STT contribution as well. Here, σ is a coefficient that measures the STT strength. This coefficient can be calculated from the magnetic properties of the excited layer, such as its spin-polarization efficiency, its saturation magnetization and its thickness (see formula 4.b in Ref [83]). In parallel the STT is also proportional to the current flowing through the layer I [14]. Finally, $\boldsymbol{P}$ indicates the direction of polarization of the current. In a trilayer FM/NM/FM structure, $\boldsymbol{P}$ is given by the direction of the magnetization of the polarizing layer (which is fixed).

The STT is required to maintain self-sustained oscillations of the magnetization, because it works as an energy source that will counterbalance the losses due to the damping. Typically the polarization direction $\boldsymbol{P}$ and the current sign are chosen so that along the trajectory of the magnetization the STT is in opposite direction with the damping torque (as in Fig. I.6). Otherwise the STT acts as a supplementary damping, forcing the magnetization to its static equilibrium state at a faster rate.

Compensation of the damping by the anti-damping is achieved for a sufficient current density, which marks the threshold for self-sustained oscillations. As we mentioned earlier this current density is of the order of 10^{10} to 10^{12} A/m^2 in typical STO geometries. This

14. Actually it is the current density rather than the current that is meaningful. Indeed, written in this form the prefactor σ is inversely proportional to the area of the magnetic layer.

current is called the *critical current* and its determination in various configurations of STOs, whether in experiments or simulations, is a required step for the characterization of STOs. [15]

We conclude with a remark on the STT term in the LLGS equation. In Sec.I.1.1.2, we provided physical arguments explaining why the STT has this particular form, but it is a macroscopic picture that accounts for the longitudinal spin-torque only. Going to the microscopic level, the STT actually manifests itself as the sum of a longitudinal *and* transverse STT. While the longitudinal STT was predicted in first instance by Slonczewski[85] and Berger[5] in 1996, Zhang *et al.* demonstrated later in Ref. [102] that a transverse STT must be taken into account as well.

The transverse STT has the following form in the LLGS equation :

$$\boldsymbol{T}_{\perp} = -\gamma_0 b_j \boldsymbol{M} \times \boldsymbol{P}. \tag{I.7}$$

By analogy to the effect of a magnetic field to the dynamics, the transverse STT is also called *field-like* torque, as it acts as if an additional field of amplitude b_j and direction $\boldsymbol{P}$ was applied. Typically, the transverse STT is of much smaller magnitude than the longitudinal STT so in most cases the transverse STT is neglected in the LLGS equation. This is especially true in spin-valves, but in MTJ the transverse STT is expected to be of higher magnitude and can affect the dynamics. Notably the bias dependence of the transverse and longitudinal STT in MTJ have been examined theoretically [88, 31] and measured experimentally [32], and indicate that for appropriate bias both torques can be of similar magnitude.

However, the role of transverse STT on the dynamics is beyond the scope of in this manuscript ; from now on we will neglect the influence of the of transverse STT with respect to the longitudinal STT.

I.2 Self-sustained oscillators : Autonomous dynamics

Up to now we have introduced the basic concepts and ideas behind magnetization dynamics and the spintronics that will be necessary to understand the functioning of the STO. But in contrast to other spintronic devices, the STO presents distinctive features which makes it a self-oscillating system. Most notably, it does not require that an external RF magnetic field or RF current is applied so that oscillations of the magnetization are sustained in time.

So in order to appreciate some essential properties of the STO, we will discuss in this section the main aspects of self-sustained oscillators in the framework of non-linear dynamics. Moreover an important motivation of this thesis is to explore synchronization mechanisms in STOs, and to do so the first step is to clarify simple notions such as phase and amplitude in self-sustained oscillators.

First we will give a general introduction on self-sustained oscillations and examples in nature. Then we review some properties of self-sustained oscillators and what differentiate them from other types of oscillators along with the related mathematical notions. In

15. Obtaining the critical current as a function of the applied field is a typical exercise. It allows one to draw *state diagrams* to visualize the boundaries between static and dynamical states of a STO [42, 35, 28].

particular the distinction between isochronous and non-ischronous oscillations is briefly discussed. Finally, the KTS model for STO dynamics in autonomous regime is introduced.

I.2.1 Introduction to self-sustained oscillations

To start with, I would like to point out that the contents in this section and the next one on synchronization of self-sustained oscillators are inspired in large part by the excellent textbook and review from A. Pikovsky, M. Rosenblum and J. Kurths on synchronization phenomena. It provides intuitive physical insight in simple systems where mathematics can be kept to a minimum (Part I) as well as a detailed review of these systems - and more complex ones - on a quantitative level (Part II and III). It has been a very valuable source of information and understanding throughout my thesis in a field I was not familiar with. The interested reader is greatly encouraged to explore further the aspects that we discuss here in ref. [67].

What are the common points between a firefly that emits pulses, a person on a swing, a beating human heart, or a Spin transfer torque oscillator ? These systems all share an essential property : they continue generating a steady rhythm when they are taken apart from their environment, which is what we designate by *self-sustained* oscillations. To maintain these oscillations, these systems must have an internal source of energy to compensate for the dissipation which damps out oscillations.

Self-sustained oscillators are a subset of a larger group of dynamical systems that are called *non-linear* systems ; mathematically, these systems are modeled by non-linear differential equations [16].

In self-sustained oscillators, the periodicity of their oscillations is a property of the system. We make the distinction between two types of oscillating systems which share the same feature of maintained oscillations over time : (i) *autonomous* systems, namely self-sustained oscillators ; (ii) *forced* systems, typically systems have a *resonating* element on top of which the application of a periodical, external stimulus must be applied to sustain oscillations.

In the case of ferromagnetic resonance (FMR) experiments, we certainly observe sustained oscillations of the magnetization over time, but it is only due to the maintained application of an external periodical stimulus providing the energy, the RF magnetic field. The periodicity of the magnetization oscillation is determined uniquely by the periodicity of the RF field. Then it makes the piece of ferromagnetic material a forced oscillating system, and not an autonomous system.

In contrast, the STO, if we take the system made of the three layers FM/NM/FM, is an autonomous/self-oscillating system and not a forced system. Like the FMR setup, it relies on sustained oscillation of the magnetization of a piece of ferromagnetic material (the FL), but in that case the periodicity of the oscillations is not fixed by the periodicity of an external stimulus providing energy, but it is rather an internal property of the STO. Here the source of energy (the current) is a *constant* stimulus which does not force the oscillation to a specific periodicity. Simply put, it is a given combination of the applied current I and the applied field H that sets up a working point of the system (I_0, H_0) which in turn determines the periodicity of the magnetization oscillations. The

16. In contrast with other *linear* oscillators that do not contain a source of energy and can be modeled by linear differential equations. However linear oscillators are not autonomous systems and cannot generate a rhythm on their own.

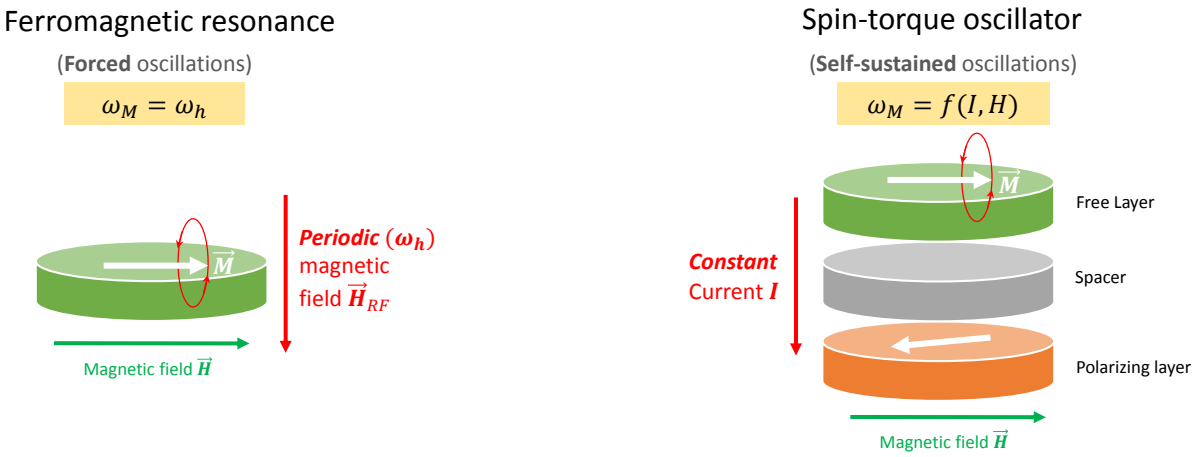

Figure I.6 – Comparison between two systems for FMR and a STO. In both cases, oscillations of the magnetization (with frequency ω_h) are sustained over time. For FMR, the source of energy is an *oscillating* magnetic field whose frequency ω_h determines that of the magnetization oscillations ($\omega_m = \omega_h$), corresponding to the case of a forced system. For the STO, the source of energy is a *constant* current, and the frequency of the magnetization oscillations is an internal property of the system ($\omega_M = f(I, H)$).

comparison between FMR and the STO is schematically illustrated in Fig. I.6.

We finish by examples in biology. On one hand, there is the periodical stimulus that any living body experiences on Earth, the 24 hours cycle of day and night. On the other hand, the behavior of human and animals is regulated by a similar 24 hours cycle of rest and activity, sleep and wakefulness, which is called the *circadian rhythm*. The circadian rhythm is also responsible for the timely production of the appropriate hormones, or adjustment of the body heat depending on the time of the day. Then the question comes up : what happens to the circadian rhythm and the body when the external stimulus, the 24 hours alternation between light and dark, is turned off ?

J.J. De Mairan was the first scientist to investigate this question in 1729 by making experiments on haricot beans. He noticed that the leaves of his plant were moving up and down at specific moments during the day. Then he put the same plant in a closed environment to check whether or not leaves were continuing to move in the absence of an external day/night cycle. He did find that the leaves were continuing the same motion without information from the outside. Likewise, later on experiments with animals and humans have shown that the circadian rhythm still exists in the absence of the 24 hours light and day cycle.

It indicates that living systems do have an internal biological clock that is regulated by the environment, but does not necessary need it to continue operating. Then in living systems the circadian rhythm is generated by a type of biological clock that is an active, self-sustained oscillator. Evidently the situation in living systems is quite complex ; if we take the case of humans, quantification of the circadian cycle is a challenging task and varies from one individual to another, from 13 to 65 hours in extreme cases [62, 11].

I.2.2 Periodic oscillations : mathematical concepts

I.2.2.1 Representation of an oscillator : limit cycle and complex variable

An oscillator generates a periodic output. Mathematically, this periodic output can take the form of an oscillating variable, say $x(t)$. It can represent any physical quantity depending on the type of oscillator, the angle of a clock's pendulum, body temperature in a living being, or magnetoresistive voltage in the case of the STO.

In order to describe the state of the oscillator at any moment of time, we start by measuring the value of $x(t)$. However knowing $x(t)$ is not sufficient to completely describe the state of the oscillator, because for a given $x(t)$ it may be in "ascending" (derivative of x with time is positive) or "descending" (derivative of x with time is negative) state. We need at least one other variable to describe the state of the oscillator, and two is a minimum. For the STO, we need a priori three variables to fully describe the system : the three spatial coordinates of the magnetization m_x, m_y, m_z [17].

Now let us suppose that our oscillator can be completely described by the time-evolution of the couple (x,y). We can plot the $x(t)$ and $y(t)$ variables in the same graph (see Fig. I.7(a)). For periodic oscillations we obtain a plot that is a closed curve in the (x, y) plane, and this closed curve is called the *limit cycle*. Here for simplicity we consider a circular limit cycle, but in general the limit cycle has an arbitrary shape.

It is not practical to analyze the properties of the oscillation using only variables x and y. There are two essential characteristics of periodic oscillations : the intensity of the oscillations and their periodicity. The intensity of the oscillations is measured by the *amplitude* A, while their periodicity is measured by either the *period* T or the inverse quantity the *frequency* $f = 1/T$.

In the stationary state, both of these quantities, the amplitude and the period, are stable and do not change with time. Now how can we define a constant amplitude and period from oscillating variables x and y ?

In the general case (an arbitrary limit cycle) this is a difficult task that may require careful changes of variables [18]. However for a circular limit cycle, it is quite simple. We consider the complex number $a(t) = x(t)+iy(t)$, and we switch from the Cartesian coordinates to polar coordinates. Then we obtain $a(t) = A\exp(i\phi(t))$, with $A = \sqrt{x(t)^2 + y(t)^2}$, the modulus of $a(t)$, which gives a constant value for A, the intensity of the oscillations. Likewise, $\phi(t) = \arctan x(t)/y(t)$.

$\phi(t)$ is the *phase* of the oscillator, which is 2π periodic. The time required for the phase to make one round trip of the limit cycle is always the same in the stationary regime, and this time is the period of the oscillation T. The phase can be written as $\phi(t) = \omega_0 t + \phi_0$, where ω_0 is the *angular frequency* linked to the period by $\omega_0 = 2\pi/T$. In Fig. I.7(b), the notion of phase and the amplitude are pictured on the limit cycle.

17. The macrospin approximation enables the use of two coordinates instead of three. Indeed, it considers that the norm of the magnetization is constant, so that with the supplementary constraint $\sqrt{m_x^2 + m_y^2 + m_z^2} = 1$, two variables are sufficient to analyze the dynamics.

18. In the second chapter of this manuscript, the change of variable from the magnetization coordinates m_x, m_y, m_x to a complex variable $c(t)$ is examined in detail for the IPP precession.

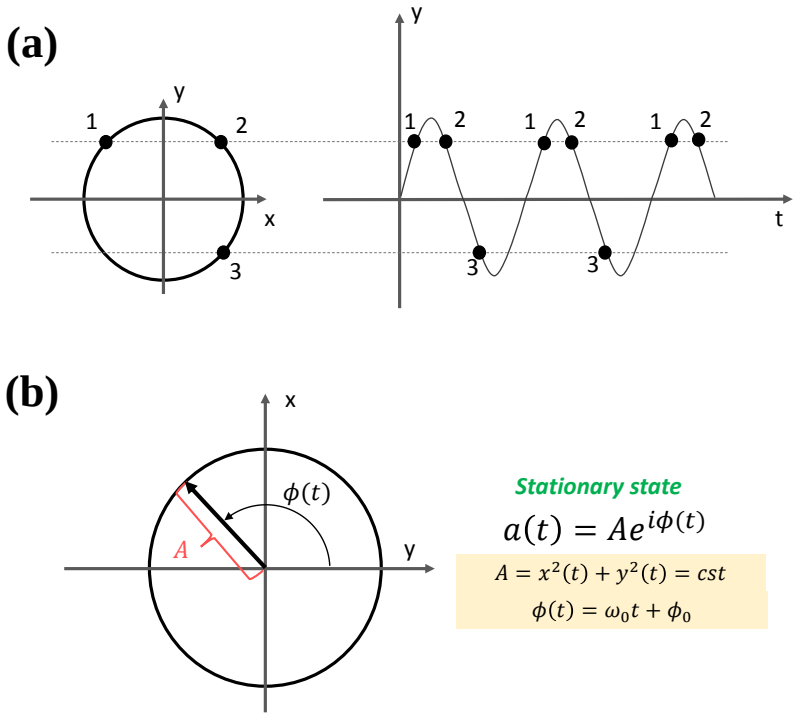

Figure I.7 – Periodic oscillations for a circular limit cycle. (a) Limit cycle and corresponding time-evolution of the variable $x(t)$. Oscillator states 1 (ascending motion) and 2 (descending motion) are different but the variable $x(t)$ has the same value for both states. One also has to know about $y(t)$ to fully describe the oscillation. (b) Visualization of the *phase* ϕ and *amplitude* A of the oscillation using the limit cycle. In that case the use of complex variable $a(t)$ for the analysis is appropriate

I.2.2.2 Stability of phase and amplitude in self-sustained oscillators

The phase and the amplitude are concepts that apply equally for any type of oscillator - whether we have an harmonic oscillator, a self-sustained oscillator or a damped oscillator, we should always be able to define at a given moment t its phase and its amplitude.

We mentioned that self-sustained oscillations rely on the balance between the energy source and the dissipation. The energy source is characterized by the anti-damping rate Γ_- and the dissipation by the damping rate Γ_+ [19]. Usually, the anti-damping rate depends on the physical quantity that provides energy to the system : for an STO Γ_- is proportional to the applied DC current I. So when energy is supplied, Γ_- increases until $\Gamma_- = \Gamma_+$, which marks the threshold for the onset of self-sustained oscillations. The critical current I_C measures this down limit for the energy supply : only for $I_{DC} \geq I_C$, the STO enters the sustained regime of oscillations.

Typically, for $I_{DC} = I_C$ the oscillation amplitude is zero and the limit cycle is reduced to a point. As the energy source builds up the oscillation amplitude increases. At this time the non-linearity of the system intervenes to stabilize the amplitude of the oscillations. In the absence of non-linearity, the oscillation amplitude would increase indefinitely. [20]. This non-linearity translates into a dependence of the damping rates on the amplitude A, $\Gamma_-(A)$ and $\Gamma_+(A)$, so that when the energy supply is increased, oscillations stabilize at an amplitude A given by $\Gamma_-(A) = \Gamma_+(A)$.

Now we consider the effect of a perturbation on the dynamics (Fig. I.8). In the stationary state, the amplitude of the oscillations is A. Suppose a disturbance in the system is causing the amplitude to be modified by $\pm dA$. To illustrate we take a positive perturbation in amplitude, i.e. $+dA$. Then the damping rates are $\Gamma_+(A + dA)$ and $\Gamma_-(A + dA)$. Looking at Fig. I.8(a), we see now that for an amplitude $A + dA$ the dissipation is more important that the energy source, giving $\Gamma_+(A + dA) > \Gamma_-(A + dA)$. At that point the system is not supplied enough energy to sustain oscillations with an amplitude $(A + dA)$, so that it diminishes its amplitude until there is enough energy to compensate the dissipation. Finally, it stabilizes at an amplitude A when the energy supply and the dissipation are balanced. The reversed reasoning explains the effect of a negative perturbation $-dA$ on the amplitude.

In Fig. I.8(b) and (c) (respectively $+dA$ and $-dA$), the effect of the perturbation on the trajectory in the phase plane is represented. We see that in both cases, after the perturbation is applied the phase point relaxes in a spiraling motion to the limit cycle - this is why the limit cycle is called an *attractor* of the limit cycle.

Here, we have provided an explanation as to how the amplitude responds to a perturbation - the non-linearity provides a feedback mechanism which stabilizes the amplitude, which relaxes back to the equilibrium value A. Now how about the phase ? Consider a disturbance that does not modify the amplitude, but pushes the phase at little ahead or behind its usual motion. How does the system respond ? In contrast to the amplitude, the non-linearity in the system does not provide a feedback that damps out the perturbation in the phase. Indeed, the phase has the expression $\phi(t) = \omega_0 t + \phi_0$ - it is equivalent to change the initial phase from ϕ_0 to ϕ_1 - and there is no preferred value. This is why we

19. An analysis of these terms for a STO will be performed when the KTS model is introduced.

20. A typical example of "infinite" amplification of oscillations is the case of an amplifier plugged to a microphone and a speaker. When the microphone is put close to the speaker, one hears a loud noise that corresponds to an excessive amplification of a registered buzz.

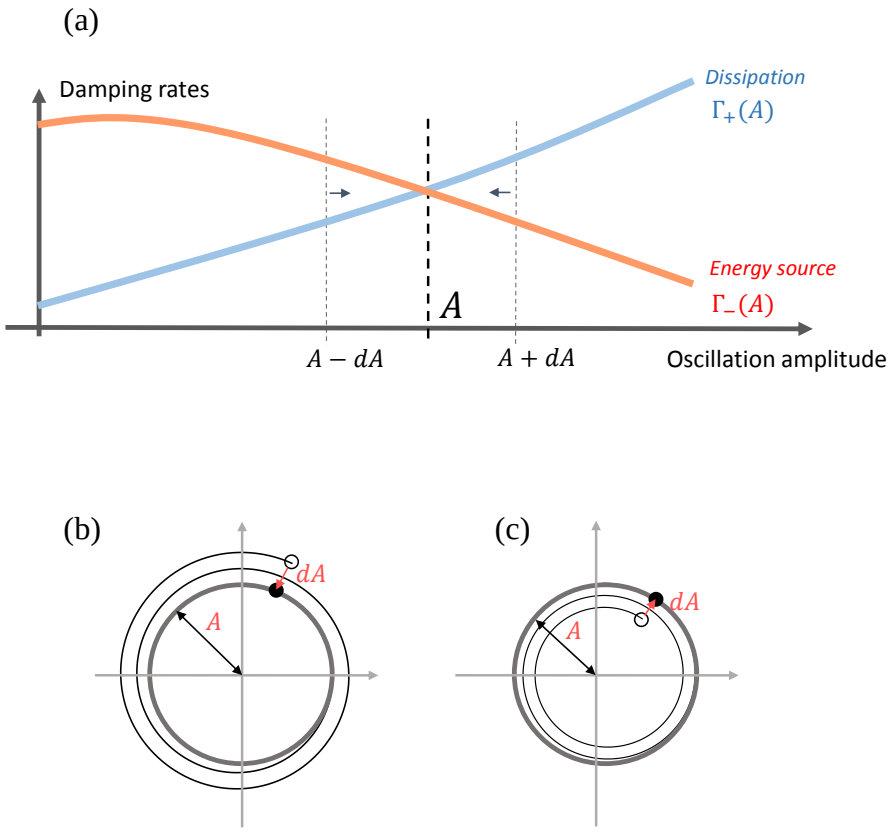

Figure I.8 – Effect of a disturbance dA in amplitude on self-sustained oscillations. (a) Interplay between the energy source and the dissipation. The amplitude A is stabilized for $\Gamma_+(A) = \Gamma_-(A)$. (b), (c) Influence on the dynamics in the phase plane (b) for a positive perturbation $dA > 0$ and (c) for a negative perturbation $dA < 0$.

say that the phase is in *neutral equilibrium*.

The difference between the response to a perturbation of the phase and the amplitude can be summarized as follows : the phase is free, and the amplitude is stable. The "freedom" of the phase in self-sustained oscillators explains why the thermal noise leads to a random-walk type of phase noise, and more importantly for us, it means that the phase of the oscillator can be easily adjusted by the action of an external force, thus enabling synchronization phenomena in oscillators.

I.2.3 The KTS model in autonomous regime for a STO

I.2.3.1 Introduction to the KTS model

At this point we have not introduced a mathematical formulation for the dynamics of a self-sustained oscillator. Nevertheless we mentioned that, for a quasilinear oscillator, we can use a complex variable $a(t) = A\cos(\omega_0 t + \phi_0)$ to analyze essential oscillator quantities such as the phase and the amplitude.

For an STO, the physical quantity that oscillates is the magnetization. Then in order to treat a STO as a self-sustained oscillator, the idea is to find a way to convert the magnetization coordinates (m_x, m_y, m_z) into a complex oscillator variable. Using this new variable, the corresponding limit cycle for the dynamics will be a circle (or very close to it). Now magnetization dynamics are governed by the LLGS equation - by using this change of variables, it is a priori possible to rewrite the LLGS equation into a non-linear equation typical of self-sustained oscillator dynamics.

This motivation is behind the formalism developed by J.V. Kim, V. Tiberkevich and A. Slavin for Spin-Torque oscillators [83], which we refer to as the *KTS model*. This formalism was initially introduced by A. Slavin in 2005 which has been since then the most consistent contributor to the model. It is now an important reference in the field of STO dynamics. In particular, the formalism developed within the KTS model has been for me an indispensable aid for the appreciation of the STO dynamics, and it is the foundation on which the findings of this thesis have been constructed.

In the first stages, the model provided good agreement with some key, elementary experimental results for STOs in autonomous regime : dependence on the threshold current with the applied field [84], on the generated microwave power with applied current [91], and on the generation linewidth with field and current [40, 41]. In addition, predictions were made in [80] for the synchronization of an array of coupled STOs via microwave current.

In 2008, the change of variables from the magnetization coordinates to the oscillation variable is exposed in detail, as well as the corresponding transformation of the different terms (precession, damping, and STT) in the LLGS equation. It is the theoretical basis of the model and relies on classical Hamiltonian formalism for spin waves [82].

Then in 2009 a thorough review of the model was formulated in 30 pages [83], exposing its features as well as summarizing the findings. The interested reader is encouraged to further investigate this paper, as (i) it presents the general approach for oscillations for several types of configuration of a STO [21] and (ii) we will only limit ourselves here to a qualitative description of the model and a few of its features [22].

21. In the second chapter we will apply the KTS formalism *only* for one particular type of configuration, the in-plane precession.

22. For instance, the influence of noise on the dynamics will not be addressed.

Lately the KTS formalism has been used for the analysis in more complex configurations amongst which : (i) non-macrospin configurations of a STO [26, 87] (ii) non-autonomous and transient dynamics [22, 103, 104, 19] (iii) Spin-Hall oscillators [12].

I.2.3.2 Features of the KTS model in the autonomous regime

Here we present the essential features of the KTS model in the autonomous regime. We also underline one of the most distinctive aspects of the STO compared to other self-sustained oscillators : the significant coupling between phase and amplitude via the non-linearity N, and its influence on the dynamics.

According to the KTS model, the equation of motion for a self-sustained oscillator in autonomous regime reads :

$$\frac{dc}{dt} = -i\omega(p)c + \Gamma_+(p)c - \Gamma_-(p)c. \tag{I.8}$$

Here, the complex oscillator variable is $c = \sqrt{(}p) \exp i\phi$. p is the power, which is simply the square of the amplitude of the oscillations $|c|$. $\omega(p)$ is the generation frequency of the oscillator, $\Gamma_+(p)$ is the damping rate (the dissipation), and $\Gamma_-(p)$ is the anti-damping rate (the energy supply). c is a dimensionless variable, while ω, Γ_+ and Γ_- are in units of angular frequency (rad/s).

We obtain a system of coupled first order differential equations [23]. Nevertheless, it is a non-linear equation in c because of the dependence of the terms of the RHS of the equation on p, so straightforward calculation of an analytic solution is a priori not possible. If we make a quick analogy with the LLGS equation, the KTS formulation has a similar form and we can make the equivalence between (i) Precession and generation frequency $\omega(p)$ (ii) Magnetic damping and dissipation $\Gamma_+(p)$ (iii) STT and energy supply $\Gamma_-(p)$.

By multiplying both sides of Eq. I.8 by the complex conjugate c^*, we obtain a set of two real, differential equations for the amplitude and the phase of the oscillations :

$$\begin{aligned} \frac{dp}{dt} &= -\,2\left[\Gamma_+(p) - \Gamma_-(p)\right] p, \\ \frac{d\phi}{dt} &= -\,\omega(p). \end{aligned} \tag{I.9}$$

We make a few remarks for the stationary state ($dp/dt = 0$) : (i) the balance between energy supply and dissipation is verified by since we obtain $\Gamma_+(p) = \Gamma_-(p)$ (the RHS of the amplitude equation is zero) and (ii) the angular frequency $d\phi/dt$ is stable as well [24].

Up to the first order in p, we explicit the form of the generation frequency and damping rates (for an obliquely magnetized STO[83]),

$$\omega(p) = \omega_r + Np, \tag{I.10}$$
$$\Gamma_+(p) = \Gamma_0(1 + Qp), \tag{I.11}$$
$$\Gamma_-(p) = \sigma I(1 - p), \tag{I.12}$$

where, in the first line, ω_r is the resonant frequency (the FMR frequency in macrospin

23. c is a complex variable, and it is the sum of the real and cthe complex components.
24. Careful : the angular frequency $d\phi/dt$ is *negative* in KTS formalism.

approximation), ranging from a 100 MHz in Vortex-based STO up to several tens of GHz for in-plane magnetized STOs, and N is the non-linearity. In the second line, Γ_0 stands for the damping prefactor which is proportional to the Gilbert damping α, and Q is the damping non-linearity. In the third line σ is a quantity that measures the STT intensity and I is the applied DC current which supplies the energy to sustain the oscillations.

Let us make a few remarks. First, this form is an approximation that uses a Taylor expansion in powers of p, so it is implicitly assumed that the power p remains small, and the domain of validity of the approximation is something to be examined case-by-case. In the third chapter of the manuscript where we conduct macrospin simulations, we make sure the power p is below 0.3. Second, the non-linear parameters, here N and Q, depend strongly on the STO configuration : (i) the magnetic properties of the free-layer (saturation magnetization M_S, thickness ...) but also (ii) control parameters setting the STO working point, notably the applied magnetic field $\boldsymbol{H}_a$ direction and amplitude. A remarkable difference is the change of sign of the non-linearity N when the magnetization goes from in-plane (negative shift) to out-of-plane (positive shift) oscillations [83].

In addition, using this formula we can calculate analytically some interesting quantities. The *critical current* I_c corresponds to the threshold for the onset of the oscillations. By equating $\Gamma_+(p=0) = \Gamma_-(p=0)$, the critical current I_C reads

$$I_C = \Gamma_0/\sigma. \tag{I.13}$$

For $I > I_C$, the power p of oscillations can be calculated analytically as a function of the current I using again $\Gamma_+(p) = \Gamma_-(p)$. Using the notation of [83] for the supercriticality $\zeta = I/I_C$, and the Taylor expansion of Eq. I.10, the power p reads

$$p = \frac{\zeta - 1}{\zeta + Q}. \tag{I.14}$$

- **Oscillator parameters**

1/ *Non-linearity N*

The non-linearity $N = d\omega/dp$ is arguably the most important parameter of the STO. It is also called *phase-amplitude* coupling, or agility of the oscillator. Contrary to "conventional" self-sustained oscillators where it is assumed that N is very small (*isochronous* or *quasilinear* oscillators), the non-linearity N can be substantial in STOs (*non-isochronous* oscillators). In STOs the non-linearity essentially works one-way, from the amplitude to the phase and the effect can be summarized in a very general way : *the modification of the amplitude of oscillations induces changes in the phase.*

This has far-reaching consequences on the dynamics of the STO, namely : (i) Strong dependence of the generation frequency on the amplitude. When the oscillation amplitude grows from 0 to p_0, we witness a frequency-shift in the generation frequency of Np_0. Experimentally it translates into a change of the generation frequency with the applied current [69, 13, 33, 56, 47]. Typically the agility in current ranges from ten to a few hundreds of MHz/mA. (ii) Linewidth broadening. Non-linear linewidth broadening has been theoretically explained using the idea of "renormalization of the phase noise" [41, 40]. It has been followed and experimentally verified by the works of Quinsat *et al.* using time-frequency measurements of the noise [71, 73]. (iii) Synchronization properties. It is the subject of this thesis and will be examined in depth throughout the manuscript.

2/ *Amplitude relaxation rate* Γ_p

The amplitude relaxation rate Γ_p indicates the characteristic time required for a small perturbation in amplitude to be damped out. This quantity is especially important when one studies the effect of noise on the system, or more generally the effect of an external signal on the STO. Simply put, Γ_p works as a cutoff frequency ($f_p = \Gamma_p/2\pi$) : when the noise frequency f_n is below f_p we observe a random-walk type for the phase noise PSD ($1/f^2$), close to f_p it decreases sharply by following a $1/f^4$ dependence, then stabilizes back to a $1/f^2$ dependence for $f_n >> f_p$ [71].

The amplitude relaxation rate is simply worked out by solving the amplitude equation of Eq. I.9 for small power deviations, $p = p_0 + \delta p$, p_0 being the stationary power, and we get

$$\begin{aligned} \frac{d\delta p}{dt} &= -2\left[\Gamma_+(p_0+\delta p) - \Gamma_-(p_0+\delta p)\right](p_0+\delta p), \\ &= -2\Gamma_p \delta p, \end{aligned} \tag{I.15}$$

so that we obtain for the amplitude relaxation rate Γ_p,

$$\Gamma_p = \left(\frac{d\Gamma_+(p)}{dp} - \frac{\Gamma_-(p)}{dp}\right) p_0. \tag{I.16}$$

We end with the normalized non-linearity coefficient ν, defined as follows :

$$\nu = \frac{N p_0}{\Gamma_+(p)}. \tag{I.17}$$

ν has the advantage of being a dimensionless variable, and measures the relative influence of the frequency-shift Np_0 on the amplitude relaxation rate Γ_p.

To conclude this section on self-sustained oscillators in the autonomous regime, let us summarize : we first gave examples of self-sustained oscillators in nature, and what differentiates them from other oscillators. Then we introduced the mathematical concepts of phase, amplitude and limit cycle and we examined the stability of phase and amplitude fluctuations. Finally, we gave an overview of the KTS model in autonomous regime, and underlined its features as a self-sustained oscillator model such as the balance between energy supply and dissipation. We also discussed a few specifics of the model when applied to STOs, such as the strong non-linearity N, and the role of the non-linear parameters ν and Γ_p.

I.3 Synchronization of self-sustained oscillators

Up to now, two aspects have been examined in the introduction : the STT-induced magnetization dynamics in a magnetic multilayer structure, and self-sustained oscillations and their properties. The KTS model offers a way to put these two aspects together by modeling the behavior of an oscillating magnetic system - the STO - using concepts from non-linear dynamics.

We recall that the topic of the thesis is the investigation of synchronization mechanisms of a STO by a RF current, and their experimental characterization. In this last part of the introduction we address the synchronization of self-sustained oscillators.

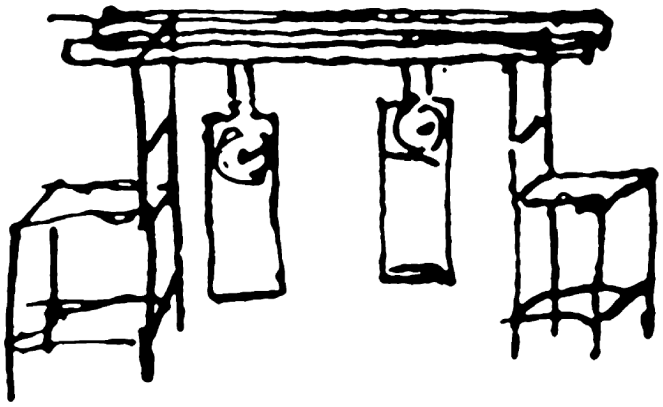

Figure I.9 – Drawing made by Christiaan Huygens in 1665 on the synchronization of two clocks placed on a wooden support.

First we make a general review of synchronization in various natural systems and underline the basic concepts. Then the more specific subject of synchronization to a driving force is examined : the evolution of the phase-difference in the locking-range, higher order synchronization and Arnold Tongues will be considered. Finally synchronization phenomena in spin-torque oscillators will be reviewed, amongst which : injection-locking experiments, and the current modeling of synchronization using KTS formalism.

I.3.1 Introduction to synchronization

I.3.1.1 Synchronous systems in nature / General introduction

Synchronization is a word used in everyday language : depending on the person you ask, it may call to an array of different things. Co-workers setting up a meeting in the afternoon need synchronization so that everybody is available at a given moment and find each other to discuss. Musicians playing in a band require synchronization with one another then it becomes pleasant to the ear : otherwise the harmony cannot be kept up. The dancer wants body synchronization with its partner and the beat of the music so that the link is preserved. In telecommunications, the user of a mobile device needs synchronization of its data to be able to access the same data with other connected devices.

The common understanding of synchronization is basically “things happening at the same time”. It makes sense, as the word comes from the ancient Greek “$\sigma\upsilon\nu$”(*syn*) and “$\chi\rho\acute{o}\nu\acute{o}\varsigma$”(*chronos*), respectively meaning “with” and “time”.

In a scientific context, the study of synchronization phenomena is an active subject of research in both man-made devices and natural systems : synchronization of pendulum clocks, electronic generators, lasers, but also synchronization of the firing of neurons, adjustment of the heart rate of a horse to the motion of its body, synchronization of the biological clock of animals and plants to the cycle of day and night, etc.

We define synchronization phenomenon [67] as follows : *Adjustment of rhythms of oscillating objects due to their weak interaction.*

The first observation and explanation of synchronization as it is meant above was done by Christiaan Huygens during the seventeenth century in 1665 : he initially described the effect as the “sympathy of two clocks”.

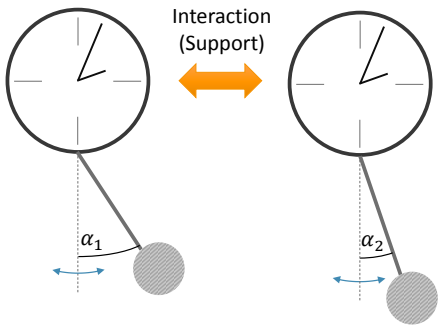

Figure I.10 – A system that exhibits synchronization : Two coupled pendulum clocks. The coupling is represented by the yellow arrow. For the experiment of Huygens, the coupling is provided by a common wooden support, which transmits a vibration from one clock to another. A priori the two clocks are not identical : if the frequency detuning is not too large and there is enough coupling, the two clocks synchronize their motion with each other.

Huygens was a Dutch mathematician, astronomer and physicist, known amongst other things for the discovery of the first moon and the true shape of the rings of Saturn. He is also the inventor of the pendulum clock.

According to a letter he wrote to his father, Huygens discovered the effect of synchronization when he was sick and stayed in bed. He spent a couple days watching two clocks hanging on the wall, and made this observation :

> It is quite worth noting that when we suspended two clock so constructed from two hooks imbedded in the same wooden beam, the motions of each pendulum in opposite swings were so much in agreement that they never receded the least bit from each other and the sound of each was always heard simultaneously. Further, if this agreement was disturbed by some interference, it reestablished itself in a short time. For a long time I was amazed at this unexpected result, but after a careful examination I finally found that the cause of this is due to the motion of the beam, even though this is hardly perceptible.

He saw that two similar clocks perfectly timed their motion with each other, and explained it was due to an extremely small motion of the wooden support. Nowadays it would be said this is an example of *mutual synchronization* where the *coupling* is provided by the wooden support.

I.3.1.2 Basic concepts

Let us consider a system made of two coupled, non-identical clocks as in Fig. I.10. The angle between the pendulum and the vertical axis is α_1 for the first clock and α_2 for the second clock : it oscillates periodically from the left to the right. From the period $T_{1,2}$ of the oscillations the frequency $f_{1,2}$ of each clock can be determined.

When put apart, their respective frequencies are f_1^0 and f_2^0. These two frequencies are called *natural* frequencies, i.e. it is the frequency of each clock on its own. A priori, f_0^1 and f_0^2 are not the same for non-identical oscillators. The difference between the natural frequencies f_0^1 and f_0^2 is the *frequency detuning*, or frequency mismatch, $\Delta f^0 = f_1^0 - f_2^0$.

When put together (for example on a common support), a certain *coupling* takes effect. The coupling has several attributes : (i) the type of coupling. For a wooden beam support, we envisage several type of couplings depending on composition of the beam or how of the beam is attached to the ground - for example one type of coupling works through a longitudinal vibration of the beam, and the other type of coupling works through a

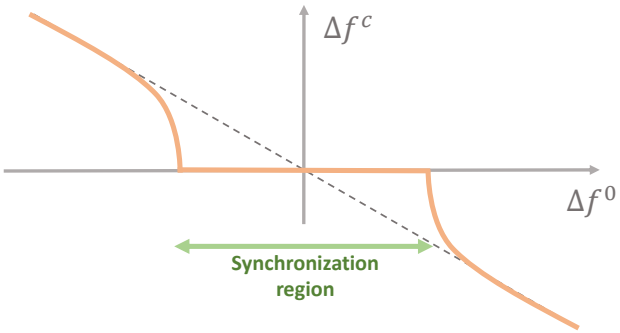

Figure I.11 – Detuning plot Δf^c (difference of the coupled frequencies) versus Δf^0 (detuning, difference of the natural frequencies) for a given coupling strength. When the detuning between the two oscillators is small enough, the two oscillators synchronize and the $\Delta f^c = 0$. The range of detuning marks the synchronization region, or locking-range.

bending vibration of beam. (ii) The coupling intensity ϵ : if the beam is completely rigid and has no degrees of freedom, or that the clocks are attached separately, the clocks will not interact - this is this case of a coupling strength $\epsilon = 0$.

Due to the coupling, the frequency of each clock is influenced by the other : we write f_1^c and f_2^c the respective frequencies of the coupled clocks. For a given coupling intensity ϵ and frequency detuning δf, the coupled frequencies may behave differently.

If the coupling is too weak or the frequency detuning is too important, the interaction will not lead to substantial changes. The clocks will continue oscillating as if they were never put in contact, and we will have $f_1^c \approx f_1^0$ and $f_2^c \approx f_2^0$. Otherwise, the frequencies of the two clocks become equal, or entrained, i.e. $f_1^c = f_2^c$: it is the signature that *synchronization* of the oscillations takes place.

A typical plot for synchronization experiments is the *detuning plot*, i.e. a plot of $\Delta f^c = f_1^c - f_2^c$ (the coupled frequency difference) as a function of $\Delta f = f_1^0 - f_0^2$ (the detuning). To trace this plot, the coupling is kept constant, and we gradually change the detuning between the two clocks. In this case it can be done with the following series of measurements : we pick one clock (say the left clock), and vary the length of pendulum, from being a little shorter to a little longer than the right pendulum. It will change the natural frequency of the left clock, while the natural frequency of the right clock remains constant. Then for each length of the left pendulum, we put the two clocks together, and measure the difference of the coupled frequencies Δf^c.

By plotting the results of the experiment we would obtain a curve as in Fig. I.11. We notice a region in the center where the frequencies of the two coupled clocks are equal $\Delta f^c = 0$. It holds for a certain range of detuning ; otherwise the coupling is not sufficient to make the two clock oscillate at the same frequency. This range of detuning corresponds to the *synchronization region*, or the *locking-range*.

The locking-range is an essential quantity to determine for the characterization of synchronization. Usually it is easier to tune the frequencies of the oscillators than to change the coupling. For a given coupling the width of the locking-range provides good indication of whether or not synchronization is possible in a given configuration of the system.

We approached synchronization from the viewpoint of the frequency : two synchronized

oscillators have the same frequency. However the effect on the phase has not been introduced. From a mathematical perspective, the angular frequency ω is the time-derivative of the phase $\omega = d\phi/dt$: then if the difference of the angular frequencies is zero in the synchronized regime, accordingly the difference of the phases must be constant with time, i.e.,

$$\phi_1(t) - \phi_2(t) = cst. \tag{I.18}$$

This is why *phase-locking* is used as an equivalent term for synchronization : but we emphasize that if synchronization translates into the *identity* of frequencies, it does not necessarily mean that the two phases are equal ! The two phases are locked, and *the phase difference is constant* in synchronized regime.

For the example of the two coupled clocks, we roughly have two regimes of synchronous motion. Either the two pendulae simultaneously move from the left to the right (*in-phase* synchronization) or the two pendulae move in opposite directions, the first from the left to the right and the other from the right to the left (*out-of-phase* synchronization). In both cases the clocks have the same frequency, but the phase-difference is not the same.

We say that synchronization induces a phase-shift : pendulae moving in the same direction have a phase-shift of 0, and pendulae moving in opposite directions have a phase-shift of π.

To summarize, there are two factors deciding whether or not synchronization is possible when two oscillators are put in contact : (i) the coupling intensity and (ii) the frequency detuning.

I.3.1.3 Conditions for synchronization

The fact that two variables are measured and are oscillating at the same frequency does not necessarily imply that we observe synchronization of two systems. The definition of synchronization is valid in certain cases, and most importantly two conditions must be observed, self-sustained oscillations and weak coupling.

1/ *Self-sustained oscillations*

We look at the necessity of self-sustained oscillations for synchronization using the the comparison between FMR and a STO. In the FMR setup, the oscillations of the magnetization of a ferromagnet are sustained by applying an external RF field. It seems as if we observe synchronization between the ferromagnet and the RF field, since the frequency of magnetization oscillations is the same as the frequency of the RF field. However one cannot consider this as an example of synchronization because one the oscillators, the ferromagnet, cannot maintain oscillations on its own : it is not a self-sustained oscillator. As a consequence, we cannot speak of an adjustment of rhythms here. In contrast the STO is a self-sustained oscillator and can maintain oscillations without an external RF force : the energy supply is the DC current. By applying an RF force (such as a RF field or a RF current) we can adjust its frequency to that of the external force : we observe synchronization. Synchronization therefore requires self-sustained oscillations for at least one of the two oscillators, and should not be confused with other phenomena such as resonance where the entrained system is a *damped* oscillator.

2/ *Weak coupling*

There is a difference between synchronous motion and synchronization. Let us go back to the example of the two clocks and we consider coupling the two clocks by attaching the extremities of two pendulae by a rigid link. Obviously the two pendulae will move synchronously and if one of the clocks stops, the other is stopped as well. Once again it seems that we observe synchronization. It is not the case because the coupling is *too strong* : we cannot decompose the whole system into two auto-oscillating systems. Simply put, the oscillations of the left and the right pendulae correspond to two different outputs of the same oscillating system : we do not have synchronization of two distinct systems.

In this instance finding the difference between weak and strong coupling is simple : but usually it is difficult to determine what is a strong and a weak coupling. In synchronization phenomena the adjustment of rhythms occurs for a limited range of detuning between the two oscillators because the coupling is weak - if this adjustment of rhythms occurs for virtually the whole range of detuning, we are in a presence of a strong coupling, and we cannot speak of synchronization.

Throughout the analytical calculations and the simulations we have to verify that we are within the condition of weak coupling. For synchronization of the STO to a RF current, the considered approach is to characterize the coupling strength by the RF/DC current ratio $\epsilon = i_{RF}/i_{DC}$. In both Chapter 2 and 3 we limit ourselves to the case of $\epsilon \leq 1$.

I.3.2 Frequency adjustment to a driving force

Here we treat synchronization of a self-sustained oscillator to a driving external force. It is the simplest case of synchronization. It also corresponds to the case examined in this manuscript, where the STO is driven by a periodic force (the RF current). In the case the coupling acts one-way : from the external force to the oscillator.

Synchronization by an external force is largely used in microwave oscillators to stabilize a signal. Typically, a weak but precise [25] oscillator (the external force) is used to entrain another oscillator producing a large output, but very sensitive to noise. In microwave engineering, the external force is a RF current and the oscillator to be synchronized is an active electronic circuit having a negative resistance element. The term used is *injection-locking* of oscillators[1, 48]. It is a classic topic in the investigation of microwave oscillators. In addition, injection-locked oscillators can perform other functions than only signal generation, such as amplification, detection of a phase-modulated or amplitude-modulated signal [48], but also frequency-division [74, 96].

I.3.2.1 Phase-locking across the synchronization region : Force and detuning

Here we describe synchronization to a driving force regardless of the type of self-sustained oscillator and of the type of the driving force. We will look at the effect of the external force on the phase of the oscillator *inside the synchronization region* in three steps as in [67] : (i) Detuning without force (ii) Force without detuning (iii) Force and detuning.

We consider a self-sustained oscillator where the dynamics can be by modeled by the complex variable $a(t) = A\exp(i\omega_0 t + \phi_0)$ [26], where the amplitude of the oscillations is A, its frequency is ω_0, and its phase is $\phi(t) = \omega t + \phi_0$. We look at the effect of a *weak* external force with expression $f(t) = \epsilon\cos(\omega_e t)$. Here its amplitude is ϵ, its frequency is ω_e and its

25. By precise it is meant that the period of the oscillations is very stable with respect to noise.
26. As in Sec.I.I.2, the limit cycle for this oscillator is a circle.

phase is $\phi_e(t) = \omega_e t$ (for simplicity we consider that at $t = 0$, the phase of the external force is zero). We introduce the *phase difference* between the two oscillators $\psi = \phi - \phi_e$ and the detuning $\omega_0 - \omega_e$.

Self-sustained oscillators have the two following characteristics : the amplitude is stable, and the phase is free. Since the external force is weak, it does not affect the amplitude of the oscillator [27] : only the phase is adjusted ! Consequently we only focus on the phase dynamics.

More precisely we will focus on the dynamics of the phase difference between the oscillator and the force : $\psi(t) = \phi(t) - \phi_e(t)$. In particular we make the analogy between the phase dynamics and the dynamics of a light particle in a viscous fluid.

To do so, we consider the *rotating frame* at ω_e to analyze the dynamics : indeed in the static frame, the free-running oscillator has a frequency ω_0 and the phase point rotates around the limit cycle with a velocity ω_0. Since in the synchronized regime the oscillator adjusts its frequency to the frequency ω_e of the driving force, in the rotating frame at ω_e, the phase point ψ is immobile across the synchronization region.

1/ *Detuning without force.*

In this case the force has zero amplitude ($\epsilon = 0$) and there is no frequency entrainment. Consequently the external force does not act on the phase of the oscillator. There are three possible cases depending on the detuning $\omega_0 - \omega_e$: positive detuning $\omega_0 - \omega_e > 0$, no detuning $\omega_0 = \omega_e$, and negative detuning $\omega_0 < 0$ (respectively (a)/(d), (b)/(e) and (c)/(f) in Fig. I.12).

For a zero detuning the phase point ψ is immobile in the rotating frame (b). The particle (e) is on a horizontal plane : it is in neutral equilibrium and no position on the plane is favored. When the detuning is positive or negative (a) and (b), in the rotating frame at ω, the detuning continuously acts on the phase so that the phase point ψ rotates clockwise or anti-clockwise at a $\omega_0 - \omega_e$: ψ increases linearly with time. Because here the force is zero, it has no effect on the phase of the oscillator and consequently the phase of the oscillator cannot be locked to that of the external force, regardless of the detuning. From the viewpoint of the particle (d) and (f), the effect of the detuning is a tilting of the plane : the particle slides with a constant velocity.

2/ *Force without detuning*

Here we suppose that we switch on the force, i.e. $\epsilon \neq 0$, but that this force is applied with zero detuning $\omega_e = \omega_0$ so that the force has the expression $\epsilon \cos(\omega_0 t)$. In the rotating frame the effect of the external force is represented by a constant vector of magnitude ϵ with angle ψ_0. This angle depends on the way the force and the oscillator are coupled and typically for a quasi-linear oscillator this angle is equal to $\pi/2$.

We considered the external force is sufficiently weak so that it does not act on the amplitude but only on the phase. The effect of the force on the phase depends on the position of the phase point ψ on the limit cycle, which is illustrated in Fig. I.13(a). At points A and B the direction of the force is perpendicular to the tangent of the limit cycle, as the consequence the effect on the phase is zero. These are the two equilibrium points. To know which point corresponds to a stable or an unstable equilibrium, we look at the effect on the phase close to points A and B. Close to point B, we see that the external

27. This is valid for a quasi-linear oscillator, i.e. when the non-linearity is very small. Otherwise, for a strongly non-linear oscillators, changes of the phase due to synchronization translate in changes of the amplitude as well : we develop this specificity of the STOs in Chapter 2 and 3.

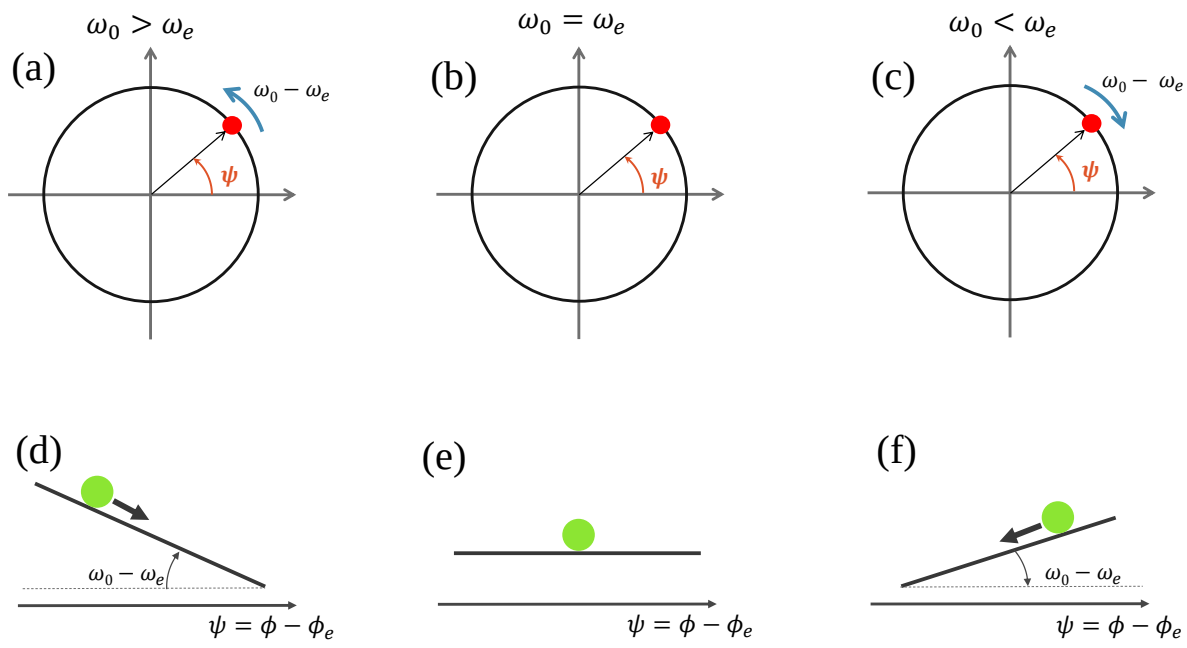

Figure I.12 – (a),(b),(c) : Dynamics of the phase-difference $\psi = \phi - \phi_e$ in the reference frame rotating at ω (external force frequency), for an external force of zero amplitude $\epsilon = 0$. The oscillator is not entrained by the external force. (b) no detuning : the phase point is at rest. (a) and (c), respectively positive and negative detuning : the phase point is rotating counterclockwise (a) with a velocity $\omega_0 - \omega_e$ and clockwise (c) with a velocity $\omega_0 - \omega_e$.
(d),(e),(f) Analogy between the phase-difference and a particle in a viscous fluid. (e) no detuning : the particle is in a neutral equilibrium and the phase-difference is constant with time. A positive (d) or negative (f) detuning corresponds respectively to a downwards and a upwards shift of the plane : the particle is sliding with constant velocity and the phase-difference increases linearly with time.

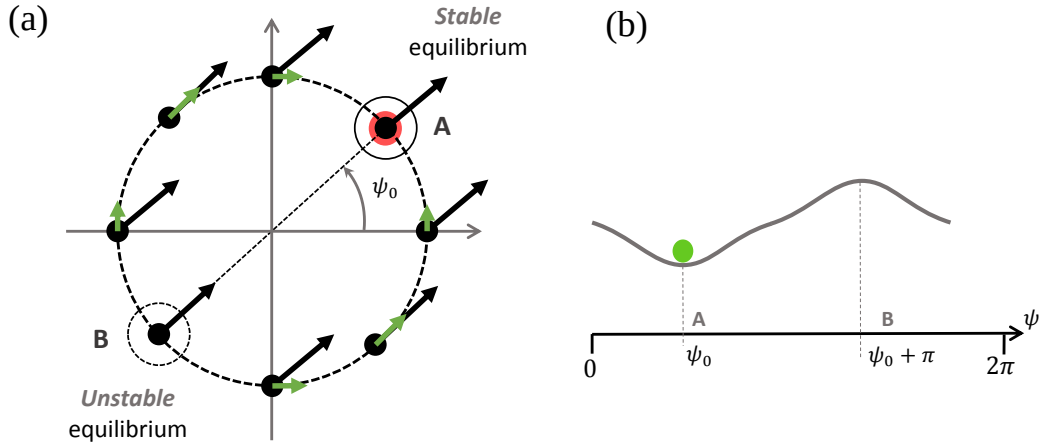

Figure I.13 – (a) Dynamics of the phase-difference ψ with an external force in the absence of detuning. Here the effect of the external force depends on the position of the phase difference ψ. There are two equilibrium points where the effect of the force cancels : A -stable equilibrium and B - unstable equilibrium. The value ψ_0 where the phase stabilizes is what is called in this manuscript the additional phase-difference. (b) Analogy : the external force creates a non-flat potential and the particle goes to minimum of the potential.

force tends to pull the phase away from equilibrium, while close to point A the external force pulls the phase closer to equilibrium. Then A is the stable equilibrium and B is the unstable equilibrium. The analogy with the motion of the particle is shown in Fig. I.13(b) : in the absence of a force and without detuning the plane is flat and horizontal and the particle is in neutral equilibrium (Fig. I.12(e)). However, when the force is turned on, the plane remains horizontal but the surface (the potential) is bent and a minimum for $\psi = \psi_0$ (maximum for $\psi = \psi_0 + \pi$) is formed.

To summarize, the force *stabilizes* the phase-difference at $\psi = \psi_0$. Here ψ_0 is what we call the *additional phase-difference* : it is the phase difference at zero detuning [28].

3/ *Force and detuning*

Here we address the complete picture : phase-locking when both factors, the force and the detuning, are taken into account in the phase dynamics. We consider the phase-locked regime, i.e. when the detuning is small enough. The case of large detuning (quasi-periodic motion of the phase) is rapidly discussed at the end.

We take the case of a positive detuning, $\omega_0 - \omega_e > 0$. In the rotating frame, the effect of the detuning is the same regardless of the value of the phase. It pushes the phase point ψ in a counterclockwise motion (blue arrows in Fig. I.14). In contrast, we remarked that the effect of the external force depends on the value of ψ (green arrows in Fig. I.14(a)). At some points it promotes the motion counterclockwise and enhances the effect of the detuning (green and blue arrows add up) while at other points it promotes the motion clockwise, and counterbalances the effect of the detuning (green and blue arrows compensate each other).

28. see the additional phase-difference ψ_0 at f and $2f$ in the summarizing table at the end of Chapter 2, Tab. **??**. The additional phase-difference is also extracted from macrospin simulations in Chapter 3 at f and $2f$ in Fig. III.9

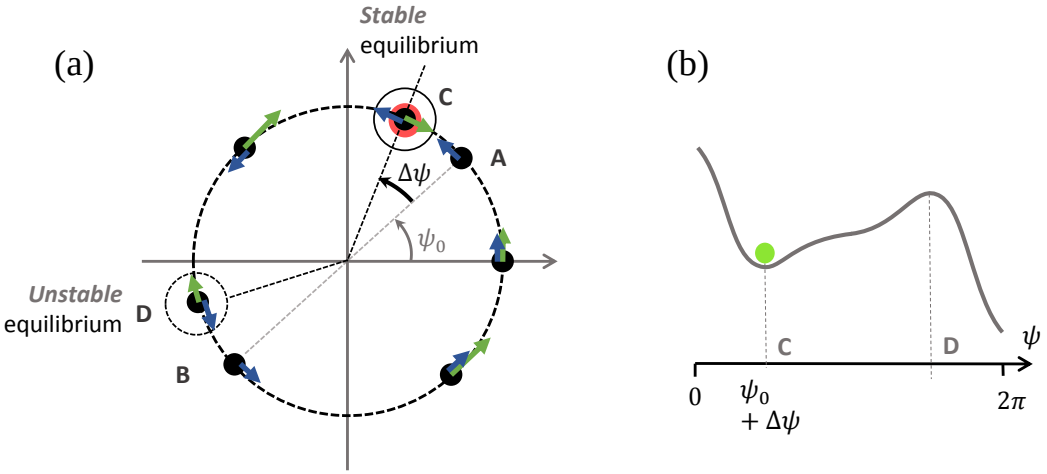

Figure I.14 – (a) Phase difference ψ dynamics with an external force and a positive detuning. The addition of the detuning creates a continual counterclockwise motion on the phase point along the limit cycle (blue arrows) and while the effect of the force depends on the position of the phase point (green arrows). At point C and D the effect of the detuning and of the external force are exactly compensated, and the stable equilibrium point is shifted from A (without detuning) to C (with detuning). The shift due to the detuning is labeled $\Delta\psi$. (b) Analogy : the surface is bent by the force (creating a minimum and a maximum of potential) but is also tilted by the detuning, which slightly shifts the position of the minimum. The particle rests in the minimum and we have a phase-locked regime.

For two values of ψ the effect of the detuning and the force are exactly compensated. As a consequence a new balance is obtained and the addition of the detuning shifts the equilibrium positions from A to C and from B to D. Likewise, there is a stable and unstable equilibrium point and the phase-difference stabilizes to a new point $\psi = \psi_0 + \Delta\psi$ (see Fig. I.14), where $\Delta\psi$ is the shift due to the effect of the detuning.

The analogy with the particle moving in a viscous fluid gives us the following picture : (i) the force bends the surface and forms and minimum and a maximum of potential ; (ii) the detuning tilts the surface with respect to the horizontal plane - a small detuning induces a small tilting, and a large detuning induces a large tilting. By taking into account these two aspects, we obtain Fig. I.14(b) for a small detuning and the particle rests at the minimum given by $\psi = \psi_0 + \Delta\psi$.

I.3.2.2 Phase dynamics : the Adler equation

By analyzing the motion of the phase point ψ in the rotating frame with ω_e, we have seen that the combined effect of two factors (force and detuning) determines the stable value of the phase difference ψ in synchronized regime : the force and the detuning.

Now we suppose that the intensity of the force remains constant and the detuning is varied from the left extremity to the right extremity of the synchronization region. The value of the phase-difference varies accordingly. For each detuning there is one stable equilibrium for the phase-difference, which comes from the balance between the effect of the force and this specific value of detuning. From there we make an important observation. In synchronized regime, the phase-difference is constant with time, i.e. $d\psi/dt = 0$, but

the value of the phase-difference changes across the synchronization region : (i) the type of coupling and the intensity of the force determines what we call the additional phase-difference ψ_0 (ii) the detuning $\omega_0 - \omega_e$ leads a supplementary phase-shift $\Delta\psi(\omega_0 - \omega_e)$, so that in the end the stable value of the phase difference reads $\psi = \psi_0 + \Delta\psi$. The phase-difference has typically a dependence in inverse trigonometric function on the detuning through $\Delta\psi$ [29].

The behavior of the phase difference for synchronization to an external force was examined in 1946 by Adler for the case of an oscillating signal impressed upon an electronic oscillator circuit[1](see Fig. I.15(a)). It is an example of injection-locking. The frequency of the external signal is varied close to the generating frequency of the oscillator and the author discusses phase dynamics inside and outside of the locking-range.

The following differential equation is established for the phase-difference α between the oscillator and the external signal (known as the Adler equation),

$$\frac{d\alpha}{dt} = -B\sin(\alpha) + \Delta\omega_0. \tag{I.19}$$

In the article $d\alpha/dt$ is named *beat frequency*, which refers to the frequency difference between the forced oscillator frequency ω and the external signal frequency ω_1 (what we called the forced frequency difference). The author does not use the term phase-difference for α, but the meaning is equivalent. Here, $\Delta\omega_0 = \omega_0 - \omega_1$ is the difference between the free-running frequency of the signal ω_0 and the frequency of the external signal ω_1, it corresponds to the detuning. B is proportional to the voltage ratio E_1/E, where E_1 is the voltage of the external signal and E is the voltage induced in the grid coil of the circuit. To make a connection with our picture of synchronization, we say that E_1 corresponds to the external force strength, and E measures the amplitude of the oscillations generated by the electronic circuit. It is also assumed that $E_1 << E$, which coincides with the assumption of a *weak* external signal that is required for synchronization.

Now Eq. I.19 portrays the dynamics of the phase difference for *any* detuning $\Delta\omega_0$, i.e. it depicts the phase-locked regime but also the quasi-periodic motion of the phase-difference for a large detuning. Here we restrict ourselves to the behavior in phase-locked regime, i.e. when $d\alpha/dt = 0$. Then Eq. I.19 reads

$$\Delta\omega_0 = B\sin(\alpha). \tag{I.20}$$

Since $-1 \leq \sin(\alpha) \leq 1$, this expression is valid only for $|\Delta\omega_0| < B$. Therefore the phase-locked regime is obtained for a detuning is smaller than B. In other words, the quantity B in Eq. I.19 corresponds to the *locking-range* for synchronization.

From here we derive the expression of the phase difference α in synchronized regime as a function of the detuning and the locking-range,

$$\alpha = \arcsin(\Delta\omega_0/B). \tag{I.21}$$

For a zero detuning, we obtain $\alpha = 0$. It corresponds to what we called the additional phase difference ψ_0, in this case it is equal to zero. We also have the phase-shift due to the detuning (i.e. $\Delta\psi$). At the left extremity of the locking-range ($\Delta\omega_0 = -B$) the phase difference is $\alpha = -\pi/2$, while at the right extremity of the locking-range ($\Delta\omega_0 = B$) the phase difference is $\alpha = \pi/2$. In this example, it shows that across the synchronization

29. See macrospin simulation results for the evolution of the phase difference as a function of the detuning in Sec.III.3, Fig. III.7.

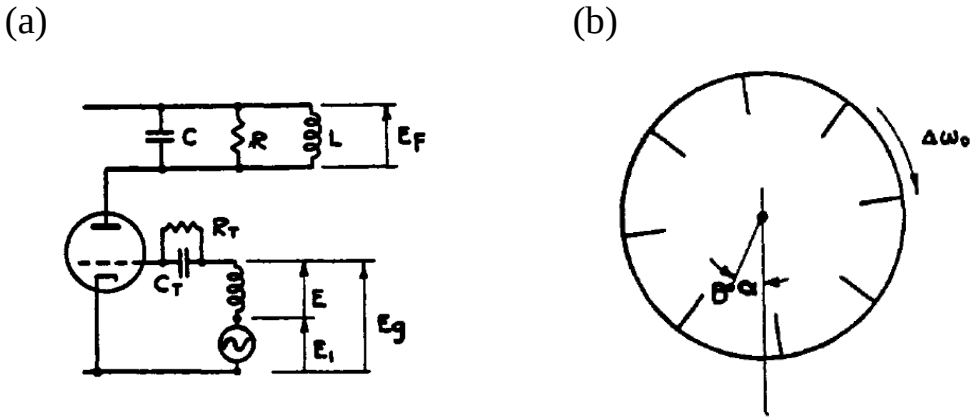

Figure I.15 – (a) Electronic oscillator circuit on which on external oscillating signal is impressed (b) Analogy between the phase dynamics of Eq. I.19 and the motion of a pendulum in a rotating container filled with liquid. The liquid is thick enough so that it completely follows the rotation of the container. Here the angle α between the pendulum and the vertical axis corresponds to the phase-difference and the angular velocity of the container $\Delta\omega_0$ corresponds to the detuning.

region, the phase-difference stabilizes at values in the interval $[-\pi/2; \pi/2]$.

The discussion ends with an analogy between the phase dynamics depicted in Eq. I.19 and the mechanical model of a pendulum in a rotating container filled with a liquid. As we can see in Fig. I.15(b), the angle α is the angle of the pendulum with the vertical axis. The pendulum has a certain weight B, and as a consequence gravity pulls the pendulum down and the force is proportional to $B\sin(\alpha)$. Here the inertia of the pendulum is negligible. In the meantime the container is rotating at an angular velocity $\Delta\omega_0$. We consider that the viscosity of the liquid is such that the liquid completely follows the rotation of the drum. Then the pendulum is entrained with the rotation of the liquid as well, but the weight of the pendulum opposes a resistance to its motion with the liquid and the pendulum tends to rest back to its vertical position.

Let us look at the possible scenarios depending on the rotation speed of the drum : (i) $\Delta\omega_0 = 0$ - no rotation. The pendulum is vertical with $\alpha = 0$, at rest ; (ii) $\Delta\omega_0$ is "small", the drum rotates at a low speed. After some transient time, the pendulum stabilizes at an angle α_∞ with the vertical. The higher the rotation speed of the drum, the higher the angle α_∞ : however the pendulum cannot stabilize over the horizontal position which sets the limit $|\alpha_\infty| < \pi/2$; (iii) $\Delta\omega_0$ is large, the drum rotates at a high speed. Here the effect of the gravity is not enough to counterbalance the rotation of the pendulum, and the fluid takes the pendulum along with its rotation : as the speed of the drum increases, the motion of the pendulum goes from a quasiperiodic rotation to by fully entrained by the liquid.

The cases (i) and (ii) correspond to the phase dynamics inside the synchronization region when the detuning is small enough - the phase difference is stabilized and the phase-locked regime is reached. Case (iii) corresponds to a large detuning and describes the dynamics outside of the synchronization region.

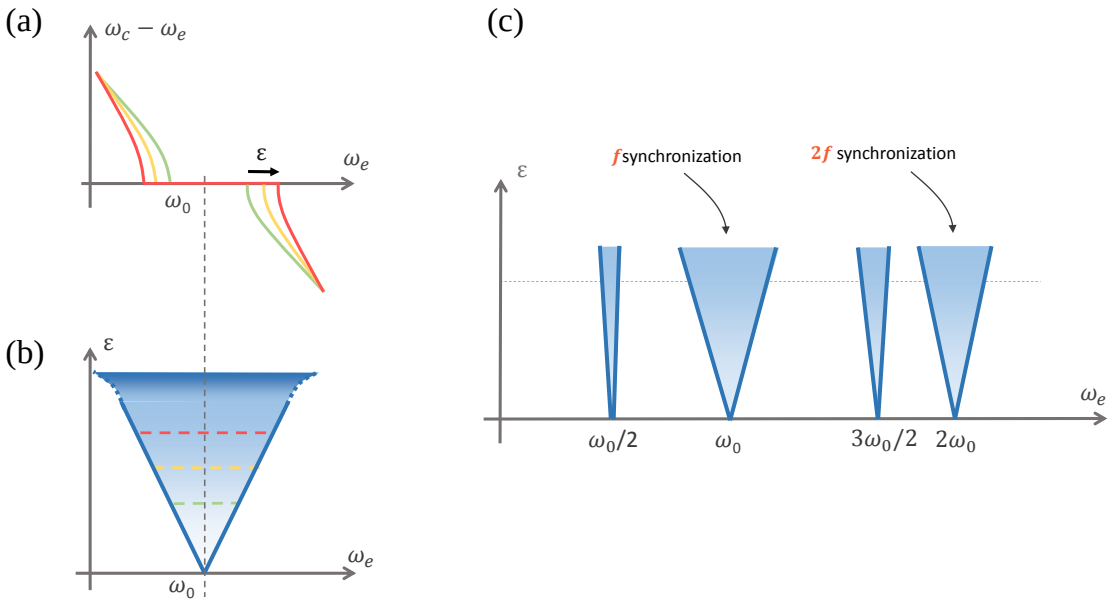

Figure I.16 – (a) Detuning plot for three different values of the forcing amplitude ϵ. As ϵ increases, the locking-range grows as well. (b) The synchronization region in the (ϵ, ω_e) plane, also called *Arnold tongue*.(c) Higher order synchronization and corresponding Arnold Tongues for 1 :2, 1 :1, 3 :2 and 2 :1 synchronization. Typically the 1 :1 region is wider than the other regions.

I.3.2.3 Arnold Tongues and higher order synchronization

We have seen that for a fixed amplitude ϵ of the external force, the synchronized regime is reached for a sufficiently small detuning $\omega_0 - \omega_e$. The locking-range corresponds to the maximum range of detuning above which synchronization breaks down. Now what happens when the amplitude of the external force ϵ increases ? The intuitive answer is that the locking-range increases with the external force amplitude. It seems indeed sensible to suppose that it gets easier to lock to an external force when this force gains more weight.

To quantitatively measure the influence of the external force on the locking-range, we plot the series of detuning plots (as in Fig. I.11) for different values of the external force amplitude ϵ. As the external force amplitude increases, the locking-range increases as well (Fig. I.16(a)). From there we determine a region in the (ϵ, ω_e) plane where the phase-locked regime is reached (blue region in Fig. I.16(b))and this region is designated the *Arnold Tongue*. For small ϵ the Arnold Tongue has straight borders and the locking-range increases linearly with ϵ, which is typically the case for small forcing amplitudes. At higher forcing amplitudes the borders of the Arnold tongues are not straight anymore, and the picture of synchronization is more complex in that instance.

We have assumed up to now in this section that synchronization requires the frequency of the external force to be close to that of the oscillator so that in synchronized regime the frequency of the oscillator becomes equal to that of the external force. However, this is not always the case because in some instances we reach a synchronized state when the frequency of the external force is quite different from that of the oscillator. This is what

we designate by *Higher order synchronization*. Higher order synchronization is a central point of this thesis. Indeed it is devoted in large part to the comparison of synchronization mechanisms depending on whether the RF current is injected close to the STO frequency or close to *twice* the STO frequency. Basically higher order synchronization generalizes the idea that in the synchronized regime the frequencies of the two oscillators are equal. Instead we affirm that for with (n, m) positive integers, the condition for synchronization is that n times the frequency of the external source ω_e is equal to m times the frequency of the oscillator ω_c. This is also called $n : m$ synchronization and can be expressed as

$$n\omega_e = m\omega_c \tag{I.22}$$

Relation I.22 virtually allows synchronization for any frequencies ω_c and ω_e, as we can always find a couple of integers (n, m) so that $n\omega_e \approx m\omega_c$. However the higher order synchronization regions are typically much narrower than the $1 : 1$ synchronization region. As n and m increase, experimental measurements of the locking-range become more and more difficult and often synchronization cannot be performed efficiently.

The Arnold tongues for higher order synchronization are schematically represented in Fig. I.16(c). As we can see, the region for $1 : 1$ synchronization is wider than the other regions, indicating that synchronization is favored in the $1 : 1$ configuration.

However the situation is not always as such, and sometimes higher order synchronization is favored over to the $1 : 1$ synchronization. This will be discussed in the rest of the manuscript for the synchronization of a STO to a RF current : in particular we will see that depending on the configuration of the STO and amplitude of the oscillation, either the $1 : 1$ regime or the $2 : 1$ regime is favored. For the rest of the manuscript the $1 : 1$ regime will be designated *f-synchronization* and the $2 : 1$ regime the *$2f$-synchronization* (see Fig. I.16(c)).

I.3.3 Synchronization phenomena : Application to STOs

We have now reviewed the essential features of synchronization, namely the notion of frequency adjustment, conditions of weak coupling and small detuning and also the phase-locking mechanisms for synchronization to an external force. We conclued by introducing Arnold Tongues and higher order synchronization. In this final part of the introduction we discuss synchronization in the context of Spin-torque oscillators. For 10 years now the topic of synchronization in Spin Torque oscillation has a been a very active one. The interest for synchronization in STOs is fueled by a double motivation :

1. *Practical applications* : STOs are very promising candidates for tunable frequency synthesis in the GHz range, but cannot yet compete with voltage controlled oscillators (VCOs) in terms of signal properties, concerning in particular the output power and the noise level. Synchronization provides a way to greatly reduce the level of noise. Similarly to injection-locking in classic electronic oscillators, the phase of the STO can be stabilized by an external RF current and the linewidth can be reduced in MTJ-based STO by two orders of magnitude[72, 19] and even five orders of magnitude using a RF field [30].
2. *Basic research* : STOs turn out to be great self-sustained oscillating systems to for the study of synchronization phenomena. Experimentally synchronization can be achieved through several types of couplings using RF magnetic fields [30, 92], RF currents [72, 75, 51, 22] or propagating spin-waves [39, 77]. In addition we

have various STO configurations in which synchronization has been experimentally investigated : nanocontacts [77], nanopillar macrospin STOs [22, 72], nanopillar vortex STOs [30, 51] and Spin-Hall oscillators [12]. To finish, the STO also exhibits higher order synchronization regimes : the $2f$-synchronization interestingly yields the best results in experiments using in-plane magnetized STOs [72, 30, 51] but also, for a RF driving field, fractional synchronization regimes ($n : m$ synchronization) have been investigated experimentally and theoretically in [92].

I.3.3.1 State of the art : Experimental realizations and KTS model for synchronization to an external force

Here we review a few notable experimental realizations of synchronization in STOs, plus we examine phase-locking to an external force via the KTS formalism according to the 2009 article [83] of Slavin *et al.*. We consider the findings from four different articles that are quickly reviewed in the following.

• **Mutual Synchronization via propagating spin-waves : Kaka *et al.* [39] and Mancoff *et al.* [55], 2005** The prospect of connecting an array of STOs in order to coherently generate a low linewidth and high output signal, that is, with enhanced properties compared to an individual STO, started with the experimental works of Kaka *et al.* [39] and Mancoff *et al.* [55]. Both works were published in September 2005 and report similar results. Two nanocontact STOs put in close proximity (from 100 nm in [55] to 500 nm in [39]) can phase-lock with each other, translating into frequency entrainment, reduced signal linewidth and increased signal power. Here we choose to discuss the results in the experiments of Kaka *et al.* which, compared to the setup of Mancoff *et al.*, have the advantage of clearly showing the difference between synchronized regime and autonomous regime by biasing *separately* the two coupled point-contact STOs.

The structure is a two nanocontact device : two metallic contacts with 40nm cross section are used to inject a current into a thin magnetic multilayer structure [Ta (5 nm)/Cu (50 nm)/Co90Fe10 (20 nm)/Cu (5 nm)/Ni80Fe20 (5 nm)/Cu (1.5 nm)/Au (2.5 m)]. The contacts are separated by a distance of $r = 500$nm (see Fig. I.17) and are biased respectively by I_A and I_B. The measurements are taken with the device placed in an external 740 mT magnetic field oriented 75° from the film plane. For each contact and a sufficient current bias, self-sustained oscillations of the magnetization take place in an area localized below the contact, and generate a magnetoresistive signal collected by a spectrum analyzer.

The interesting part with the nanocontact geometry is that it involves two characteristic lengths : (i) the cross section of the nanocontact, which is reduced to 40 nm here so that the large current density flowing allows the excitation of the magnetization ; (ii) the lateral size of the magnetic stack, which is not limited to the area cross section of the nanocontact and extends to the size of the device. With this type of geometry two nanocontacts STOs can couple because the excited magnetic layer is the same for both. The mechanism proposed for the coupling between the two contacts is *propagating spin-waves*. The excitation of the magnetization below each contact generates propagating spin-waves with $\boldsymbol{k} \neq 0$ in the magnetic layer. These spin-waves decay with the distance from the contact, but if we take two contacts and the contacts are close enough, then the spin-wave propagating from one contact to the other retains enough information and the coupling is sufficient to enable synchronization between the two STOs.

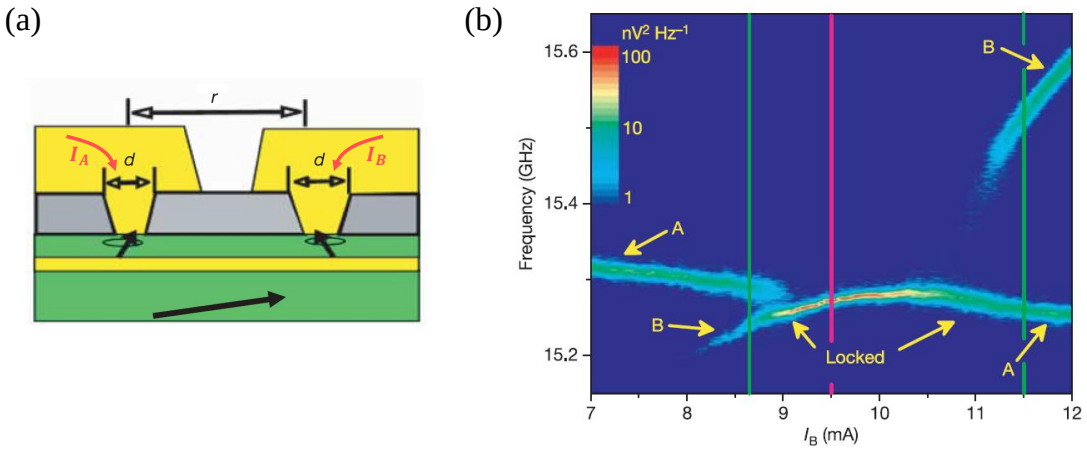

Figure I.17 – (a) Two nanocontact STO device structure used for mutual phase-locking experiments. The two STOs can be biased separately (I_A and I_B) and the magnetization starts to precess in a localized area below each nanocontact. As a consequence propagating spin-waves are emitted from this area and convey information from one nanocontact to the other, which creates a coupling and enables synchronization. (b) Phase-locking behaviour : combined PSD from the sum of the signals from the two nanocontacts. Here the current bias in the first nanocontact I_A is kept constant at 7 mA while I_B is swept from 7 mA to 12 mA, which varies the detuning between the two STO. The region in the middle from $I_B = 8.6$ mA to $I_B = 11.5$ mA is indicative of phase-locked regime - the peaks A and B merge together, plus the linewidth is reduced by 1 order of magnitude. From [39].

The second condition is the frequency detuning. Unless the two STO precess at similar frequencies, synchronization does not take effect. Fig. I.17(b) shows the combined PSD obtained from the addition of the two output signals collected at each contact. The current in the first contact is constant $I_A = 7$ mA while the current is the second nanocontact is swept from $I_B = 7$mA to $I_B = 12$ mA. Here varying the bias current in STO B allows one the vary the detuning between STO A and B by changing the frequency of STO B [30]. We can see in Fig. I.17(b) that in the range of currents $I_B =$ 8.5mA to $I_B =$ 11.5mA a phase-locked regime is reached causing peaks A and B to merge together at a common frequency and enhancing greatly the signal quality.

• **Coupling efficiency to a RF current : Georges *et al.* [22], 2008** Following the mutual phase-locking experiments of Kaka *et al.*, several groups have examined the possibility of using a common *microwave current* to synchronize an array of STOs. The theoretical investigation was conducted for example in [80, 27, 90]. Here we review an experimental realization of phase-locking of a STO to a RF current from George *et al.* [22]

In this article, an RF microwave current is used to phase-lock a single STO at f. The sample is a 70×170 nm^2 elliptic nanopillar patterned from a [Py(15nm)/ Cu(10nm)/ Py(3nm)] spin valve. It is perpendicularly magnetized with an out-of-plane field. The study focuses in particular on the experimental extraction of the coupling strength ϵ, which

30. We suppose the current changes the detuning by tuning the frequency only, but we can expect that the coupling intensity is also tuned by the current to a certain degree, since the emitted spin-wave power depends on the current.

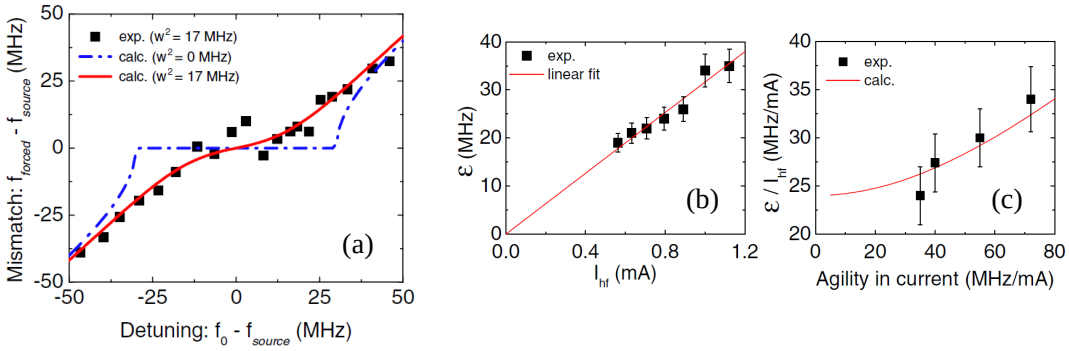

Figure I.18 – (a) Experimental detuning plot (black dots) $f_{forced} - f_{source}$ vs $f_0 - f_{source}$ for synchronization of a spin-valve STO to a RF current. (b) Variation of the locking-range ϵ extracted from fits of the detuning plots (a) versus RF current amplitude (external force amplitude). The locking-range increases linearly with i_{hf}. (c) Ratio ϵ/i_{hf} as a function of the agility in current df/dI. The ratio ϵ/i_{hf} increases with the agility in current, indicating that the synchronization region (the Arnold Tongue) widens. From [22].

is actually the locking-range, and its evolution with the microwave source amplitude, i_{rf}. This is similar to building the Arnold Tongues (the evolution of the locking range with the external force amplitude). To obtain the locking-range the detuning between the source and the STO must be varied. Interestingly here, the detuning is not varied by changing the external source frequency f_{source}. Instead the DC current is applied from -5 to -8mA thus causing the free-running STO frequency f_0 to vary accordingly from 1.84 to 1.94 GHz, while the source frequency is maintained at $f_{source} = 1.90$ GHz.

Fig. I.18(a) shows the detuning plot $f_{forced} - f_{source}$ vs $f_0 - f_{source}$ for a RF current amplitude $i_{hf} = 1,1$mA. The black squares are experimental points while the plain red lines are obtained from a fit of expression (5) (from the reference) for the forced frequency. Here the effect of thermal noise on synchronization is particularly important : this why is expression (5) has a corrective factor for the noise, allowing for extraction of the locking-range ϵ. For zero noise, expression (5) gives the blue dotted line that is typical for synchronization in the absence of noise (as in Fig. I.11 from Sec.I.3.1).

The evolution of the locking-range ϵ [31] with i_{hf} is shown in Fig. I.18(b). Black squares are experimental points while the red line is linear fit of the data. The locking-range is extracted using the method described above, i.e. by fit of expression (5) to the experimental data of Fig. I.18(a) for several values of i_{hf}. We recall from the previous section that for synchronization to an external force, the locking-range increases linearly with the force amplitude as long as the force amplitude is not too large, and Fig. I.18(b) effectively confirms this dependence.

We conclude with Fig. I.18(c), in which the ratio ϵ/i_{hf} is plotted as a function of the agility in current df/dI. The ratio ϵ/i_{hf} is a particularly noticeable quantity : it is the locking-range divided by the external force amplitude, which has the advantage of not being relative to the external force amplitude, and really measures the efficiency of the coupling of the STO with the RF current. Using the picture of the Arnold Tongues, it corresponds (in the limit of a weak forcing amplitude) to a measure of how open, or how wide is a particular Arnold Tongue. Later in the manuscript we will use this quantity to quantify and compare the synchronization efficiency at f and $2f$.

31. Up to now the notation ϵ has stood for the external force amplitude. We remark that in the reference ϵ represents instead the locking-range.

In Fig. I.18(c), the ratio ϵ/i_{hf} is obtained through linear fit of (b) and the agility in current is varied by changing the operating point of the STO (I_{DC}, H). The idea is to correlate the coupling efficiency with the agility in current, i.e. the non-linearity of the STO according to Eq.(4) in the reference. Fig. I.18(c) shows that indeed the non-linearity enhances the locking-range.

• Fractional synchronization to a microwave field : Urazhdin [93] *et al.*, 2010

In the previous section we discussed higher order synchronization, i.e. the occurrence of synchronization when the frequency of the source and the frequency of the oscillator are not necessarily close (1 :1 synchronization). This article from Urazhdin *et al.* examines synchronization of higher order (the said "fractional synchronization" regimes in the reference) in a STO when the driving force is a *microwave field*. It starts with experiments then it analyzes the results using macrospin simulations and symmetry arguments.

It is the first experimental demonstration of fractional synchronization in a STO. Experiments are carried out at 5 K on a 100 nm × 50 nm spin-valve nanopillar. The microwave magnetic field h_e is applied in-plane using a microstrip on top of the STO, generating a microwave field up to $h_e = 30$ Oe at 45° from the easy axis. The bias magnetic field $H_0 = 350$ Oe is applied collinear to the microwave field.

Fig. I.19 shows the experimental dependence of the PSD on the frequency of the microwave field ω_e for $h_e = 13$ Oe and $I_0 = 1.3$ mA. The synchronization regimes are reached when the forced frequency of the oscillator f_0' follows a linear relationship with the frequency of the source. Here eight different synchronization regime are identified : the integer regimes $r = 1, 2, 3$ and the rational regime $r = 5/2$ are particularly noticeable. In the article the regime $r = 2$ is quantitatively characterized and shows considerable enhancement of the signal characteristics (the linewidth is reduced by four orders of magnitude) confirming a very stable phase-locked state.

In the second part of the article the authors propose an interpretation of the results using a decomposition of the equation of the phase dynamics into a Fourier series. To sum up the outcome of the analysis in one sentence, we say that the direction of the microwave field $\boldsymbol{h_e}$ with respect to the symmetry axis of the oscillation orbit $\boldsymbol{s}$ determines the occurrence of specific synchronization regimes. Let us take a microwave field *aligned* with the symmetry axis ($\boldsymbol{h}_e \parallel \boldsymbol{s}$). In this case the *even* integer synchronization regime are prominent, $r = 2, 4, 6....$ On the other hand, a microwave field applied *perpendicular* to the symmetry axis ($\boldsymbol{h}_e \perp \boldsymbol{s}$) will favor instead the *odd* integer synchronization regimes, $r = 1, 3, 5....$ The rational synchronization regimes $r = p/q$ are found in the intermediate case as in Fig. I.19(a), where the microwave field has both a longitudinal and a perpendicular component with respect to $\boldsymbol{s}$.

This analysis is backed up by numerical macrospin calculations from which the dependence of the forced frequency versus the microwave field frequency is calculated (right panel of Fig. I.19). Fig. I.19(b) (resp. (c)) shows the results for a microwave field applied parallel to the symmetry axis (resp. perpendicular to the easy axis). $r = 2$ and $r = 4$ regimes are favored for (b) while $r = 1$ and $r = 3$ are favored for (c). The intermediate configuration (20° between $\boldsymbol{h}_e$ and $\boldsymbol{s}$) resembling that of the experiments is shown in Fig. I.19(d). There the fractional synchronization regimes can be identified as well.

The authors conclude by making the remark that measurements of the fractional synchronization regime can be utilized to obtain information about the oscillation characteristics in nanoscale systems, which are not accessible to direct imaging techniques.

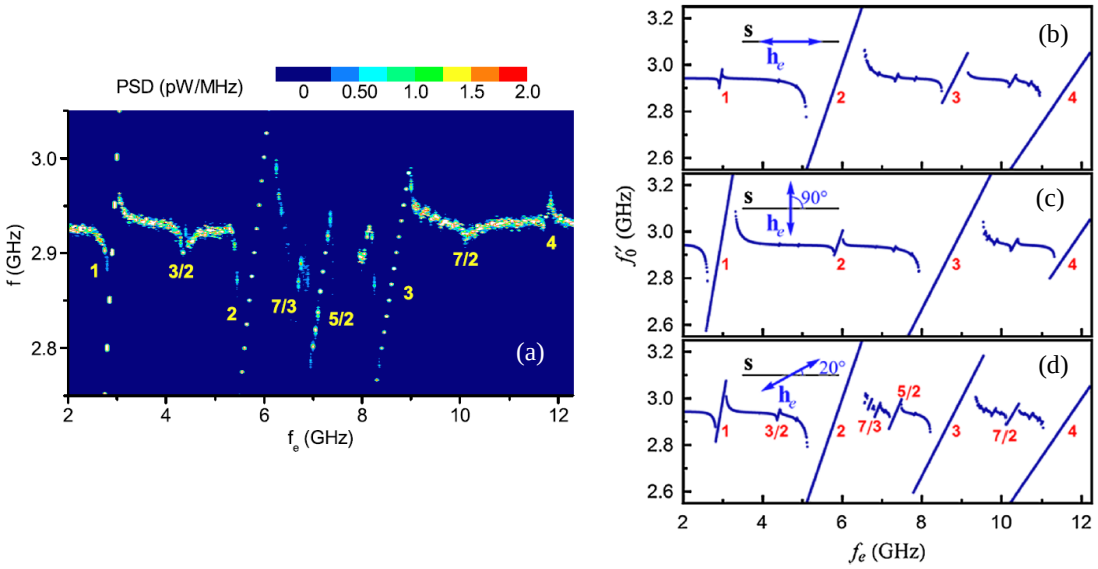

Figure I.19 – (a) Experimental dependence at 5 K of the PSD on the frequency of the microwave field applied at in-plane at 45° from the easy axis. Locking with the microwave field is achieved when f follows a linear relationship with f_e. Several (n :m) synchronization regimes are identified. (b),(c),(d) Macrospin simulations for the same dependence of the STO frequency on f_e for 3 different orientations of the microwave field $\boldsymbol{h}_e$ with respect to the symmetry axis $\boldsymbol{s}$ of the oscillation orbit : (b) $\boldsymbol{h}_e \parallel \boldsymbol{s}$, (c) $\boldsymbol{h}_e \parallel \boldsymbol{s}$ and (d) 20° angle between $\boldsymbol{h}_e$ and $\boldsymbol{s}$. The orientation of $\boldsymbol{h}_e$ with respect to $\boldsymbol{s}$ determines which synchronization regimes are favored.

This idea that the characteristics of the oscillation orbit are linked to the synchronization properties is central in this thesis. While this article focuses on role of a single characteristic of the orbit, the symmetry axis, in this manuscript we will also examine the role of two other characteristics, namely the *geometry* (in particular the ellipticity), and the *amplitude* of the orbit.

- **KTS model for synchronization to an external source : Slavin *et al.*, 2009**

To conclude with this rapid review on the recent literature of synchronization in STOs, we discuss phase-locking by an external force according to KTS formalism. As we mentioned the KTS model is widely used to interpret the STO dynamics in free-running regime but in the synchronized regime as well [22, 19, 12].

According to the review article [83], the non-autonomous dynamics of a STO can be modeled as follows

$$\frac{dc}{dt} = -i\omega(p)c - \Gamma_+(p)c + \Gamma_-(p)c + \underbrace{f_e e^{-i\omega_e t}}_{\text{External perturbation}} . \tag{I.23}$$

The distinction with Eq. I.8 for the autonomous dynamics lies in the inclusion of supplementary term $f_e e^{-i\omega_e t}$ in the RHS of the equation of motion. Here, f_e stands for an *effective amplitude* of the external force. Depending on whether an RF current or an RF field is injected, f_e takes two distinct expressions [83]. For an RF current, the amplitude

f_e of the locking-signal can be written approximately [32] as

$$f_e = \sigma \Delta I \tan(\gamma_0)/(2\sqrt{2}),$$

where γ_0 is the angle between the polarizer and the equilibrium magnetization of the free-layer, and ΔI is the amplitude of the RF current.

From there the set of two differential equations for the power and phase is derived by multiplication of Eq. I.23 by c^* and identification of the real and imaginary parts ((41a) and (41b) in [83])

$$\begin{aligned} \frac{dp}{dt} &= -2[\Gamma_-(p) - \Gamma_+(p)]p + 2F_e\sqrt{p}\cos(\omega_e t + \phi_e - \psi_e), \\ \frac{d\phi}{dt} &= -\omega(p) - F_e/\sqrt{p}\sin(\omega_e t + \phi_e - \psi_e). \end{aligned} \tag{I.24}$$

Here, F_e is the modulus of f_e, as f_e is a priori a complex number [33]. Eq. I.24 shows that, in this form, the external force acts on both the power and the phase.

Let us go back to some comments made in the previous section on synchronization to an external force. One of the requirements is to have a weak external force, which is considered in the article where it is mentioned that $F_e \to 0$. Using this approximation, it is said that Eq. I.24 can be "expanded in a Taylor series using the driving force amplitude and the power deviation as small parameters, i.e. $\delta p = p - p_0 \approx F_e$ ". In other terms the requirement is that the external force does not lead to substantial power variations, i.e. $\delta p << p_0$.

Two cases are distinguished :

(i) The non-linearity of the STO is small $\nu << 1$, so that the STO is weakly non-linear. As a consequence, the power variations due to the external force are negligible once inserted in the phase equation via the non-linearity N. Then only the phase equation of Eq. I.24 is of interest for the phase-locking.

The locking-range reads

$$\Delta\Omega = \frac{Fe}{\sqrt{p_0}}, \tag{I.25}$$

and the additional phase difference $\Delta\psi_0$ (phase-difference at zero detuning) gives

$$\Delta\psi_0 = 0. \tag{I.26}$$

(ii) The non-linearity of the STO is important $\nu >> 1$, so that the STO is strongly non-linear. The power variations are still small $\delta p << 1$ but this time they cannot be neglected once inserted in the phase equation. After an operation of renormalization of the phase (see Eq. (50) in the reference) the locking-range reads

$$\Delta\Omega = \frac{Fe}{\sqrt{p_0}}\sqrt{1+\nu^2}, \tag{I.27}$$

32. The expression f_e for locking to a RF current is given by Eq.(8b) in ref. [80] : it has been calculated for an out-of-plane oscillation of the magnetization.

33. For synchronization to a RF field, $f_e = \gamma(h_x + ih_y)/\sqrt{2}$, Eq.(8a) in ref. [80]

and the additional phase-difference gives

$$.\Delta\psi_0 = -\arctan\nu \tag{I.28}$$

In this instance we see that the locking-range is increased due to the non-linearity ν by a factor $\sqrt{1+\nu^2}$ and the solicited mechanism for synchronization when ν is important is *non-linear frequency matching*. In the experimental works of Georges *et al.* on injection locking that we reviewed, it is this mechanism of non-linear frequency matching that is demonstrated experimentally, Fig. I.18(c). However it is the agility, df/di, instead of ν that is used to quantify the non-linearity.

I.3.3.2 Approach and motivation of this thesis

From the beginning to the end, these three years and a few months of PhD involved research work based on the study and the practical application of synchronization phenomena in a STO. We saw in this first chapter that STOs are nanoscaled self-sustained oscillators with a complex nature, and their dynamics are modeled by the LLGS equation, a highly non-nonlinear equation. As a result the study of synchronization phenomena in STOs is particularly stimulating because the coupling between STOs comes out in various forms, and they are just as many configurations in which a STO can operate.

One single thesis is evidently not enough to cover and analyze all of the aspects of synchronization in STOs. In addition, there are practical considerations as well because since we do experimental work, we do not have access to an infinite number of distinct samples neither to many different setups. For instance the available setup for RF measurements generates in-plane bias magnetic fields only, so the out-of-plane precession (OPP) regime of a STO cannot be experimentally investigated [34]. Another example is the patterning of the STO devices ; since we mostly work with MTJ-based STO, the STO device cannot be fabricated in the nanocontact structure but only in nanopillar structure where the material stack is etched from top to bottom.

Initially, the proposed subject of this thesis was "Synchronization of an array of Spin-Torque oscillators". The goal was to realize a device made out of four similar MTJ-based nanopillars, where the top and the bottom electrodes are common for the four nanopillars. A constant current is injected in the device and is distributed equally in the pillars, and for a sufficient current density steady-state precession of the magnetization takes effect. Then an RF signal is generated by each pillar, and due to the electrical coupling provided by the common electrodes, the four pillars generate a coherent, synchronized signal. This signal has enhanced signal properties compared to the output of a single STO, going one step further towards the realization of a tunable frequency RF synthesizer based on STOs, able to compete in the telecommunication market with classical electronic oscillators.

The subject had the features of an ambitious and yet realistic project. In the previous years the experimental realization of mutual synchronization of two STOs through coupling with spin-waves was done in [39], injection-locking of a STO was also demonstrated in [75, 23], and the theoretical background for synchronization of an array of STO by an electrical current was developed for instance in [21, 90].

34. This is true for typical in-plane polarized STOs : however it is possible to reach the out-of-plane precession with an in-plane applied magnetic field using a STO structure having a perpendicular polarizer [33].

In addition, the work in the PhD implied a twofold approach : (i) the RF measurements with the in-depth analysis of STO dynamics would be performed in Spintec facilities, while (ii) the optimization of the magnetic stack and the ultra-low RA MTJ would be done with the expertise of LETI by practical experience in a 300 mm clean room chip fab.

In the first year we worked in this direction : first elementary RF measurements of single pillar STO in autonomous regime were performed along with a bibliographic study on STO dynamics and synchronization phenomena, and in parallel we started the optimization of the MTJ on the Ion-beam deposition machine Aviza IBD3000 coupled with full sheet characterization of the deposited wafers (resistance area-product, TMR).

We mention that the mutual synchronization of the four pillars did not give the expected results. Moreover, it is delicate in this case to clearly identify the factors accountable for the fact that the device did not perform well. There are several explanations put forth : (i) the electrical coupling provided by the contacts is not sufficient, for example the RF current generated by each pillar is of too small amplitude to induce significant coupling with the other pillars ; (ii) inhomogeneous distribution of the characteristics of the pillars. Due to nanofabrication the pillars are not exactly similar, and as a consequence they do not generate frequencies close enough, then the detuning is too large for synchronization ; (iii) additional phase-shifts : as it was advanced in [90], depending on the value of the phase-shift, one reaches either a regime of frustration or phase-locking (iv) signal properties in the autonomous regime of the individual devices : the critical current being relatively high,

As the thesis went on we progressively switched to the subject to the study of a single nanopillar STO locked to a RF current. Experimentally, it focuses on the *characterization* of the synchronized regime at room temperature when the RF current is injected at $2f$. It is true that several works have already observed experimentally injection-locking in a STO at room temperature in various configurations of a STO [75, 23, 51, 20], and the group from Spintec as well [57, 72]. We still aim to present in this thesis a characterization of injection-locking using new angles, with special attention to the conditions for synchronization (in particular the condition of weak coupling through $\epsilon = i_{rf}/I_{DC}$, and the necessity for a self-sustained regime of oscillations $I > I_C$) but also using specific time-domain characterization techniques, which we wish can provide original information about the phase-difference in synchronized regime.

Because we also need to find out about why a given configuration of the system (STO + RF current source) is more suitable for synchronization experiments than another, we investigate the mechanisms involved in the synchronization process. A particularly interesting question for STOs concerns why the synchronization by a RF current *at* $2f$ usually yields the best enhancement of the signal in experiments. STOs exhibit an important non-linearity, which is remarkable compared to other conventional self-sustained oscillators, and what are the implications in terms of synchronization properties ? In addition, current theoretical models do not make a clear distinction between synchronization at f and $2f$ [83]. Is it justified ? Is there a need for a specific analysis of the synchronization process at $2f$?

During this thesis we conducted the analysis of synchronization mechanisms through two approaches : (i) An analytical development using the KTS formalism, starting from the transformation of the LLGS equation for an IPP to a self-sustained oscillator equation, to the examination and of the phase and amplitude expressions in synchronized regime and ; (ii) Macrospin simulations at 0 K for the IPP regime, and quantitative comparison with the

analytical results obtained after the mathematical development. Whenever possible, the findings are accompanied with a physical interpretation along with a link to characteristics of the oscillation orbit.

Part B : Mechanisms of synchronization

In the first part of the manuscript, we presented the prerequisites to understand magnetization dynamics in STOs with the help of the LLGS equation, then we explained how weakly non-linear oscillators behave under the influence of a driving signal as in [67], and finally we gave an overview on the rich synchronization phenomena observed in STOs. In this part we want to find out about synchronization of a STO to a driving current without thermal noise. This part contains the most significant findings of my thesis, and we thoroughly disclose synchronization mechanisms at $2f$ that we compare with the already described synchronization at f.

To introduce this part of the manuscript, let us consider the following argument : We have seen earlier that the phenomenon of synchronization is described as *adjustment of rhythms of oscillators due to an interaction*. For synchronization to a driving force, the driven oscillator adjusts its frequency to that of the force. Now if we go to STOs, we have seen in Sec.II.1 that in autonomous steady-state regime, it is possible for the STOs to change their generation frequency in various ways. From the KTS formulation, we recall two main courses of action. The first one is changing the resonant frequency ω_r, which is possible by modifying the direction and the amplitude of the effective field. The second way is changing the frequency-shift due to amplitude Np_0 by varying the DC current over the threshold, and the strong non-linearity in STO makes this option particularly interesting. With this in mind, the reader may ask : I understand this from a dynamical standpoint, but how does it translate into magnetization dynamics ? What kind of information does it provide on the magnetization precession orbits ?

The link can be made in cases where the magnetic configuration of the STO remains rather simple. Here we choose the in-plane precession configuration where building this link requires only a few approximations, and it resembles our experiments. Moreover, we make during the rest of this manuscript the following observation which will greatly help for interpretation of the results : *In the steady-state regime, the frequency of a STO is given by the characteristics of the magnetization precession orbit* namely (i) its geometry and symmetry axis (ii) its amplitude.

So synchronization to an external source is frequency adjustment to that of the source, and on the other hand we know that in autonomous state the STO frequency depends on the characteristics of the precession orbit, e.g. its amplitude or more generally its shape. The reader should then apprehend part B with these general questions in mind : How is the magnetization orbit modified so that the STO can adjust its frequency to that of the driving force ? What are the different ways that the driving force can act on the magnetization orbit ?

Part B is organized as follows : In Chap. II we extend the KTS model in the IPP case to synchronization at $2f$. The analysis is centered from the dynamical standpoint on power and frequency variations from the autonomous to the synchronized state, and we obtain in particular analytic expressions for the locking-range at $2f$. We also derive equations for synchronization at f that we compare with our expressions at $2f$. In Chap. III, we will confront the model with macrospin simulations. From the same magnetic configuration, we also underline the differences in behavior with amplitude between f and $2f$ synchronization and stress the need for two separate treatments.

Chapter II

Locking to a RF current : Extension of the KTS model

In this chapter the KTS model is used to understand magnetization dynamics under the influence of a RF current applied at $2f$ and f, for an in-plane precession (IPP) type of the magnetization.

We will start by having a look at the free magnetic energy in the in-plane configuration. In the small precession angle approximation, the free magnetic energy is linearized and from there the FMR frequency as well as the ellipticity of the IPP orbit will be extracted. The LLGS equation will be explicited in this configuration too. We will then examine the change of variables from the magnetization coordinates (m_x, m_y, m_z) to the dimensionless oscillator variable $c(t)$ according to [82] in which it was first introduced.

Using this change of variables the LLGS equation will be rewritten so as to obtain the characteristic reduced oscillator equation of the KTS model. Due to the properties of the IPP configuration, the transformation into the oscillator equation will give rise to oscillating terms. We will demonstrate that the form of these oscillating terms determines the synchronization properties of our system by investigating the effect of a RF current on the STT term.

Finally the phase and power equations will be derived separately for (i) RF injection close to $2f$ and (ii) RF injection close to f. Synchronization in the stationary state will be inspected in both cases by the analysis of the amplitude deviations, the phase-difference and the locking-range. We will expose the differences between synchronization at $2f$ and f. Interestingly, we will see that synchronization at $2f$ obeys a much more intuitive process than synchronization at f, which is beautifully evidenced using the KTS formalism.

II.1 Magnetization dynamics for the IPP

II.1.1 Macrospin Approximation

We start with the description of the magnetic configuration at equilibrium. Throughout this part, we consider the macrospin approximation, which means that the magnetization of the magnetic layers is homogeneous, and all spins in each magnetic layer behave as single one, which is enabled by the typically large exchange energy in ferromagnets. This is a strong approximation, and evidently the vortex state cannot be described within this approximation, but macrospin gives the features of IPP and OPP where magnetization of the layers is homogeneous.

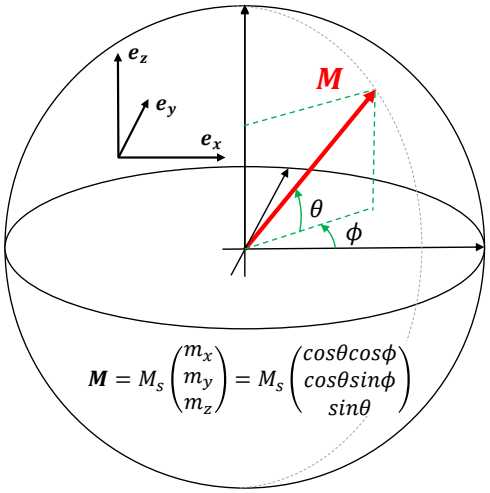

Figure II.1 – The magnetization vector $\boldsymbol{M}$ within macrospin approximation. In macrospin approximation, only the direction of the magnetization changes but not its norm. Angles θ and ϕ are sufficient to describe magnetization dynamics.

In experiments the macrospin approximation is valid in a few cases.

• *If the nanopillar diameter remains relatively small* (in our case, for CoFeB $d \leq$ 100nm). The magnetic layer finds a balance between the exchange energy and the dipolar energy. When the layer diameter increases, long range interaction between the spins becomes important and in order to minimize the dipolar energy, spins start to tilt with respect to each other. Strictly speaking in this case the macrospin condition is not fulfilled but one can still define an effective magnetization and the macrospin approximation is considered valid if the large majority of the spins have the same magnetization direction. When the diameters increases, magnetic domains start to emerge, leading for example to supplementary peaks in the output signal spectrum, where the peak frequency is given by the effective field acting on each domain (see for example "edge modes").

• *If the current density flowing in the pillar in "not too important"*. By "not too important" we mean when the current-induced Oersted field - spatially inhomogeneous - is small compared to the total effective field - spatially homogeneous. For example Dumas *et al* in [18] evaluate to role of the Oersted field in nanocontact-based STOs. In their configuration, they obtain above the critical current an Oersted field of about 1 kOe on the edge of the pillar, which leads to inhomogeneous spatial profiles of the magnetization, but more importantly to two different precession modes at separate frequencies. For an infinite wire of diameter 70 nm, the correspondence between Oersted field and current yields $dH/dI = 56$ Oe/mA when at the edge of the pillar. In our MTJ-based STO, the critical current is about $0.5 - 1$ mA for these pillar sizes, so the corresponding Oersted field is of a few tens of Oersteds. Knowing that we apply in-plane fields of $H_b \approx 500$ Oe, the Oersted field remains well below the applied field in amplitude. Only minor changes of the magnetization profiles due to the Oersted field are expected as long as the applied current is close to the critical current.

Within the macrospin approximation the behavior of the magnetic layer is completely described by the reduced magnetization vector $\boldsymbol{m} = \boldsymbol{M}/M_s$, where M_s is the saturation magnetization. The norm of this vector is constant throughout the dynamics, and only its direction changes. The magnetization vector $\boldsymbol{M}$ is shown in Fig.II.1 and moves on the surface of the sphere. As a consequence, the magnetization coordinates (m_x, m_y, m_z) in

the cartesian system are linked according to Eq. II.1

$$m_x^2 + m_y^2 + m_z^2 = 1. \tag{II.1}$$

This relation will allow us to greatly simplify the LLGS equation later. In particular, we can reduce the dynamics to the motion of two variables (for IPP m_y and m_z) instead of three, and as we will see later peculiarities of the IPP precession come from the evolution of the m_x component when the precession angle grows.

II.1.2 Static equilibrium

Now let us consider the static equilibrium state for a high symmetry IPP configuration. Fig. II.2 (a) shows the relative orientation of the PL and FL in the static state, as well as the direction of the applied bias field $\boldsymbol{H}_b$. White arrows stand for the magnetization direction. In our case, the PL and the FL are both stabilized in-plane. The static equilibrium is given by the minimum of the free energy density for the free layer,

$$E = -\boldsymbol{H}_b.\boldsymbol{M} - \frac{1}{2}(\boldsymbol{M}.\boldsymbol{H}_a) - \frac{1}{2}(\boldsymbol{M}.\boldsymbol{H}_d). \tag{II.2}$$

Here M_s is the saturation magnetization. In this form, the free energy takes into account the Zeeman interaction with the external magnetic field, the uniaxial anisotropy and magnetostatic interactions.

One can define an effective field as the variational derivative of the free-energy with respect to the magnetization vector $\boldsymbol{M}$,

$$\boldsymbol{H}_{eff} = -\frac{\delta E}{\delta \boldsymbol{M}}, \tag{II.3}$$

which is the sum of the following three contributions :

$$\boldsymbol{H}_{eff} = \boldsymbol{H}_b + \boldsymbol{H}_d + \boldsymbol{H}_a. \tag{II.4}$$

Here $\boldsymbol{H}_b$ is the applied magnetic field, $\boldsymbol{H}_a$ is the effective uniaxial anisotropy field which determines the easy axis and $\boldsymbol{H}_d$ is the dipolar field that apply to the free layer. The Oersted field is not taken into account. We can review :

• **Uniaxial anisotropy field**. The uniaxial anisotropy field is actually a sum of contributions $H_a = H_{a1} + H_{a2}$ that have two distinct origins. (i) H_{a1} Uniaxial magnetocristalline anisotropy. The anisotropy field is connected with the magnetocristalline anisotropy constant K_a through the relation $H_{a1} = 2K_a/M_s$. (ii) H_{a2} uniaxial shape anisotropy. This is actually a contribution from the dipolar interaction, but it is possible to write it in some cases as an uniaxial anisotropy field, which facilitates the comparison with the external applied field. In the instance of a circular pillar, the magnetization does not have a preferred orientation in the plane. However, if the pillar is elliptical, then the major axis of the ellipse becomes a preferred direction for the magnetization - the easy axis - due to dipolar interaction. Thus, it can be modeled as an uniaxial anisotropy field

$$H_{a2} \approx 4\pi M_s \frac{t}{w}\frac{l-w}{l+w},$$

where t is the layer thickness, w the minor axis and l the major axis. We take both contributions to be along the same axis, $\hat{\mathbf{e}}_x$, that will define the easy axis of magnetization

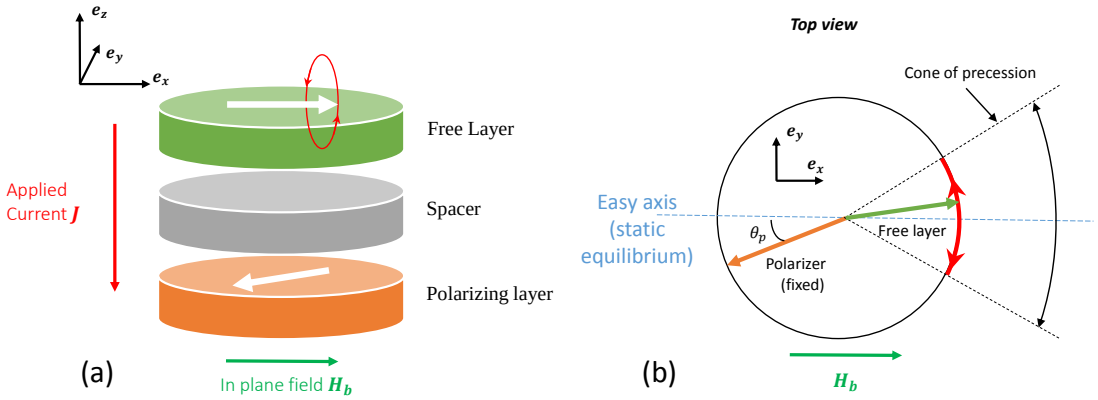

Figure II.2 – Magnetic configuration of the STO in IPP.

and the equilibrium direction in the absence of an external field.

• **Applied field**. The applied field is applied along the $\hat{\mathbf{e}}_x$ direction too. In experiments, its amplitude is comparable or usually superior to the uniaxial anisotropy field when pillars are strongly elliptic. For the sake of simplicity, we restrict ourselves to the case when the external field does not induce symmetry breaking in the system and chose the direction of the easy axis defined by the anisotropy field, $\boldsymbol{H}_a$. It is worth noting that in this configuration, as long as the m_x component of the magnetization remains positive, the uniaxial anisotropy field $\boldsymbol{H}_a$ plays a rather similar role to that of the applied field $\boldsymbol{H}_b$, in the sense that both $\boldsymbol{H}_a$ and $\boldsymbol{H}_b$ act. In our case, this anisotropy field is of the order of one 100^{th} of the saturation magnetization.

• **Magnetostatic field**. We assume here that the free layer is magnetically isolated from the rest of the stack. This means that we consider that the magnetostatic field produced by the polarizer does not affect the free-layer. No static or dynamic interactions with the polarizer are considered here in the dipolar field. As a consequence, in the thin-film approximation, the dipolar field takes this simple form II.5(c). In our case, the saturation magnetization is much higher than the applied field and the uniaxial anisotropy field, and it forces the magnetization in plane at the static equilibrium.

So in our configuration, we apply a bias field along the $\hat{\mathbf{e}}_x$ axis [1], which is also the anisotropy axis so that we have a high symmetry case. Then the three fields making up the total effective field in Eq. II.4 read

$$\boldsymbol{H}_b = H_b \hat{\mathbf{e}}_x, \tag{II.5a}$$
$$\boldsymbol{H}_a = H_a(\boldsymbol{m}.\hat{\mathbf{e}}_x)\hat{\mathbf{e}}_x, \tag{II.5b}$$
$$\boldsymbol{H}_d = -4\pi M_s(\boldsymbol{m}.\hat{\mathbf{e}}_z)\hat{\mathbf{e}}_z. \tag{II.5c}$$

Here, $\boldsymbol{m}$ stands for the normalized magnetization vector, i.e. $\boldsymbol{m} = \boldsymbol{M}/M_s$. Since there are no magnetic interactions of the polarizer with the free layer, the orientation of the polarizer with respect to the free layer does not lead to changes in the free energy. From Eq. II.2, one can see that free energy is minimum when $\boldsymbol{M}$is in the positive $\hat{\mathbf{e}}_x$ direction.

1. In the positive direction so that the FL and the polarizer are in anti-parallel configuration.

II.1.3 Linearization of the free energy

In STOs, different precession modes are linked to different shape of the precession orbits. The peculiarities of precession orbits define dynamic attributes of the system, and we will see later the effect on synchronization properties. The most simple case is the circular Out-Of-Plane (OPP) orbit. This type of orbit facilitates the reduction of the magnetization coordinates to the c variable, so it is commonly used as an example in the KTS model. As for the IPP, interesting properties arise from the fact that the precession orbit is not a circle, but rather an ellipse.

How to determine the geometry of the precession orbits ? In first approximation, only the *conservative term* in the LLGS equation is kept, i.e. the precession term. With only the precession term remaining then the free energy of the system is conserved, and the whole dynamic properties are determined by the effective field. In particular, the free energy *equipotentials* can be drawn on the unit sphere as a function of the magnetization angles ϕ and θ. Then the possible magnetization trajectories in steady-state can be worked out simply by following the equipotentials.

In order to find both FMR frequency and the ellipticity of the IPP orbit, we will use this fact. First, we only consider variations of the magnetization close to the stable point. In other words, the cone of precession is extremely small. If we take the notations from Fig. II.1, it means that the angles θ and ϕ are close to zero. In Fig. II.3 a representation of the magnetization IPP orbit in these conditions is shown. For small angles, we perform a Taylor expansion of the magnetization coordinates m_x, m_y, m_z, and keeping terms up to the second order only we obtain :

$$\begin{aligned} m_x &\approx 1 - \frac{\phi^2}{2} - \frac{\theta^2}{2}, \\ m_y &\approx \phi, \\ m_z &\approx \theta. \end{aligned}$$

One can easily verify that the norm of the magnetization vector (m_x, m_y, m_z) is equal to 1 in these conditions. The total free energy from Eq. II.2 reads then :

$$\begin{aligned} E &= M_s \left[-H_b \left(1 - \frac{\phi^2}{2} - \frac{\theta^2}{2} \right) + \frac{1}{2} 4\pi M_s \theta^2 + \frac{1}{2} H_a \left(\theta^2 + \phi^2 \right) \right] \\ &= M_s \left[-H_b + \underbrace{\frac{\phi^2}{2} \left(H_b + H_a \right)}_{\text{Motion along } \hat{\mathbf{e}}_y} + \underbrace{\frac{\theta^2}{2} \left(H_b + H_a + 4\pi M_s \right)}_{\text{Motion along } \hat{\mathbf{e}}_z} \right] \end{aligned} \tag{II.6}$$

On this equation, the first term represents the minimum of the free energy, and the two other are small perturbations around this state. The second term indicates the energy cost of tilting the magnetization in plane, while the third indicates the energy cost of tilting it out of plane. One can notice that, for the same angular change along $\hat{\mathbf{e}}_y$ and $\hat{\mathbf{e}}_z$, it costs much more to tilt the magnetization out of plane (2nd term) due to the demagnetizing field $H_d = 4\pi M_s$ that prevails over other fields. So, for the same energy cost, the precession angle in plane will be much more important than the precession angle out of plane. Since the magnetization trajectory follows energy equipotentials, we have a first qualitative

explanation as to why the IPP trajectory is elliptical.

The free energy also allows us to obtain the FMR frequency and its square root dependence with the applied field according to the Kittel formula [43]. To do so, we utilize the expression derived in [4, 86] returning the FMR frequency from the second derivatives of the free energy with respect to polar ϕ and azimuthal angle θ (θ is the angle between $\boldsymbol{m}$ and the normal $\hat{\mathbf{e}}_z$)

$$\frac{\omega_r}{\gamma} = \frac{1}{M_s \sin\theta}\sqrt{\frac{\partial^2 E}{\partial\phi^2}\frac{\partial^2 E}{\partial\theta^2} - \left(\frac{\partial^2 E}{\partial\phi\partial\theta}\right)^2}\Bigg|_{\theta_0,\phi_0}, \tag{II.7}$$

where θ_0 and ϕ_0 stand for the magnetization angles at equilibrium. To conform with the notation we choose in this section for the azimuthal angle θ, we make the substitution in the above formula $\theta \mapsto \pi/2 - \theta$. Eq. II.8 that can be simplified in our conditions ($\phi_0 = 0, \theta_0 = 0$) to :

$$\frac{\omega_r}{\gamma} = \frac{1}{M_s}\sqrt{\frac{\partial^2 E}{\partial\phi^2}\frac{\partial^2 E}{\partial\theta^2}}\Bigg|_{0,0}. \tag{II.8}$$

Applying formula II.8 to the energy II.6, the FMR frequency yields

$$\omega_r = \gamma\sqrt{(H_b + H_a + 4\pi M_s)(H_b + H_a)}, \tag{II.9}$$

in the limit where $H_a << H_b << 4\pi M_s$, then the FMR frequency increases directly as the square-root of the applied bias field H_b.

• **Ellipticity**. Now we address the question of ellipticity of the IPP in the same conditions of magnetization variations close to the stable state. As we will see later, the ellipticity of the IPP orbit plays a determinant role in the dynamics. Whenever possible, dynamic parameters will be expressed as a function of the ellipticity, and because we want to link synchronization properties at $2f$ with geometrical factors of the precession orbit similarly to the work of Urazhdin *et al.* [92].

We introduce the *ellipticity* of the IPP trajectory. In geometry the shape of an ellipse is determined by the ratio of the semi-minor axis b over the semi-major axis a. We use it as a definition for the ellipticity e_0

$$e_0 = \frac{b}{a}.$$

In all cases the ellipticity is between 0 and 1. Strong ellipticity gives $e_0 \approx 0$ while $e_0 = 1$ for a circle with no ellipticity. Applying this definition the IPP orbit in the small angle approximation, then the ellipticity of the IPP is provided by the ratio m_{z0}/m_{y0}, where m_{z0} corresponds the m_z coordinate in point (B)(Fig.II.3) and m_{y0} corresponds to the m_y coordinate in point (A) (Fig.II.3). When the precession angle grows, then the magnetization does not precesses in the $(\hat{\mathbf{e}}_y, \hat{\mathbf{e}}_z)$ plane anymore, so strictly speaking the ellipticity of the IPP trajectory would require another definition. Nevertheless the ratio m_{z0}/m_{y0} remains approximately constant when the precession angle is increased and we will keep m_{z0}/m_{y0} for our definition of ellipticity.

Let us explicit the ellipticity in the small angle approximation. For that we recall that the IPP orbit draws along the energy equipotentials, so it follows that $E_{(A)} = E_{(B)}$. At point (A), $(\phi, \theta) = (m_{y0}, 0)$ and at point (B) $(\phi, \theta) = (0, m_{z0})$. The free energies at point

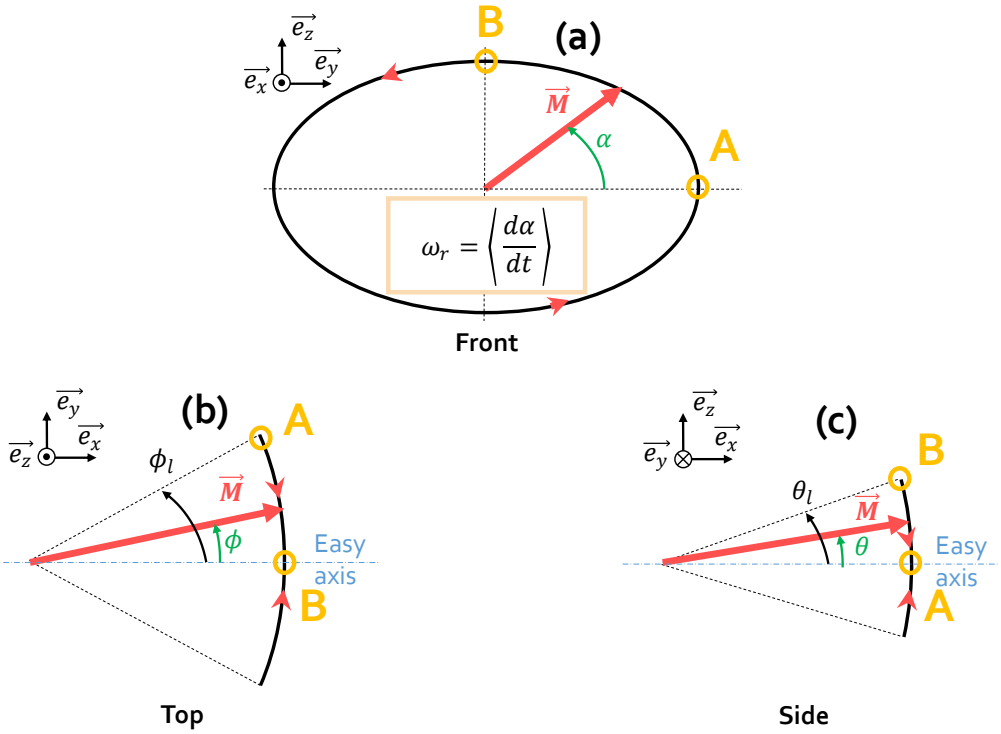

Figure II.3 – Schematic representation of the the elliptic magnetization precession in IPP close to the stable position. **(a)** Front view : Projection onto the $(\hat{\mathbf{e}}_y, \hat{\mathbf{e}}_z)$ plane. The FMR frequency is given by the angular velocity (time derivative of α) of the magnetization projection. **(b)** Top view : Projection onto the $(\hat{\mathbf{e}}_x, \hat{\mathbf{e}}_y)$ plane. Point (A) represents the maximum value of m_y for this orbit. **(c)** Side view : Projection onto the $(\hat{\mathbf{e}}_x, \hat{\mathbf{e}}_z)$ plane. Point (B) represents the maximum value of m_z

(A) and (B) read then

$$E_{(A)} = -H_b + \frac{{m_{y0}}^2}{2}(H_b + H_a), \tag{II.10a}$$

$$E_{(B)} = -H_b + \frac{{m_{z0}}^2}{2}(H_b + H_a + 4\pi M_s). \tag{II.10b}$$

Writing $E_{(A)} = E_{(B)}$ yields after simplification

$$\frac{{m_{y0}}^2}{2}(H_b + H_a) = \frac{{m_{z0}}^2}{2}(H_b + H_a + 4\pi M_s), \tag{II.11}$$

and finally we can obtain the ellipticity e_0

$$e_0 = \frac{m_{y0}}{m_{z0}} = \sqrt{\frac{H_b + H_a}{H_b + H_a + 4\pi M_s}}, \tag{II.12}$$

or written with the second derivatives of the energy with respect to θ and ϕ [2]

$$e_0 = \sqrt{\left(\frac{\partial^2 E}{\partial \phi^2}\right) / \left(\frac{\partial^2 E}{\partial \theta^2}\right)\Bigg|_{\theta_0,\phi_0}}. \tag{II.13}$$

The expressionII.12 indicates that close to the stable point, the ellipticity *does not depend on the precession angle*, in the manner of the FMR frequency. Formula II.13 is also interesting because it directly links the ellipticity with the free energy. One may think of the energy valley in the bottom of which the magnetization is stabilized. The second derivative of the free energy with respect to ϕ corresponds to the curvature of the energy surface at the stable point in the $\hat{\mathbf{e}}_y$ direction, and with respect to θ it is the curvature in the $\hat{\mathbf{e}}_z$ direction. For our symmetry ($\phi_{eq} = 0, \theta_{eq} = 0$), only these terms matter, and it gives us both ellipticity and the FMR frequency. The square root of the *product* of the energy derivatives provides us the FMR frequency, whereas the square root of the *ratio* provides the ellipticity of the magnetization orbit. We will encounter later these quantities during the change of variable of the KTS model.

Moreover, one has $4\pi M_s >> H_b + H_a$ for ferromagnetic thin films due to the strength of the demagnetizing field, yielding an ellipticity $e_0 << 1$. Strong ellipticity will allow us to make simplifying assumptions later on to be able to compare f and $2f$ synchronization.

II.1.4 The LLGS equation in IPP

In the last subsection, the ellipticity and the FMR frequency for the IPP were derived (i) from the free energy and (ii) close to the equilibrium. We found that FMR frequency and ellipticity do not depend on the precession angle up to the second order. When the precession angle increases, we can expect that these two quantities will not be constant anymore, also indicating the limits of the linear expansion. Now let us write the complete LLGS equation for IPP. We keep the macrospin approximation and relation II.1 still holds, and the effective field remains the same. But this time, the STT and the magnetic damping will be taken into account in the LLGS equation, and more importantly we will

2. Using Bogoliubov transformations this expression for the ellipticity as a function of the second derivation can be obtained as well.

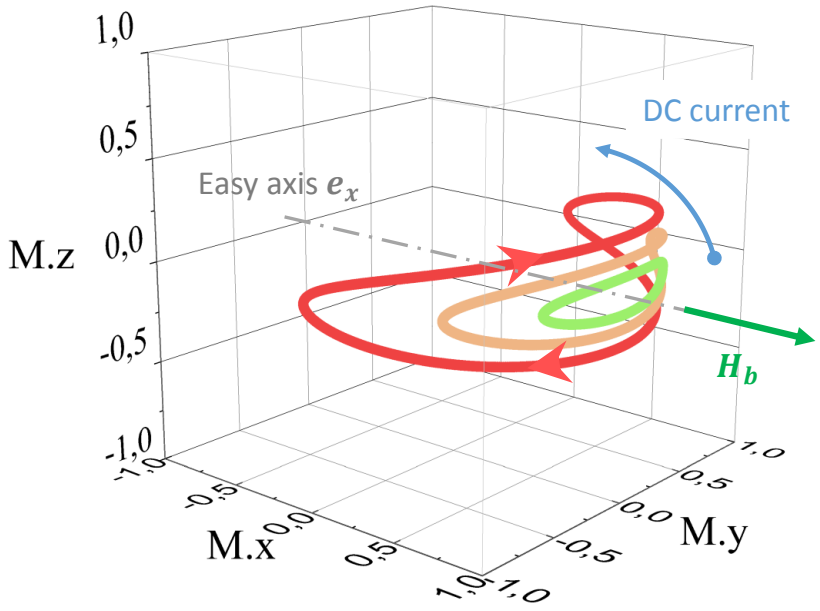

Figure II.4 – Magnetization orbits for IPP (In plane precession) type from macrospin simulations from small to high precession angles. Only a DC current is applied in addition to the bias field of 40 mT. The parameters for simulations are provided in Chapter 4. Current density $J_{app} = (4,5(\text{green}); 4,8(\text{orange}); 5,8(\text{red})\ 10^{11}\text{A/m}^2)$. As the applied current increases, the precession angle grows.

go beyond the small angle approximation.

As we will see in Section 2, the KTS transformation does not require one to write the magnetization in circular coordinates, so the LLGS equation will be expressed simply as a function of the magnetization vector in Cartesian coordinates (m_x, m_y, m_z).

We recall from Chapter 1 that the LLGS equation for magnetization dynamics under application of an external current J reads

$$\frac{\partial \boldsymbol{m}}{\partial t} = -\gamma(\boldsymbol{m} \times \boldsymbol{H}_{\text{eff}}) + \alpha(\boldsymbol{m} \times \frac{\boldsymbol{m}}{dt}) - \sigma J \boldsymbol{m} \times (\boldsymbol{m} \times \boldsymbol{e}_p) \tag{II.14}$$

Here we neglect the "field-like" contribution of the STT to the dynamics, as it has been discussed previously in Sec.I.1.2. In this form, numerical integration is more tedious because of the time-derivative of the magnetization in the RHS of Eq. II.14. By replacing the time-derivative in the damping by the complete RHS of II.14, we obtain the Landau-Lifshitz form of Eq. II.14 for magnetization dynamics

$$\frac{\partial \boldsymbol{m}}{\partial t} = -\gamma'(\boldsymbol{m} \times \boldsymbol{H}_{\text{eff}}) - \alpha\gamma'\left(\boldsymbol{m} \times (\boldsymbol{m} \times \boldsymbol{H}_{\text{eff}})\right) - \frac{\sigma J}{1+\alpha^2}\left[\boldsymbol{m} \times (\boldsymbol{m} \times \boldsymbol{e}_p) - \alpha(\boldsymbol{m} \times \boldsymbol{e}_p)\right]. \tag{II.15}$$

Here, $\gamma' = \gamma/(1+\alpha^2)$. We note that the LLGS equation written above is valid for any value of the Gilbert damping α. We also remark that the transformation into the Landau-Lifshitz form gives an additional term having the symmetry of a field-like term in $(\boldsymbol{m} \times \boldsymbol{e}_p)$. During macrospin simulations, it is the above form that is solved numerically (without assumptions on α) for more precision. Nevertheless, from there on the analytical develop-

ment assumes that $\alpha << 1$, thus giving $\gamma' \approx \gamma$, and the pseudo "field-like" term can be neglected too.

Finally, compared to the last subsection, the dynamics are now modified due to the addition of the damping and the spin-torque. The spin torque forces us to take into account the polarizer direction and the current intensity.

The polarizer is in-plane and its direction is given by

$$\boldsymbol{e}_p = \begin{pmatrix} P_x \\ P_y \\ 0 \end{pmatrix}$$

We now have all the elements to write II.15 for our configuration. We substitute the effective field as well as the magnetization vector by their components in Cartesian basis, and Eq. II.15 yields :

$$\begin{aligned} \begin{pmatrix} \dot{m}_x \\ \dot{m}_y \\ \dot{m}_y \end{pmatrix} = &- \gamma \begin{pmatrix} m_x \\ m_y \\ m_z \end{pmatrix} \times \begin{pmatrix} H_b + H_a m_x \\ 0 \\ -4\pi M_s m_z \end{pmatrix} \\ &- \alpha\gamma \begin{pmatrix} m_x \\ m_y \\ m_z \end{pmatrix} \times \left[\begin{pmatrix} m_x \\ m_y \\ m_z \end{pmatrix} \times \begin{pmatrix} H_b + H_a m_x \\ 0 \\ -4\pi M_s m_z \end{pmatrix} \right] \\ &- \sigma J \begin{pmatrix} m_x \\ m_y \\ m_z \end{pmatrix} \times \left[\begin{pmatrix} m_x \\ m_y \\ m_z \end{pmatrix} \times \begin{pmatrix} P_x \\ P_y \\ 0 \end{pmatrix} \right]. \end{aligned} \tag{II.16}$$

After development of the cross products, Eq. II.16 reads

$$\begin{aligned} \begin{pmatrix} \dot{m}_z \\ \dot{m}_y \\ \dot{m}_z \end{pmatrix} = &- \gamma \begin{pmatrix} -M_s m_y m_z \\ H_b m_z + (H_a + 4\pi M_s) m_z m_x \\ -(H_b + H_a m_x) m_y \end{pmatrix} \\ &- \alpha\gamma \begin{pmatrix} -m_y^2 (H_b + H_a m_x) - [m_z^2 (H_b + H_a m_x) + m_x m_z^2 4\pi M_s] \\ -m_y 4\pi M_s m_z^2 + (H_b + H_a m_x) m_y m_x \\ H_b m_z + [(H_a + 4\pi M_s) m_z m_x]\, m_x + 4\pi M_s m_z m_y^2 \end{pmatrix} \\ &- \sigma J P_x \begin{pmatrix} -(m_y^2 + m_z^2) \\ -m_x m_y \\ -m_x m_z \end{pmatrix} - \sigma J P_y \begin{pmatrix} m_x m_y \\ m_z^2 + m_x^2 \\ -m_y m_z \end{pmatrix} \end{aligned} \tag{II.17}$$

Eq. II.17 is a set of three coupled non-linear first order differential equations for m_x ,m_y and m_z. We remark that we have split the spin-torque contribution into two terms : one with the prefactor P_x and the other with the prefactor P_y. It means that depending on the orientation of the polarizer in the plane, the spin-torque term will contribute differently to the dynamics. The effect of the polarizer direction on synchronization at f and $2f$ will be analyzed in more detail in the coming chapter.

It is tedious to solve analytically Eq. II.17 in this form. However, an appropriate change of variable from the magnetization components to a dimensionless oscillator variable will allow us to analyze the magnetization dynamics with an auto-oscillator formalism under a much simpler form so that the underlying mechanisms can be clarified. Next we introduce the three steps of the change of variable and explain where the terms responsible for

synchronization at f and $2f$ in the c-equation arise from.

II.2 Derivation of the $c-$equation of motion

In the last section we have introduced the magnetization dynamics for the IPP with a study in the linear regime, close to the equilibrium. In this configuration we have shown that the FMR frequency and the ellipticity of the IPP can be derived from the free energy. However, the situation becomes more complex as the system is driven further away from equilibrium. Indeed, when the precession amplitude increases, the linear regime approximation is not sufficient. In that case, it is required to take into account the effect of the STT and the damping on the dynamics, and treat the STO not as a resonator but as a non-linear, self-sustained oscillator.

The KTS model was introduced in order to solve analytically the LLGS equation away from the small angle precession approximation (non-linear regime) using a general oscillator formalism. This formalism enables the use of well-defined concepts from non-linear sciences such as limit cycles, phase, amplitude and ultimately synchronization [67]. With an appropriate change of variable, the LLGS equation is transformed into a differential equation regrouping three contributions : precession, damping and anti-damping.

In this thesis we want to understand the dynamics in the non-linear regime for the IPP using KTS formalism, in the presence of both DC and RF currents. The first step is to examine carefully how the transformation from the LLGS equation to the oscillator equation is carried out. This section shows the complete analytic development, with emphasis on the special features due to (i) the addition of the RF current and (ii) geometrical properties of the IPP orbit.

The peculiarity of the IPP is that its orbit is not circular like the OPP orbit in the high symmetry case. As we will see in this section, this ellipticity has consequences in the change of variable. The change of variables requires the introduction of a few mathematical coefficients, and whenever possible we will link these coefficients with the geometrical properties of the IPP orbit and the magnetic configuration.

II.2.1 The 3 steps of the change of variables of the KTS model

Here we will give explanations as to how the change of variable is made for the IPP. As in [82], we will express the Hamiltonian of the system as a function of the new oscillator variable a, then b and c. The change of variables is based on "Classic Hamiltonian formalism for spin-waves in magnetic films"[82]. It is at the heart of the KTS model, in the sense that it gives strong theoretical ground to justify why we can study magnetization dynamics - and more generally spin-waves - using the KTS formalism. The transformations are based on non-linear spin-wave theory from the book of Y.S. L'Vov [54]. There the theory is developed in the general case, *i.e.* for spin-waves with any $\boldsymbol{k}$ vector [3].

The Hamiltonian we speak of here is a classical one (commutation relations do not intervene here) and it turns out that it corresponds the renormalized free energy of the system as we will see later. We will monitor the evolution of the Hamiltonian as the change of variable is carried out but the new equation of motion (i.e. the LLGS equation expressed with the variable $c(t)$ instead of the magnetization coordinates) will be presented only at the end of the change of variable at page 75.

3. Here we study the dynamics in the framework of macrospin approximation, which signifies that do not take into account the propagation of spin-waves, so that their wavevector is $|\boldsymbol{k}| = 0$.

In the introductory chapter we examined the equation of motion (Eq. I.8) in autonomous regime according to KTS formalism, and concluded that it portrays the dynamics of a self-sustained oscillator, thus giving a first validation of its use *as a phenomenological model* to describe the dynamics of the STO. However up to now we have no information on how calculate the parameters involved in the transformation, in particular the nonlinear parameters N, Q, and we have not assessed the domain of validity of the Taylor expansion of Eq. I.10.

Slavin and Tiberkevich presented extensively the 3 steps of the change of variable based on the Hamiltonian formalism in their paper from 2008 [82], which serves as a the basis for the analytical derivation presented in this manuscript. Here we have reexamined the change of variable and due to the peculiarities of the IPP orbit we find interesting behaviors that have not been reported yet.

Ultimately, the goal of this change of variable is to obtain an oscillator variable $c(t) = |c| \exp i\phi(t)$, whereby we can describe magnetization dynamics. This new oscillator variable enables one to separate amplitude and phase so that we can study these two quantities independently,

$$\begin{cases} |c|^2 & = p, \\ \frac{d\phi}{dt} & = \omega. \end{cases} \tag{II.18}$$

Note that we define here a general *stationary* regime which can be dynamic or static. The *dynamic stationary* regime means the precession orbit does not change with time, even though magnetization changes with time ($p = p_0 = cst \neq 0$ and $\omega = cst$), while the *static stationary* regime means that magnetization is stabilized at the energy minimum ($p_0 = 0$ and $\omega = \omega_0 = cst$) [4].

In the following we present the three steps of the change of variable for the IPP according to [82].

• **Step I** : $(m_x, m_y, m_z) \mapsto (a, a^*)$

General properties

Let

$$a = \frac{m_y - i m_z}{\sqrt{2(1 + m_x)}}. \tag{II.19}$$

The inverse transformation yields

$$\begin{aligned} m_x &= 1 - |a|^2, \\ m_y &= (a + a^*)\sqrt{1 - |a|^2}, \\ m_z &= i(a - a^*)\sqrt{1 - |a|^2}. \end{aligned} \tag{II.20a}$$

This first transformation leads us to a complex dimensionless variable. Most importantly this change of variable reduces the number of variables from three to two ; instead of having three magnetization coordinates we have now the real and imaginary part of a complex variable. We note that this transformation is performed *regardless* of the magne-

4. For the IPP $p_0 = 0$ corresponds to a magnetization at the energy minimum, however for the OPP p_0 corresponds to an energy minimum.

tic parameters, so that in this step only the equilibrium magnetization direction matters.

Following [82], the LLGS equation can be rewritten as a perturbed Hamiltonian equation. Here we note that the Hamiltonian used in this derivation corresponds to a classical measure of the energy of the system as it derives directly from the magnetic energy E, and the Hamiltonian $\mathcal{H}$ reads :

$$\mathcal{H} = \gamma E / 2M_s \tag{II.21}$$

We note that the Hamiltonian we define here is a normalized quantity, that is $\mathcal{H}$ is expressed in units of angular frequency (rad/s).

$$\frac{\partial a}{\partial t} = -i\frac{\delta \mathcal{H}}{\delta a^*} + F_a, \tag{II.22}$$

where

$$F_a = -i\frac{\partial a}{\partial \boldsymbol{M}}.\boldsymbol{T}_e. \tag{II.23}$$

In Eq. II.22, $\frac{\delta \mathcal{H}}{\delta a^*}$ designates the functional derivative of the Hamiltonian with respect to a^*. F_a stands for the perturbative force, that directly comes from the torque $\boldsymbol{T}_e$. This perturbative approach is valid because the torque $\boldsymbol{T}_e$ is the sum of the two non-conservatives torques (STT and damping) which are much smaller than the precession torque. From now on, only canonical transformations of the complex variables are performed, in other terms the perturbed Hamiltonian form in II.22 remains valid when one transforms $a \mapsto b \mapsto c$, and only the expression for the perturbative force F_a is modified.

Hamiltonian

Let us now calculate the Hamiltonian $\mathcal{H}$ as a function of the complex variable a. To do so, it is required that we rewrite the LLGS equation as a function of the new dimensionless variable, and the Hamiltonian will be deduced from the precession term. Using relations II.20a and II.1 to substitute m_x, m_y and m_z in the LLGS equation, a few lines of calculations yield

$$\begin{aligned}\left.\frac{\partial a}{\partial t}\right|_{\text{precession}} &= -i\left[(\omega_H + \omega_A + \frac{\omega_M}{2})a - \frac{\omega_M}{2}a^*\right] \\ &\quad - i\left[-(2\omega_A + \omega_M)a^*a^2 + \frac{3}{4}\omega_M a a^{*2} + \frac{1}{4}\omega_M a^3\right].\end{aligned} \tag{II.24}$$

In the equation above, we define the frequencies ω as follows

$$\begin{aligned}\omega_H &= \gamma H_b, \\ \omega_A &= \gamma H_a, \\ \omega_M &= 4\pi\gamma M_s.\end{aligned}$$

Using the form II.22, we can identify the RHS of the above equation with the derivative of the Hamiltonian $\mathcal{H}$ with respect to the complex conjugate $a*$. The Hamiltonian $\mathcal{H}$ then reads

$$\begin{aligned}\mathcal{H}(a) =&(\omega_H + \omega_A + \frac{\omega_M}{2})|a|^2 - \frac{\omega_M}{4}(a^2 + a^{*2}) \\ &+ \frac{\omega_M}{4}|a|^2(a^{*2} + a^2) - (\omega_A + \frac{\omega_M}{2})|a|^4. \end{aligned} \tag{II.25}$$

Similarly to [82], we regroup the terms of Eq. II.25 in this form :

$$\begin{aligned}\mathcal{H}(a) =&\mathrm{A}|a|^2 + \frac{1}{2}\mathrm{B}(a^2 + a^{*2}) \\ &+ \mathrm{V}_1|a|^4 + \mathrm{V}_2|a|^2(a^2 + a^{*2}), \end{aligned} \tag{II.26}$$

where coefficients A,B,V_1,V_2 are in units of rad/s

$$\begin{aligned}\mathrm{A} &= \omega_H + \omega_A + \frac{\omega_M}{2}, \\ \mathrm{B} &= -\frac{\omega_M}{2}, \\ \mathrm{V}_1 &= \omega_A + \frac{\omega_M}{2}, \\ \mathrm{V}_2 &= -\frac{\omega_M}{4}. \end{aligned} \tag{II.27}$$

Expression II.26 is a special case of Eq. (3.16) from [82] when the equilibrium direction of the magnetization is set along the $\hat{\mathbf{e}}_x$ axis.

Let us look quickly at Expression II.26. The Hamiltonian here is the total free energy normalized by the saturation magnetization, expressed as a function of the a variable instead of the magnetization coordinates. When the magnetization coordinates go along the IPP orbits, we know that the free energy is constant. So, along IPP orbits, the Hamiltonian is constant with time, which is what we should find in expression II.26.

It is required to examine the form of the Hamiltonian in a variable to know if the change of variable is adequate or if we need another variable. For a given IPP orbit, if we suppose that a is the adequate oscillator variable already, then it means that $|a|^2$ should be constant with time. At the same time, the Hamiltonian $\mathcal{H}$ also has to be constant with time, so it should not depend on the phase of the variable a which is time-dependent, but only on the norm $|a|^2$ corresponding to the amplitude of oscillations.

In Eq. II.26, terms with prefactors A and V_1 depend on the amplitude $|a|^2$ only. However we also have the terms with prefactors B and V_2 which have an explicit dependence on the oscillator phase via $a^{*2} + a^2$. As a consequence, the Hamiltonian depends on the phase of a through these two terms, which indicates that the variable a is not the appropriate oscillator variable yet. This is why a second transformation is required ; as we will see next, the objective of the transformation $(a, a*) \mapsto (b, b*)$ is to diagonalize the quadratic part of the Hamiltonian II.26, so as to eliminate terms with dependence on $a^{*2} + a^2$ [5].

• **Step II** : $(a, a^*) \mapsto (b, b^*)$.
General properties

5. Only the lowest order term (with coefficient B) in $a^{*2} + a^2$ can be eliminated with this transformation. The higher order term in V_2, which has a dependence of the type $|a|^2(a^{*2} + a^2)$ cannot be eliminated with this method and will be neglected later on.

Following [82] we perform the next step of the change of variables

$$b = u.a + v.a^*. \tag{II.28}$$

Let us look at the geometrical properties of this transformation for any couple of real parameters $(u, v) \in \Re^2$. Eq. II.28 can also be written as

$$\begin{cases} Re(b) &= (u+v)Re(a) \\ Im(b) &= (u-v)Im(a) \end{cases}. \tag{II.29}$$

Provided parameters u and v are real, this transformation is a stretching of the $\hat{\mathbf{e}}_x$ and $\hat{\mathbf{e}}_y$ axis in the complex plane. The real part grows by a factor $u+v$, while the imaginary part is reduced by a factor $u-v$. Since we ultimately want to obtain a circular cycle for the variable c in the phase plane ($|c|$ is constant during the motion), we see that this transformation is appropriate when one wants to transform an elliptic trajectory with ellipticity given by $e_t = (u-v)/(u+v)$ in the plane into a circular one.

Hamiltonian

Let us first explicit the transformation parameters u and v from [82]

$$\begin{aligned} u &= \sqrt{\frac{A+\omega_r}{2\omega_r}}, \\ v &= -\sqrt{\frac{A-\omega_r}{2\omega_r}}, \end{aligned} \tag{II.30}$$

where ω_r is the FMR frequency, equal to $\sqrt{(A+B)(A-B)}$. First let us have a look at the Hamiltonian written in terms of b and $b*$. The Hamiltonian Eq. II.26 reads now after transformation

$$\mathcal{H}(b) = \omega_r|b|^2 + \mathcal{W}_1|b|^2(b+b*) + \mathcal{W}_2(b^3+b*^3) + \mathcal{T}|b|^4. \tag{II.31}$$

The expression of the higher order coefficients $\mathcal{W}_1, \mathcal{W}_2$ and $\mathcal{T}$ is given by Eq. 3.25 in [82]. It is not necessary to explicit these coefficients here, but we can discuss the general form of the above expression. Similarly to Eq. II.26, the Hamiltonian is made up of two "stationary" terms : (i) a second order term in $|b|^2$ with prefactor ω_r and (ii) a forth order term in $|b|^4$. These terms do not depend on the phase of b, so their contribution to the Hamiltonian must be kept. On the other hand, the second term with coefficient B from Eq. II.26 in $a^{*2}+a^2$ having explicit dependance on the phase has been eliminated from the Hamiltonian, and only third order terms with explicit dependance on the phase remain in Eq. II.31 (terms with coefficients $\mathcal{W}_1$ and $\mathcal{W}_2$).

To conclude with the Hamiltonian expressed in $(b, b*)$, the second step has allowed one to "push" the explicit phase dependance from the second order in $(a, a*)$ to the third order in $(b, b*)$. By doing so, we will be able to neglect later on this explicit phase dependence and only keep the stationary contributions in $|b|^2$ and $|b|^4$.

Ellipticity

As a remark, we note that the parameters B and v are *negative* in this definition. We decided to keep them negative in order to stay consistent with the already existing

notation. However, it creates some unnecessary complexion because not all parameters are defined positive, and renders physical interpretation more tedious. This being said, we introduce the *ellipticity* of the mathematical transformation $(a, a^*) \mapsto (b, b^*)$ $e_t = (u+v)/(u-v)$ as a function of A and B

$$\begin{aligned} e_t = \frac{u+v}{u-v} =& \frac{u^2-v^2}{u^2+v^2-2uv}, \\ =& \frac{1}{A/\omega_r - B/\omega_r}, \\ =& \sqrt{\frac{A+B}{A-B}}. \end{aligned} \tag{II.32}$$

Now factors A and B from the Hamiltonian in a (Eq. II.26) can be linked to the last section where we extracted the FMR frequency and the ellipticity. From Eq. II.27 we have

$$\begin{aligned} A - B =& \omega_H + \omega_A = \gamma \left.\frac{\partial^2 E}{\partial \phi^2}\right|_{\phi_0=0,\theta_0=0}, \\ A + B =& \omega_H + \omega_A + \omega_M = \gamma \left.\frac{\partial^2 E}{\partial \theta^2}\right|_{\phi_0=0,\theta_0=0}, \end{aligned} \tag{II.33}$$

so that, in the end :

$$e_t = \frac{u+v}{u-v} = \sqrt{\frac{H_a + H_b}{H_a + H_b + 4\pi M_s}} = e_0. \tag{II.34}$$

We see that the ellipticity e_t of the transformation $(a, a^*) \mapsto (b, b^*)$ is equal to the ellipticity e_0 introduced in Sec.II.1.3. corresponding to that of the IPP trajectory (m_y^{max}/m_z^{max}). It shows that we can trace back the properties of the mathematical transformation we develop here to the geometrical properties of the IPP trajectory, which are determined from the magnetic energy landscape (see Eq. II.13 in Sec.II.1.3). Fig. II.5 shows the evolution of the ellipticity with the in-plane applied field (i) using the analytic formula II.34 and (ii) from the ratio m_y^{max}/m_z^{max} extracted from macrospin simulations close to the critical current.

We observe here that the most important finding is that the ellipticity of the IPP trajectory in FMR e_0 calculated in the last section is *exactly the same* as the ellipticity e_t introduced during the second transformation with the parameters u and v. This observation will greatly help us to justify the necessary approximations later on during the derivation of the c-equation.

- **Step III** : $(b, b^*) \mapsto (c, c^*)$

$$c = \sqrt{\frac{A}{\omega_r}} b \tag{II.35}$$

The last transformation is a homothetic transformation. ω_r is the FMR frequency, and A is the coefficient introduced in Eq. II.27. It follows Eq. (3.26) in [82], where we only kept the zero order term. It normalizes the variable so that, in the whole range of precession amplitude, $0 < p < 1$.

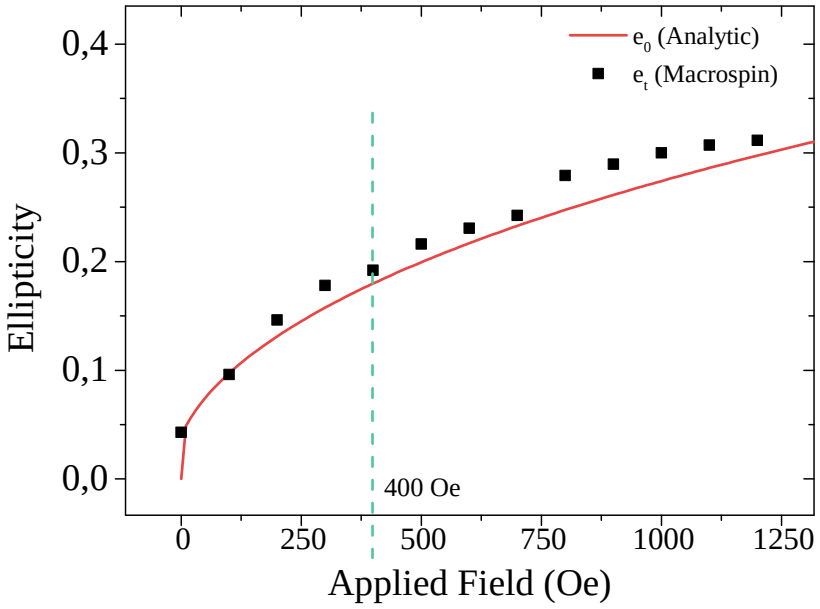

Figure II.5 – Ellipticity of the IPP trajectory as a function of the in-plane applied field. The red line corresponds to the analytic formula, while black dots correspond to the manual extraction of m_y^{max}/m_z^{max} from macrospin trajectories (parameters in Tab. III.1).

The third step of the transformation is a simple renormalization of the variable, so we will not discuss the form of the Hamiltonian after the third transformation. It is beyond the scope of this thesis to discuss the change of variable in the general case (i.e. for any type of magnetization orbit) as it has already been detailed in [82, 83]. We only underline the specifics of the transformation when the magnetization orbit is elliptic, as in the IPP.

To summarize, we can see that one way to understand the steps involved in this transformation is to analyze it as a series of geometrical transformations. Here we have not examined in detail how the parameters involved in the transformation are found. However, it helps us understanding how geometrical properties of the trajectory impact the different steps of the transformation. Since we are interested in the IPP trajectory that is elliptic, we may certainly expect that the second step of the transformation is of crucial importance in IPP - it may not be for an circular trajectory such as for the OPP orbit.

Fig. II.6 shows the IPP trajectory in 3D computed from macrospin simulations (a), and its projection on the three planes (b). In Fig. II.6(c) is then shown the same trajectory computed from macrospin simulations, but after application of the change of variables introduced in this section. In comparison with Fig. (a) and (b) where the trajectory is plotted in cartesian basis $(\hat{\mathbf{e}}_x, \hat{\mathbf{e}}_y, \hat{\mathbf{e}}_z)$ in Fig. (c) it is in the complex plane that the trajectory is plotted. Looking at Fig. II.6(c), one may argue that change of variable is not completely accurate even after the last change of variable, because the limit cycle is not perfectly circular but rather a little distorted, so it would mean that c is not the appropriate oscillator variable. There are two explanations : (i) The coefficients involved in the change of variable are determined from the Hamiltonian, which is directly the magnetic

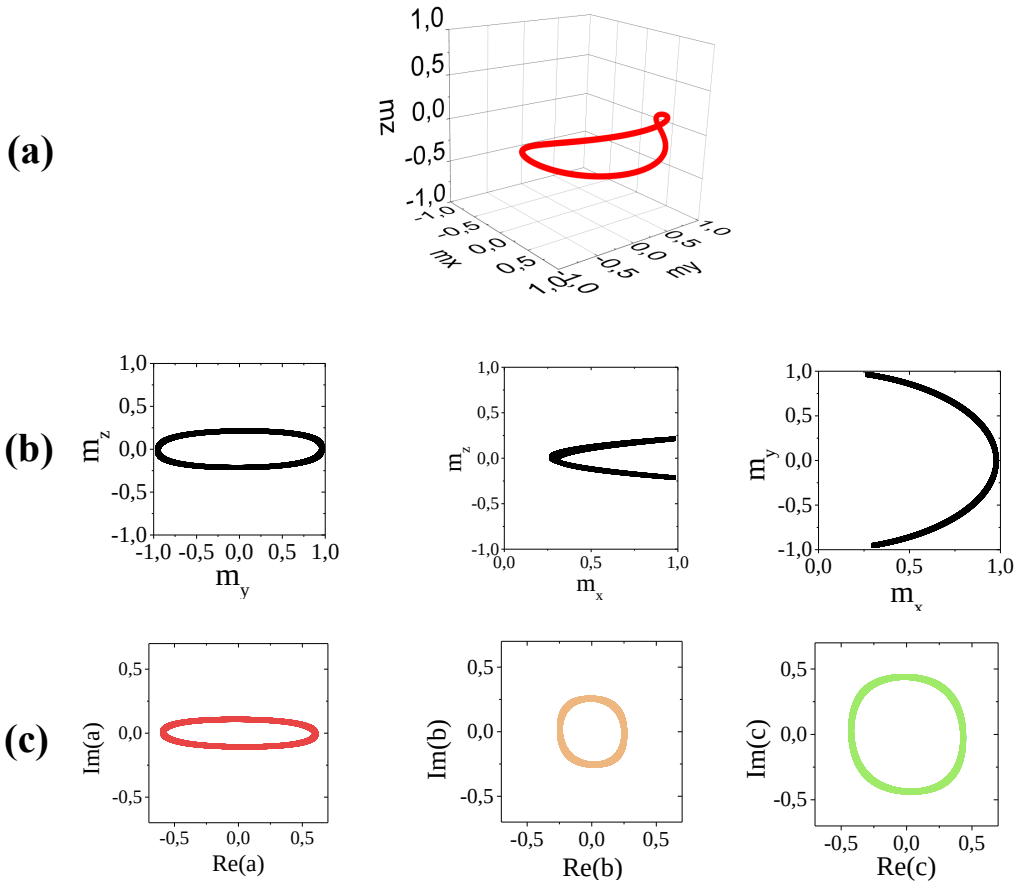

Figure II.6 – Illustration of the transformation steps for an IPP trajectory with $H_b = 400$ Oe, $J_{DC} = 5.2x10^{11}$ A/m^2 (results from macrospin simulations). (a) 3D representation of the trajectory. (b) 2D projections of the trajectory (a). From left to right, planes $(\hat{\mathbf{e}}_y, \hat{\mathbf{e}}_z)$,$(\hat{\mathbf{e}}_x, \hat{\mathbf{e}}_z)$ and $(\hat{\mathbf{e}}_x, \hat{\mathbf{e}}_y)$. (c) Representation in the complex plane of the dimensionless oscillator variables (from left to right a,b,c) after each transformation. From trajectory (a).

free energy, and none of these coefficients depend on other factors such as the DC current. These other factors also have an influence on the precession orbit : for example, not only the DC current changes the precession amplitude, but depending on the polarizer direction, the orbit "shape" (e.g. the symmetry axis) may be modified as well. These modifications of the orbit are not taken into account in the change of variable, and as a consequence the variable in the end is not a "perfect" oscillator variable. (ii) Compared to the initial derivation from [82], the last step $b \mapsto c$ is a homothetic transformation only. In the paper (see Eq. (3.26)), a more complex transformation is performed to eliminate (as said) "Non-resonant Three-Wave processes".

II.2.2 Averaging the equation of motion : Coupling factors

Up to now, we have analyzed the Hamiltonian expressed as a function of the new oscillator variable. Since the Hamiltonian is conservative and does not include dissipative contributions, the effect of the spin-torque on the dynamics has not been investigated. Yet we want to use the KTS model to understand how the RF current couples with the STO, so we need to rewrite instead of the Hamiltonian the complete LLGS equation as a function of c. In particular, this analysis will allow us to understand why synchronization at f and $2f$ obey two distinct mechanisms.

While applying the change of variable to the LLGS equation we will discuss which terms we can safely omit and those we must keep. To this aim, calculations have been performed to convert the full LLGS equation into the reduced c-form. The subsequent changes of variables have been explicited and given physical justification in Sec. I.2.1, so for the sake of brevity we will not detail the transformation of the LLGS equation at each step, but we will only show the equation of motion in the c-variable. Approximations to obtain the simplified KTS equation (as in Sec. I.2.3) are made and justified after all transformations are performed.

The change of variable is applied to the LLGS equation in the IPP configuration given by expression II.17. Then we apply the transformations from a to b to c as explicited in the beginning of this section, and keep all the terms up to the 3rd order in c, c^*, or any combination of both (all terms higher than the third order are regrouped with the notation "capital o" $O(|c|^4)$). We write separately the contribution to the precession, the damping and finally the spin-torque :

$$\left(\frac{dc}{dt}\right)_{Prec} = -i \left[\begin{array}{r} \omega_r c \\ + \left[\frac{1}{4}\omega_M(u^4+v^4) + (2\omega_A+\omega_M)uv(u^2+v^2) + \frac{6}{4}\omega_M u^2v^2\right]\frac{\omega_r}{A}c^3 \\ - \left[3\omega_M uv(u^2+v^2) + (2\omega_A+\omega_M)(u^4+v^4+4u^2v^2)\right]\frac{\omega_r}{A}c^2c^* \\ +3\left[\frac{1}{4}\omega_M(u^4+v^4) + (2\omega_A+\omega_M)uv(u^2+v^2) + \frac{3}{2}\omega_M u^2v^2\right]\frac{\omega_r}{A}cc^{*2} \\ - \left[uv(u^2v^2)\omega_M + 2u^2v^2(2\omega_A+\omega_M)\right]\frac{\omega_r}{A}c^{*3} + O(|c|^4) \end{array} \right] \tag{II.36}$$

$$\left(\frac{dc}{dt}\right)_{Damp} = \alpha \begin{bmatrix} -(\omega_H + \omega_A + \frac{\omega_M}{2})c + \omega_M c^* \\ -\left[\frac{3}{4}uv\omega_A + uv\omega_H + \frac{3}{4}(u+v)^2\omega_M\right]\frac{\omega_0}{A}cc^{*2} \\ +\left[3uv\omega_M + (u^2+v^2)(\omega_H + 3\omega_A + \frac{3}{2}\omega_M)\right]\frac{\omega_r}{A}c^2c^* \\ -\left[uv(\omega_H + 3\omega_A + \frac{3}{2}\omega_M) + \frac{3}{2}(u^2+v^2)\omega_M\right]\frac{\omega_r}{A}c^3 + O(|c|^4) \end{bmatrix} \tag{II.37}$$

$$\left(\frac{dc}{dt}\right)_{STT} = \begin{array}{l} -P_x\sigma J\left[c - (u^2+v^2)\frac{\omega_r}{A}c^2c* + uv\frac{\omega_r}{A}c^3 + uv\frac{\omega_r}{A}cc^{*2}\right] \\ +P_y\sigma J\frac{(u+v)}{4}\left[2\sqrt{\frac{A}{\omega_r}} - 3(u-v)^2\sqrt{\frac{\omega_r}{A}}(cc^* + c^2)\right] \\ +O(|c|^4) \end{array} \tag{II.38}$$

We have not talked yet about synchronization, either at f or $2f$. During the 3 steps of the transformation of the LLGS equation to the reduced c-equation, we have not made assumptions as to the form of the current density J (whether it is a constant or oscillating quantity), since we will consider resonant interactions only when writing power and phase equations at the end. The idea is to find where in the transformation oscillating terms arise, and which of these terms must be taken into account and which can be neglected. We note that even in our configuration when the symmetry is important, the three steps of transformation will never give a perfectly circular trajectory in the complex plane, and we have to disregard higher order contributions to find the simplified, analytical form of the KTS model as in ref. [83].

It is difficult looking at the raw equations to understand what is going on, so it requires some clarification. We will simplify these equations in two ways, as described in the following.

I/ Oscillating contributions.

We want a model that can represent the behavior of a self-sustained oscillator in the autonomous regime, but it must take into account the coupling with the RF current. We will be making the distinction between two types of terms based on their dependance on c and c^* :

1. Slow-oscillating contributions.
2. Fast-oscillating contributions.
   Non-resonant
   Resonant

We must keep in mind that the main advantage of using an oscillator formalism instead of the LLGS equation is that we can present dynamics using a variable whose phase and amplitude can be analyzed separately [6]. To do so, we use the following mathematical

6. In STOs phase and amplitude cannot be fully decoupled. However, in steady-state the coupling is one-way only, i.e. the amplitude has influence on the phase via the non-linearity but the phase does not influence the amplitude. Thus the most direct way to solve the system is to solve the amplitude equation first, and then the phase equation.

relation II.39, that holds for any number $c = \sqrt{p}e^{i\phi} \in \mathbb{C}$:

$$c^* \left(\frac{dc}{dt} \right) = \frac{1}{2} \frac{dp}{dt} + ip \frac{d\phi}{dt}. \tag{II.39}$$

This relation allows one to separate contributions in the c-equation from (i) the amplitude (strictly speaking the power $p = |c|^2$) by keeping the *real part* and (ii) the phase by keeping the *imaginary part*. However the c-equation must be multiplied by c^* beforehand. So it means that if the dynamics of the STO obey a differential equation of the type $dc/dt = f(c,t)$ as in the KTS model, then we obtain for the time derivatives of the amplitude and phase :

$$\begin{cases} \frac{dp}{dt} & = 2Re\left(f(c,t).c^*\right) \\ \frac{d\phi}{dt} & = \frac{1}{p} Im\left(f(c,t).c^*\right) \end{cases} \tag{II.40}$$

Phase and amplitude dynamics do not obey the same time-scales, which is visible in practice by comparing the amplitude relaxation rate Γ_p and the STO generation frequency ω_0 [7]. Γ_p is at least one order of magnitude smaller than ω_0, and it means that the STO must wait for 10 periods minimum for a perturbation in amplitude to be damped out. So we will restrict ourselves to the case where only *slow variations of the amplitude are allowed* : we will neglect all the terms containing the fast oscillations (i.e. at $\omega_0 t$ or $2\omega_0 t$) in the final amplitude equation. This is equivalent to averaging over the period of oscillations $T = 2\pi/\omega_0$.

For the moment, the amplitude equation is not written and we have the complex form only, so we need to anticipate which terms will be fast-oscillating and those which will be slow-oscillating in the amplitude equation.

The simplest case is when there are no external RF contributions to the dynamics, whether its a RF field or a RF current. In this case no *resonant interaction* between the STO and an external source is possible (see Eq. II.43). In our case, we only have a RF current but no RF field. As a consequence, resonant interactions can take effect only in the STT term in which the current enters directly, but *not* in the precession or in the damping term. In the case of synchronization to a RF field, we expect that on the contrary resonant interactions arise in the precessing or damping term in which the external magnetic field contributes.

So we start with the precession and damping contributions, where simplification is straightforward. To find out which terms can be safely neglected, one has to examine their dependence in (c, c^*). If we look at the precession contribution of Eq. II.36, there are five terms, each having a specific dependence on c, c^*. Now we recall from Eq. II.40 that phase and amplitude equations are obtained by multiplying the c-equation by the complex conjugate c^*, so these five terms will be multiplied by c^*. The first and the third term will give respectively a dependence in $|c|^2$ and $|c|^4$ which *are not* direct functions of the phase ϕ. However, the second, forth and fifth terms will respectively give a dependence in c^3c^*, cc^{*3} and c^{*4} after multiplication, which *are* direct functions of the phase ϕ.

The former terms will be kept because they are slow-oscillating (or constant), while the latter will be neglected because they are fast-oscillating and will be averaged out. So simplification of the precession and damping contribution is carried out as follows : *The*

7. ω_0 is the generation frequency in autonomous regime, and ω_r is the FMR frequency. Notations are different compared to [82] where instead ω_0 is the FMR frequency and ω_g is the generation frequency.

only terms that will be kept are those whose dependence is in the form $c^n c^{*(n-1)}$.

Then the contribution from the precession II.36 reads

$$\left(\frac{dc}{dt}\right)_{Prec} = -i\left[\begin{array}{l}\omega_r \\ -\left[3\omega_M uv(u^2+v^2)+(2\omega_A+\omega_M)(u^4+v^4+4u^2v^2)\right]\frac{\omega_r}{A}p\end{array}\right]c+O(|c|^4) \tag{II.41}$$

We apply the same reasoning to the damping term and Eq.II.37 yields

$$\left(\frac{dc}{dt}\right)_{Damp} = \alpha\left[\begin{array}{l}-(\omega_H+\omega_A+\frac{\omega_M}{2}) \\ +\left[3uv\omega_M+(u^2+v^2)(\omega_H+3\omega_A+\frac{3}{2}\omega_M)\right]\frac{\omega_r}{A}p\end{array}\right]c+O(|c|^4) \tag{II.42}$$

Simplification of the spin-torque term is not so straightforward, because we also need to take into account the *coupling with the RF current*. As a consequence, our study on synchronization requires that we retain fast oscillating terms that would have been neglected in the free-running regime, as it has been done for the precession and the damping.

Mathematically, the coupling translates into the mixing of two fast-oscillating sine waves to obtain a slow-oscillating wave in the phase and power equations. One of these fast-oscillating sine waves comes from the RF current $J_{AC} = A\cos\omega_e t$ and the other from a combination of c and c^*. The LLGS being a strongly non-linear equation, this mixing between the RF current and the magnetization (the c-variable) takes effect in a variety of ways. As a consequence, peculiarities in the mixing between the oscillator variable c and the RF current in the c-equation will arise, and it results in specific couplings. In particular, it is the coupling difference between f and $2f$ that leads to two distinct synchronization mechanisms.

In a general context, the *resonant condition* between an oscillator of frequency ω_0 and an external source with frequency ω_e is fulfilled when :

$$n\omega_e - k\omega_0 \approx 0 \tag{II.43}$$

Synchronization at f happens for $n = 1$ and $k = 1$, while synchronization at $2f$ happens for $n = 1$ and $k = 2$. So, in order to clarify the spin-torque contribution, we will retain (i) the slow-oscillating terms *in the absence of RF current*, as it was done for the precession and damping contributions and (ii) fast oscillating terms in (c, c^*) that lead to resonant conditions at f or at $2f$ with the RF current [8].

We start by factorizing the STT term of Eq.II.38 by c

$$\left(\frac{dc}{dt}\right)_{STT} = \begin{array}{l}-P_x\sigma J\left[1-\frac{\omega_r}{A}\left((u^2+v^2)cc^*-2uv(c^2+c^{*2})\right)\right]c \\ +P_y\sigma J\frac{(u+v)}{4}\left[2\sqrt{\frac{A}{\omega_r}}-3(u-v)^2\sqrt{\frac{\omega_r}{A}}(c^*+c)c\right] \\ +O(|c|^4).\end{array} \tag{II.44}$$

8. Here we limit the analysis to resonant interactions at f and $2f$. Higher synchronization regimes and fractional synchronization are not examined

We see in the previous equation that some terms can be regrouped : we have the sum $c^2 + c^{*2}$ in the P_x part and the sum $c + c^*$ in the P_y part. Using the notation $c = \sqrt{p}e^{i\phi}$, these terms can be written respectively $p\cos(2\phi)/2$ and $\sqrt{p}\cos(\phi)/2$:

$$\begin{aligned}\left(\frac{dc}{dt}\right)_{STT} = & -P_x\sigma J\left[1-\frac{\omega_r}{A}p\left((u^2+v^2)-2uv\cos(2\phi)\right)\right]c \\ & + \frac{P_y(u+v)\sigma J}{2\sqrt{1-\frac{\omega_r}{A}p(u^2+v^2-2uv\cos(2\phi))}}\sqrt{\frac{A}{\omega_r}}\left[1-3(u-v)^2c\sqrt{p}\cos(\phi)\right] \\ & + O(|c|^4)\end{aligned} \tag{II.45}$$

First we remark in II.45 that we have split the STT contribution into two parts to account for the polarization direction, the P_x part and the P_y, respectively due to spin-polarization along the longitudinal direction ($\hat{\mathbf{e}}_x$) and along the transverse direction ($\hat{\mathbf{e}}_y$).

In this equation we see clearly that resonance conditions at $2f$ can be satisfied through multiplication of the term in $\cos(2\phi)$ by the RF component of the current when $\omega_e \approx 2\omega_0$. We also remark that this oscillating term at $2f$ is included in the P_x part. We also note that fast oscillating terms at $2f$ are multiplied by p, which signifies that when oscillation amplitude is small($p \approx 0$), the RF current cannot couple efficiently with the system at $2f$. In particular, a non-zero precession amplitude is a *necessary condition* for synchronization at $2f$.

As for synchronization at f, let us examine the second term in the R.H.S. of II.45, which regroups the P_y part. There is a constant term and a fast oscillating term with the form $\sqrt{p}\cos(\phi)c$. In the absence of a RF current (autonomous regime), these two terms are neglected in the dynamics [80], but they are responsible for coupling at f. Ultimately, they will translate differently in the phase and amplitude equations as we will explain in the next section. Now let us write these equations in a more comprehensive manner.

II/ Compact form.

We are interested in knowing how the geometry of the orbit impacts general dynamic properties, and synchronization in particular. Whenever possible, we will express the transformation coefficients, such as A, u and v as a function of the ellipticity of the orbit e_0 to rewrite the previous expressions.

We start with the contribution to precession. Following the notations from [83], Eq. II.41 reads :

$$\left(\frac{dc}{dt}\right)_{Prec} = -i\omega(p)c = -i\left[\omega_r + Np\right]c, \tag{II.46}$$

where N, the non-linear frequency shift is defined by

$$N = -\frac{A}{\omega_r}\left[\frac{3}{2}\omega_M g_1(e_0) + (2\omega_A + \omega_M)(1 - \frac{1}{2}\left(g_1(e_0)\right)^2)\right]. \tag{II.47}$$

The damping contribution from Eq. II.42 reads

$$\left(\frac{dc}{dt}\right)_{Damp} = -\Gamma_+(p)c = -\Gamma_0\left[1 + Qp\right]c, \tag{II.48}$$

where factors Γ_0, the damping rate and Q, the damping non-linearity, are given by

$$\begin{aligned}\Gamma_0 &= \alpha A,\\ Q &= -\left[-\frac{3}{2}\omega_M g_1(e_0) + \omega_H + 3\omega_A + \frac{3}{2}\omega_M\right]\frac{1}{A}.\end{aligned} \tag{II.49}$$

Finally the spin-torque contribution from Eq. II.44 yields

$$\left(\frac{dc}{dt}\right)_{STT} = \begin{array}{l} -P_x\sigma J\left[1 - p\left(1 + g_1(e_0)\cos(2\phi)\right)\right]c \\ +P_y\dfrac{\sigma J g_2(e_0)}{2}\left[1 - 6c\sqrt{p}\cos(\phi)\right]. \end{array} \tag{II.50}$$

Here, g_1 and g_2 are parameters deriving directly from the ellipticity e_0 of the IPP trajectory :

$$\begin{aligned} g_1(e_0) &= \frac{1-e_0^2}{1+e_0^2},\\ g_2(e_0) &= \sqrt{\frac{1+e_0^2}{2}}, \end{aligned} \tag{II.51}$$

with the limiting cases

$$\begin{aligned} &\text{High ellipticity} : \lim_{e_0\to 0} g_1(e_0) = 1 \quad \text{and} \quad \lim_{e_0\to 0} g_2(e_0) = 1/\sqrt{2};\\ &\text{Low ellipticity (circle)} : \lim_{e_0\to 1} g_1(e_0) = 0 \quad \text{and} \quad \lim_{e_0\to 1} g_2(e_0) = 1. \end{aligned}$$

The two parameters g_1 and g_2 measure the role of the ellipticity on the dynamics. In the first line of Eq. II.50, we see that the influence of the ellipticity is critical when it comes to synchronization at $2f$. For a *small* ellipticity e_0, g_1 goes to zero, so that the oscillating contribution $g_1(e_0)\cos(2\phi)$ is negligible and the coupling will be too weak to allow locking to the RF current at $2f$. In contrast, a *large* ellipticity gives $g_1(e_0) \approx 1$, which makes the oscillating contribution $g_1(e_0)\cos(2\phi)$ important and ultimately enables locking to the RF current at $2f$ [9].

We have here general expressions for the three terms to the dynamics, precession, damping and spin-torque. Compared to [82], we have managed to write these expressions *without* calling coefficients u or v defined during the c-transformation, whose physical meaning is difficult to clarify. When the contributions are written as such, one can directly evaluate the effect of the ellipticity on the dynamics, which is one of the main points of interest here.

Under IPP conditions, the demagnetizing field dominates over the applied field and anisotropy field, so the ellipticity is important or in other terms e_0 is close to 0. With the macrospin simulations parameters used in the next chapter (see Table III.1), the ellipticity gives $e_0 = 0.18$, yielding $g_1(e_0) = 0.92 \approx 1$ and $g_2(e_0) = 0.72 \approx 1/\sqrt{2}$. Under the assumption of important ellipticity, we can simplify Eq. II.50 and we regroup the contribution from the precession, damping and STT term, so that we finally write :

9. The ellipticity also acts on synchronization properties at f (see second line of Eq. II.50) via g_2, but on a less significant manner $1/\sqrt{2} \leq g_2 \leq 1$.

$$\frac{dc}{dt} = \left(\frac{dc}{dt}\right)_{Prec} + \left(\frac{dc}{dt}\right)_{Damp} + \left(\frac{dc}{dt}\right)_{STT},$$
$$\frac{dc}{dt} = -i\left[\omega_r + Np\right]c - \Gamma_0\left[1 + Qp\right]c$$
$$+ P_x\sigma J\left[1 - p\left(1 + cos(2\phi)\right)\right]c + P_y\frac{\sigma J}{2\sqrt{2}}\left[1 - 6c\sqrt{p}\cos(\phi)\right]. \quad \text{(II.52)}$$

We obtain an equation similar to that of the KTS model as in [83], in which we have the basic blocks of precession, damping and anti-damping. The anti-damping (STT term with prefactor P_x) is similar to [83] with the exception of the oscillating dependence $\cos(2\phi)$ within the anti-damping. As to the STT term with prefactor P_y, while it comes from the STT it does not play the role of an anti-damping and does not compensate the damping as the P_x term does. Moreover, if the RF current is turned off, this P_y term does not contribute to the dynamics and is neglected [80].

II.3 Comparative analysis of the synchronized regime at f and $2f$

This section is dedicated to the study of the synchronized regime of the STO when the frequency of the RF current is close to f or $2f$, with emphasis on the new features of synchronization at $2f$. We note the model developed here for synchronization does not take into account the influence of noise (see models with noise for STOs at f [22, 12]), and it focuses here on the *stationary* regime, i.e. the transition from the autonomous to the synchronized regime (see [104]), or the response to a perturbation in synchronized regime will not be discussed at this stage.

The most significant analytical results of my thesis are developed in this section and the following chapter is dedicated to test and validate the model with macrospin simulations. We will discuss the following aspects :

- Frequency and amplitude deviations in the synchronized regime
- Influence of the oscillation amplitude on coupling sensitivity
- Evolution of the phase-difference within the locking-range
- Synchronization mechanisms at $2f$
- Comparison with existing theory ([83])

The first three aspects will be analyzed at both f and $2f$ and we will evidence similarities and difference between the two configurations.

II.3.1 Power and phase in the synchronized regime at $2f$

Synchronization at $2f$ in STOs due to a microwave current has not been fully treated analytically in oscillator formalism yet, but there are some notable contributions. The recent thesis work of Zarudniev [100] has brought some insight on synchronization at $2f$ in IPP in STOs. Without going into details, Zarudniev also made an analytic development to explain synchronization at $2f$ using oscillator formalism, where he also used a complex variable to account for the magnetization. He obtains an equation for the oscillator dynamics very similar to that of Slavin *et al.*, but with a much simplified transformation. From

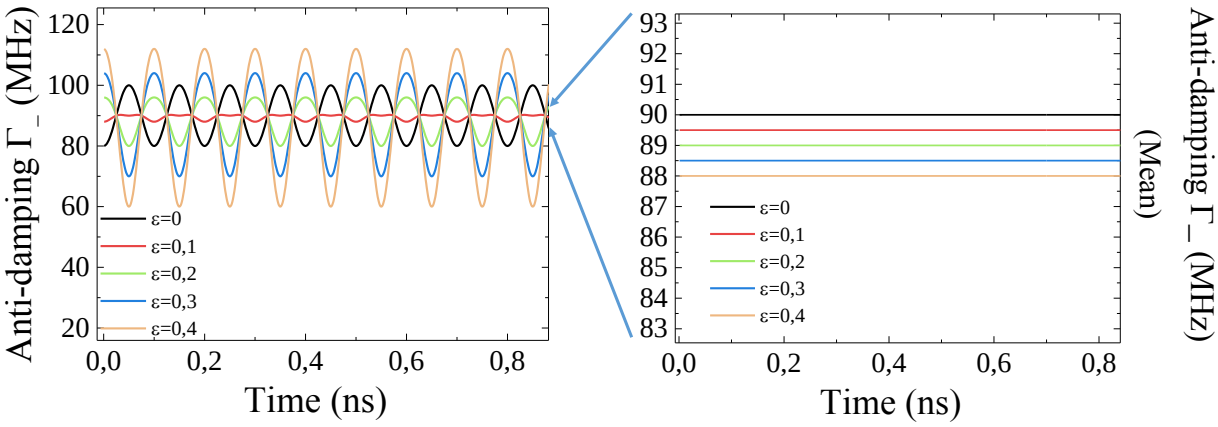

Figure II.7 – Time-dependence of the anti-damping $\Gamma_-(t) = \Gamma J\,(1 - p(1 + \cos(2\omega_0 t)))$ for different amplitudes ϵ of the RF current (numerical calculations). The RF current is accounted in $J = 1 + \epsilon\cos(\omega_e t)$, where $\omega_e = 2\omega_0$ ($2f$ synchronization). Calculations have been made with $\Gamma/2\pi = 100$MHz, $p = 0.1$, and $\omega_0/2\pi = 5$GHz. (a) Complete time-dependence. Oscillations are at $2\omega_0$ and will be damped out because amplitude relaxation is much slower ($\Gamma_p << 2\omega_0$) (b) Mean value of the anti-damping (slow oscillations) obtained after simplification. Increasing ϵ modifies the mean-value of the anti-damping due to mixing with the RF current.

there, he provides expressions for amplitude and phase in synchronous state at $2f$ and f, and evidences two distinct coupling efficiencies at f and $2f$ (coupling factors). However, the analysis of the synchronization mechanism is not performed (e.g. no information on the locking-range), and no physical interpretation is given as to the consequences of the form of the coupling factors on synchronization.

Here we will try to extract as much information as possible from our mathematical expression of phase and power in stationary synchronized state. New arguments to explain the synchronization mechanism at $2f$ will be presented, and in particular we emphasize the clear link between frequency and amplitude adjustment for synchronization at $2f$, and the essential role played by the non-linearity.

Let us continue the mathematical derivation for synchronization at $2f$. We start by writing the current density J as the sum of a DC and a microwave component

$$J = J_{DC}(1 + \epsilon\cos(\phi_e)).$$

Here, J_{DC} is the amplitude of the DC current, ϵ stands for the amplitude ratio of the microwave and DC component J_{RF}/J_{DC}, and ϕ_e is the phase of the external force. We make a few remarks. First, we choose the notation ϵ, because we consider a relative *weak* driving force in order for us to remain in conditions of weak forcing to avoid undesirable effects such as irregular or even chaotic motion (see discussion in Sec. I.3.2). This will be followed all along the manuscript. Secondly, the external phase is $\phi_e = \omega_e t$, where ω_e is the frequency of the external force. We note that the initial phase of the external force is set to zero at $t = 0$. Finally for synchronization at $2f$, we suppose that ω_e is close to $2\omega_0$ to allow for resonance at $2f$.

We rewrite now the c-equation to keep the coupling factors that allow for resonant

interaction at $2f$, and replace the current density by the expression above. Eq. II.52 yields

$$\frac{dc}{dt} = -i\left[\omega_r + Np\right]c - \Gamma_0\left[1+Qp\right]c + P_x\sigma J_{DC}\left(1+\epsilon\cos(\phi_e)\right)\left[1-p\left(1+g_1(e_0)\cos(2\phi)\right)\right]c. \tag{II.53}$$

We remark that at $2f$ only the P_x contribution to the spin-torque is kept here because the P_y part does not lead to resonant interaction at $2f$. On the contrary, it will be the P_y contribution that leads to synchronization at f.

To study dynamics in the framework of synchronization, we need to introduce the *phase difference* ψ that will be kept after averaging the fast-oscillating contribution [10]. At $2f$, the phase difference is defined as follows

$$\psi = \phi_e + 2\phi. \tag{II.54}$$

We note that we take the *sum* of the external force phase ϕ_e and the STO phase ϕ rather than the difference. It comes from the fact that the phase of the STO is negative in our definition of c, i.e. $\phi = -\omega_{STO}t + \phi_0$, so summation of the phases corresponds actually to a subtraction of frequencies.

Using trigonometric identities to develop the STT term, Eq. II.55 gives

$$\begin{aligned}\frac{dc}{dt} =& -i\left[\omega_r + Np\right]c - \Gamma_0\left[1+Qp\right]c \\ &+ P_x\sigma J_{DC}\left[(1-p) + \epsilon\cos(\phi_e) + \epsilon p/2\left(\cos(\phi_e+2\phi)+\cos(\phi_e-2\phi)\right)\right]c.\end{aligned} \tag{II.55}$$

We have three oscillating terms. Terms in ϕ_e and $\phi_e - 2\phi$ oscillate respectively at about ω_{STO} and $3\omega_{STO}$. Therefore, these terms are fast-oscillating and will be neglected. The term in $\phi_e + \phi = \psi$ oscillates at a frequency $|\omega_e - 2\omega_{STO}|$, which makes it a slow-oscillating term for resonant conditions at $2f$, and this term will be kept.

We simplify Eq. II.55 to obtain the final c-equation for synchronization at $2f$

$$\frac{dc}{dt} = -i\omega(p)c - \Gamma_+(p)c + \Gamma_-^s(p,\psi)c, \tag{II.56}$$

where

$$\boxed{\Gamma_-^s(p,\psi) = P_x\sigma J_{DC}\left[1 - p(1+\frac{\epsilon}{2}\cos(\psi))\right]}. \tag{II.57}$$

Here $\Gamma_-^s(p)$ is the anti-damping in the synchronized state at $2f$. Expression II.56 leads to the essential features of synchronization at $2f$, and we can already make a few comments. First, we retrieve the equation of motion in the autonomous regime if the RF current is turned off. By setting $\epsilon = 0$, the anti-damping has the form of the autonomous regime. If we compare this equation with that of the autonomous regime, the *only* difference lies in the introduction of an additional mixing term in $\cos(\psi)$ in the anti-damping, and this mixing term induces changes of the non-linearity of the anti-damping. It is this modification of the anti-damping non-linearity due to mixing that is at the source of the specific phenomenon of synchronization at $2f$. We will explore the consequences of this fact in the following.

It is much more natural to understand synchronization at $2f$ as a *perturbation of the anti-damping* rather than a *perturbation of the whole c-equation*. Once again, this is a

10. The phase difference ψ is sometimes called the *slow phase* : close to resonance conditions (in our case $\omega_e \approx 2\omega_0$), ψ corresponds to a much lower frequency that the one of ϕ or ϕ_e, making it a "slow-phase".

specificity of synchronization at $2f$ for IPP orbits. At f, a perturbative approach of the whole c-equation is required.

We derive now phase and power equations. Multiplying the complex equation II.56 by c^* and using relation II.39 to identify the real and imaginary part, one finally gets the set of differential equations for power and phase :

$$\boxed{\begin{aligned} \frac{1}{2}\frac{dp}{dt} &= -\Gamma_0\left[1+Qp\right]p + P_x\sigma J_{DC}\left[1-p(1+\frac{\epsilon}{2}\cos(\psi))\right]p, \\ \frac{d\phi}{dt} &= -(\omega_r + Np). \end{aligned}} \tag{II.58}$$

We see that the mixing term enters only in the power equation, but the phase equation remains the same as in the autonomous regime. However, these are coupled differential equations, and because of the frequency non-linearity N, power variations due to synchronization will be accounted for in the phase.

We will solve the power equation in the *stationary regime*, i.e. we set $dp/dt = 0$ to determine the stationary power in the synchronized state. We also consider a perturbative approach for the power in the synchronized state. Indeed, due to the smallness of the external force, synchronization induces only small perturbations to the power obtained in the autonomous regime.

A trivial solution of the power equation in stationary regime is $p = 0$, which happens when the DC current is below the critical current and it corresponds to the absence of oscillations. In that case, the mixing term goes to zero, and synchronization is not possible, so we will only consider $p > 0$ [11].

We introduce the following notations for the stationary power

$$p_s = p_0 + \delta p_s, \qquad \text{with } \frac{\delta p_s}{p_0} << 1.$$

Here p_s is the stationary *forced power*, i.e. the stationary power in synchronized regime. p_0 is the free-running power, i.e. the power in autonomous regime and δp_s represents the *forced power variations* due to synchronization. Let us replace p in the power equation of II.58 by its value $p_s = p_0 + \delta p_s$, and we will linearize close to the autonomous, stationary power p_0. It yields

$$0 = -\Gamma_0\left[1+Q(p_0+\delta p_s)\right] + P_x\sigma J_{DC}\left[1-(p_0+\delta p_s)(1+\frac{\epsilon}{2}\cos(\psi))\right], \tag{II.59}$$

which gives after expansion

$$\underbrace{\Gamma_0\left[1+Qp_0\right] = P_x\sigma J_{DC}\left[1-p_0\right]}_{=0 \text{ (by definition of } p_0)} - P_x\sigma J_{DC}\frac{\epsilon}{2}p_0\cos(\psi) - \delta p_s\left[\Gamma_0 Q + P_x\sigma J_{DC}\right], \tag{II.60}$$

so that we obtain for the forced power variations δp_s

$$\boxed{\delta p_s = \lambda p_0 \frac{\epsilon}{2}\cos(\psi)}. \tag{II.61}$$

11. Study of synchronization at $2f$ in vortex-type STOs below and over the onset of self-sustained oscillation has been performed in [6].

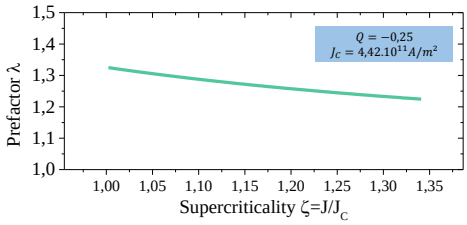

Figure II.8 – Evolution of the the prefactor λ versus DC current density using macrospin simulations parameters of Table III.1.

Here, λ is a prefactor given by

$$\lambda = \frac{P_x \sigma J_{DC}}{P_x \sigma J_{DC} + \Gamma_0 Q}.$$

The forced power variation is small compared to p_0 for small ϵ, and it is a direct function of the slow-phase ψ. The prefactor λ depends on the DC current density and the magnetic properties, but will be very close to 1 in our conditions [12].

We now insert the stationary power $p_s = p_0 + \delta p_s$ into the phase equation of II.61. It gives

$$\begin{aligned} \frac{d\phi}{dt} &= -(\omega_r + N p_0 + N \delta p_s), \\ &= -(\omega_0 + N p_0 \lambda \frac{\epsilon}{2} \cos(\psi)). \end{aligned} \tag{II.62}$$

The angular velocity $d\phi/dt$ can be expressed as a function of the slow-phase ψ as follows

$$\frac{d\phi}{dt} = \frac{1}{2}\left[\frac{d\psi}{dt} - \omega_e\right].$$

Replacing $d\phi/dt$ by the expression above in Eq. II.62 gives

$$\frac{d\psi}{dt} = \omega_e - 2\omega_0 - N p_0 \lambda \epsilon \cos(\psi)), \tag{II.63}$$

that we finally rewrite to obtain a typical Adler equation

$$\frac{d\psi}{dt} = \delta\omega_e + \Delta\Omega \cos(\psi), \tag{II.64}$$

where $\delta\omega_e = \omega_e - 2\omega_0$ is the *detuning*, i.e. the difference between the unforced STO frequency ω_0 and twice the source frequency $2\omega_e$. The *locking-range* $\Delta\Omega$ is given by

$$\boxed{\Delta\Omega = -N p_0 \lambda \epsilon}. \tag{II.65}$$

Note that we keep the minus sign because for the IPP Np_0 is negative and the locking-range is defined positive. The expression for the locking-range is straightforward. The first point is that it shows that the locking-range at $2f$ is directly proportional to the

12. This is primarily due to the fact that the damping non-linearity Q is close to zero. Using our macrospin simulations parameters (Table III.1) we obtain $Q \approx -0.24$. In Fig. II.8 the evolution of λ with the current density $J_D C$ over the critical current is shown.

driving force amplitude ϵ, which is a natural result in synchronization. The second point is the linear dependence of the locking-range with the frequency shift Np_0, which is arguably the most notable result of this analytical development. Indeed, the frequency shift $Np_0 = \omega_0(p_0) - \omega_r$ measures the change of frequency due to the increase of the precession amplitude and is an essential characteristic of the STO - it is particularly remarkable that the frequency shift and the locking-range are linked in such a direct fashion.

Indeed, it is only because the STO is strongly non-linear that synchronization at $2f$ is enabled. This formula underlines the role played by the precession amplitude on the synchronization efficiency. When the oscillation amplitude goes to zero, the locking-range becomes zero because the RF current cannot couple with the STO and synchronization at $2f$ cannot be realized. On the contrary, important precession amplitudes will strongly favor synchronization at $2f$.

II.3.2 Mechanisms of synchronization at $2f$: Amplitude and frequency adjustment

Now that the essential equations for synchronization at $2f$ are established, let us discuss in more detail mechanisms of synchronization at $2f$. We remember the introduction given in the first chapter of this manuscript on the slow-phase dynamics for synchronization to a driving force in the case of weakly non-linear oscillators. Can we translate this picture to our case of synchronization at $2f$, where the non-linearity is essential for synchronization ?

When one looks at the slow phase-dynamics (Eq. II.3.2), it has all the features of an Adler equation, and it is the signature that we have phase-locking dynamics, or synchronization. We can do the analysis of this equation. Experimentally, one has access to two control parameters for synchronization by a microwave current : (i) The amplitude of the RF signal - which is taken into account through ϵ - and (ii) the external force frequency ω_e. The amplitude of the RF signal plays directly on the locking-range : the stronger the amplitude, the wider the locking-range. This a usual result [1, 25, 57] that we find back through the linear dependence of the locking-range on ϵ II.65. Once the locking-range is fixed by the RF current amplitude, then the RF current frequency will determine the STO behavior *in the locking-range*.

Moreover, in the locking-range, the slow-phase ψ is constant. Then, rewriting Eq. with $d\psi/dt = 0$ yields

$$\cos(\psi) = -\frac{\delta\omega_e}{\Delta\Omega}, \qquad \text{under the condition that } \delta\omega_e \leq \Delta\Omega. \tag{II.66}$$

Since cosine is an even function, in theory two values of the slow-phase ψ are possible for a given detuning. Amongst these two values only one is stable - it can be verified by linearizing the slow-phase equation - and all the stable values of ψ are in the $[0;\pi]$ interval. Therefore, within the locking-range, the external source frequency determines the value of the slow-phase, and the slow-phase in the locking-range is given by

$$\boxed{\psi = \arccos(-\frac{\delta\omega_e}{\Delta\Omega})}. \tag{II.67}$$

It is interesting to look at the phase difference value at zero detuning. In the theory of

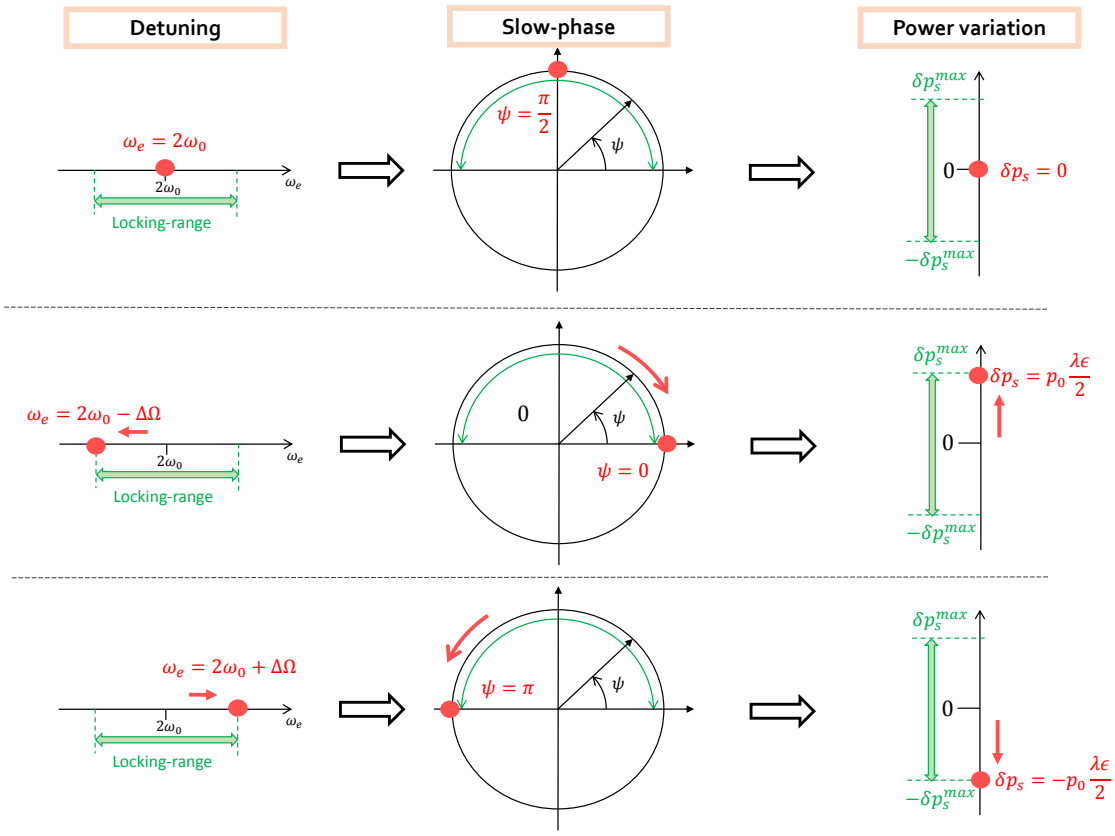

Figure II.9 – Schematics of phase-locking mechanism in the locking-range at $2f$. The control parameter is the external source frequency ω_e. As ω_e is swept in the locking-range, the slow-phase adjusts its value in the $[0;\pi]$ interval, which in turn modifies the power (i.e. the amplitude) at $2f$. Top : Zero detuning (center of the locking-range). Center : Maximum negative detuning (left extremity of locking-range). Bottom : Maximum positive detuning (right extremity of locking-range).

Adler, one obtains $\sin(\psi)$ instead of $\cos(\psi)$ in the slow-phase equation. As a consequence, Adler's synchronization gives $\psi(\delta\omega = 0) = 0$ while our case gives $\psi(\delta\omega = 0) = \pi/2$. This slow-phase at zero detuning is called the *additional phase-difference* for which we adopt the notation $\psi_0 = \psi(\delta\omega = 0)$. While we see that at $2f$ it is constant, we will see later on that for synchronization at f, the additional phase-difference has a more sophisticated form.

As we mentioned earlier in the manuscript, in a wide context synchronization to an external source is seen as adjustment of the self-sustained oscillator frequency to that of the source. This identity of frequencies is achieved by reaching a constant (or at least bounded) phase-difference between the oscillator and the source. So the basic picture of synchronization to an external source reads : "In the locking-range the detuning sets the phase difference value, and that value ensures that the forced oscillator adjusts its frequency to the source". From there, two questions arise : (i) How to determine the value of the phase-difference from the detuning ? (ii) Once the phase difference is determined, how does it translate into the identity of frequencies ?

Finding the answer to these questions will allow us to understand the peculiarities of synchronization in a given system. In Fig. II.9 phase-locking mechanisms are explained. The answer to the first question, how to determine the phase difference from the detuning

is pictured in the figure and the mathematical expression is given by solving Eq. II.3.2 for $d\psi/dt = 0$, which gives the formula II.67.

However, what is particularly interesting for synchronization at $2f$ in IPP is that there is a direct correspondence between amplitude and frequency adjustment. The right part of Fig. II.9 shows power variations depending on the value of the slow phase ψ and these power variations are determined by formula II.61. Now, the second question arises, how does the fixed slow-phase ensure that there is identity of frequencies for synchronization at $2f$? In the case of synchronization at $2f$, it is quite easy to answer. It is *only* via the non-linearity of the STO that its frequency is adjusted. First, the slow-phase value determines amplitude adjustment, and then amplitude adjustment translates into frequency adjustment via the non-linearity N.

The phase equation in the synchronized regime at $2f$ of Eq. II.58 shows the direct dependence between frequency and amplitude adjustment at $2f$. As one can see, coupling with the RF current does not take place in the phase equation, but intervenes only in the amplitude equation. Replacing the power by $p_0 + \delta p_s$ in the phase equation from II.58 gives

$$\begin{aligned}\frac{d\phi}{dt} &= -\left(\omega_r + Np_0 + N\delta p_s\right),\\ &= -\left(\omega_0 + N\delta p_s\right).\end{aligned}$$

$d\phi/dt$ is the STO frequency, and in the synchronous regime, we use the notation $d\phi/dt = -\omega_s$ (forced frequency) for the STO frequency to avoid confusion with the frequency in autonomous regime, ω_0 (free-running frequency). Similarly to the power, we define *forced frequency variations* in the locking-range by $\delta\omega_s = \omega_s - \omega_0$. Therefore Eq. **??** gives

$$\boxed{\delta\omega_s = N\delta p_s}. \tag{II.68}$$

Relation II.68 underlines a special feature of synchronization at $2f$, namely the frequency and amplitude variations in the synchronized regime are directly connected by the non-linearity N, in the same way than in autonomous regime. While it looks like a trivial result, we stress that it is a particularity of synchronization at $2f$; on the contrary at f, synchronous frequency and power are not directly linked with the non-linearity N as we will see next.

II.3.3 Power and phase in the synchronized regime at f

We will close this chapter, and more generally the analytic results of this manuscript by making the derivation of the phase and power equations in the synchronized state at f, and compare the results with synchronization at $2f$. We recall that equations for synchronization at f were previously derived in [80, 83] which will be compared to the results of our derivation. In the particular case of IPP higher order contributions will be taken into account for better precision and the domain of validity of the derived equations at f will be examined in more detail.

Let us start with the equation of motion II.52 including all fast-oscillating contributions (f and $2f$). Here we will only keep oscillating contributions at f. It means that the terms in $\cos(2\phi)$ can be neglected because they will not lead to any mixing. As a consequence, we can predict already that when the RF current is injected at f the P_x component of the spin-torque will be the same as in autonomous regime. Moreover, we write the current

density J as the sum of RF and DC contributions, where the RF frequency of the current is in the vicinity of the STO frequency, i.e. $d\phi_e/dt = \omega_e \approx \omega_0$.

In that case, the STT term of Eq. II.52 reads

$$\left(\frac{dc}{dt}\right)_{STT} = P_x \sigma J_{DC} \left[1-p\right] c + P_y \frac{\sigma J_{DC} \epsilon \cos(\phi_e)}{2\sqrt{2}} \left[1 - 6c\sqrt{p}\cos(\phi)\right]. \tag{II.69}$$

We already note here a fundamental difference with synchronization at $2f$. At $2f$, only the P_x part of the STT has to be taken into account, meaning that the DC component and the RF component at $2f$ of the applied current act in a similar way. In other terms, both components act on the magnetization with the same symmetry : an axial symmetry along the $\hat{\mathbf{e}}_x$ axis. On the contrary, at f, we need to separate the P_x and P_y parts of the STT : in the P_x part, only the DC current has to be taken into account, while in the P_y part it is the RF component of the current that matters. The interpretation is that the DC part of the current acts with a axial symmetry along $\hat{\mathbf{e}}_x$ as usual but this time the RF part breaks the symmetry because a component of the polarization P_y along the transverse direction is required.

We will introduce the slow-phase at f, $\psi = \phi_e + \phi$. Using the same reasoning as for synchronization at $2f$, we will keep only slow oscillating terms for the power equation. However it is more tricky for synchronization at f. Indeed at f coupling is enabled with the term with prefactor P_y in Eq. II.69, which is multiplied by $1-6c\sqrt{p}\cos(\phi)$. In Ref.[82] only the contribution in zero order of $|c|$ is kept, i.e. it is considered that the additional contribution $\sqrt{p}\cos(\phi)$ in third order in $|c|$ is negligible. For precision we keep this additional term and as we will see in the next chapter, even for relatively small values of p ($p \approx 1/6$) this additional correction leads to important changes.

In Ref. [83], the coupled equations for phase and amplitude for synchronization at f were derived (Eq. $49a, 49b$) and mixing terms appear in both equations, a cos term in the phase and a sin term in the amplitude. The question is how to obtain mixing terms acting on both phase and amplitude ? At $2f$, the mixing term only intervenes in the amplitude equation (see Eq. II.58), because the coupling term, in the c-equation, is written in the form $\propto pc\cos(\psi)$. Once this term is multiplied by c^*, it gives only a *real* contribution $\propto p^2\cos(\psi)$, and the real part corresponds to the amplitude. At f, the situation is different because the mixing intervenes later on when one writes the phase and amplitude equations and multiply by c^*, and in this case it leads to coupling in phase and amplitude, because both *real* and *imaginary* components appear. The mathematical process to obtain coupling at f and $2f$ is illustrated schematically in Fig. II.10.

We continue the derivation of Eq. II.69 to write power and phase equations by multiplying by c^*

$$\begin{aligned}
\left(\frac{dc}{dt}\right)_{STT} c^* =& \Gamma_-(p)p + P_y \frac{\sigma J_{DC}\epsilon\cos(\phi_e)}{2\sqrt{2}}\left[c^* - 6p\sqrt{p}\cos(\phi)\right], \\
=& \Gamma_-(p)p + P_y \frac{\sigma J_{DC}\epsilon\cos(\phi_e)}{2\sqrt{2}}\left[\sqrt{p}(\cos(\phi) - i\sin(\phi)) - 6p\sqrt{p}\cos(\phi)\right], \\
=& \Gamma_-(p)p + \underbrace{P_y \frac{\sigma J_{DC}\epsilon}{4\sqrt{2}}\left[\sqrt{p}(\cos(\psi) - i\sin(\psi)) - 6p\sqrt{p}\cos(\psi)\right]}_{\text{Keeping only slow-oscillating terms from mixing}}.
\end{aligned} \tag{II.70}$$

By identifying real and imaginary parts, one finally obtains the differential phase and

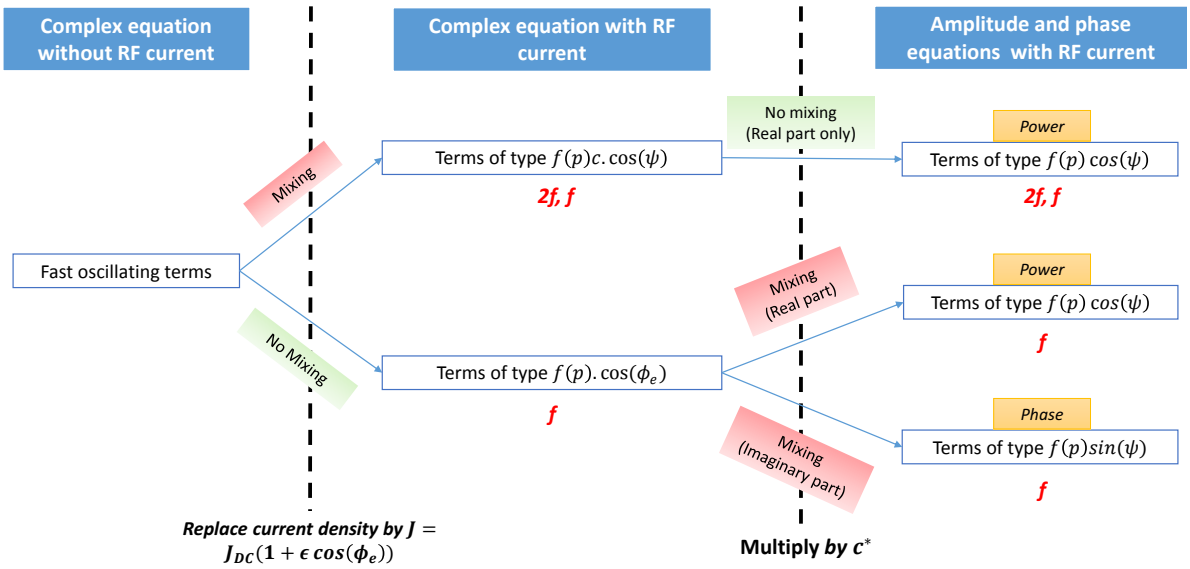

Figure II.10 – Obtaining of mixing at f and $2f$ in KTS formalism. At $2f$, mixing terms appear only in the amplitude equation. At f, mixing terms appear in both phase and amplitude equations. First oscillating terms at f and $2f$ are identified in the c-equation. Then, depending of the form of these terms, mixing will be taken into account either (i) when one writes the RF component of the current (ii) when phase and amplitude equations are calculated.

power equations for synchronization at f with mathematical relation II.39,

$$\boxed{\begin{aligned}\frac{dp}{dt} &= -2\left[\Gamma_+(p)-\Gamma_-(p)\right]p + 2C_e\sqrt{p}\left[1-6p\right]\cos(\psi),\\ \frac{d\phi}{dt} &= -(\omega_r + Np) - \frac{C_e}{\sqrt{p}}\sin(\psi).\end{aligned}} \tag{II.71}$$

where

$$C_e = P_y\sigma\frac{J_{DC}\epsilon}{4\sqrt{2}} \tag{II.72}$$

is a prefactor indicating the coupling strength at f. It corresponds to the external force "effective" amplitude f_e as in Ref.[83].

The coupled equations II.71 for phase and power in synchronized state at f are very similar to the ones of Slavin *et al.* in [83]. The same dependence of the coupling strength in $\sqrt{p}$ in the amplitude and in $1/\sqrt{p}$ in the phase is obtained. In contrast to $2f$, we do get directly the mixing term in the amplitude *and* the phase equation. We can also verify that when the RF current is turned off ($C_e = 0$), then one finds the expression for phase and amplitude in the autonomous regime.

However there a few notable differences with the expression of [83], namely :

- The expression for the prefactor C_e (or effective external force in [83] F_e). We obtain a factor 2 difference with the one of [83].
- The higher order corrections of the coupling strength in the amplitude equation. It is required that we take into account corrections in p when precession angles become important. In particular there is a factor 6 in the correction, so even for relatively small values of p, this correction is important and needs to be included in the IPP case.

Now we can continue to study the dynamics in the stationary synchronous regime at f. As for $2f$, we start with $dp/dt = 0$ for the stationary regime and from there we calculate forced power variations $\delta p_s = p_s - p_0$ by linearizing the power equation close to the free-running power p_0. Introducing the damping rate Γ_p of amplitude deviations, in the stationary state the power equation II.71 gives in first order of δp_s

$$0 = -2\Gamma_p \delta p_s + 2C_e\sqrt{p_0}(1-6p_0)\cos(\psi), \tag{II.73}$$

so that

$$\frac{\delta p_s}{p_0} = \frac{C_e(1-6p_0)}{\Gamma_p\sqrt{p_0}}\cos(\psi). \tag{II.74}$$

We note that obtaining this expression requires the assumption that $\delta p_s/p_0 \ll 1$, and it must remain valid in the totality of the locking-range, i.e. for $-1 < \cos(\psi) < 1$. If we look at the expression of $\delta p_s/p_0$, we see that it tends asymptotically to $+\infty$ when p_0 goes to zero due to the product $\Gamma_p\sqrt{p_0}$. This indicates that the formula is not valid for very small powers. More generally the condition $\frac{C_e}{\Gamma_p\sqrt{p_0}} \ll 1$ has to be fulfilled so that $\delta p_s/p_0 \ll 1$. It is difficult to estimate the domain of validity of this condition and it should be done specifically for each case. At $2f$, the domain of validity of the condition $\delta p_s/p_0 \ll 1$ is determined by the RF/DC current ratio ϵ only ; however at f, the domain of validity of the condition $\delta p_s/p_0 \ll 1$ is determined by ϵ but also depends in a non-trivial way on the amplitude p_0. As a consequence, the condition $\delta p_s/p_0 \ll 1$ is much more restrictive at f than at $2f$ (see macrospin results for the locking-range III.4.2).

Similarly to $2f$, we insert the power variations δp_s into the phase equation, but this time in the phase equation there is already a mixing term in $\sin(\psi)$, so we will add the two contributions. The phase equation reads

$$\begin{aligned}
&\frac{d\phi}{dt} = -(\omega_0 + N\delta p_s) - \frac{C_e}{\sqrt{p}}\sin(\psi),\\
\Leftrightarrow\ &\frac{d\psi}{dt} = -\omega_0 + \omega_e - Np_0\frac{C_e(1-6p_0)}{\Gamma_p\sqrt{p_0}}\cos(\psi) - \frac{C_e}{\sqrt{p}}\sin(\psi),\\
&= \delta\omega_e - \frac{C_e}{\sqrt{p_0}}\left((1-6p_0)\nu\cos(\psi) + \sin(\psi)\right),
\end{aligned} \tag{II.75}$$

where $\delta\omega_e = \omega_e - \omega_0$ is the detuning at f and ν the dimensionless non-linearity coefficient. The two contributions due to mixing in the phase (in $\sin(\psi)$ and power (in $\cos(\psi)$) can be recognized in the slow-phase equation. Here, the non-linearity coefficient ν indicates the role played by amplitude adjustment compared to direct phase adjustment in the phase-locking process. In the case where $\nu \gg 1$, it is amplitude adjustment that prevails over direct phase adjustment, leading to a behavior in the locking-range very similar to that of synchronization at $2f$. We can rewrite the phase equation in order to merge amplitude and phase contributions by introducing the *additional phase-difference*, ψ_0 corresponding to ψ at zero detuning. Equation II.76 reads then

$$\frac{d\psi}{dt} = \delta\omega_e + \Delta\Omega\sin(\psi + \psi_0), \tag{II.76}$$

where $\Delta\Omega$ is the locking-range at f given by

$$\Delta\Omega = \frac{C_e}{\sqrt{p_0}}\sqrt{1+\left[\nu(1-6p_0)\right]^2} \tag{II.77}$$

and the additional phase-difference ψ_0 is given by

$$\psi_0 = -\arctan(\nu(1-6p_0)). \tag{II.78}$$

The factor $\nu(1-6p_0)$ intervenes in the locking-range expression as well as in the additional phase-shift expression. In terms of synchronization properties, it means that, at f, the non-linearity enhances the locking-range but also induces an additional phase-shift. Depending on the relative force of amplitude adjustment over direct phase adjustment, this additional phase-shift varies in the interval $[-\pi/2;+\pi/2]$. In the case of strong non-linearity $\nu \gg 1$, the additional phase-shift is close to $\pi/2$. This is to be contrasted with synchronization at $2f$ where the phase-shift is *fixed* at $\psi_0 = \pi/2$, regardless of the strength of the non-linearity.

We also note that the expressions obtained for the locking-range and the additional phase-shift are those of Ref. [83] with the difference that in the present expression, we take into account the first order dependence in p_0 with the factor $1-6p_0$. The prefactor of 6 makes the correction important even with quite small values of p_0. One of the major consequences of the correction is that the enhancement of the locking-range due to amplitude adjustment $\nu(1-6p_0)$ goes to zero when the precession amplitude increases. It is translated mathematically by the factor $1-6p_0 = 0$ when $p_0 = 1/6$. This additional phase-shift will be analyzed in more detail in the next chapter through macrospin simulations.

To conclude with the analytical derivation of the equations of synchronization at f, we rewrite the first expression of II.76 with the forced STO frequency $d\phi/dt = -\omega_s$. Similarly to the case of $2f$, we define forced frequency variations in the locking-range at f by $\delta\omega_s = \omega_s - \omega_0$, then we have

$$\delta\omega_s = N\delta p_s + \frac{C_e}{\sqrt{p}}\sin(\psi). \tag{II.79}$$

The previous equation shows a peculiarity of synchronization at f with respect to synchronization at $2f$. We see that at f $N\delta p_s \neq \delta\omega_s$ because the second term corresponding to direct phase adjustment cannot be neglected. It means that frequency and amplitude in synchronous regime at f are not connected via the non-linearity as in the autonomous regime $Np_0 = \omega_0 - \omega_r$, thus the interpretation of synchronization at f with the KTS model is more complex than at $2f$.

As such, the KTS model for synchronization f does not provide specific information about the effect on the injected RF current f on magnetization trajectories. We know that after transformation to the complex coordinates, both phase and amplitude are involved in the synchronization process but it remains difficult to translate this statement into an understanding of the motion of the magnetization in the synchronized state. It is natural to assume that amplitude deviations δp_s correspond to growth or reduction of precession amplitude along IPP orbits, but it is much more difficult to visualize how the direct phase contribution $\frac{C_e}{\sqrt{p}}\sin(\psi)$ acts on the motion of the magnetization. Does it accelerate or reduce the angular velocity of the magnetization along the trajectory without modifying the precession orbit ? Or does it correspond to a modification of the precession orbit, i.e.

	Coupling at **2f**	Coupling at **f**
Zero order in |c|	/	$P_y \dfrac{\sigma J}{2\sqrt{2}}$
First order in |c|	/	/
Second order in |c|	/	$P_y \dfrac{\sigma J}{2\sqrt{2}} \left[-6\sqrt{p}\cos(\phi)\right] c$
Third order in |c|	$-P_x \sigma J \left[p\cos(2\phi)\right] c$	/

TABLE II.1 – Coupling factors with the RF current in the equation of motion II.52 at f and $2f$. Their dependence in powers of |c| determines the evolution of synchronization properties with precession amplitude.

stretching or tilting of the overall orbit in a given direction, which would not translate into modification of the reduced amplitude p ? To answer these questions, it is necessary to perform macrospin simulations so that we can establish a link between magnetization trajectories in the synchronized state and analytical results from the KTS model.

II.3.4 Discussion : External force and coupling factors

As we saw in the first chapter, Slavin *et al.* proposed a general form for synchronization of an STO to a external force. The addition of an external force translates into the inclusion of a perturbative term $f_e e^{-i\omega_e t}$ in the equation of motion as follows

$$\frac{dc}{dt} = -i\omega(p)c - \Gamma_+(p)c + \Gamma_-(p)c + \underbrace{f_e e^{-i\omega_e t}}_{\text{External force}} . \tag{II.80}$$

Now in [83], it is not mentioned whether this form for the external force is valid at f or at $2f$. Using our derivation in IPP, is it possible to put the the contribution from the RF current in the form of an effective external force as in Eq. II.80 ?

Let us suppose an RF current is injected at f. In this case, only oscillating terms at f will be kept, i.e. the P_y contribution from the STT. For simplicity, we do not include the higher order term $-6c\sqrt{p}\cos(\phi)$. Then the equation of motion II.52 reads

$$\frac{dc}{dt} = -i\omega(p)c - \Gamma_+(p)c + \Gamma_-(p)c + P_y \frac{\sigma J_{DC} \epsilon \cos(\omega_e t)}{2\sqrt{2}}. \tag{II.81}$$

For small angles γ_0, $\tan(\gamma_0) \approx P_y$, and $J_{DC}\epsilon$ corresponds to the amplitude of the RF current, or ΔI in [83]. If we rewrite the last term of Eq. II.81 in the form of $f_e \cos(\omega_e t)$, then we obtain the same effective force amplitude f_e, using $\cos(\omega_e t)$ instead of $e^{i\omega_e t}$.In conclusion, at f, it is possible to rewrite the contribution from the RF current using a perturbative force $f_e \cos(\omega_e t)$.

However at $2f$, only oscillating terms at $2f$ are kept and the P_y part of the STT does not contribute. In this case the equation of motion reads instead (Eq.II.56)

$$\frac{dc}{dt} = -i\omega(p)c - \Gamma_+(p)c + \Gamma^s_-(p,\psi)c,$$

where the anti-damping in synchronized state, Γ^s_- is given by

$$\Gamma_{-}^{s}(p,\psi) = P_x \sigma J_{DC} \left[1 - p(1 + \frac{\epsilon}{2}\cos(\psi))\right].$$

Here the driving force at $2f$ acts as a perturbation of the anti-damping. Hence the general form of Eq. II.80 is not adapted to the case of synchronization at $2f$ because it presupposes that the external force acts as a perturbation of the whole equation of motion, which is not the case here. At $2f$ it is impossible to write the influence of the RF current as a perturbative force $f_e e^{i\omega_e t}$.

The disadvantage of Eq.II.80 to account for synchronization in STOs is that it looks like the most general form, but writing the equation this way can be misleading. When one includes a small RF current or RF field in the LLGS equation, it couples with the (m_x, m_y, m_z) components of the magnetization in different ways. As a consequence, we expect that in the c-equation, several terms accounting for several types of coupling arise. In particular, the analytical development here shows the RF current couples with the magnetization differently depending on whether it is injected at f or at $2f$. In the form of [83] the effect of the external force is thus written in one way and one way only in the c-equation once the type of perturbation is chosen (current/field). Then it is restrictive because written as such, it does not allow for the fact that the same type of external perturbation can couple differently with the STO at f and $2f$.

Slavin *et al.* mention in [83] that

> "Strictly speaking, interaction of a spin-torque oscillator with a microwave current or a microwave magnetic field depends on the power of the excited spin wave mode $|c|^2$, i.e. the effective amplitude f_e of the locking signal is a function of $|c|^2$. For simplicity, we neglect this dependance, assuming the limit $|c|^2 \to 0$. The theory of phase-locking developed in this section can be easily generalized to the case of an arbitrary dependance of the "driving" force on the auto-oscillation power - one simply has to replace in all the equations the constant amplitude f_e by the value $f_e(p_0)$, where p_0 is the free-running power of the oscillator."

In a few words, this paragraph states that the amplitude of the effective external force f_e depends on the precession amplitude ("power of the excited spin-wave mode"), but this dependance is neglected because it does not change qualitatively the synchronization features and $|c|^2$ is small. The possibility of an effective external force depending on spin-wave amplitude $|c|$ is covered, but it is maintained that any driving RF force can be modeled through an effective external force as in II.80.

Actually, the use of "effective external force" can be source of confusion, because its leads to the belief that there is a one-to-one correspondence between the actual external force (the RF current or RF field) and an effective force that necessarily manifests itself by the addition of a perturbative term $f_e e^{-i\omega_e t}$ in the c-equation. To avoid this confusion, we separate clearly : (i) *the external force amplitude* which is directly the amplitude of the RF current in our case and ; (ii) instead of an effective force specific *coupling factors* emerging in the c-equation after transformation, which determine synchronization features.

II.3.5 Summary of the analytical results

In this chapter we have derived approximate analytical expressions for synchronization at f and $2f$ for the IPP based on the KTS model without thermal noise. From the same

	Synchronization at **2f**	Synchronization at **f**
Locking-range $\Delta\Omega$	$\Delta\Omega = -\lambda N p_0 \epsilon$	$\Delta\Omega = \frac{C_e}{\sqrt{p_0}}\sqrt{1+[\nu(1-6p_0)]^2}$
Additional phase difference ψ_0	$\psi_0 = \pi/2$	$\psi_0 = -\arctan(\nu(1-6p_0))$
Power variations δp_s	$\delta\omega_s = N\delta p_s$	$\delta\omega_s \neq N\delta p_s$
Evolution in the locking-range		
Phase difference ψ	$\psi = \arcsin\left(\frac{\delta\omega_e}{\Delta\Omega}\right) + \pi/2$	$\psi = \arcsin\left(\frac{\delta\omega_e}{\Delta\Omega}\right) + \psi_0$
Power variations δp_s	$\frac{\delta p_s}{p_0} = \lambda\frac{\epsilon}{2}\cos(\psi)$	$\frac{\delta p_s}{p_0} = \frac{C_e(1-6p_0)}{\Gamma_p\sqrt{p_0}}\cos(\psi)$

TABLE II.2 – Comparison of the analytical results in the KTS model for synchronization at f and $2f$

starting hypotheses, i.e. strong ellipticity and relatively small precession amplitude, the full transformation of the LLGS equation into a complex self-sustained oscillator variable was performed in the presence of both RF and DC current. The geometrical properties of the three transformation steps from [82] were analyzed, which allowed us to make simplifying assumptions based on the ellipticity of the IPP trajectory.

Then we focused on identifying coupling factors between the STO and the RF current in the complex c-equation. It turns out that different coupling factors arise at f and $2f$ which lead to distinct synchronization mechanisms at f and $2f$. To provide understanding for the essential properties of synchronization, analysis of the *stationary synchronized regime* was performed. While equations for synchronization at f were established previously [83, 82], we derived new analytical expressions for synchronization at $2f$ within the framework of the KTS model.

We also remark that for the analysis of the synchronized regime (starting from Sec.II.3) we made the assumption that the ellipticity of the IPP trajectory was important, so that $g_1(e_0) \approx 1$ and $g_2(e_0) = \approx 1/\sqrt{2}$. The approximation was made in order to have a simpler notation and focus on the role of the precession amplitude rather than on the ellipticity, but one can also keep the ellipticity parameters g_1 and g_2 in the derivation. In this case, one can easily calculate the locking-range at $2f$ which reads instead

$$\Delta\Omega = -g_1(e_0)\lambda N p_0 \epsilon. \tag{II.82}$$

Here we see that the locking-range at $2f$ is multiplied by the factor $g_1(e_0)$: if $g_1(e_0)$ goes to zero (no ellipticity) then the locking-range tends to zero as well. It gives confirmation that the ellipticity is a crucial parameter that enables synchronization at $2f$.

The same reasoning can be applied to synchronization at f, and by keeping $g_2(e_0)$ during the development the locking-range at f gives

$$\Delta\Omega = -g_2(e_0)\frac{C_e}{\sqrt{p_0}}\sqrt{1+[\nu(1-6p_0)]^2}. \tag{II.83}$$

Here the locking-range at f is multiplied by g_2 instead of g_1. At f the ellipticity impacts the dynamics in synchronized regime, but in a less significant manner : from low to high ellipticity, g_2 goes from 1 to $1/\sqrt{2}$, which is a much smaller variation than for g_1 going from 0 to 1. In contrast with $2f$, synchronization at f is favored with a lower ellipticity.

Based on these expressions, we highlight important differences between synchronization at f and $2f$, with emphasis on the original features of our approach to synchronization at $2f$:

• **Perturbation of the anti-damping**. At $2f$ synchronization arises from the introduction of a mixing term creating a perturbation within the anti-damping, which will shift the balance in amplitude. Therefore another precession orbit corresponding to a slightly bigger or smaller amplitude will be stabilized, allowing for frequency adjustment to the RF signal.

• **Direct correspondence between frequency and amplitude adjustment**. At $2f$, the only available mechanism for frequency adjustment is a change of precession amplitude. It means that the non-linearity is *necessary* for synchronization at $2f$, which contrasts with f where non-linearity only *enhances* the locking-range.

• **Symmetry between the precession orbit and the polarizer direction**. The orientation of the polarizer with respect to the orbit geometry allows one to predict synchronization ranges at f. An orientation of the polarizer along the $\hat{\mathbf{e}}_x$ axis (parallel to the symmetry axis of the orbit) favors synchronization at $2f$, while synchronization at f is enabled for a polarizer along the $\hat{\mathbf{e}}_y$ axis (perpendicular to the symmetry axis of the orbit).

• **Dependence of the synchronization properties on oscillation amplitude**. Previous works, whether experimental or theoretical, on synchronization in STOs, do not treat oscillation amplitude as a determining factor. In fact, it is assumed that since the oscillation amplitude is rather small, it does not play a significant role on the synchronization properties. But we found out that at $2f$, the oscillation amplitude *is* crucial and it is remarkable that the locking-range evolves in a linear fashion with the frequency-shift due to amplitude $\omega_0(p_0) - \omega_r = Np_0$. In the case where the oscillation amplitude goes to zero, synchronization vanishes at $2f$.

Chapter III

Macrospin simulations in the synchronized regime

In the previous chapter we formulated within the KTS model analytical expressions for synchronization at $2f$ that we compared with the previously established model for synchronization at f. As we saw, synchronization at f and $2f$ yield distinct coupling factors, which lead to two different synchronization mechanisms.

In this chapter we utilize *macrospin simulations* to investigate the synchronized regime in the same configuration, namely In-plane precession and synchronization to a driving RF current at f and $2f$. We mean by macrospin simulations the *numerical* resolution of the LLGS equation.

Through macrospin simulations a quantitative verification of the relations derived in the last chapter will be provided : we compare here the results from the numerical resolution of the LLGS equation (macrospin simulations) with the results from the analytical resolution of the reduced c-equation of motion, which is the LLGS equation after a change of variable. To do so, we will extract several synchronization parameters such as the locking-range, the phase-difference and both forced power and frequency in the stationary, synchronized regime from macrospin simulations in the IPP configuration. These parameters will be extracted as a function of simulation inputs such as the DC and RF current, which respectively control the autonomous oscillation amplitude and the driving force amplitude.

III.1 Initialization : Verification of the KTS model in autonomous regime for the IPP

In order to compare the results obtained at f and $2f$, we need to choose a magnetic configuration where both synchronization at f and $2f$ are possible. If we recall our previous calculations, it means that we need to have a P_x and a P_y component for the polarizer to observe both. We choose to tilt the polarizer in plane with respect to the easy axis (AP state) at an angle of 15°. To maximize the STT which gives rise the anti-damping, it is required that the polarizer is only slightly tilted with respect to the easy axis. As a consequence we have chosen a small tilting angle, which also corresponds to the experimental conditions (see part C of the manuscript for experimental measurements).

The simulation parameters used are summarized in Table III.1. These parameters will be kept *constant* and serve as a basis for all simulations presented in this chapter.

Magnetic configuration	
Saturation magnetization M_s (A/m)	10^6
Magnetocristalline anisotropy K_u (J/m^3)	10^3
Demagnetizing factors $(N_x; N_y; N_z)$	$(0; 0; 1)$
Volume V (nm^3)	22053.33
Area S (nm^2)	5654.7
Thickness t (nm)	3.9
Magnetic damping α	0.02
Spin-Torque efficiency $\sigma/2\pi$ (rad/ sec /Am^2)	$5.48x10^{-4}$
Polarizer angle θ_p (°)	165
In-plane (x-axis) field H_b (mT)	40
Oscillator parameters	
FMR frequency $\omega_r/2\pi$ (GHz)	$6,55$
Critical current density J_C (A/m^2)	$4,42.10^{11}$
Frequency non-linearity $N/2\pi$ (GHz/p_0)	$-3,82$
Damping rate $\Gamma_0/2\pi$ (MHz)	375
Damping non-linearity Q	$-0,24$

TABLE III.1 – Table of parameters used for macrospin simulations. The top section of the table sums up the parameters used as input for the macrospin simulations. These parameters determine the magnetic properties of the FL as well as the STT strength. The bottom section provides the corresponding parameters for the STO in KTS formalism, calculated using the analytical formulae introduced in the previous chapter at the end the change of variables. Throughout this chapter, only the attributes of the injected current will be modified, i.e. (i) DC amplitude (ii) RF amplitude (iii) RF frequency

To obtain the two coupled systems corresponding respectively to the synchronized state at f and $2f$ (Eqs. II.58 and II.71), we made the assumption that the ellipticity of the IPP trajectory is large, i.e. $e_0 \to 0$. Fig. II.5 shows the evolution of the ellipticity of the IPP trajectory as a function of the applied field H_b. We compare the ellipticity e_0 derived from the analytical formula II.12 and from the manual extraction of the ratio m_z^{max}/m_y^{max} from IPP trajectories (macrospin simulation), just above the critical current. We see that in the range of 0 to 1.2 kOe, e_0 grows from 0 to 0.3. For the rest of the simulations, we choose an applied field of $H_b = 400$ Oe. First because it corresponds to the typical applied fields in our experiments, but it also ensures that the ellipticity is important : in that case, $e_0 = 0.18$. We recall that the ellipticity is involved in the reduced c-equation via the functions g_1 and g_2 (Eq. II.51), and we made the assumption in the case of strong ellipticity that $g_1(e_0) \approx 1$ and $g_2(e_0) \approx 1/\sqrt{2}$. We have for our value of e_0 $g_1(e_0) = 0.94$ and $g_2(e_0) = 0.72$, which gives about a 5% error.

We recall that this study focuses on the dependence of the synchronization properties on the oscillation amplitude, i.e. the behavior with respect to the reduced oscillator power p. In accordance with the requirements of the KTS model, we have selected "moderate supercriticalities" so that the Taylor expansion in powers of p is valid. Therefore simulations were carried out for values of DC currents so that $J_{DC}/J_C < 1.3$.

We first extract the precession amplitude p_0 using macrospin simulations results. Macrospin simulations allow one to determine the time-dependence of the three magnetization components $m_x(t), m_y(t), m_z(t)$. Then the three transformations steps are applied to obtain the time-dependent oscillator variable $c(t)$, out of which the instantaneous phase $\phi(t)$ and power $p(t) = |c(t)|^2$ can be extracted. Fig. III.1(a) shows the evolution of the reduced power p_0 with respect to the DC current density and compares the analytic formula **??** with p_0 extracted from macrospin simulations. There is a very good agreement between the analytic formula and results from simulations, which is a first good indication of the validity of the KTS model for our range of currents (J_{DC}/J_C<1.3).

We can also extract other parameters of the KTS model. In Fig. III.1(a) the frequency shift with amplitude is plotted. The frequency shift is obtained by two methods. The first is direct analytic calculation of Np_0 - the black line - by multiplication of (i) the Non-linearity factor N (obtained from Eq. II.47) with (ii) the oscillation power $p_0(J_{DC})$ in the autonomous regime (from formula I.14 in the first chapter). The second method relies on macrospin simulations - red dots - where the STO oscillation frequency ω_0 is extracted directly from the time-traces, and the frequency difference $\omega_0(I_{DC}) - \omega_r$ is then plotted. Good quantitative agreement is reached between the analytical results and the macrospin simulations.

The amplitude relaxation rate Γ_p is obtained from the analytic formula (Eq. 27b in Ref. [83]), and reaches the typical values of zero to hundreds of MHz for $f_p = \Gamma_p/2\pi$ [71, 34].

It is also important to evaluate another determining parameter, the normalized non-linearity coefficient ν. It is expected that ν is much bigger than 1 for the IPP and typical configurations of a STO. It is plotted in Fig. III.1(b). It is calculated analytically with the ratio of the two quantities Np_0 and Γ_p from Fig. III.1(c). We see that it slightly varies with applied current, decreasing slowly from a value of 13 to 10, so the STO in the IPP configuration yields an important non-linearity with $\nu \gg 1$.

Now a consistent basis for the analysis of the synchronized state at f and $2f$ for the IPP has been established. Indeed, the KTS model applied in our situation provides

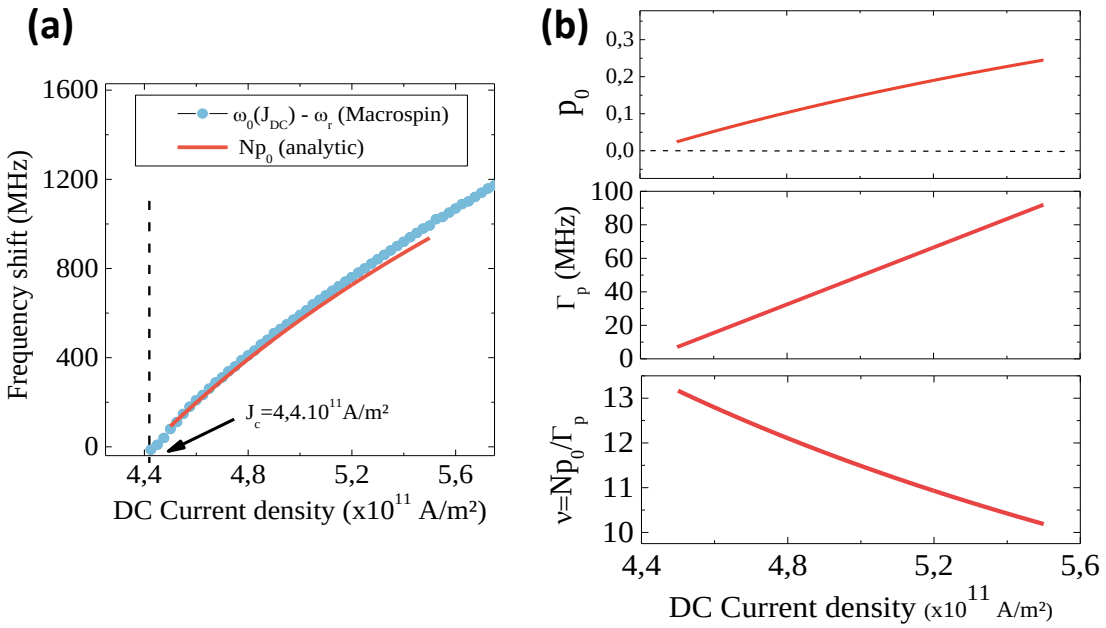

Figure III.1 – Extraction of salient oscillator quantities in the autonomous regime as a function of the DC current. (a) Comparison of the frequency shift from the analytic formula (red line) and macrospin results (blue dots). (b) KTS parameters calculated from the analytical model. From top to bottom : oscillation amplitude p_0, amplitude relaxation rate Γ_p, and non-linearity coefficient $\nu = Np_0/\Gamma_p$.

analytic expressions which do not only describe macrospin results qualitatively, but give a few predictions in very good quantitative agreement with the simulations. We note that it remains difficult to validate in our case the expression for Γ_p with macrospin simulations. In [71, 70], Γ_p has been extracted by macrospin simulations under noise using time-frequency techniques and compared with the analytic formula, where it was seen that the analytic formula slightly underestimates Γ_p. In contrast there is an excellent quantitative agreement between analytics and simulations for the frequency-shift Np_0, which will be compared later on to the locking-range at $2f$ (Sec. III.4).

III.2 Frequency and power adjustement

Up to now we have not addressed macrospin simulations in the presence of a RF current. We remember that synchronization is not a state, but a complex dynamical process, so a general approach is required. We start with the most basic characterization of synchronization, i.e. the forced STO frequency vs the external source frequency, also called detuning plots. Experimentally, these detuning plots, coupled with the linewidth plots, can be easily obtained with a spectrum analyzer and indicate whether or not a synchronized state is reached.

Furthermore, we can get back to the oscillation power p from macrospin simulations because we have direct access to the oscillator variable c via the transformation. This is extremely valuable because it allows us to analyze power variations and compare it with the model developed above, which underlines the fundamental role by these power variations to achieve frequency adjustment.

Finally, we note that the extraction of the oscillation power p is much more tedious

in experiments than in macrospin simulations. Indeed, experimentally one does not have access to the magnetization coordinates in real time, but an electric signal which is proportional to the projection of the magnetization on the polarizer axis. It is usually not possible to establish a quantitative link between oscillation amplitude and signal intensity. Moreover, synchronization induces small power changes with respect to the autonomous power (not more that $1/10^{th}$), and these variations cannot be measured directly as a change of amplitude of the output signal.

III.2.1 Comparison of synchronous power and frequency at 2f and f

Here we study the forced power and the frequency in the locking-range, at f and $2f$ for a given autonomous amplitude. We will start by choosing an amplitude p not too close to zero amplitude, but with $p \ll 1$ so that we can have a first guess of the behavior at f and $2f$. Let us pick a constant current bias of $J_{DC} = 5.4x10^{11}\mathrm{A/m^2}$, which gives $\zeta = J_{DC}/J_C = 1.22$, $p_0 = 0.24$ and corresponds to a frequency shift of $\omega_0 - \omega_r = 940$ MHz.

Once the working point of the free-running STO is decided, we choose the amplitude for the driving RF current. We note that this amplitude cannot be chosen randomly. First, we need an RF amplitude which is high enough so that the synchronization region is not negligible, making the measure possible. On the other hand, the RF current must remain smaller than the DC current so that the coupling is weak, and we can still talk of synchronization (in accordance to $\epsilon = J_{AC}/J_{DC} \ll 1$). Otherwise, undesirable effects appear at strong forcing which invalidate the analytical model developed above. Finally, the frequency of the driving RF current is swept close to the STO frequency at f or twice the STO frequency for $2f$, where the frequency and the power p of the STO is extracted for each value of the driving frequency. Typically, the RF current frequency is swept in an interval of a few hundreds of MHz close to f or $2f$, with steps of 5 or 10 MHz in order to achieve sufficient resolution.

Fig. III.2 shows the result of such an extraction of the frequency and the power of the STO when the RF current is close to f or $2f$. We note that the values of the RF current correspond here to current ratios of $0.13 \leq \epsilon \leq 0.28$ which remain small enough for our analysis to be valid. We can make a few observations :

1. **Frequency adjustment**. (top panel) The zone in the middle of the graph where the STO frequency follows the RF current frequency (or $2\omega_e$) is the locking-range, or to be precise *twice* the locking-range (by definition of $\Delta\Omega$ in Eq. II.3.2). For this particular value of DC current, the locking-range at $2f$ ranges from 150 MHz($\epsilon = 0.13$) to 300 MHz($\epsilon = 0.13$), while at f it ranges from 20 MHz($\epsilon = 0.13$) to 40 MHz($\epsilon = 0.28$). It leads to two conclusions. First, the locking-range increases with the RF current amplitude. Second, in this configuration, synchronization at $2f$ is favored over synchronization at f with a locking-range about one order of magnitude higher.
2. **Power adjustment**. (bottom panel) Frequency adjustment in the locking-range has been observed numerous times in both experiments and simulations in STOs, however to our knowledge there is no analysis yet of power variations using KTS formalism in the locking-range. It is interesting to see that power variations have a behavior that is very similar to frequency variations, in the sense that it looks as if the power "locks" to the external force in the locking-range as well. The difference is that with respect to ω_e the power has the opposite slope compared to the frequency in the locking-range, reaching a maximum at the left extremity and a minimum at

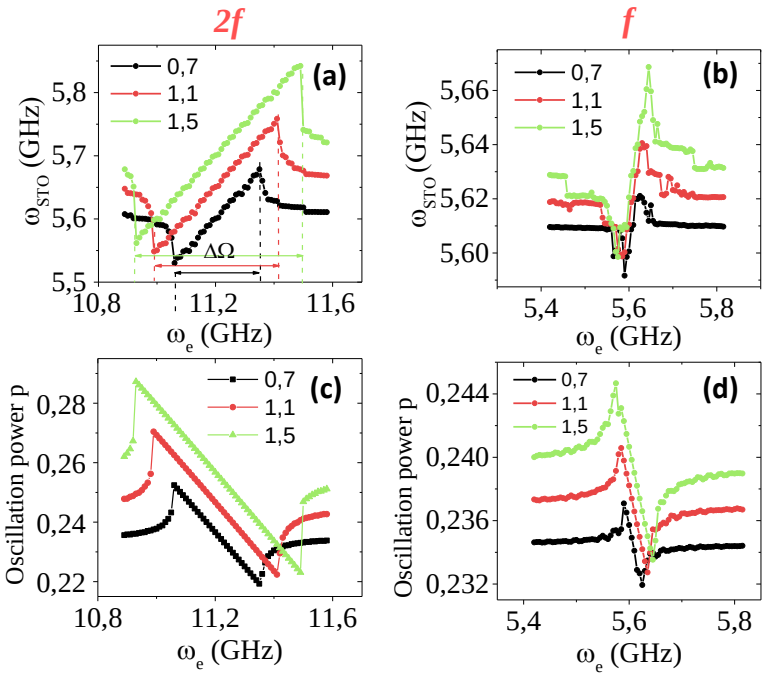

Figure III.2 – Frequency and power in the synchronized state at f and $2f$ for $J_D C = 5,4\mathrm{A/m}^2$ as a function of the driving RF current frequency ω_e. Results are shown for 3 amplitudes of the RF current : $J_{RF}(0.7; 1.1; 1.5)x10^{11}\mathrm{A/m}^2$. Plots are vertically offset for better readability. (a),(c) : ω_e is close to *twice* ω_{STO}. (b),(d) : ω_e is close to ω_{STO}. Top panel : Frequency. Bottom panel : Power.

the right extremity. In the middle of the locking-range, the driving frequency is equal to the STO frequency, and the forced power p_s is equal to the autonomous power p_0. Finally, our simulation settings seem to indicate that power changes are extracted with better precision than frequency changes. Fig. III.2(b) shows that at f we reach the lower limit in frequency resolution of about 5 MHz (which can be avoided with much longer time-traces) and it creates numerical roughness. The power extraction is not subject to this constraint, which grants better precision.

3. **Qualitative behavior at f and $2f$.** Except for the numerical roughness for the frequency at f, no qualitative difference between f and $2f$ is appreciable in frequency and power variations plots in this case. In both cases we see that the locking-range increases with the RF current. However at this point, the free-running amplitude has been fixed, so it is not possible yet to see if the synchronization properties evolve with the free-running amplitude the same way at f and $2f$.

III.2.2 Power changes in the synchronized regime at $2f$

We focus here on a more quantitative verification of the synchronization properties at $2f$ from our analytical model. Indeed, our model provides a simple expression for power changes at $2f$ (Eq. II.61) as a function of the slow-phase ψ. In the locking-range, we can rewrite the slow phase as a function of the detuning and the locking-range (Eq. II.67), so it is possible to establish a formula for the power variations as a function of the detuning $\delta\omega_e$, which gives

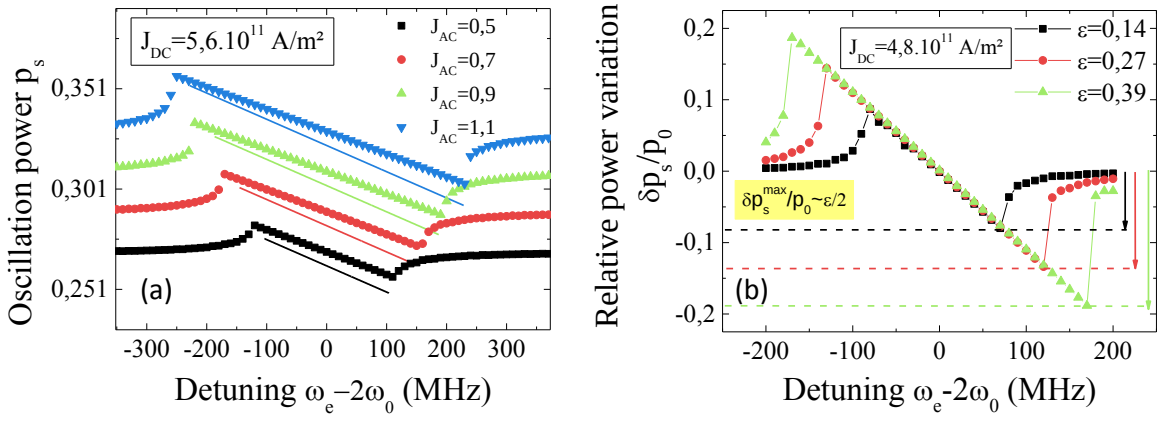

Figure III.3 – Power variation in the locking-range at $2f$ for several RF current amplitudes. (a) Comparison with $J_{DC} = 5,6.10^{11}\mathrm{A/m^2}$ between macrospin simulations (dots) and analytic formula III.1 (lines) with the approximation $\lambda = 1$ (curves are offset for clarity). (b) *Relative* power variation $\delta p_s/p_0$ for $J_{DC} = 4,8.10^{11}\mathrm{A/m^2}$ for several ϵ values (macrospin simulations). Arrows indicate maximum power changes when ϵ increases.

$$\delta p_s = -\frac{\lambda p_0 \epsilon}{2}\frac{\delta\omega_e}{\Delta\Omega}. \tag{III.1}$$

Under the approximation $\lambda \approx 1$, we see the maximum power variations in absolute value are reached at the two extremities of the locking-range, i.e. when $\delta\omega_e = \pm\Delta\Omega$. The maximum relative power variation, $\delta p_s/p_0$, is given by $\epsilon/2$ which is readily verifiable by macrospin simulations (see Fig.III.3(b)). A very satisfactory quantitative agreement is reached. In the locking-range, power variations follow a linear dependence with the detuning, crossing zero in the middle of the locking-range.

We finalize the discussion on frequency and power variations in the synchronized state at $2f$ with the verification of the formula $\delta\omega_s = N\delta p_s$ established in the previous chapter, and valid for $2f$ synchronization only. We remind the reader of its physical significance : it means that in the synchronous regime at $2f$, the frequency adjustment $\delta\omega_s$ is achieved *only* through adjustment of the precession amplitude δp_s. The variations of power and frequency are directly connected by the non-linearity N, which is *exactly* the same as in the autonomous regime.

An interesting consequence of this fact is that it gives one another way to extract the non-linearity factor N, arguably the most important characteristic of a STO which determines its agility. Rather than using the frequency vs DC current in the autonomous regime to extract N, one can now extract from frequency and power in the locking-range a coupling factor which is N. The method has the advantage to extract a *local* non-linearity, i.e. the derivative $d\omega/dp$ for a given DC current [1].

Fig. III.4 shows the comparison between the extraction of N in the free-running regime and in the synchronized regime at $2f$. There is a 4% difference for the value of N between the two methods of extraction.

1. In KTS formalism, the non-linearity N does not depend on the power p, so N is defined globally. However, experiments show that in some cases the non-linearity N depends on the applied DC current, which requires then a "local" definition of the non-linearity N, i.e. $N(I_{DC})$. See for example f vs I characteristics in Fig. 3 from [35]

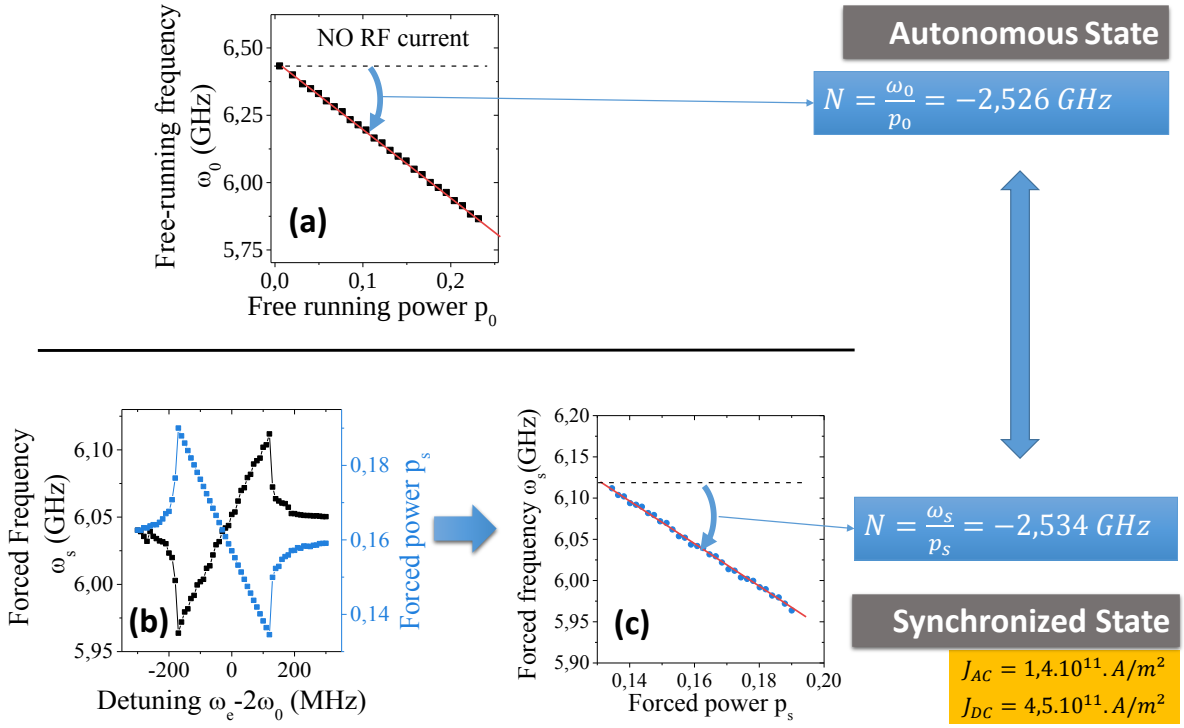

Figure III.4 – Extraction of the non-linearity N from macrospin simulations. (a) Extraction of N from Frequency ω_0 vs Power p_0 in free-running regime. (a) is obtained from f vs J_{DC} characteristics (not shown). (b),(c) Synchronized state at $2f$. (b) Forced frequency ω_s (black) and power p_s(blue) vs. detuning. (c) Extraction of N from ω_s vs p_s dependence obtained from (b).

To conclude with this section on power and frequency in the synchronized state, we remind the reader of the essential features covered :

• **Verification of the model at** $2f$. Macrospin simulations can provide not only the STO frequency in synchronized state at f and $2f$, but the power as well. This allows us to monitor frequency and amplitude changes simultaneously in the locking-range, and stress the interplay between frequency and amplitude adjustment. In particular, the model provides us a simple analytic expression for power deviations which agrees very well with macrospin results, both qualitatively and quantitatively. In accordance with the model, synchronous power and frequency at $2f$ provide another way to extract the non-linearity factor N.

• **Comparison** f **vs** $2f$. Looking at frequency and power variations in the locking-range, there is no obvious qualitative difference between synchronization at f and $2f$. However this partial analysis still showed quantitative differences, such as a locking-range of one order of magnitude higher at $2f$ than at f in our case.

III.3 Analysis of the phase difference

In the second chapter of this manuscript, we introduced synchronization in a general context where we stated that in synchronous state, *the phase difference is constant*, which is why the term "phase-locking" is often used instead of synchronization. In our case where thermal fluctuations are absent, we note that it is allowed to say that in synchronized state, the phase-difference is not only bounded but *constant with time*.

In this section, we will investigate with the help of macrospin simulations the behavior of the phase difference (or slow-phase) in the synchronized state at f and $2f$. To this end, we have extracted the instantaneous phase of the STO from macrospin simulations, which will be compared to that of the driving RF current to obtain the phase difference $\psi(t)$, where $\psi(t) = \phi(t) + \phi_e(t)$ at f, and $\psi(t) = 2\phi(t) + \phi_e(t)$ at $2f$. We will restrict ourselves to the study of the phase difference in the locking-range only where the phase is constant. Just outside the locking-range, the phase-difference is not constant anymore but alternates moments when the phase varies slowly with time and rapid phase-slips [67], which corresponds to a quasi periodic motion of the STO.

To ensure the phase difference is constant with time, we computed its variance that we plotted with respect to the detuning. Fig. III.5 shows macrospin simulation results for the phase difference in the the locking-range. In Fig. III.5(a), the phase-difference variance is plotted alongside the forced STO frequency and as we can see in the locking-range the variance is equal to zero, which confirms the phase-locking effect. In parallel the time-dependence of the phase difference is presented inside and outside the locking-range in Fig. III.5(b).

III.3.1 Phase-difference in the locking-range

We start by looking at the evolution of the phase-difference at $2f$ in the locking-range. Macrospin simulation results are shown in Fig. III.6 for a fixed DC current $J_{DC} = 5.6x10^{11}\mathrm{A/m^2}$ and four values of RF current. Fig. III.6(a) shows the total evolution in the locking-range, and we see that the phase difference is varying in the interval $[0, \pi]$, reaching approximately $\pi/2$ in the middle of the locking-range. As a matter of fact, the phase-difference at $2f$ is entirely determined by the ratio $\delta\omega_e/\Delta\Omega$ (see Eq. II.67 or schematics in Fig. II.9).

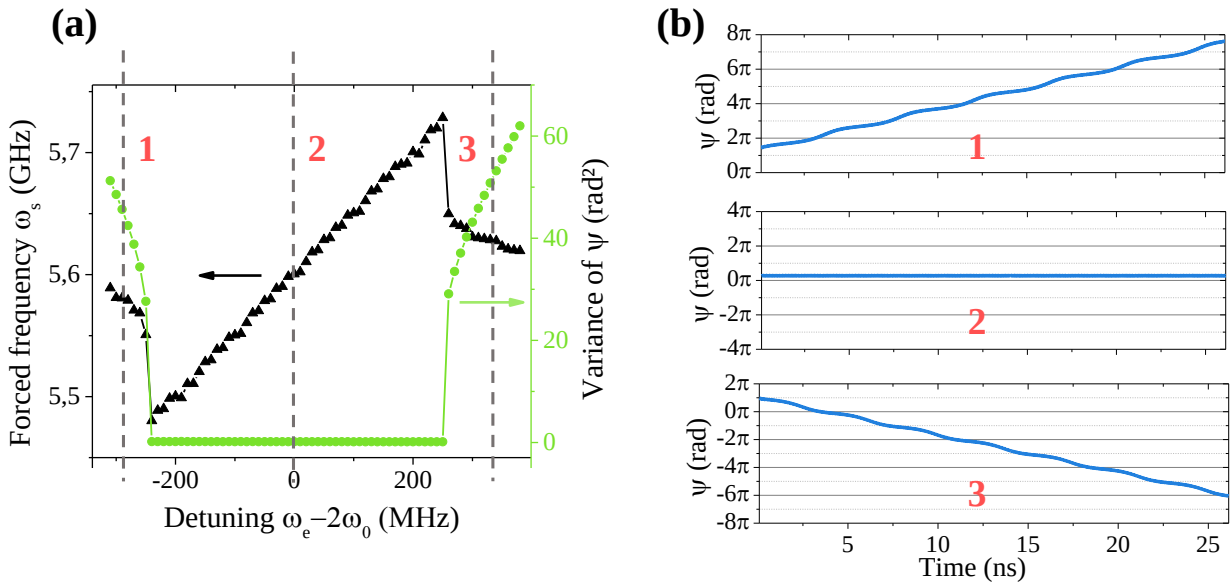

Figure III.5 – From macrospin simulations. (a) At $2f$, variance of the phase difference ψ (green) and STO frequency (black) as a function of the detuning for $J_{DC} = 5,4.10^{11}$ A/m^2 and $\epsilon = 0.24$. In the locking-range, the phase-difference is constant with time, which gives a variance of 0. (b) Time-dependence of the phase-difference outside the left boundary (1) in the center (2) and outside the right boundary (3) of the locking-range in (a)

Our simulations show however that there are some discrepancies with the model at $2f$. First we see that the analytic formula provides a better fit for positive detuning than negative detuning(Fig. III.6). Secondly, instead of having $\psi_0 = \pi/2$ for the additional phase-difference ψ_0, simulations give a slightly higher value of $\pi/2 + \pi/20$rad. A possible explanation for these discrepancies is that some asymmetry has been introduced in the simulations due to the tilting of the polarizer (15 degrees from $\hat{\mathbf{e}}_x$). As a consequence the geometry of the trajectory does not obey perfect axial symmetry with $\hat{\mathbf{e}}_x$, which can be translated into asymmetric synchronization properties in the locking-range.

To validate further our analytical results for the phase-difference at $2f$, we will extract the locking-range from the evolution of the variance of the phase-difference as a function of the detuning $\delta\omega_e$ with plots such as Fig. III.6. While the next section is dedicated to a detailed analysis of the evolution of the locking-range at f and $2f$, we show here partial results for the locking-range at $2f$ as a function of the current ratio ϵ in order to validate our method.

Eq. II.67 provides the analytic expression for the phase-difference as a function of the ratio of the detuning on the locking-range $\delta\omega_e/\Delta\Omega$. Using this formula, we can extract the locking-range using the ψ versus ω_e dependence (e.g. Fig. III.6), where $\delta\omega_e$ is the variable and $\Delta\Omega$ the fitting parameter. Fig. III.7 shows the results of such an extraction of the locking-range, compared with the manual method of extraction from classic detuning plots such as in Fig. III.2. As we can see, at $2f$ the phase-difference allows one to extract the locking-range with good accuracy in this case.

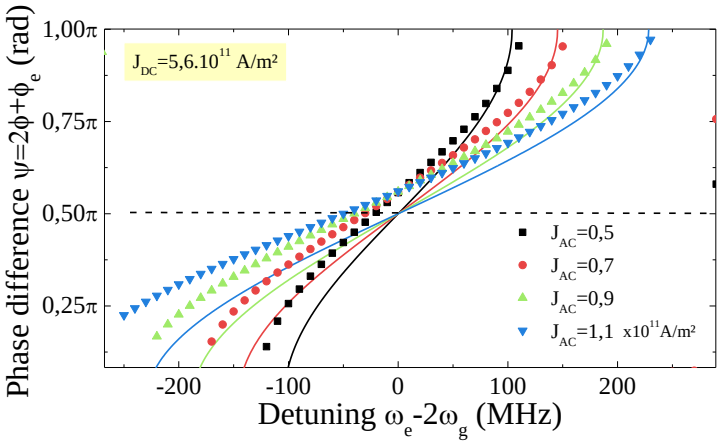

Figure III.6 – Phase difference in the locking-range at $2f$ as a function of the detuning for several RF current amplitudes. Dots (simulation), lines (analytic formula II.67). Simulations indicate a small shift of the additional phase-difference ψ_0 from $\pi/2$ (theory)

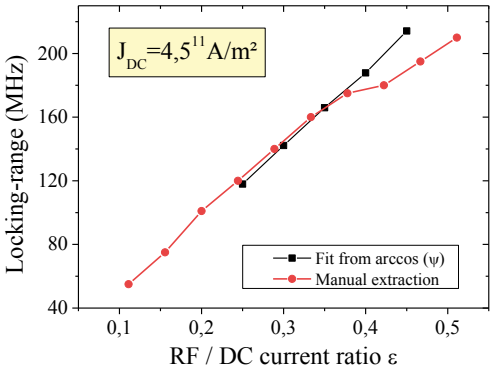

Figure III.7 – Extraction of the locking-range at $2f$ from the phase-difference. (black) Fit from the analytic formula II.67 applied to ψ vs $\delta\omega$ plots. (red) Manual extraction of the locking-range.

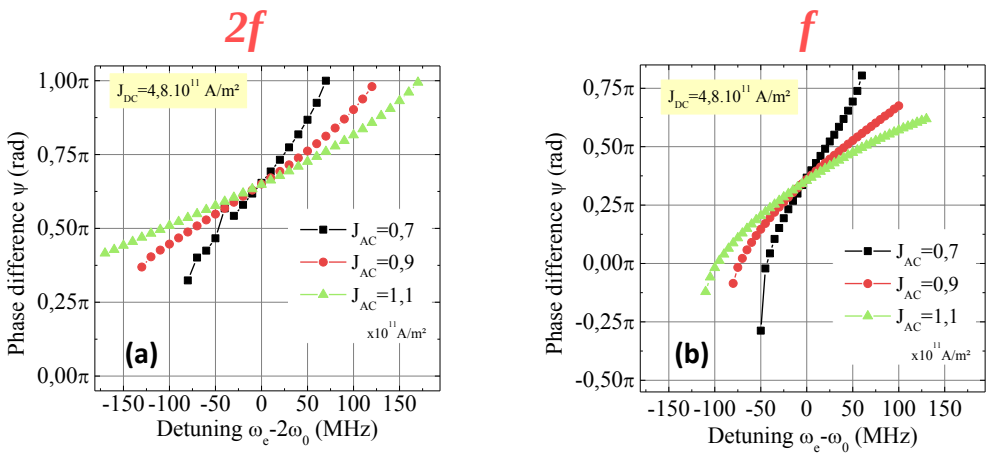

Figure III.8 – Comparison of the phase difference in the locking range for a DC current density of $J_DC = 4,8.10^{11}\mathrm{A/m^2}$ as the AC current increases. (a) $2f$, $\psi = \phi_e + 2\phi$ (b) f, $\psi = \phi_e + \phi$. While the locking-range is comparable is both cases, the phase difference does not behave in the same fashion.

Let us now compare the phase-difference at f and $2f$. From the previous analysis of the simulation results on frequency and power in the synchronized state, there did not seem to be an important qualitative difference in behavior between synchronization at f and $2f$ for a given DC current. Fig. III.8 shows side by side the evolution of the phase difference ψ at f and $2f$ in the locking range. The DC current density has been chosen in such a way that locking-ranges at f and $2f$ that are approximately equal (here roughly $50, 100$ and 150 MHz for each value of the AC current) so as to obtain the same number of points for f and $2f$. We note that the DC current is close to the critical current so the precession amplitude is rather small.

In both cases, f and $2f$, there is a notable asymmetry between positive and negative detuning in the behavior of the phase-difference. According to the analytic formulae II.67 and II.76, at both f and $2f$, the phase difference as a function of the detuning obeys a dependence of an inverse trigonometric function. In that case, the behavior should be symmetric with respect to the zero detuning point.

At $2f$, for the three values of the AC current, we see that there is an important discrepancy with the model due to asymmetry. Indeed, the phase difference is expected to go from 0 to π in the locking range, reaching $\pi/2$ in the middle of the locking-range. As we can see, at the right extremity of the locking-range the phase-difference reaches π as expected, but at the left extremity the phase-difference hardly reaches the minimum of $\pi/4$ where it should go to zero.

At f, the asymmetry is also visible. Compared to $2f$, it is also clear that in the locking-range, the phase-difference takes specific values. For example, if we take the black curve, between f and $2f$ the overall trend is the same. Roughly, both phases at f and $2f$ cover in the locking-range an interval a length of π. It corresponds to the same AC current, the same DC current. However the additional-phase difference ψ_0 is not the same ($\pi/2+\pi/10$ at f, and $\pi/2-\pi/10$ at $2f$) and it translates into a vertical shift of the data.

Another interesting observation is that when the AC current is increased, for both f and $2f$ we see not only the expected quantitative changes in the phase-difference (due to the increase of the locking-range) but also *qualitative changes* in the behaviour with

the detuning. For example, the asymmetry between positive and negative detuning seems to increase with ϵ. However according to the model, no qualitative change in the phase-difference is expected when the AC current amplitude changes, as long as the current ratio ϵ remains small enough (condition of weak forcing). For the maximum value of the AC current, $\epsilon = 0.2$. How can we account for this change ?

From the previous chapter we recall the starting hypothesis allowing our analytical development to be valid : in the synchronized regime at f and $2f$ the forced amplitude deviations must be much smaller than the steady-state amplitude. Translated mathematically, it gives $\delta p_s/p_0 \ll 1$.

As a matter of fact, at $2f$ (Eq. II.61), the relative power variation $\delta p_s/p_0$ depends almost exclusively on ϵ (and evidently on ψ) so it is sufficient that $\epsilon \ll 1$ to ensure that $\delta p_s/p_0 \ll 1$ [2]. Nevertheless, at f, having $\epsilon << 1$ *does not* certify that the condition $\delta p_s/p_0 << 1$ is fulfilled. Looking at Eq. II.74, ϵ but also other STO parameters are involved in the amplitude deviations. We can anticipate that when the amplitude p_0 is small, the denominator of Eq. II.74 vanishes due to the product of Γ_p by $\sqrt{p_0}$, which in turn will make the relative power variation go to infinity, even for extremely small values of ϵ. Even more simply, the formula is invalid for $p_0 = 0$.

To sum up, the condition $\delta p_s/p_0 \ll 1$ sets the domain of validity of the model at f and $2f$. Especially for synchronization at f and low amplitude, this condition may not be respected and the analytic expressions obtained will not describe our results accurately. In that case, we expect that undesirable effects related to strong forcing arise such in the behavior of the phase difference with the RF current amplitude, *qualitative changes* with ϵ.

III.3.2 Additional phase-difference

We have analyzed the behavior of the phase-difference as a function of the detuning, in the locking-range for two values of the DC current, corresponding to small and important precession angles. We saw important qualitative and quantitative differences between f and $2f$ that were predicted by the model. However, while the model is in good agreement with the macrospin data at $2f$ (see e.g. for $J_{DC} = 5, 6.10^{11}\mathrm{A/m^2}$), only limited agreement is reached when the oscillation amplitude is small, in particular at f.

This underlines the fact that synchronization properties depend strongly on the oscillation amplitude, and that it is required that we explore a little further the role of oscillation amplitude on the phase difference behavior. To do so, we will look at the additional phase-difference ψ_0 (i.e. the phase-difference at zero detuning) and follow its evolution with respect to the autonomous oscillation amplitude, p_0. This is being performed by varying the DC current.

We recall that we have obtained two different analytic expressions for the additional phase-difference at f and $2f$. At $2f$, $\psi_0 = \pi/2$ and at f, $\psi_0 = -\arctan(\nu(1 - 6p_0))$. While at $2f$, the additional phase-difference does not depend on the amplitude, at f the dependence with p_0 is more complex. In [83, 90], only a "zero order" ψ_0 is expressed, i.e. $\psi_0 = \arctan(\nu)$ and the dependence in p_0 is ignored [3]. On the contrary, our derivation takes into account the first order contribution in p_0 to ψ_0 (Eq. II.78), and in our range of

2. Eq. II.61 also features the prefactor λ, which can slightly increase the ratio $\delta p_s/p_0$ when the DC current is close to the critical current, regardless of ϵ.

3. While ν is generally assumed to be constant, it actually varies a little with the amplitude (Fig. III.1). However this variation is of 20% max in our range of current.

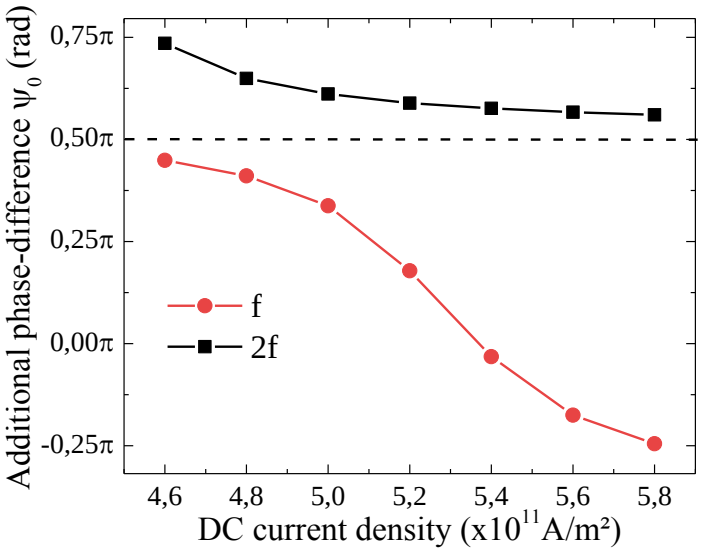

Figure III.9 – Additional phase-difference ψ_0 at f and $2f$ as a function of the DC current. At $2f$ ψ_0 is roughly constant and close to $\pi/2$, whereas at f, it decreases with DC current from $\pi/2$ to $-\pi/4$.

currents, we expect that at f ψ_0 will depend on amplitude.

To extract the additional phase difference as a function of the amplitude, we selected seven values of DC current, from 4.6 to $5.8x10^{11}$A/m^2 corresponding to steady-state amplitudes $0.06 \leq p_0 \leq 0.30$. The same values for the DC current will be used for the extraction of the locking-range for different amplitudes. Then for each value of the DC current we plotted the phase difference ψ as a function of the detuning in plots such as Fig. III.6, for three values of the AC current. We used three different values of the AC current in order to make sure that the additional phase-difference remains constant with the AC current. It can be verified on Fig. III.6, where at both f and $2f$, we see that the three sets of data cross at the same point at zero detuning. This point will provide the additional phase-difference.

Fig. III.9 shows the results of the extraction of the additional phase-difference with respect to the DC current at f and $2f$ with this method. We make a few observations. First, as expected, the additional phase-difference does not behave in the same fashion at f and $2f$. For a weak amplitude (DC current $J_{DC} = 4.6x10^{11}$A/m^2), ψ_0 at $2f$ and at f have comparable values, i.e. close to $\pi/2$. However, when the oscillation amplitude increases the additional phase-difference at f differs strongly from that at $2f$. If we take $J_{DC} = 5.8x10^{11}$A/m^2, then $\psi_0 \approx \pi/2$ at $2f$, while at f $\psi_0 \approx -\pi/4$, which makes a difference close to π. It means (in the center of the locking-range) that for *low oscillation amplitude* the driving RF current has to be put in $\pi/2$ *phase lead* with the STO for both f and $2f$ while for *high oscillation amplitude* the driving RF current remains in $\pi/2$ phase lead at $2f$ but must be put in about $\pi/2$ *phase delay* at f. Secondly, at $2f$, we see that the additional phase-difference is close to $\pi/2$, and decreases slightly from $3\pi/4$ to about $\pi/2$. This is to be compared to the theoretical prediction of $\psi_0 = \pi/2$. The agreement is satisfactory in our range of current. Lastly, at f, the additional phase-difference varies considerably in our range of currents. It corresponds to a half rotation, and decreases

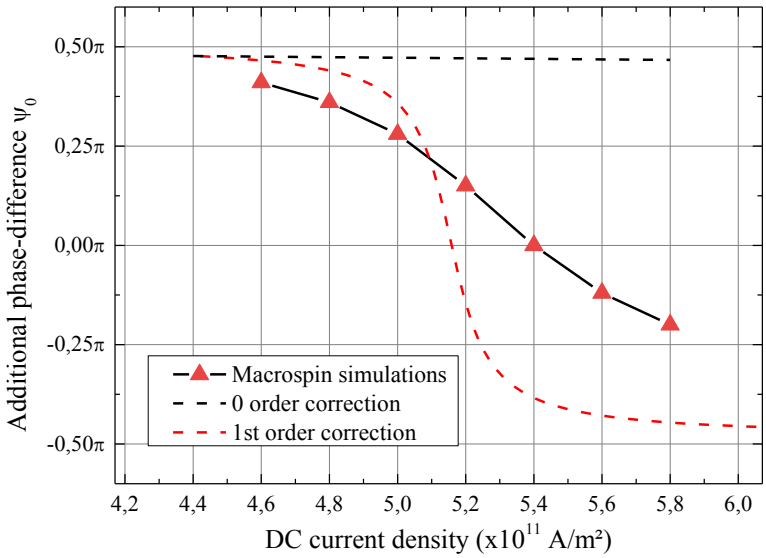

.

Figure III.10 – Additional phase-difference at f as a function of the DC current from macrospin simulations (triangles). Comparison with the analytical results in dashed lines. (black) No correction $\psi_0 = -\arctan(\nu)$; (red) Correction $\psi_0 = -\arctan(\nu(1-6p_0))$

sharply from $\pi/2$ to almost $-\pi/2$. This is an important result which was not predicted in previous cases. In particular, when one looks at the formula $\psi_0 = -\arctan(\nu)$ [83], no significant dependence of the additional phase-difference on amplitude is expected. This decrease can be explained by the introduction of a first order term in p_0 in the additional phase-difference.

Fig. III.10 brings together the analytic formulae and the macrospin results for the additional phase-difference at f. In its simplest form, the additional phase-difference is given by $\psi_0 = -\arctan(\nu)$. Since $-\nu \approx 12 \gg 1$, then ψ_0 should be very close to $\pi/2$. The calculation gives the black dashed line. At very low amplitude it conforms with the data, but quickly deviates away from the analytic formula.

The first order correction (Eq. II.78) introduces a prefactor of $1-6p_0$. A more satisfying agreement is reached when the first order correction is taken into account. It explains the following features which are not justified at the zeroth order, namely the overall qualitative behavior of the additional phase-difference with p_0, and the sign change.

When $p_0 = 1/6$, which corresponds to $J_{AC} \approx 5.1x10^{11}\mathrm{A/m^2}$, we get $\psi_0 = 0$. This is seen on Fig. III.10 when the dashed red lines crosses the $\psi_0 = 0$ axis. Simulations still indicate some discrepancies with the model, as the red line decreases much more sharply than the macrospin data. In order to enhance the accuracy, second order correction in p_0 is probably required.

It is actually important to determine the additional phase-difference as a function of the amplitude for two reasons.

First, as it was advanced in Ref. [90], if one wants to synchronize several STOs via electrical coupling, it is necessary to take into account the additional phase difference (called intrinsic phase-shift) in order to fully synchronize the array. Now if the amplitude

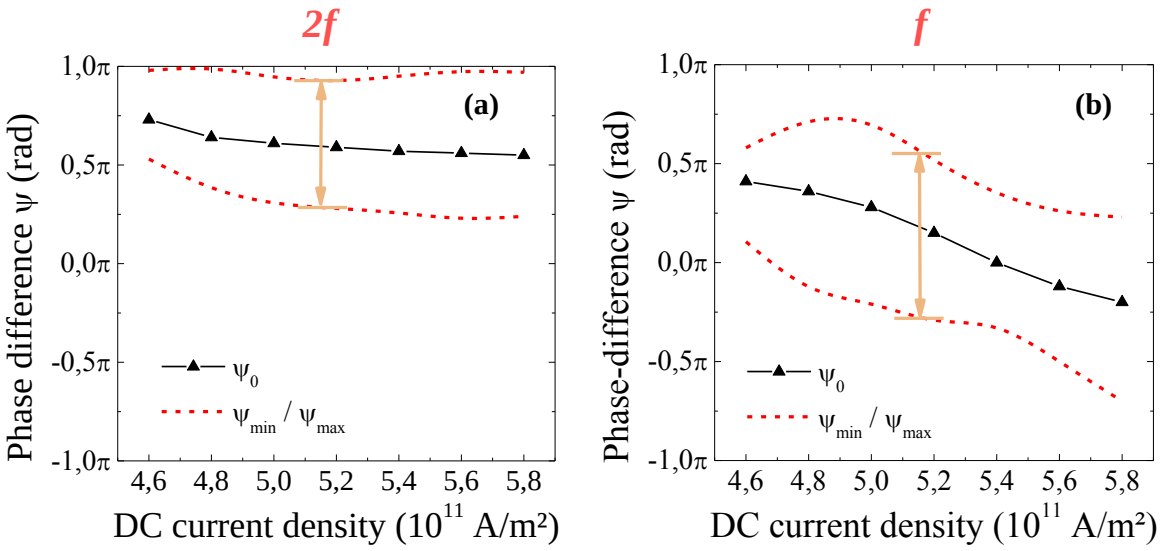

Figure III.11 – Phase-difference in the locking-range as a function of the DC current density from macrospin simulations. (a) Phase-difference at $2f$. (b) Phase-difference at f. Black triangles indicate ψ_0, and the two red dotted lines correspond to the extrema for ψ at the boundaries of the locking-range. Extrema have been evaluated for AC/DC current ratio of $\epsilon \approx 0.2$.

acts on the additional phase-difference, then it needs to be considered for the circuit design [4]. Second, and this remark is valid for f, the initial phase-difference is directly linked with the enhancement of the locking-range due to the non-linearity. As it will be examined in the next section, it is rather difficult to obtain a good agreement between the analytic formula and the simulation results for the locking-range at f, and the difficulty comes from the "non-linearity enhanced part" of the locking-range expression II.77 [5]. It is determinant to obtain the locking-range with good accuracy if one wants to realize efficient electrical synchronization, therefore solid predictions for the additional phase-difference as a function of the amplitude are certainly valuable.

To close the discussion on the phase difference in the synchronized regime, we compare the overall behavior of the phase-difference as a function of the amplitude from macrospin simulations.

Fig. III.11 shows the phase-difference at $2f$ (a) and f (b) as a function of the DC current density. While the evolution of ψ_0 with amplitude has already been talked about, here we focus instead on the manner the locking-range changes with amplitude using the phase-difference.

As we already noticed from Fig. III.8, simulations seem to indicate that the phase-difference does not actually cover an interval of the type $[\psi_0 - \pi/2, \psi_0 + \pi/2]$ throughout the locking-range, as it is predicted from the phase-difference equation. It covers usually a little less than interval of π. This seems to be the case for both f and $2f$,where Fig. III.11 shows that the interval between the two extremal values of ψ (red dotted lines) changes with the amplitude.

However it is difficult to determine precisely the interval length for ψ from simulations.

4. while the amplitude substantially acts on the additional phase-difference at f, it does not at $2f$, simplifying the problem at $2f$ (for IPP precession)

5. Indeed, the analytical calculation of the non-linear parameter ν responsible for the locking-range enhancement at f is approximate and limits the domain of validity of the formula II.77

When one examines Fig. III.8(b) and compares the left extremity of the black curve with the other two, then it looks like the resolution in frequency (x axis) is not sufficient to provide a good estimate of the phase-difference extrema. As a matter of fact, close to the extremities of the locking-range, the derivative of the phase-difference with respect to the detuning is much higher than the one in the center : in other words, at the extremities of the locking-range small variations of the detuning lead to important variations of the phase-difference.

This explains why some points for the phase-difference seem to be missing close to the extremities of the locking-range, and in simulations we probably underestimate the length of the interval of values taken by ψ. It is reasonable to suppose that with substantially higher resolution in frequency, the green and red curves from Fig. III.8(b) would reach minima of $-\pi/3$ rather than $-\pi/6$.

III.4 Synchronization regions at f and $2f$

III.4.1 Arnold tongues and coupling sensitivity at $2f$

In the last section we have focused on monitoring the evolution of important quantities in the synchronized regime such as the power, or the phase-difference *in* the locking-range. Study of the phase-difference evidenced important differences in behavior between f and $2f$, in particular we showed that the additional phase-difference remains approximately constant (close to $\pi/2$) at $2f$ with the precession amplitude, but at f it greatly changes, from $\pi/2$ to $-\pi/4$ in our range of amplitudes. Finally, macrospin simulations exhibit a good qualitative agreement with the model at both f and $2f$. However only *limited* quantitative agreement is reached for f, whereas a good quantitative agreement is reached at $2f$ for the phase-difference and the power.

Now in this section we focus on the locking-range. As we mentioned earlier, the locking-range is arguably the most important quantity to characterize in synchronization. Having predictions for the locking-range allows one to find in advance whether or not synchronization can be achieved for a given configuration. Experimentally, the locking-range is also connected with linewidth reduction via the forcing strength - as the forcing strength increases, the locking-range widens and the linewidth reduction effect is enhanced. Finally, the locking-range is the experimental quantity that is the most straightforward to extract : the first step to validate our analytical development with experiments is to extract the locking-range and confront the model with it.

Let us go back to a specific feature of the STO, the strong non-linearity, or phase-amplitude coupling. Compared to other weakly non-linear oscillators, what kind of changes can we expect for the locking-range ? At $2f$ - but not at f - we showed that forced frequency and amplitude follow the same relation as in the autonomous regime, i.e. $\delta\omega_s = N\delta p_s$, which means that frequency adjustment is achieved through amplitude change, and it was confirmed by macrospin simulations. Now how does it translate in the locking-range ?

In the last chapter we provided an analytic formula II.65 for the locking-range at $2f$ as a function of the RF / DC current ratio ϵ and the precession amplitude p_0. We made the assumption that ϵ is small ensuring that the locking-range evolves *linearly* with ϵ. The precession amplitude intervenes in the locking-range expression also via a linear dependence with the frequency-shift Np_0.

Simple insight from the picture of synchronization applied to STOs can help us find back this formula.

To start, we recall from the introductory part of this manuscript that the locking-range makes up the synchronization regions, also called Arnold tongues. Arnold tongues are obtained by plotting the locking-range for different values of the forcing amplitude. In our case, the forcing amplitude is represented by the RF / DC current ratio ϵ. In the picture of synchronization in weakly non-linear oscillators, the borders of the Arnold tongue delimiting the synchronization region are straight lines, or in other words the locking-range increases linearly with ϵ [6]. This is an intuitive and typical result for synchronization to a weak external force, and is found in analytical formulae for the locking-range at both f and $2f$.

From this observation we can deduce an interesting physical quantity. Whenever borders of an Arnold tongue are straight, we can define the *coupling sensitivity* from the *opening* of a tongue. The opening of the tongue indicates how wide will be the synchronization region, and whether or not synchronization is realizable. It has the advantage of not depending on the forcing strength ϵ, which makes it a general measure of how efficiently the STO can couple to the external force in a given configuration. Mathematically, it the derivative of the locking-range with respect to the forcing amplitude ϵ.

As a consequence, the coupling sensitivity at $2f$ can be deduced from the dependence of the locking-range on ϵ. Using expression II.65, we obtain $d\Omega/d\epsilon \approx Np_0$ (using $\lambda \approx 1$). It means that in our configuration the coupling sensitivity is equal the frequency shift in the autonomous regime Np_0. This a very valuable property of synchronization at $2f$ which allows one to predict the synchronization range from experimental f vs I characteristics knowing that $\omega_0(I) - \omega_r = Np_0$

It can be explained as follows. Let us consider the mechanism of frequency adjustment at $2f$. We mentioned that frequency adjustment is performed *only* through amplitude change ($\delta\omega_s = N\delta p_s$). So it means that amplitude regulates the synchronization process at $2f$, in other terms if one increases the steady-state amplitude, the available window for frequency adjustment increases as well. The obvious limiting factor for amplitude change is the downwards limit, since one cannot go below zero amplitude. Then, starting with a precession amplitude close to zero gives almost no room for amplitude adjustment : the coupling sensitivity vanishes. On the other hand, starting with an important precession amplitude gives a lot of room for amplitude adjustment : as a consequence, the coupling sensitivity is much enhanced.

This relation between the frequency shift in the autonomous regime and the coupling sensitivity at $2f$ is schematically illustrated in Fig. III.12. Fig. III.12(a) shows the frequency-shift versus amplitude in the autonomous regime, and Fig. III.12(b) represents the synchronization regions for different precession amplitudes.

III.4.2 Locking-range at f and $2f$

Methods

Now that we provided the physical arguments to explain why coupling sensitivity and frequency shift in autonomous regime are linked, we will check the level of agreement between the analytical formula and the macrospin simulations results. Furthermore, we will compare the coupling sensitivity at f and $2f$ in our configuration.

6. In the limit where ϵ remains small.

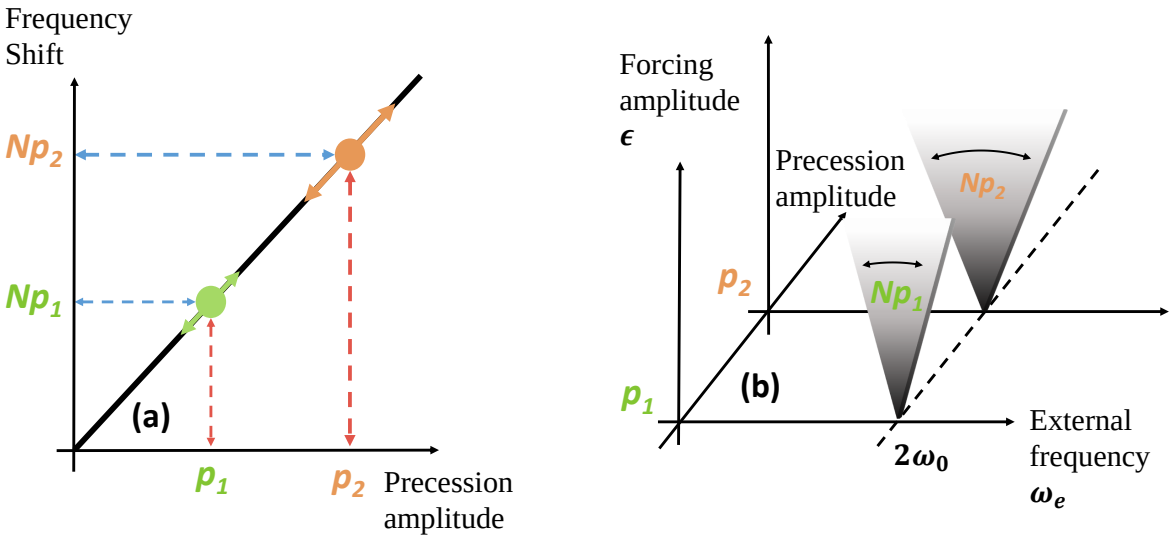

Figure III.12 – Schematic representation of the frequency / amplitude adjustment process for synchronization at $2f$. (a) Non-linearity in autonomous regime. Varying the DC current changes the precession amplitude, which in turn shifts the generation frequency by a factor Np. (b) Arnold Tongues for synchronization at $2f$ for different precession amplitudes. As the amplitude is increased, the available window for amplitude adjustment increases too. Due to the STO non-linearity (a), it translates into an enhanced window for frequency adjustment to the driving force, and consequently the synchronization region widens. It gives a coupling sensitivity that is equal the frequency-shift Np.

In order to evaluate the role played by the precession amplitude on the synchronization properties, we remember that the quantity of interest for us is more the coupling sensitivity than the locking-range itself. However the coupling-sensitivity cannot be extracted directly from macrospin simulations, but the locking-range can be obtained from detuning plots.

So extracting the coupling sensitivity follows the same procedure as building Arnold Tongues : First a precession amplitude for the STO is chosen (which corresponds to setting the DC current), and then the locking-range is extracted for several forcing amplitudes (corresponding to RF / DC current ratios ϵ). In the limit of small forcing, the locking-range should depend linearly on ϵ, which allows one to obtain the coupling sensitivity from the slope.

To summarize, our study on the coupling sensitivity (and the verification of the analytical predictions) requires macrospin simulations to be run in a configuration where the system fulfills the four following conditions :

- High ellipticity
- Coupling at f and $2f$ allowed
- Moderate precession amplitudes
- Weak forcing

The first two conditions are satisfied from the magnetic configuration of the system at zero amplitude (i.e. without DC or RF current). The applied field has been set in order to make sure that is gives important ellipticity (see Fig. II.5), and the polarizer has been tilted in plane to allow for synchronization at f.

From this configuration, moderate precession amplitudes and weak forcing can be achieved by choosing an appropriate couple of values of the RF and DC current.

To conduct this study, we picked seven values of the DC current density from 4.6 to $5.8x10^{11}\mathrm{A/m^2}$ corresponding to moderate precession amplitudes $p_0 < 0.3$. Then for each DC current, the RF current amplitude was varied from 0.5 to $2.1x10^{11}\mathrm{A/m^2}$ in steps of $0.2x10^{11}\mathrm{A/m^2}$ for a total of nine points.

Once the DC and the RF amplitude are set, the locking-range is extracted for a given couple (J_{DC}, ϵ). To do so, the RF current frequency is swept close to ω_0 or $2\omega_0$ by steps of 5 or 10 MHz depending on the width of the locking-range. Then, for each frequency of the RF current, the time-dependence of the phase difference ψ is extracted in order to obtain the locking-range. If the variance of the phase difference is equal to zero, it corresponds to a point inside the locking-range. Here, the locking-range is read graphically from the variance of the phase difference versus detuning plots such as the black curve in Fig. III.5.

Locking-range vs forcing amplitude

We first verify that in our range of amplitudes, the locking-range has a linear dependence with ϵ in accordance with the model, whether it is at f or $2f$. Fig. III.13 shows the results from the extraction of the locking-range from the method described above. Here, $0 \leq \epsilon \leq 0.4$, so the RF / DC current ratio remains small enough.

Let us examine the locking-range at $2f$ (Fig. III.13(a)). We see that it does increase linearly with ϵ in the whole range of DC currents. By doing a linear interpolation for each DC current, one also confirms that each set of data goes through the origin, so that there is *no threshold* above which synchronization is enabled [7]. In addition, the slope increases

7. Recent works have evidenced a threshold in the case of synchronization at $2f$ of a vortex-based

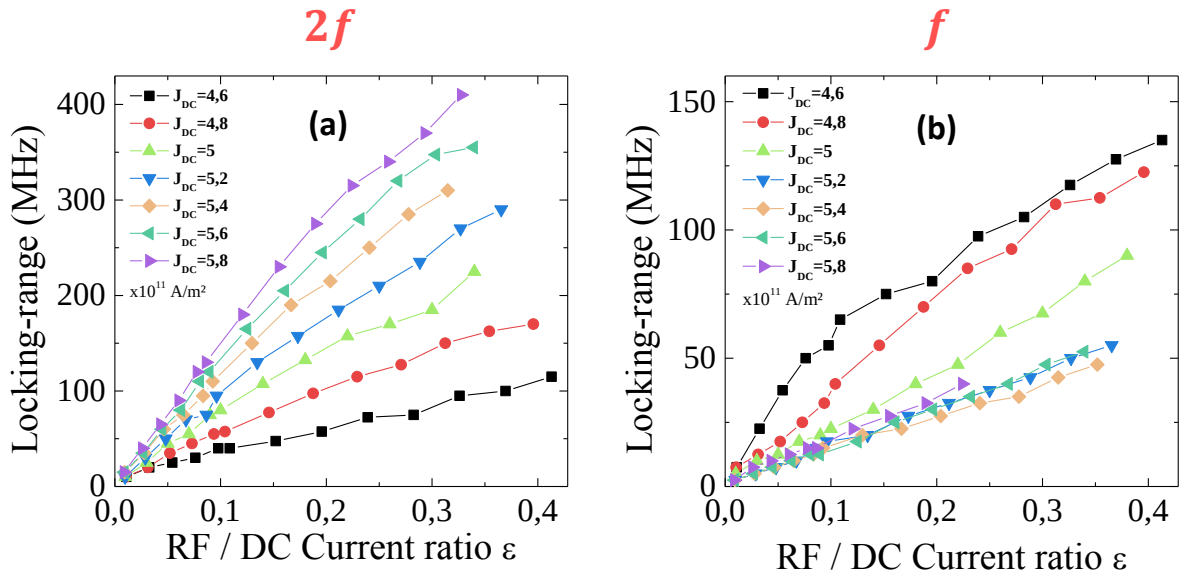

Figure III.13 – Locking-range versus current ratio ϵ extracted from macrospin simulations. Each color corresponds to one DC current density, i.e. a starting precession amplitude. (a) Locking range at $2f$. (b) Locking-range at f. Except for $J_{DC} = 4.6x10^{11}\mathrm{A/m^2}$, the locking-range increases linearly with ϵ.

along with the DC current, showing that the coupling sensitivity increases with the DC current as well.

The locking-range at f (Fig. III.13(b)) also increases linearly with ϵ for *almost* the whole range of DC current. Indeed, for $J_{DC} = 4.6x10^{11}$ A/m^2, we can see that the locking-range increases linearly with ϵ up to $\epsilon = 0.1$, and then the slope is reduced up to $\epsilon = 0.4$. This discrepancy with the model at f close to the critical current was already observed during the analysis of the phase-difference at f. We offer the same explanation as before : at f and close to the critical current, the condition $\delta p_s/p_0$ is much harder to fulfill, and if this condition is not satisfied, then qualitative agreement with the model is compromised. Finally, we also see that, in contrast with synchronization at $2f$, the overall slope decreases with the DC current up to $J_{DC} = 5.2x10^{11}$ A/m^2 then roughly stabilizes.

Comparison of the coupling sensitivity

The coupling sensitivity is obtained from the evolution of the locking-range with the forcing amplitude ϵ as in Fig. III.13. Each curve corresponding to a particular precession amplitude, the coupling sensitivity is extracted from the derivative of the locking-range range with respect to ϵ. We have verified that the locking-range evolves linearly with ϵ, or in other terms the borders of the Arnold tongues are straight. As a consequence, the coupling sensitivity is simply the slope and does not depend on ϵ, so that the quantity we extract is only a function of the STO parameters, and not the forcing amplitude. This reasoning is valid in the limit of weak forcing. At strong forcing, the coupling sensitivity most likely depends on ϵ.

STO by RF current [57, 6]. However in our case, the absence of thermal fluctuations and the DC current being over the critical current give a simple situation where no threshold is expected.

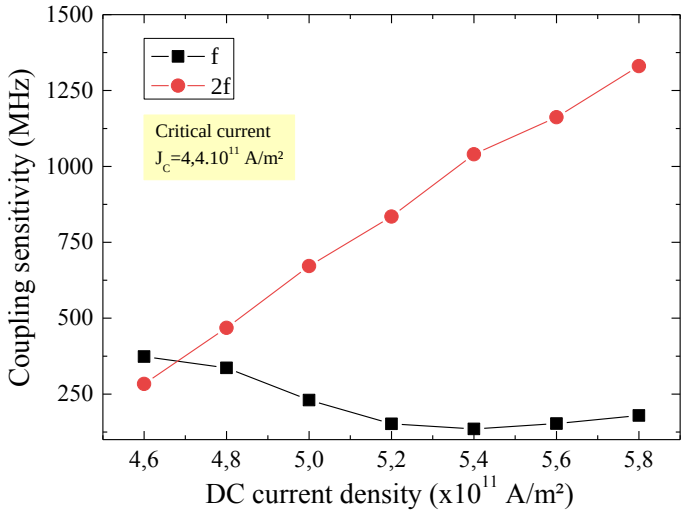

Figure III.14 – Coupling sensitivity of an IPP STO to a RF current at f and $2f$ versus DC current (precession amplitude). (red) $2f$ synchronization (black) f synchronization. Coupling sensitivity evolve in opposite fashion with precession amplitude between f and $2f$.

Results of the extraction of the coupling sensitivity from Fig. III.13(a) and (b) are shown in Fig. III.14. This comparison of the coupling sensitivity between f and $2f$ provides arguably the most remarkable evidence that synchronization at f and $2f$ obey two separate mechanisms. Indeed, as we can see on Fig. III.14, the evolution of the coupling sensitivity with precession amplitude enables us to discriminate between synchronization at f and $2f$: at $2f$, the coupling sensitivity *increases* with the precession amplitude (starts at 250MHz for $J_{DC} = 4.6x10^{11}\mathrm{A/m^2}$ and reaches 1300 MHz for $J_{DC} = 5.8x10^{11}\mathrm{A/m^2}$), whereas at f it *decreases* then lightly increases with the precession amplitude (starts at 400MHz for $J_{DC} = 4.6x10^{11}\mathrm{A/m^2}$ and reaches 150 MHz for $J_{DC} = 5.8x10^{11}\mathrm{A/m^2}$).

Moreover, this graph indicates us that in order to tell if a given configuration favors synchronization at $2f$ or at f, then the initial precession amplitude must absolutely be taken into account. Otherwise, one may reach contradictory results. Let us take the example of two people comparing coupling sensitivities. Measuring at *low* precession amplitudes (say $J_{DC} = 4.6x10^{11}\mathrm{A/m^2}$), the first person concludes that for this STO configuration synchronization at f and $2f$ are equally favored. However the second person measured coupling sensitivities at at *high* oscillation amplitude (say $J_{DC} = 5.8x10^{11}\mathrm{A/m^2}$) and comes to the different conclusion that the coupling sensitivity is about 6 times more important at $2f$ than at f, and synchronization at $2f$ is largely favored.

Agreement with the model

We start the verification of the model with coupling sensitivity at $2f$. According to the analytical formula II.65 the coupling sensitivity equals the frequency shift in autonomous regime (in the limit where $\lambda = 1$). Fig. III.15 shows the comparison with the model for both cases at $2f$ (a) and f (b).

At $2f$, the macrospin results for the coupling sensitivity have been compared with the analytic formula II.65 and the frequency shift $\omega_0(J_D C) - \omega_r$, obtained from macrospin simulations in autonomous regime (as in Fig. III.1). We note that the analytic formula

differs from the frequency shift by the factor λ explaining the small shift between the blue and black solid lines in Fig. III.15(a). As we can see, there is a very good quantitative agreement between the coupling sensitivity and the frequency shift with less than a 10% error margin in the whole range of DC currents.

It shows that the frequency shift in autonomous regime provides an excellent estimate (in IPP regime) for the coupling sensitivity at $2f$. This is an important point of interest, because we expect that this type of relation can be observed for synchronization in other non-linear systems : the frequency shift as well as the coupling sensitivity are quantities that can be defined in the general case. It also proves the KTS model provides a reliable formalism to analyze synchronization properties. Moreover, the frequency shift is straightforward to extract in experiments, since one only requires the f vs I characteristics. Then one has to compare the frequency shift with the coupling sensitivity to validate the model experimentally.

However, the quality of the agreement with the model at f is not as good as at $2f$. Fig III.15(b) shows the coupling sensitivity extracted from macrospin simulations and its comparison with the analytic formula II.77, with or without a first order correction in p. The dark blue curve corresponds the analytic formula without the correction, where the non-linearity enhancement is given by ν only. This form has been used to fit experimental results at f in [22, 51] and at $2f$ in [19].

We remark that the agreement is better in the situation where the first order correction is taken into account (in light blue). In particular, the correction accounts qualitatively for the increase of the coupling sensitivity at high oscillation amplitudes, when without correction the coupling sensitivity continuously decreases in a $1/\sqrt{p_0}$ fashion. The quantitative agreement is also improved. Indeed, without the correction, the coupling sensitivity is overestimated all along by at least a factor of 2, while the correction gives a much closer approximation to macrospin results.

As we mentioned in the previous section on the phase-difference, the evolution of the additional phase difference ψ_0 at f with the precession amplitude is in limited agreement with the model, and the agreement is better when the correction is taken into account. The quality of the agreement for the coupling sensitivity here can be directly related to the one of the additional-phase difference. Indeed, since the "enhancement" of the coupling sensitivity ($\sqrt{1+(\nu(1-6p_0))^2}$) and the additional phase difference ψ_0 are linked, it is no surprise that the correction that yields a better estimate of the phase-difference ψ_0 also estimates the coupling sensitivity with better precision.

We conclude with the remark that the analytical formula at f gives a coupling sensitivity that goes to infinity when the amplitude is zero. Close to the critical current, the formula does not give a good approximation regardless of the correction.

III.4.3 Magnetization orbits in the synchronized regime

Using oscillator formalism applied to the IPP in STOs, we managed to obtain analytic expressions for important quantities that characterize synchronization, such as the phase-difference, the forced power and frequency, and finally the locking-range and the coupling sensitivity at both f and $2f$. These quantities were then extracted from macrospin simulations and we confronted the model with the results.

Both the model and the simulations indicated that synchronization at f and $2f$ do not obey the same rules : the analysis of the analytical expressions at f and $2f$ revealed the

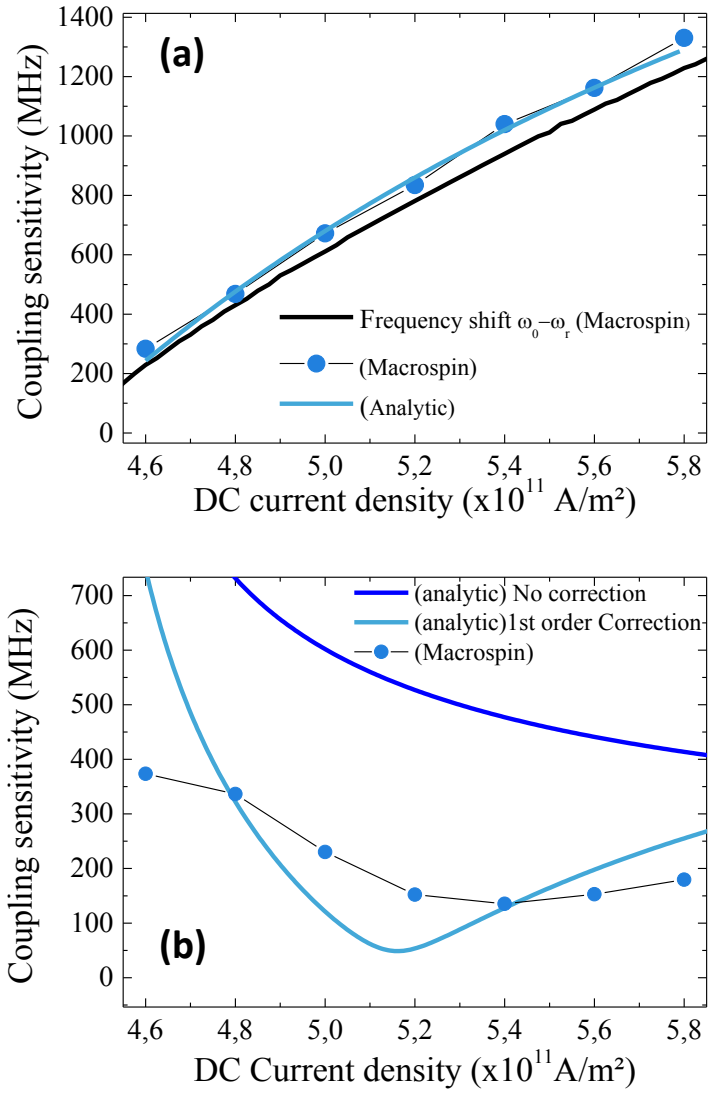

Figure III.15 – Coupling sensitivity versus DC current and comparison with the model. (a) $2f$: macrospin results (blue dots) are compared with the autonomous frequency shift ω_0-ω_r (black line) and the analytic formula II.65 without approximation $\lambda = 1$ (blue line). (b) f : macrospin results are compared with the analytical formula II.77 (i) (dark blue) without correction factor $(1 - 6p_0)$ (ii) (light blue) with correction.

differences in the mechanism of frequency and amplitude adjustment, and the simulations quantitatively brought confirmation of these differences.

However, we have not really analyzed how the frequency adjustment due to the RF current translates into modification of the magnetization orbits. From a mathematical perspective, the analytical development indicates us that the frequency adjustment in STOs is performed either through *amplitude adjustment* (see Eq. II.58 where the mixing term intervenes in the power equation and is re-injected in the phase equation via the non-linearity) or *direct phase adjustment* (see Eq. II.71 where the mixing term intervenes directly in the phase equation). At $2f$, only the first process is involved but at f, both amplitude and direct phase adjustment are involved.

We make the separation between these two processes because of the mathematical form of our equations, however the physical meaning of these process is not always straightforward. To clarify the meaning we need to translate from phase and amplitude adjustment in oscillator formalism to a modification of the motion of the magnetization.

In the case of amplitude adjustment, the translation is simple : amplitude adjustment is performed via growth or increase of the orbit amplitude along autonomous IPP orbits, which is is the synchronization mechanism at $2f$.

However, direct phase adjustment can be interpreted in several ways. Either modification of the angular velocity of the magnetization *without* modification of orbit (the magnetization speeds up or slows down its motion along the orbit, and as a consequence the STO frequency is adjusted), or modification of the orbit in such a way that the normalized amplitude p does not change - for example, tilting or stretching of the orbit.

Synchronization at f involves direct phase adjustment as well as amplitude adjustment. As a consequence, synchronization at f induces (i) a change of the procession amplitude (ii) modification of angular velocity or tilting/stretching of the precession orbit.

Fig. III.16 shows magnetization orbits from macrospin simulations in the synchronized state at f and $2f$. We chose a DC current where the coupling sensitivities at f and $2f$ are similar. In order to compare how orbits are modified at f and $2f$, and what the difference is between the two, the RF current frequency is chosen so that the forced STO frequency is the same at f and $2f$. The green curve corresponds to the center of the locking-range : at f, $\omega_e = \omega_0$ and at $2f$, $\omega_e = \omega_0$. The blue curve corresponds the right extremity of the locking-range, and the red to the left extremity.

These graphs show a few things. First, it confirms that at f and $2f$, precession orbits are modified due to the RF current, even though modifications are small. Second, it shows (see Fig. III.16(b),(d)) that synchronization at f and $2f$ do not induce the same changes in the orbits, even when the forced STO frequency is the same at the end. It shows that synchronization via a RF current offers a way to explore how several precession orbits can lead to the same precession frequency.

Besides, we can visualize how synchronization mechanisms differ between f and $2f$. At f, we remember that it is required that the polarizer is tilted in plane with respect to the easy axis, so that it produces a perpendicular component, P_y which allows for synchronization. This induces an asymmetry with respect to the easy axis $\hat{\mathbf{e}}_x$, and as a consequence the RF spin-torque does not have the same effect depending on whether m_y is positive or negative. In Fig. III.16(d) we see that, within the locking range, the trajectory is stretched further away when m_y is positive, indicating the RF spin-torque

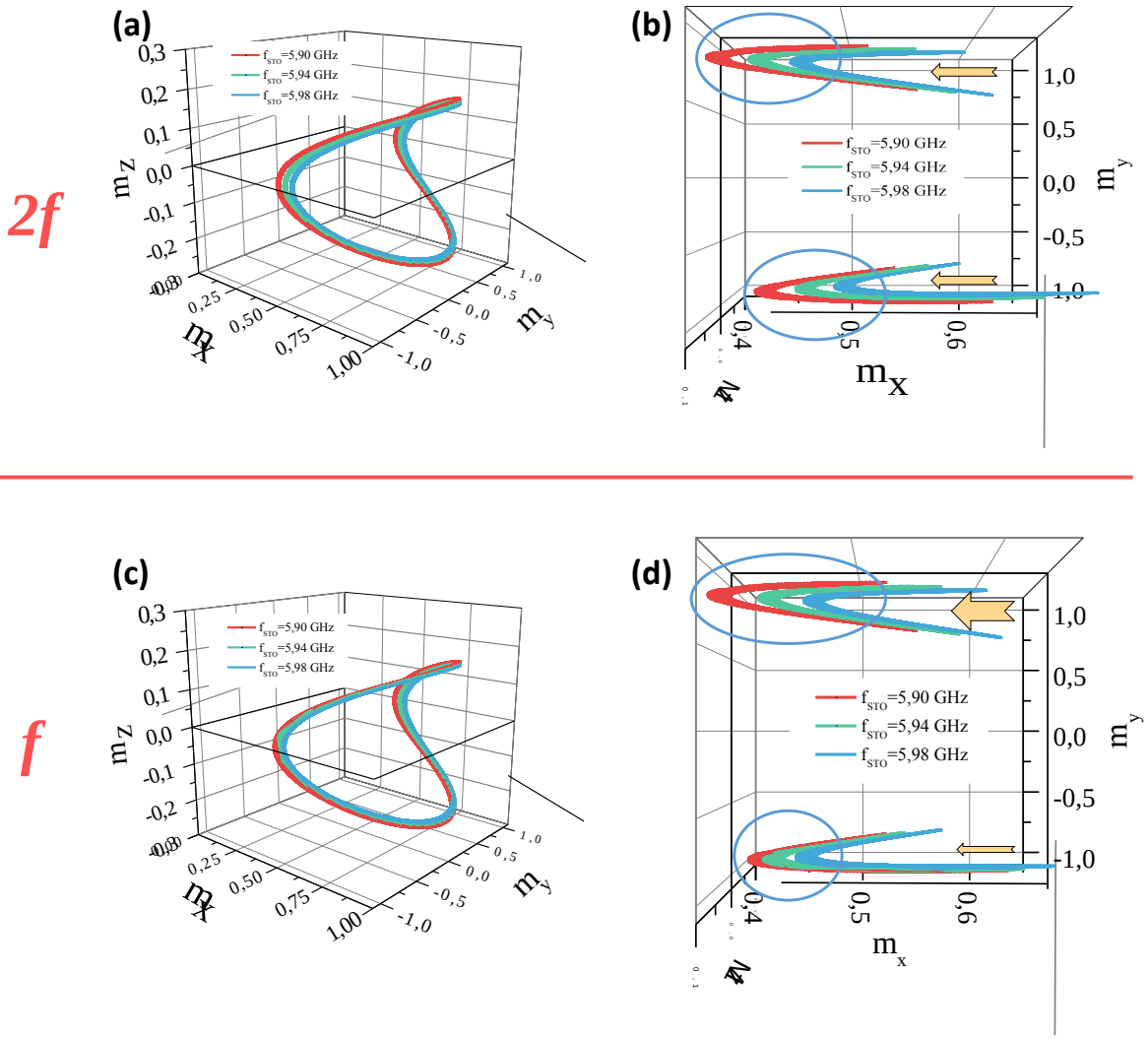

Figure III.16 – Comparison between IPP orbits in synchronized state at f and $2f$ from macrospin simulations. Free-running frequency $\omega_0/2\pi = 5.94$ GHz, $J_{DC} = 5x10^{11}\mathrm{A/m^2}$ and $J_{AC} = 1.5x10^{11}\mathrm{A/m^2}$. The RF current current frequency is swept close to $2\omega_0$ (a),(b) and then ω_0 (c),(d). (a), (c) : 3D orbits. (b), (d) : Top view of the orbits (zoom on $0.4 \leq m_x \leq 0.65$). Minor differences between f and $2f$ are observable and at $2f$, synchronization does not induce supplementary asymmetry in the orbit. However at f, the spin-torque from the RF current acts in an asymmetric manner depending on the sign of m_y : the orbit is stretched further when m_y is positive.

has more effect in that case. At $2f$, synchronization requires the longitudinal component of the polarizer P_x, which does not induce symmetry breaking with respect to $\hat{\mathbf{e}}_x$. As a consequence, the spin-torque acts in a symmetric manner on the orbit as in Fig. III.16(b).

To conclude with this Chapter on macrospin simulations in synchronized regime, let us recall the essential findings. First we ran the simulations in autonomous regime and extracted the non-linear parameters and compared it with the analytical predictions. Then as we went on to the synchronized regime, we compared the behavior between f and $2f$ of typical synchronization parameters, such as the phase difference and the locking-range. In accordance with the analytical derivation from the previous chapter, macrospin simulations confirmed that f and $2f$ synchronization are two distinct processes. The most remarkable difference comes from the evolution of the coupling sensitivity with the oscillation amplitude : at f the coupling sensitivity decreases with the amplitude while at $2f$ it increases with the amplitude, and is equal to the frequency-shift Np_0. Finally we looked at magnetization orbits in synchronized regime and visualized how synchronization translates into modification of the orbits.

Part C : Experimental Characterization

In the previous part of this manuscript we have used the auto-oscillator formalism developed by Slavin *et al.* [83] to understand synchronization mechanisms of an IPP STO to a driving RF current at f and $2f$. We extended the existing theory of synchronization at f to synchronization at $2f$ where we evidenced significant differences between the two processes. In particular, a thorough investigation of synchronization at $2f$ has shown that the non-linearity, which is intrinsically strong in the STOs, is the parameter that enables synchronization at $2f$. Frequency adjustment to the source at $2f$ is only performed through growth or reduction of the precession amplitude, which is a specific feature of synchronization at $2f$.

Macrospin simulations were performed in order to validate quantitatively the model developed. In particular, the coupling sensitivity as a function of the precession amplitude was analyzed, and a remarkably good agreement was reached between the model and the simulation at $2f$ (less than a 10% error), while corrections from the original model were required in order to obtain qualitative agreement, and acceptably good quantitative agreement.

As we remember, there is originally one important, applied motivation for the study of synchronization in STOs and for this thesis : at room temperature, one has to enhance the output signal characteristics for the STO to be competitive as frequency synthesizers. The output power has to be increased but most notably the *coherence* of the STO signal is the main issue to be addressed, which is why synchronization of an array of STOs was proposed.

Electrical synchronization (i.e. via the RF current) is the option that has been investigated during this thesis and we have been preparing in Spintec and LETI experimental STO devices based on MTJ where several nanopillars were connected in parallel via a common electrode. However, the anticipated effects of linewidth reduction and power increase due to mutual synchronization were not observed. Up to now, electrical synchronization of two or more STOs remains a challenge and no group has reported successful experiments on this matter.

In this final part of the manuscript we report the experimental results obtained not for mutual synchronization of STO, but for synchronization of a MTJ-based STO to a driving current at $2f$, or injection-locking at $2f$. Whenever possible, the experimental results will be discussed in comparison with the theory developed in the previous part. Part C is divided in two chapters.

In Chapter V we will review the techniques and methods required for the experimental characterization of injection-locked MTJ-based STOs. During this thesis I dedicated an important portion of time to optimize the deposition process of MTJs in clean room : this aspect will be discussed first. Then the subject of microwave circuit design and analysis in injection-locked STOs will be considered. Finally we will talk about processing (time and frequency domain) of the STO RF signals, and the particular techniques employed for the characterization of synchronization in STOs.

Chapter VI consists of the experimental results obtained on $2f$ injection-locked STOs at room temperature. First the self-sustained precession spectra of MTJ-based STOs in the absence of RF current will be analyzed. The coherence in synchronized state is discussed next and in particular the evolution of phase-noise. Finally, the output power, the phase-difference as well as the locking-range are extracted experimentally and will be compared to the model.

Chapter IV

Experimental methods : from materials to microwave circuits

IV.1 Tunnel junctions for STO devices

IV.1.1 Types of STO

The fabrication of a STO device can be realized in various ways. A STO fulfills a function of frequency generation, so that it generates an AC signal for the output by injecting a DC current. It relies on spin-transfer torque for the excitation and giant magnetoresistance for the readout.

The basic building block for the realization of a STO is the magnetic "sandwich" consisting of the Polarizing layer / Spacer / Free Layer stack [1]. The polarizing layer, or polarizer as well as the free layer are both ferromagnetic materials, and the spacer is non-magnetic so that the the two other layers are magnetically decoupled. The polarizer magnetization must be fixed and the free layer magnetization oscillates.

The essential part of engineering of a STO device is to realize the magnetic sandwich in such a way that the best compromise between the STT strength and the output power is reached. On top of it, if one wants to integrate a STO into a CMOS architecture, then the device must be realized on a silicon substrate, which requires the presence of a buffer layer so that the magnetic "sandwich" is realizable.

The STT effect typically requires current densities in the order of 10^{10} to 10^{12}A/m^2. It corresponds to more than 10 000 times the current density that flows into high tension lines ! These current densities can be reached only when the current flows through a very reduced area, and in practice pillars are build with a radius of 50 to 200 nm.

In order to realize the magnetic structure, there are several options available :

• **Nanopillar / Nanocontact**. The difference between the two configurations is shown in Fig. IV.1. For the nanopillar, the whole magnetic stack is etched in order to build a pillar with a typically diameter of a 100nm. In the case of a nanocontact, only the top electrode is etched. The rest of the stack remains full sheet. It is interesting to use the nanocontact geometry if one wants to study STOs coupled via spin-waves [39]. However in nanocontact the current flows in a larger area than the one determined by the contact

1. Unless an other type of current-induced excitation is used. For recent Spin-Hall oscillators, pure in-plane spin current flowing in a underlying Pt layer induces self-sustained oscillation of the above magnetic layer[53, 12]

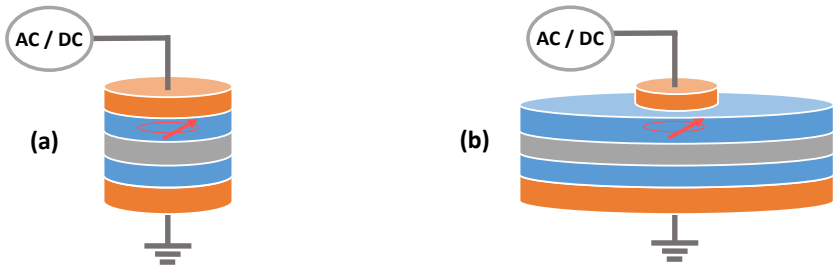

Figure IV.1 – Comparison of two types of STO structure : Nanopillar (a) and Nanocontact (b). The magnetic multilayer PL / Spacer / FL is in blue and gray, and the top and bottom contacts are in orange.

size, and typically higher currents are required to compensate for lateral current leak.

• **Magnetic Tunnel Junction / Spin Valve**. Spin valves correspond to the case where the spacer is metallic whereas in magnetic tunnel junctions the spacer is insulating. Spin valves have typically magnetoresistance ratios of only a few %. MTJs yield a much higher magnetoresistance ratio in the order of 100% but the insulating barrier gives the overall stack a much higher resistance. Engineering an MTJ needs a special expertise : typically, high TMR ratios are wanted for enhanced output signal, but at the same time the RA [2] must remain low enough so that the applied voltage is lower than the breakdown voltage at the required current densities for self-sustained precession.

• **In-plane / Out-of-plane / Vortex**. The magnetic configuration of the two layers, the PL and the FL, can be changed too. We study here the typical configuration where both the PL and FL are in-plane, uniformly magnetized. One can tilt the orientation of the magnetic layers out-of-plane. In Spintec were also prepared and analyzed in 2007 devices where the polarizer is tilted out-of-plane combined with an in-plane free layer[33] in a spin-valve structure. More recently groups have worked on the opposite structure, using a MTJ where the polarizer is in plane and the FL is stabilized out of plane using strong perpendicular anisotropy [101, 46, 45]. Finally, non-uniformly magnetized layers is also an option, and in particular the vortex configuration for the FL or the PL has given very interesting results, and an oscillator model analogous to the KTS model has been developed to account for self-sustained precession of the magnetization in vortex state [89, 6].

The type of STO that we study here is an in-plane magnetized magnetic tunnel junction in a nanopillar geometry.

IV.1.2 Materials for a MTJ-based STO

Here we will examine the complete magnetic stack that is used for a MTJ-based STO and will discuss in particular the challenge to realize low-RA MTJs, with the results obtained during the first year on full-sheet wafers deposited with the Aviza IBD at LETI.

Magnetic stack

Realizing the magnetic stack for STOs demands dedicated engineering. Fig. IV.2 shows the composition of the magnetic stack deposited in the LETI clean room on 200mm wafers.

2. RA : resistance area product. It is the product of the resistance times the area of the junction. It is expressed in $\Omega.\mu m^2$

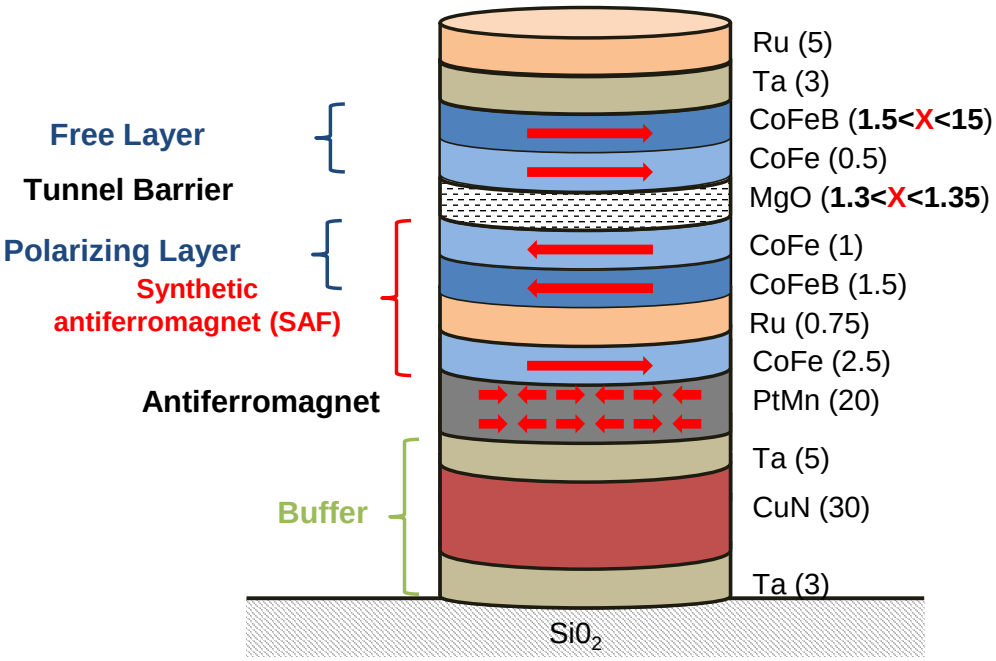

Figure IV.2 – Composition of the magnetic stack used for the experimental realization of an in-plane, MTJ-based STO on a silicon substrate. Thicknesses in nm. The basic blocks are (i) the magnetic tunnel junction (blue/white/blue), (ii) the synthetic antiferromagnet (SAF) (blue/pink/blue), (iii) the antiferromagnet (grey). This magnetic stack typically yields a magnetoresistance of about 100% and an RA of about 2 $\Omega\mu m^2$.

Let us examine the stack from bottom to top.

The buffer layer provides a buffer on which the rest of the magnetic stack can grow, but the buffer layer must also be metallic so that it has a low electrical resistance, and therefore can be used as the bottom electrode of the device.

The antiferromagnet layer (here PtMn) generates a strong exchange bias on top of which the above magnetic layer stabilizes its magnetization. In practice, after deposition the magnetic stack is annealed above the blocking temperature of the antiferromagnet under a strong in-plane magnetic field, then cooled down to room temperature. The antiferromagnet magnetic moments are then oriented in the direction of the applied magnetic field, and the magnetization of the above layer is then pinned in the same direction. This direction will set the magnetic easy axis of the magnetization of the device (unless the device is etched into an elliptical pillar, where the direction of the major axis of the ellipse is not that of magnetization of the pinned layers).

The SAF is composed of two magnetic layers made of CoFeB in opposite direction separated by a thin layer of ruthenium. The antiferromagnetic coupling between the two layers is assured by the Ruderman-Kittel-Kasuya-Yoshida (RKKY) interaction [7]. The goal of the SAF is to ensure that the stray field emitted by the polarizer is channeled towards the bottom layer of the SAF. In this way, the polarizer and the free layer are magnetically decoupled [3].

On top of the SAF is the magnetic tunnel junction. The MTJ is the most critical element of the magnetic stack and will be discussed in more detail later. It consists in our

3. In practice, the dipolar coupling is not completely suppressed, and simulations have shown that even with a SAF in the structure, the *dynamical dipolar coupling* between the free layer and the polarizer needs to be taken into account[29, 49].

case of two layers of CoFeB separated by a very thin insulating layer of magnesium oxide (MgO) of about 1 nm thickness. Strictly speaking, each ferromagnetic electrode is not one layer of CoFeB, but is actually composed of two ferromagnetic layers, CoFe (thinner) and CoFeB (thicker). The layer of CoFe is here to prevent the boron diffusion into the MgO barrier, but after annealing the two layers of CoFe and CoFeB form one continuous ferromagnetic material.

Finally, the top electrode is composed of the metallic materials Ru and Ta (the pillar will be ultimately covered by a thicker layer of Ta during the nanofabrication process).

Deposition of the MTJ and full sheet results

In order to prepare our own MTJ devices, I have worked in the clean room during the first year of my thesis on the deposition, annealing, and full sheet characterization of the magnetic stack presented above. Most of the work has involved optimization of the tunnel barrier in order to reach the objectives of TMR and RA that were set for our STO devices : **RA below** $2\Omega\mu m^2$ and **TMR above** 80%.

Deposition is performed with an AVIZA IBD 300A apparatus on 200mm silicon wafers. IBD stands for Ion Beam Deposition, a type of sputter deposition. In IBD, a beam made from ionized argon gas is focused and accelerated onto a target composed of the material to deposit. At the same time a substrate is put close to the target (a few cm away) : the sputtered atoms from the target form a gas which progressively deposits on the substrate. To go from one layer to another, one simply changes the target, and the thickness of the layer can be monitored by modifying the deposition time and the beam intensity.

A IBD machine has three modules : Etching, deposition and oxidation. Etching cleans the targets before use, deposition is the nominal functioning with deposition of the material and finally oxidation is performed in a separate chamber to perform oxidation on the surface on the substrate. Oxidation can be performed in two ways : radicalar oxidation or natural oxidation.

We will not review how the complete stack is deposited : however deposition of the tunnel barrier is the critical part and is actually quite tricky : we will have a few words on the different steps involved in the deposition on the junction.

We remember that we need to realize ultra-low RA tunnel junctions so that they support high current densities : it requires that the layer of MgO deposited is very thin, in the order of 1nm. The deposition of such a thin layer is difficult because it represents a few monolayers ; for MgO the lattice parameter is 4.212 Å, so 1.2 nm accounts for 3 monolayers, which means that the deposition roughness needs to be kept to a minimum. Also, MgO is a ceramic material and it contrasts with the rest of the magnetic stack which are metallic materials : the IBD process is optimal for metallic targets, and special techniques need to be employed for the deposition of ceramics.

So actually the material deposited in not MgO, because there is only a metallic Mg target, which is going to form a layer of Mg to be oxidated. The deposition of the barrier is performed in three steps :

1. Deposition of about 2 monolayers of metallic Mg
2. Oxidation
3. Deposition of about 1 monolayer of metallic Mg

The oxidation step is critical. Indeed, the quality of the interface between the tunnel barrier and the ferromagnetic electrodes will determine the TMR of the stack. In the

case of under-oxidation, there will be metallic Mg at the interface, thus limiting spin-filtering ; in the case of over oxidation, then the ferromagnetic electrodes will be oxidized as well as the Mg, and the TMR will drop. Fortunately, the oxidation process can be adjusted by varying several parameters such as the oxygen pressure, the oxidation type (radicalar oxidation or natural oxidation) and the oxydation duration. The best results were obtained for natural oxidation. Then after optimization, it was found that a duration of about 5 seconds of oxidation coupled with an oxygen pressure of $0,5$Torr are the most appropriate parameters.

During my time in the clean room I essentially focused on evaluating the influence of the thickness of the top and bottom layers of Mg separately and find out which set of parameters gives the best results in terms of TMR and RA. The couple $0,9$nm (bottom) and $0,4$nm (top) is the typical value used.

Once the full stack is deposited, the wafer is put in an annealing oven. The model used is a MATR200A. During annealing, a strong in-plane magnetic field is applied as well. This step allows one to obtain a good crystallographic structure for the stack : just after deposition, the magnetic layers are amorphous but after annealing and under the application of the external magnetic field, the epitaxial heterostructure CoFeB (001) / MgO (001) / CoFeB (001) is formed, hence yielding a good TMR ratio. We note that epitaxy is realized locally. Overall the deposition process makes it a polycrystalline structure, where B atoms are diffused to grain boundaries.

In order to evaluate the TMR and the RA of the magnetic stack once magnetic stack is deposited, we used the technique of current-in-plane tunneling[10] on full-sheet wafers. This allows one to be free from defects that may arise from the nanofabrication process : once patterned into a nanopillar, measurement of the TMR and the RA is straightforward but the values obtained are subject to the quality of the nanofabrication.

Measurements are carried out with the CAPRES (Copenhagen Applied Research) apparatus. Fig. IV.3 exhibits the TMR and RA results obtained on three batches of wafers prepared in the Aviza IBD. In these three batches the only parameter varied is the thickness of the bottom and top layer of Mg (thickness of the tunnel barrier).

Without going into too much details, during this series of measurements only 2 wafers satisfy the conditions of low RA and high TMR fixed. This low yield comes from the fact that there is a lot of variability from one batch to another, even though very similar recipes were used. We can say that the objectives were reached but not on a consistent basis. It can be explained by frequent starts and stops of the deposition machine. Indeed, one of the principal drawbacks of IBD is that a large amount of maintenance is necessary to keep the ion source operating, and since the machine has been used for research purposes rather than production, the calibration from one batch to another may be different.

In the end, the samples prepared with the Aviza deposition machine have proven to yield good TMR and low RA adequate for standard utilization. These were nanofabricated and showed STT-induced switching as well as interesting dynamic behavior. However, compared to studies in autonomous regime, injection-locking studies require the devices to be especially resistant to currents since both RF and DC bias are applied at the same time. Only ultra-low RA samples have shown to yield sufficient resilience to current for our injection-locking studies. These requirements explain why the dynamic measurements to be reported in this manuscript are carried out on samples that were provided by Hitachi GST, San Jose. These samples have an RA of 1 to 1.3 $\Omega\mu m^2$ which gives them enough

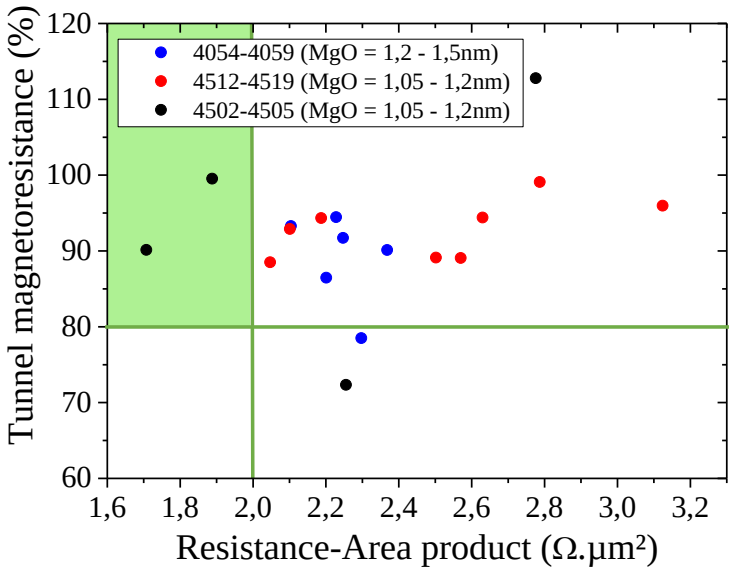

Figure IV.3 – Tunnel magnetoresistance (TMR) vs Resistance-Area product (RA) obtained on MTJ stacks deposited in LETI for 3 batches. Measurements are done via the CIPT technique on full-sheet wafers. Composition of the magnetic stack is shown in Fig. IV.2. The green region corresponds to the objectives of RA $< 2\Omega\mu m^2$ and TMR $> 80\%$

durability under electrical stress.

IV.1.3 Pinholes and Electrical stress

Ultra-low RA tunnel junctions are made of only a few monolayers of MgO. Then, even though the deposition process is optimized, junctions are very sensitive to roughness. Moreover, grain boundaries within the junctions are also a source of roughness. Therefore, there are cases in ultra-low RA junctions when a metallic short builds between the two ferromagnetic electrodes. These shorts are causing the current to flow in the junction through two channels : (i) a tunneling channel (the current is flowing through the MgO barrier) and (ii) an ohmic channel (the current passes through the short).

These shorts are well-known in ultra-low RA junctions and are called *pinholes*. They have been reported and studied for example in [64, 65, 44]. Komagaki *et al.* evidenced the role of boron diffusion on the creation of pinholes and established in particular a link between the thickness of the CoFeB electrode and the pinhole density(see Fig. IV.4). Reducing boron diffusion into the tunnel junction can be also achieved by adding a Ta capping layer on top of the CoFeB electrode, thus absorbing the boron in the tantalum rather than letting it diffuse in the junction.

Evidently pinholes are problematic when it comes to mass production of MTJs and variability, because one cannot predict in advance where and how many pinholes will be created within the junction. In [44], typical pinhole densities are in the order of 100 parts/μm^2. If we take a nanopillar of diameter 100nm, then it represents an average of 0.78 pinhole per pillar. It means that from one pillar to another, one may have none, one, two, possibly three pinholes, leading to very different behaviors from one sample to another.

However the mixed conduction regime induced by the appearance of a pinhole is

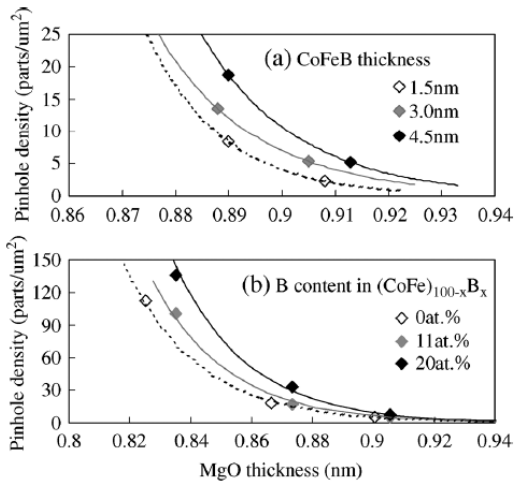

Figure IV.4 – Relation between Boron diffusion and pinhole density in ultra-low RA MTJs for various (a) CoFeB thicknesses and (b) B contents in CoFeB layer. Reproduced from [44].

not always detrimental. It weakens the barrier structure and reduces the MR ratio, but the overall resistance shrinks, thus reducing the RA as well and extending the maximum current density that can applied before breakdown. MTJs for STOs are interesting because they yield a much higher MR ratio than spin-valves, but they have a breakdown voltage that sets a top limit for the current density that is injected in the pillar. With pinholes, even if the MR is reduced by about a factor of two, it still yields a high MR ratio compared to spin valves. Pinholes therefore offer a type of compromise compared to perfect junctions, that is lessened stability and signal output but extended current range before breakdown.

Next we show static measurements obtained on patterned Aviza MTJs. The goal of these measurements is to determine how the junction behaves with current. As we discussed above, in ultra-thin tunnel barriers there is an important probability that pinholes appear. To distinguish between patterned junctions with a pinhole or without one, Houssameddine *et al.* introduced the notion of LTMR (for low TMR, one pinhole or more) and HTMR (high TMR, no pinhole) samples [35, 34].

Here we give a quick characterization of LTMR-type samples deposited in the Aviza machine. The HTMR type samples from the Aviza machine have an RA that is rather high, so only the LMTR samples have given interesting results because of their reduced RA. As we will see, we can deduce the presence of pinholes from voltage vs current characteristics, and also determine the range of current where the junction remains undamaged.

In order to start any dynamic characterization, the magnetoresistance curves must first be analyzed. Fig. IV.5 shows the evolution of magnetoresistance curves with current on nanopatterned 100 nm diameter nanopillar Aviza junctions. In a general manner, we see that the overall resistance decreases with the increase of current. However, there seems to be two regimes, first a light decrease (up to 0.5mA) then a much sharper drop of resistance for $I > 0,6$mA. The first regime can be explained by normal tunneling behavior, where an increase of the applied current is followed by a decrease of TMR[38]. However the second regime corresponds actually to an *irreversible* loss of resistance, meaning that the junction is being damaged.

From magnetoresistance curves such as Fig. IV.5 for several currents we can extract the resistance versus current and voltage versus current characteristics. Fig. IV.6 shows

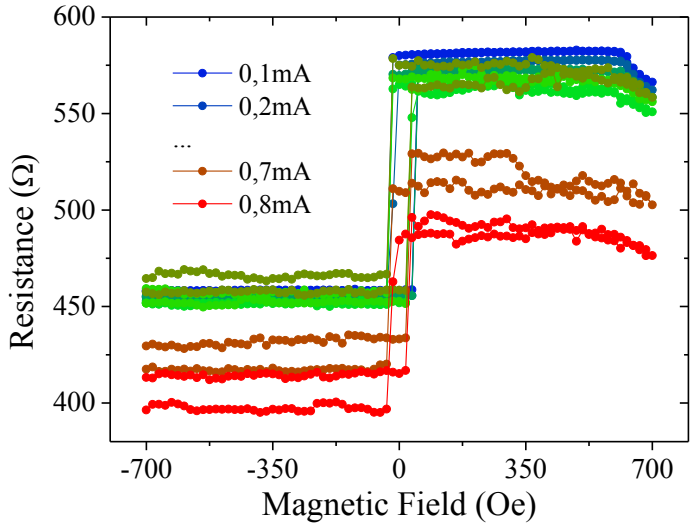

Figure IV.5 – Magnetoresistance curves for various applied currents on a 100 nm diameter nanopillar based on Aviza-an deposited MTJ LTMR sample. RA $= 3,4 \Omega\mu m^2$, TMR $= 23\%$. As the current increases, the junction is damaged and the overall resistance decreases.

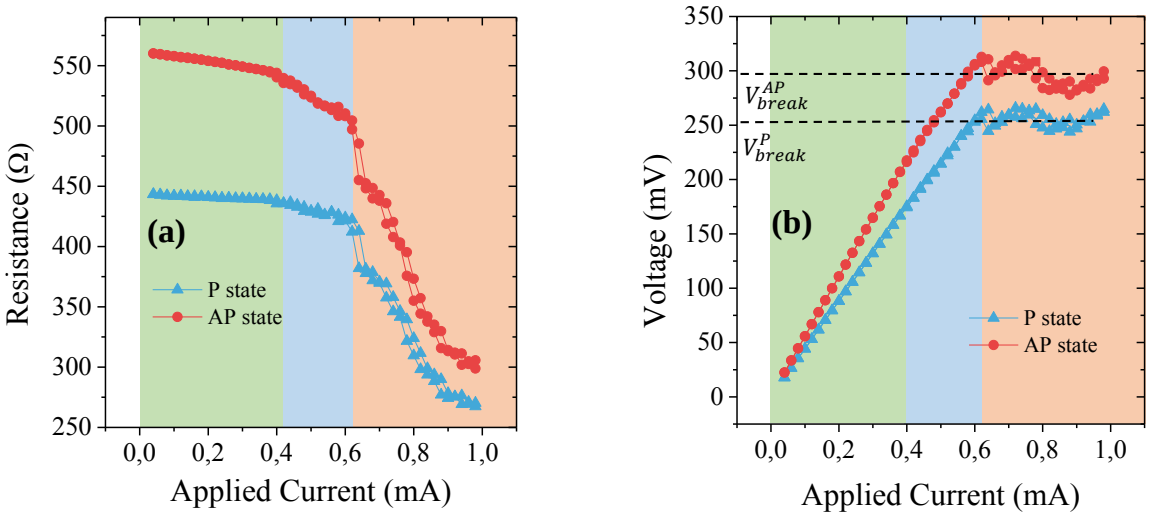

Figure IV.6 – (a) Resistance versus applied current and (b) voltage versus applied current on a 100nm diameter nanopillar Aviza-deposited MTJ LTMR sample. RA $= 3.3\ \Omega\mu m^2$, TMR $=$ 26%. P state (resp. AP) corresponds to an applied field of -175Oe (resp. +175Oe). Zones have been delimited by current range : (green) reversible behavior (blue) instability (red) irreversible behavior. On (b) the voltage saturates at about 300 mV for $I > 0.6$ mA, which indicates the presence of a pinhole.

these characteristics for the AP and P state. From Fig. IV.6 we confirm the two regimes of resistance change with current that we inferred from Fig. IV.5 : The green zone corresponds to a reversible change of resistance and the red zone corresponds to an irreversible change. We also notice an intermediate regime between 0.4 and 0.6 mA (in blue) where the resistance decreases at a slightly higher rate than in the reversible regime.

In Fig. IV.6(b) the voltage versus current characteristics indicate the presence of the 3 zones as well. As we mentioned, the red zone corresponds to an irreversible process and a damaging of the junction, but more interestingly we observe that in this region the voltage saturates (in the AP state) at about 300mV when the current increases. In other terms, it looks like there is a maximum electric field that can be applied between the two electrodes of the junction. By increasing the current one finally reaches this maximum field, and afterward the junction continuously adjusts its resistance so that the electric field is limited to this maximum.

However this "adjustment of resistance" is irreversible and reveals gradual breakdown of the junction. How does this occur ? This is where there is a strong hint that one or more pinholes are present in the junction. Pinholes are metallic shorts between the two electrodes : they can be modeled by an ohmic resistor in parallel with a tunnel resistor (MgO). Close to the breakdown, the pinhole concentrates an important part of the overall current and locally the current density is much higher than in the rest of the junction. When the the critical voltage of 300 mV is attained, any increase of current makes the the pinhole grow in size, presumably because 300 mV represents a threshold for electromigration of particular atoms in the junction. As a consequence, the area covered by the pinhole increases while the area of MgO decreases. Then, the ohmic pinhole channel is favored with respect to the tunneling channel - as a consequence, the overall resistance decreases as well as the TMR.

The continuous breakdown in LTMR junctions with relation to pinholes is examined in more detail in [64] [4], where a similar threshold of 300mV is found.

We close now this section on the fabrication of a MTJ-based STO device. Here we spoke of the material properties of the magnetic stack and in particular we pointed out the difficulties encountered when one wants to a realize a MTJ which fits for a STO device : low RA, and high TMR. The issue of the reliability of the device under a high current density is a crucial one. This why partially damaged devices having pinholes in the junction (LTMR) often give very interesting results and are used for experiments, since typically more current can be injected in a LTMR device before the junction reaches electrical breakdown.

Engineering an efficient STO device involves material optimization of the magnetic stack (in particular the MTJ), but as we will discuss next, one also has to make sure that the RF signal generated by the oscillator is collected with maximum signal output and quality. [5]

4. This article also discusses an interesting consequence of the presence of a pinhole for the STO dynamics, the creation of a magnetic coupling between the two electrodes due to the Oersted field generated by the high current density flowing in the pinhole.

5. We have not mentioned the role of the nanofabrication (etching of the pillar and of the contacts) in the preparation of the device. Evidently nanofabrication plays a crucial role and determines in an important part the qualities of the output signal of the STO.

IV.2 RF techniques : microwave circuit analysis and signal processing

IV.2.1 Experimental setup

Handling microwave signals in the GHz range requires special techniques and apparatuses. *Microwave signals* refers to alternating currents with a frequency between 300 MHz and 300 GHz so that they have a electrical wavelength between $\lambda =$ 1m and $\lambda =$ 1nm. For a frequency of 10 GHz, coaxial cables will carry a signal with a wavelength of about 3cm.

In this range of frequencies the wavelength is comparable or even smaller than the dimensions of the electrical components, and as a consequence standard circuit analysis using Kirchoff's laws is not appropriate because it requires that the phase of the electrical signal is constant over the whole circuit. So in microwave circuits, one should use the broader theory of electromagnetics and solve the Maxwell equations in the circuit instead. That being said, Maxwell equations are tedious to deal with and provide information on the electromagnetic field at every point in space, which is usually too much information for practical purposes.

So we need a theory that can describe the propagation of waves in the cables, but at the same time we are interested in using quantities like power, impedance, voltage and current from standard circuit theory. To do so, we will use the *transmission line theory* which combines the two approaches : on one hand, wave propagation is described by an approximation of Maxwell's equations and on the other hand, electronic components are considered as a point in space having an input and output impedance. The interested reader may read the textbook [68] for more details on microwave circuit analysis.

Microwave circuit analysis is then used for the design of the setup used for injection-locking in our STOs. Perhaps the most valuable part of microwave circuit analysis for our studies is the ability to estimate the microwave power actually generated by STO with good precision. Due to rather low output power (about -60 dBm) amplification of the signal is compulsory - and the overall gain of the measurement chain must be determined in order to obtain to the output power of the STO. In addition, the gain depends not only on the components of the measurements chain itself, but it depends strongly on the signal frequency and the impedance of the device. In the next subsection the impedance mismatch between the STO device and the rest of the measurement chain will be considered : we will see its influence on the output power, but also on the injection of the additional RF current into the STO for synchronization experiments.

Here we start by examining the measurement chain for the experiments on injection-locked STOs and we will analyze quickly the main features of the experimental setup. In Fig. IV.7 are shown the components of a typical RF setup used for injection-locking experiments.

We sort the components into four categories (from left to right in Fig. IV.7) :

• **Current Excitation**. Injection-locked STOs require two separate excitations : a DC current source and a RF current source. The DC current source is the primary element that will generate the DC bias which is the source of energy for the STO to enter into self-sustained precession. Typical applied currents are between 0.5 to 2 mA with a bias

voltage of 0.1 to 1 V, corresponding to a DC power in the mW range. Synchronization (or modulation) experiments require a supplementary source of RF current (on the left). This source will play the role of the small driving force to synchronizing the STO signal at f or $2f$. Experimentally the RF source delivers only a portion of the DC power to the STO : this is to be consistent with the theory of synchronization (weak forcing) but also to limit damage imposed to the junction. Precise determination of the injected RF current flowing in the junction is an issue and will be discussed later on in this chapter.

• **STO device**. The STO device is at the intersection of three different currents : the DC excitation, the RF excitation and the generated magnetoresistive RF signal. The magnetoresistive signal is much lower in intensity (in terms of power, 3 to 6 orders of magnitude below the excitation) and will be amplified by the gain chain (on the right). In contrast with the rest of the measurement chain where both cables and components are matched to 50 Ω, the STO is *not matched* in impedance, which is a significant source of RF loss [6]. In addition, the device electrodes must be designed in order to provide efficient wave-guiding, limiting losses inside the device. Finally (not shown on the diagram), an electromagnet generating an in-plane field up to 1 kOe will control the local field applied to the STO.

• **Amplification chain**. The amplification chain (right part) will provide the transfer function for amplification of the STO signal either to the oscilloscope or the spectrum analyzer [7]. Then the transfer function is saved in a Matlab routine, where the correction of the gain chain will be subtracted from the amplified signal to reach back the output signal from the STO. In the most simple configuration, measuring of the STO output necessitates that the gain chain is composed of two parts : a bias-tee to separate the DC (excitation) and RF (output) components of the signal and a broadband RF amplifier. Here the setup comprises a supplementary filter as well as a directional coupler. In the case of injection-locking at $2f$, the filter has the primary role of cutting the second harmonic due to the RF source. Otherwise, the STO signal would be hidden by the much more intense RF signal from the source. As for the directional coupler, it allows one to register the signal on the oscilloscope and the spectrum analyzer simultaneously.

• **Signal aquisition**. Two apparatuses can be utilized to save the RF signal from the STO. The first option is to use the oscilloscope that collects the time-trace of the signal. The oscilloscope we use here is a digital phosphor oscilloscope (DPO). This is a single-shot oscilloscope having a very high sampling rate (up to 50 GS/s) : the high sampling rate allows the user to measure high frequency signals up to 25 GHz, and the single-shot type (in comparison with a stroboscopic oscilloscope) allows one to inspect the noise properties of the signal. The other option is to collect, in the frequency domain, the *Power Spectral Density* (PSD) of the signal. This is performed by the Spectrum Analyzer (SA). With a spectrum analyzer, one has direct access to the most representative characteristics of the signal, i.e. the power, the linewidth and the generation frequency.

IV.2.2 Impedance matching at the device

Terminated transmission line

6. This is true for tunnel-junction based STOs - their static resistance of the device typically ranges from 100 Ω to 500 Ω. For STOs based on spin-valves, their static resistance is of about 50 Ω, limiting impedance mismatch

7. With a Vectorial Network Analyzer (VNA), one can measure the scattering matrix of each RF component separately. Afterward, one can obtain the overall transfer function of the gain chain by multiplying the matrices.

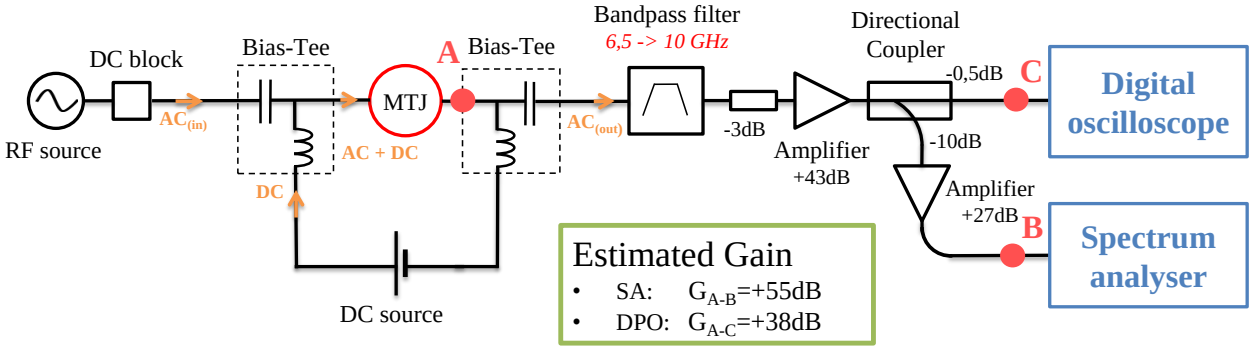

Figure IV.7 – Typical setup employed for injection-locking experiments on STOs. The spectrum analyzer and the digital oscilloscope allow respectively for measures in the frequency domain and time domain. For standard experiments (in the autonomous regime of oscillation) the RF source on the left is not included in the setup, only the DC source remains.

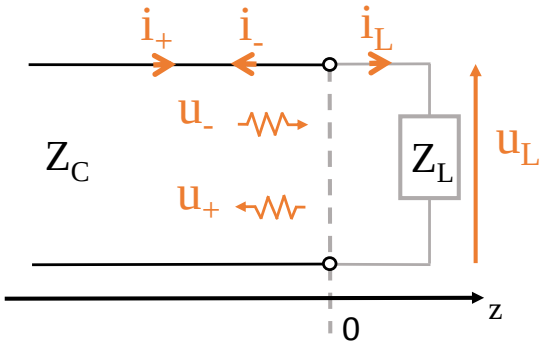

Figure IV.8 – Transmission line terminated by an arbitrary load of impedance Z_L.

We mentioned that one of the challenges of using MTJs for STOs is to take into account the impedance mismatch with the rest of the electrical circuit due to the static resistance of the MTJ. The problem of impedance mismatch is better understood when one introduces the concept of incident and reflected waves for transmission lines terminated by an arbitrary load (see Fig. IV.8). This is a standard problem in transmission line theory.

In Fig. IV.8, the transmission line has an impedance $Z_C = \sqrt{\frac{L}{C}}$ and the load has an impedance Z_L. The total voltage and current at at any point in space z of the line and time t is given by $v(z,t) = V(z)e^{i\omega t}$ and $i(z,t) = I(z)e^{-i\omega t}$. $V(z)$ and $I(z)$ are called *phasors*, and describe the spatial dependence of the waves only to simplify calculations. They are the sum of the incident (i_+, u_+) and reflected waves (i_-, u_-),

$$\begin{aligned} V(z) =& V_0^+ e^{-\gamma z} + V_0^- e^{\gamma z} \\ I(z) =& I_0^+ e^{-\gamma z} - I_0^- e^{\gamma z} \end{aligned} \quad , \tag{IV.1}$$

Here γ is the notation for the propagation constant. In the case of a lossless transmission line, $\gamma = i\omega\sqrt{LC}$. By definition of the characteristic impedance Z_C, we obtain

$V_0^+/I_0^+ = V_0^-/I_0^- = Z_C$. By convention, the reflection coefficient Γ is defined as the ratio of the reflected voltage on the incident voltage

$$\Gamma = \frac{u_-}{u_+} = \frac{V_0^-}{V_0^+}. \tag{IV.2}$$

At the end of the line, $V(z = 0) = u_L$ and $I(z = 0) = i_L$. Applying Ohm's law gives $u_L = Z_L i_l$. Using Eq. IV.1 to write $V(0) = Z_L I(0)$, one can finally obtain the ratio $\Gamma = V_0^-/V_0^+$,

$$\Gamma = \frac{Z_L - Z_C}{Z_L + Z_C}. \tag{IV.3}$$

In the case of impedance matching $Z_L = Z_C$, it follows that $\Gamma = 0$, meaning that there is no reflected wave. If $Z_L = 0$ (short) then $\Gamma = -1$, or if $Z_L = \infty$ (open) then $\Gamma = 1$. In these last two cases, the incident wave is fully reflected. In all the other cases (arbitrary Z_L) of impedance mismatch, *standing waves* arise in the line, meaning that the magnitude of the voltage is not constant along the lines. From the reflection coefficient one can define the Voltage Standing Wave Ratio (VSWR) as

$$VSWR = \frac{1 - |\Gamma|}{1 + |\Gamma|}. \tag{IV.4}$$

The time-average power P carried by a wave (u, i) at point z is defined as

$$P = \frac{1}{2} Re\left(u(z).i^*(z)\right). \tag{IV.5}$$

Then the power from the incoming wave P_+ is given by $P_+ = \left(V_0^+\right)^2 / 2Z_0$, and the power from the reflected wave reads $P_- = \left(|\Gamma| V_0^+\right)^2 / 2Z_0$. The power delivered to the load, P_L, is simply the difference of the two,

$$P_L = \frac{1}{2} \frac{\left(V_0^+\right)^2}{Z_0} (1 - |\Gamma|^2). \tag{IV.6}$$

Determination of the input impedance Z_{in}

Now that we understand the role of impedance mismatch on a terminated lossless line, let us apply the concepts to our STO device. For injection-locking experiments, we use what we call *transmission devices* in contrast with the usual reflection devices used for dynamic measurements with DC current only. The reflection devices demand that the sample is connected with one RF GSG probe (Ground-Signal-Ground) where the top electrode of the pillar is in contact with the "signal" of the probe, and the bottom electrode of the pillar is in contact with the two "grounds" of the probe. The DC bias is applied from the signal to the ground of the sample. On the other hand, transmission devices (as shown in Fig. IV.9(a)) require that the sample is connected with two GSG probes. The "signal" of the left probe is connected with the top electrode, while the "signal" of the right probe is connected with the bottom electrode. The "grounds" of each probe are not connected to the top or bottom electrode, however they are connected with each other via strip lines to provide waveguiding. In transmission devices, the DC bias is applied between the two "signals" of the probes - and the RF current is injected one side, while

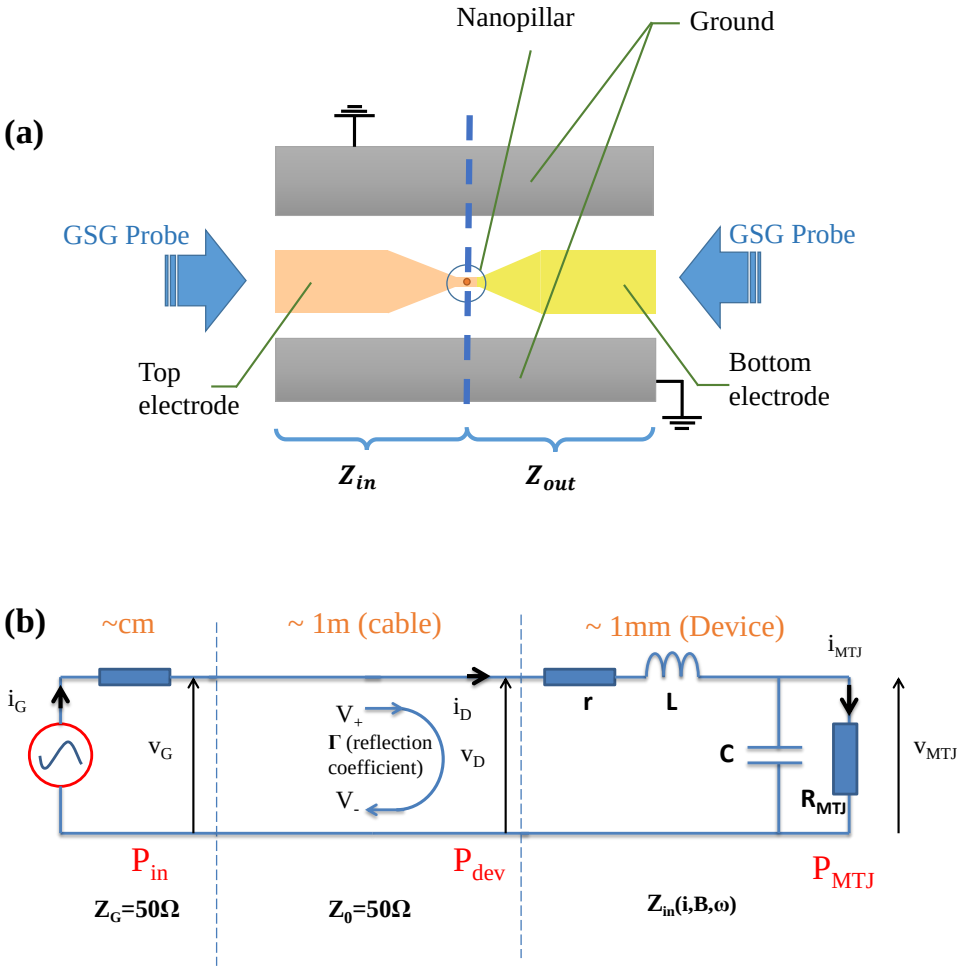

Figure IV.9 – (a) Schematic representation of a Hitachi STO device in transmission. Two GSG probes are connected on the top (left) and bottom (right) electrodes for current injection and collection in the MTJ. The two electrodes overlap (blue circle) over an area of about 4 µm at the center of which is the nanopillar. (b) Equivalent block diagram of the electrical circuit for (i) the RF source (ii) cable + probe (iii) Input impedance of STO device (left part of (a)). The problem to solve is equivalent to one of the terminated lossless transmission line.

the RF signal from the pillar is collected from the other side.

As we see on Fig. IV.9, the device is split in two parts. We consider that the RF current from the source arrives on the left, from there an *input impedance* Z_{in} corresponding to the left part can be determined. On the right side the RF signal comes out of the device and an *output impedance* Z_{out} corresponding to the right part can be determined too. And since the device is symmetric, then the output and the input impedance are the same.

The goal is to be able to refer to the problem of the terminated lossless line. From the point of view of the incoming waves, only the input impedance of the device is seen. Therefore the RF power effectively transmitted from the source to the device can be found using Eq. IV.6. To do so, one must first find the input impedance Z_{in} of the device. Fig. IV.9(b) shows a block diagram used to model the input impedance of the device.

We utilize RLC components to model the contact pads and the junction. The pads amount for the contact resistance r and the inductance L. R_{MTJ} corresponds to the static resistance of the nanopillar. The most critical parameter to evaluate is the parasitic

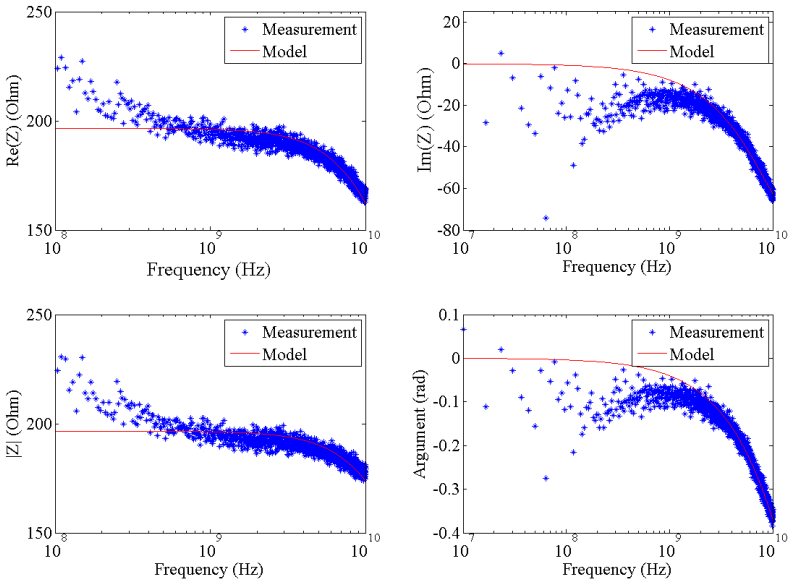

Figure IV.10 – VNA measurements (blue) for the input impedance of a Hitachi MTJ device in P state and comparison with a lumped RLC elements model (red line). Due to the parasitic capacitance, a cutoff frequency given by $f_c = 1/R_{MTJ}C$ arises close to 5 GHz. Fitting gives $r = 35\ \Omega$,$L = 36$ pH, $R_MTJ = 222\ \Omega$, and $C = 49$ fF.

capacitance C, because its value sets the cutoff frequency beyond which the RF power is dissipated in the capacitance instead of being delivered to the junction. The cutoff frequency is approximately given by $f_c = 1/R_{MTJ}C$.

In order to evaluate the RLC components, VNA measurements were performed on several STO devices. VNA measurements allow one to obtain the scattering matrix of a RF component - the VNA sends an incoming RF signal v_1^+ on one end of the device, and then measures the reflected signal v_1^- but also the transmitted signal v_2^+ on the other end. After transformation of the scattering matrix to the transmission matrix, one has access to quantities of interest such as the input or the output impedance of the device.

Fig. IV.10 shows the results acquired by VNA measurements for the input impedance Z_{in} of a Hitachi MTJ device and fitting results with the lumped RLC model equivalent to Z_{in}. The static resistance R_{MTJ} was measured beforehand, so that only three parameters have to be found. It is difficult to estimate the contact resistance and inductance precisely (the two are strongly interdependent) but the capacitance value $C = 49$ fF has been confirmed on several samples where the static resistance was varied.

It turns out from the model that the capacitance C is the primary source of RF losses in the device - the contact resistance r and the inductance l lead to a much higher cutoff frequency. Nevertheless, it remains difficult to evidence the principal source of the capacitive losses in the device, as it may come from : the overlap zone of the electrodes which creates a parallel capacitance in the immediate vicinity of the pillar, the electrodes layout which induce parasitic capacitive effects depending on the geometry (narrowing of the pads, spacing between the strips), or the substrate resistivity where high resistivity wafers are required so that the substrate does not induce an additional capacitance with the metallic pads. Previous sample realizations in Spintec on low-resistivity substrates have proven to give important capacitive losses, which can be addressed by choosing more advanced high resistivity substrates.

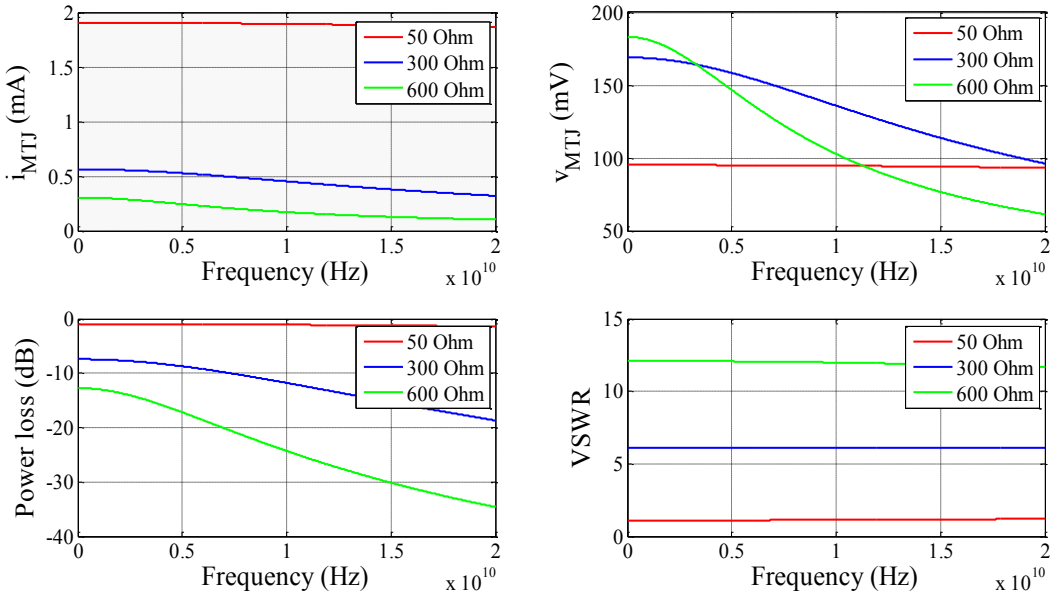

Figure IV.11 – Calculation of RF current and voltage (top panel) at the junction and power losses and VSWR (bottom panel) as a function of the RF source frequency. The RF source power is -10 dBm($i_{\text{source}} = 2$mA). The input impedance of the junction is determined using the electrical model in Fig. IV.9(b) with parameters $r = 5\ \Omega$, $L = 20$ pH, $C = 40$ fF. Results are shown for three values of the static resistance of the junction R_{MTJ}.

Injection of a RF current

In our case, impedance mismatch raises two questions : how much generated RF power from the MTJ is lost before entering the gain chain, and how much RF power can be effectively delivered to the MTJ by the RF source ?

We will focus on the second question, since the subject of this thesis is the synchronization of a STO by a RF current. In the KTS model introduced in the last two chapters, we recall that the driving force amplitude is represented by the RF / DC current ratio ϵ. Then, in order to quantitatively compare experimental results with the model, one must have access experimentally to ϵ. The DC current is not an issue, however precise evaluation of the RF current effectively flowing in the junction requires to take into account the impedance mismatch.

We have built an equivalent electrical model (Fig. IV.9(b)) for the input impedance of the device and with the help of VNA measurements, we determined the values of each component. From there, by knowing the RF power delivered by the RF source, we can retrieve the RF current flowing in the junction, but also ascertain that most of the RF power is transferred to the junction. In addition, the RF voltage applied to the junction can be determined so as to make sure that the RF source does not induce breakdown of the junction.

Fig. IV.11 shows the results from calculation of RF quantities using the electrical model introduced above. Typically injection-locking experiments were successful for a RF source power between -20 dBm and 0 dBm, and calculations were made for the intermediate value of -10 dBm. In the case where the static resistance of the pillar is of 50 Ω, there

are almost no losses and the same behavior is expected regardless of the frequency of the injected RF current. However, as one increases the junction resistance losses become significant. A pillar with a static resistance of 300 Ω will induce power losses of about −10 dBm at 5 GHz, and close to −20 dBm at 20 GHz, making power losses strongly dependent on the frequency of the injected RF current. The phenomenon is even more pronounced when the static resistance is increased up to 600 Ω, reaching losses of about −35 dBm at 20 GHz.

From this calculation we deduce that under typical conditions, only a portion of the RF power is transferred to the junction, and most of the power is dissipated either in the form of standing waves in the cables due to impedance mismatch (it depends essentially on the static resistance and is seen on the standing wave ratio), or in the parasitic capacitance from the device and it manifests with the appearance of a cutoff frequency $f_c = 1/R_{MTJ}C$ and a power drop for $f \geq f_c$.

This type of de-embedding studies serves two purposes. First it allows one to get back the actual RF current injected in the pillar rather that the one that would be delivered on a 50 Ω load, allowing a quantitative measure of the driving force amplitude ϵ introduced for the analysis of the synchronized state. Secondly, injection-locking experiments at $2f$ require that the RF current injected is at twice the generation frequency of the STO which is between 5 and 10 GHz in our case, so that the injected signal is between 10 and 20 GHz. This makes the injected signal having a frequency close or beyond the cutoff frequency, potentially preventing efficient RF current injection into the junction. This is an important factor to take into account before starting any injection-locking experiments on MTJs : one has to check that the static resistance of the device is not too important, so that losses at the injection frequency are limited and injection-locking is efficient.

IV.2.3 Signal processing and noise characterization

We will close this chapter on experimental techniques by reviewing basic concepts about signal processing for noisy oscillators. Then we will see how to apply these concepts to analyze our experimental signal using a spectrum analyzer or an oscilloscope. [8].

Basic concepts

We start with a reminder of the general form of the signal generated by a real, noisy oscillator with nominal frequency f_0, an initial phase ϕ_0 and amplitude V_O :

$$V(t) = V_0(1 + \delta V(t)) \sin(2\pi f_0 t + \phi_0 + \delta\phi(t)) \tag{IV.7}$$

Here, $\delta V(t)$ is assimilated to the *amplitude noise* and $\delta\phi(t)$ corresponds to the *phase noise*. In standard, weakly non-linear oscillators such as the VCO, the phase noise is much more important than the amplitude noise, and usually the function $\delta V(t)$ is assumed to be zero. However in STOs the strong non-linearity makes the overall noise contribution from the amplitude non-negligible and needs to be taken into account [40, 71, 26].

The phase noise takes into account the random fluctuations of the phase and the frequency of the oscillator. Depending on the origin of the fluctuations, they are several

8. The previous PhD student M. Quinsat has spent a significant amount of time and succeeded to develop time-frequency techniques to characterize and understand noise properties in STOs, using for example a dedicated method of characterization of the phase and amplitude noise in the frequency domain. A thorough discussion on the issues of coherence and signal processing in STOs is detailed in his manuscript [70].

types of noise - for example a white noise in frequency is equivalent to a random walk noise in the phase. To characterize noise, and in a more general context signal properties, it is useful to go to the frequency domain. To do so, we need to introduce the autocorrelation function and the power spectral density of a signal [97, 98].

The *autocorrelation function* $R_V(t)$ of a finite-power signal $V(t)$, in the time-domain, is defined by

$$R_V(t) = \left\langle \lim_{T\to\infty} \left[\frac{1}{T} \int_{-T/2}^{T/2} V(\tau)V(t-\tau)d\tau \right] \right\rangle . \tag{IV.8}$$

The auto-correlation function returns a value between 0 and 1 depending on the time t. It calculates with a moving average on τ how the signal at a time τ overlaps with itself at a time $t-\tau$. In other words, it is a measure of how much information is retained in the signal after a time t. For $t = 0$, $R_V(t) = 1$ for any signal. As t increases, a noisy signal will lose information, so $R_V(t)$ typically yields an exponential decrease with t.

The characteristic time of this exponential decrease can be extracted and corresponds to the *coherence time* of the signal. The more active is the noise affecting a signal, the lesser will be the coherence time. The autocorrelation function can be calculated for the complete signal, but more interestingly one can also calculate the autocorrelation function for the *phase* or the *amplitude* of the signal, giving information on how the noise affects it specifically.

We also define the *Power Spectral Density* (PSD) $S_V(f)$ of the signal, which is the Fourier transform of the autocorrelation function :

$$S_V(f) = \mathrm{TF}\left[R_V(t)\right] = \left\langle \lim_{T\to\infty} \left[\frac{1}{T} \left| \int_{-T/2}^{T/2} V(t)e^{-j2\pi ft}dt \right|^2 \right] \right\rangle \tag{IV.9}$$

The power spectral density (PSD) represents the quantity of power from the signal $V(t)$ included in the Fourier frequency interval *df*. The PSD is the quantity computed when one wants to visualize the *spectrum* of the signal. The representation of the signal $V(t)$ in the frequency domain allows one to efficiently determine quantities of interest for a generated RF signal, such as the generation frequency, power and linewidth. A spectrum analyzer computes the PSD of an electrical signal by analogic methods. Just as the autocorrelation function, the PSD can be calculated for the signal itself, but it works for the phase and amplitude of the signal as well.

Analysis tools

Experimentally, the output signal of the STO is acquired by two means. First in the frequency domain, it is the spectrum analyzer (SA) that calculates and permits visualization of the PSD of the electrical signal generated by the STO using the heterodyne method. The electrical signal is amplified through the gain chain and then fed to the spectrum analyzer. A typical initial dynamic measurement in STOs is to obtain the PSD of the STO for a large frequency span, for example from 1 to 20 GHz, and sweep the applied magnetic field in order to determine the PSD of the signal for 50 to a 100 values of the magnetic field. Once the PSD is recorded, then the gain chain needs to be taken into account and the PSD is corrected so that it corresponds to the actual output signal from the pillar. This is where the de-embedding task explained above is crucial, especially when one wants to figure out precisely the output power. The correction is carried out numerically by a Matlab routine where the inverse transfer function from the gain chain is applied to the raw PSD from the spectrum analyzer.

An important setting of the spectrum analyzer is the resolution bandwidth (RBW), which determines the frequency precision of a measurement. It corresponds to the fourier frequency interval *df* over which the power is calculated. A balance needs to be found between the acquisition time of a spectrum and the resolution bandwidth - the smaller the bandwidth, the longer will be the acquisition time for a given frequency span. Typically, we register spectra with 10 000 points, and the frequency span will fix the RBW accordingly (a span of 10 GHz necessitates a RBW of about 1 MHz). Finally, in order to limit signal instabilities, the spectra are averaged 5 to 10 times.

Secondly in the time domain, the Digital Phosphor Oscilloscope (DPO) is used to record a time-trace of the signal. The DPO is generally less sensitive to weak signals so a stronger amplification is needed than for the SA. It is used for more advanced characterization of the signal. Indeed, if direct visualization of the time trace does not typically provide important information, by recording a long-enough time traces we can gain detailed insight about the stability and the noise properties of the signal. In comparison, the only information about noise accessible from a SA is the linewidth - which is a rough measure of noise intensity.

With digital post-processing, we can extract the instantaneous phase and amplitude of the signal using the Hilbert transform of the signal [66]. The Hilbert transform calculates the analytical signal $A(t)$ ($A(t) = a(t)e^{i\phi(t)}$) from the real signal $V(t)$, and from there the phase is obtained from the argument of $A(t)$ while the amplitude is simply the modulus of $A(t)$. Once the time-dependent phase and amplitude of the signal are obtained, then their analysis is performed in the frequency domain by means of the autocorrelation function or the PSD for the phase and amplitude independently.

It is very valuable to be able to separate the contribution from the phase and the amplitude to the coherence of the signal when one has a strongly non-linear oscillator. Typically it is assumed that for an electronic oscillator frequency instabilities arise almost exclusively from phase fluctuations[78], because of the intrinsic weak non-linearities in these oscillators - only a very reduced portion of amplitude fluctuations are transferred into phase fluctuations. In STOs the non-linearity factor N measuring the conversion from amplitude to phase fluctuations is substantially higher than in other electronic oscillators, therefore independent measurements of the phase and the amplitude noise are necessary to evaluate their relative weight in the spectral purity of the signal [9].

9. By spectral purity we imply the PSD of the complete signal $V(t)$, which includes both phase and amplitude contributions. The quality of the spectral purity is estimated by the generation linewidth of the signal PSD

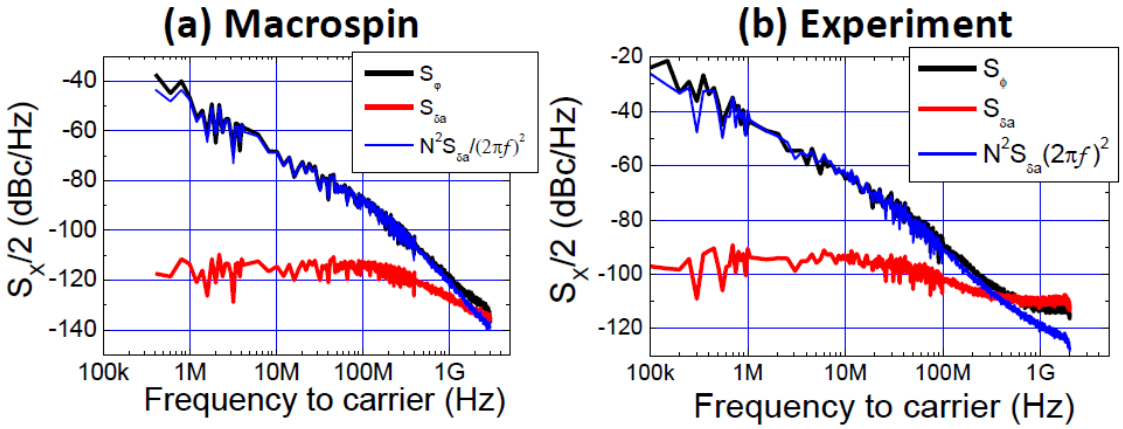

Figure IV.12 – Amplitude $S_{\delta a}$ and phase S_ϕ noise PSD for an in-plane MTJ-based STO in autonomous self-sustained regime from (a) macrospin simulations and (b) experiments. The data is presented in log-log scale, at a distance from 100 kHz to 3 GHz away from the carrier frequency. From 100 kHz to $f_p \approx 200$ MHz, phase noise follows a $1/f^2$ dependence typical of random phase walk, then goes to a $1/f^4$ dependence due to the drop in amplitude noise for $f > f_p$. From [70]. More details on the related paper on experimental measurements phase and amplitude noise for in-plane STOs in [71] and recently for vortex STOs in [26].

Chapter V

Room-temperature characterization of injection-locking at $2f$

The analytical model that we provided for the analysis of IPP precession in the stationary synchronized state in part B has helped us to build a detailed picture of the mechanisms of current-induced synchronization in a STO. However our analysis was restricted to the $0K$ temperature, stationary state situation. As a consequence, the problems of spectral purity in the synchronized state at room temperature cannot be directly addressed with our model as it is - for example it cannot provide estimations of the noise reduction in the synchronized state.

However there are some quantities such as the locking-range or the phase difference that are accessible experimentally at room-temperature and can be compared to the model. Thermal noise adds a smoothing effect on the obtained data, in some cases it will entirely mask the tendencies, but in general it limits the precision of the measurements. Maybe the simplest example is that in the presence of noise, the boundaries of the locking-range are not clearly defined, and strictly speaking neither phase or frequency locking conditions formulated for synchronization at $0K$ are fulfilled within the locking-range at room temperature. Nevertheless, the strong linewidth reduction coupled with frequency entrainment seen experimentally when the RF source is close to $2f$ leads undoubtedly to the conclusion that we identify a synchronization phenomenon.

In this final chapter we provide the experimental characterization of the synchronized state for $2f$ injection-locked MTJ-based in plane STOs at room-temperature. We will start with the analysis of the generation spectrum in the absence of RF current of our STO with respect to the applied in-plane magnetic field and DC current. Then, whenever possible, the results will be compared to the analytical model at $0K$ in the prospect that we can provide enough experimental evidence to support the idea of this specific type of synchronization where frequency adjustment is enabled only through amplitude adjustment. In parallel, the techniques that were developed at Spintec and introduced at the end of the last chapter will be utilized to provide better characterization on the STO signal coherence in synchronized state.

V.1 Dynamics of an in-plane MTJ STO without RF current

We start with dynamic measurements of an in-plane MTJ STO in the absence of RF current. Indeed, before studying the synchronized state, one must first characterize the STO dynamics in the autonomous state. We remember that a part of the study consists in evaluating the effects of precession amplitude change on the synchronization properties. So it means that we need to vary the DC current over the threshold for self-sustained oscillation (the critical current I_c). In the absence of thermal noise, the threshold is easy to determine because no oscillations are visible below the threshold. When thermal noise is present, we also observe what we call thermally induced spin-waves, i.e. oscillations *below* the threshold. As a consequence, the threshold for auto-oscillation must be determined in other ways, such as linear regression of the linewidth with current (the linewidth decreases linearly with current in the thermally induced FMR regime[83]).

So in order to stay consistent with the synchronization analysis presented before, it has been verified that all the experimental data on synchronization shown in this manuscript correspond to a self-sustained oscillations [1]. Forced excitations by a RF current at $2f$ *below* the threshold have been discussed in several recent papers [6, 19] and were labeled *parametric excitations*, but it goes beyond the scope of this thesis .

In addition, the subject of dynamical coupling between layers must be discussed in order to analyze experimental data in the autonomous regime. Indeed the KTS model (in its current form) relies on the assumption that only one layer is excited at a time [2]. In experiments this assumption does no necessarily hold and there is growing evidence that collective excitations of the magnetic layers must be taken into account in order to explain some essential features of the spectra (generation frequency and linewidth). Dynamical coupling in STOs and its consequences has been in the recent years a very active subject of research [49, 28, 29, 18, 30].

V.1.1 Generation spectra : Overview of the dynamics

Here we start by showing results on a most representative LMTR sample (i.e. the type of sample that typically served for synchronization experiments later on). Depending on the orientation of the magnetic field, the STO has two static configurations, the parallel and anti-parallel state. Then a DC current is applied through the junction and the direction of the electrons flow will determine whether it is the top layer of the SAF, the PL (SAF excitations) or the FL (FL excitations) that will be destabilized and eventually enter into self-sustained precession. For example, a positive current in our convention will favor excitation of the SAF in the P state and excitation of the FL in the AP state. A negative current will favor the excitation of the FL in the P state and the SAF in the AP state.

We are interested in the examination the steady-state oscillations of the FL, so there are two possibilities, by either applying negative currents in the P state or positive currents in the AP state. We chose the AP state because in all measurements performed the electrical signal output is much enhanced in the AP state.

1. Strictly speaking, the use of the term " synchronization" is valid *only* when the forced oscillator is a self-sustained oscillator. In other words, if the forced oscillator operates below the critical current, we should rather talk of a "resonance phenomenon"

2. In our case the FL is excited while other magnetic layers are static.

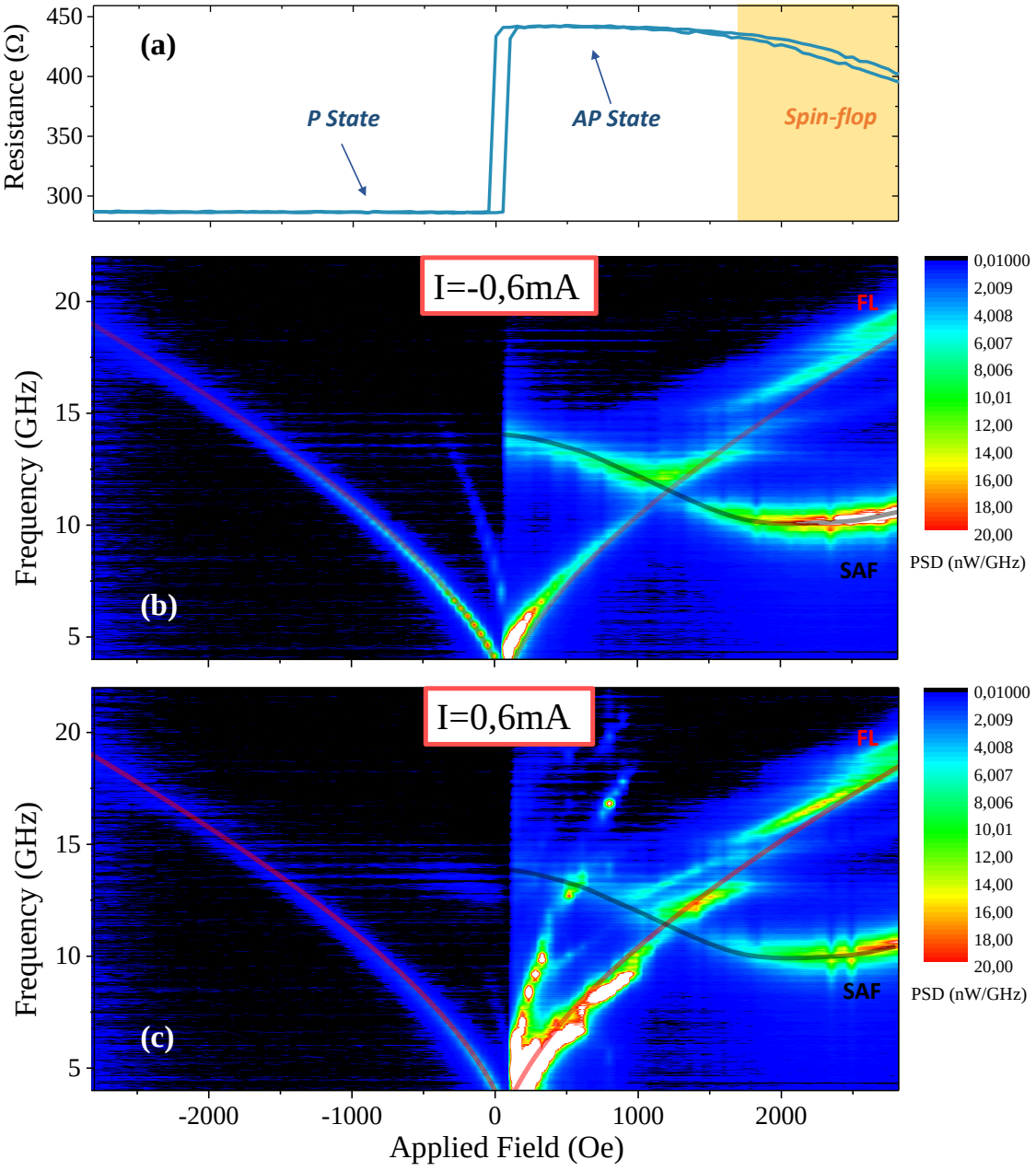

Figure V.1 – (a) Magnetoresistive cycle (resistance versus in-plane field) (b),(c) Experimental PSD of an in-plane MTJ-based STO with respect to the applied magnetic field for a positive ((b), FL favored) and negative ((c), SAF favored) DC current value. The field is applied with a 10° angle from the easy axis. The sample is a nanopillar of diameter 75 nm with RA = 1.4 $\Omega\mu m^2$, TMR = 52 %. The P state is on the left and the AP state on the right. The red line is a fit of the Kittel law for the FL and the black line is a guide to the eye for SAF excitations. Threshold for auto-oscillations of the FL : $I_C = 0.37$ mA. The PSD scale remains the same in the two plots.

Fig. V.1 shows a 2D map of the PSD of the STO signal as a function of the applied magnetic field. This type of dynamic measurement is performed once the hysteresis loop is obtained. The PSD is collected via a spectrum analyzer (RBW of 1MHz) using the setup represented in Fig. IV.7. A spectrum with a frequency span of 20GHz is recorded for each value of the applied field that is swept between -2800 and 2800 Oe with steps of 28 Oe. Fig. V.1 presents the results for several currents, which correspond to different regimes of excitation for the FL or the SAF.

The first observation is that in the P state (left part), the signal is much weaker as expected, regardless of the current value. SAF excitations in the P state are barely visible, but the FL excitations are clear. The frequency of the FL as a function of the applied field in the subcritical regime is given by the Kittel formula, and a fit of the data using this formula has been performed and is shown by the red line (it yields a saturation magnetization of $M_S = 973$ kA/m). The fit was done using the data in the P state, and then, by symmetry the fit results are also shown for the AP state. However in the AP state we see that the experimental data for the FL strays away from the Kittel formula, especially when the DC current increases.

There are several reasons why the frequency of the FL does not follow the Kittel law. According to the KTS model, because of the frequency amplitude coupling N a change of precession amplitude (induced by the increase of the current) leads to a decrease of the frequency (frequency "redshift") and most notably, because of the dynamical coupling between the SAF top layer and the FL. The most notable effect of dynamical coupling is when the SAF excitations (black lines) cross in frequency with the FL excitations where we observe frequency pulling or repelling between the two modes. This is especially visible at the intersection between the FL and the SAF (red and black lines).

According to theory, we also confirm that the direction of the current favors either the FL or the SAF excitation. For the negative current $I = -0.6$ mA, we can recognize that SAF excitations (along the black line) are favored while the FL excitations (along the red line) are favored for a positive current $I = 0.6$ mA. Finally, we also note that the second harmonic of the FL is visible as well for $I = 0.6$ mA.

If we want to study the steady-state STO dynamics within the KTS model but also reach sufficient output power then we need to look at FL oscillations in the AP state and with a positive current above the threshold $I > I_C$. In addition, the applied field must be between 0 and 1000 Oe for three reasons.

First, at about 1200 Oe, the SAF and the FL frequencies cross, and the crossing is accompanied with substantial linewidth increase. Second, over 1000 Oe the FL frequency goes beyond 10 GHz and it starts to be problematic concerning microwave transmission from the RF current source. Our current device design (see IV.2.2) exhibits important capacitive losses above 10 GHz (for $R_{MTJ} \approx 300\ \Omega$), rendering injection-locking in that range ineffective. Finally, increasing the applied field increases the critical current as well, which reduces the current range before electrical breakdown of the junction.

V.1.2 Detailed characterization : Frequency, linewidth and power

V.1.2.1 Branching behavior with field in LTMR samples

Now we can focus on the region of interest for the dynamics. Fig. V.2(a) shows the experimental PSD in the frequency domain for another MTJ elliptic 65×130 nm^2 na-

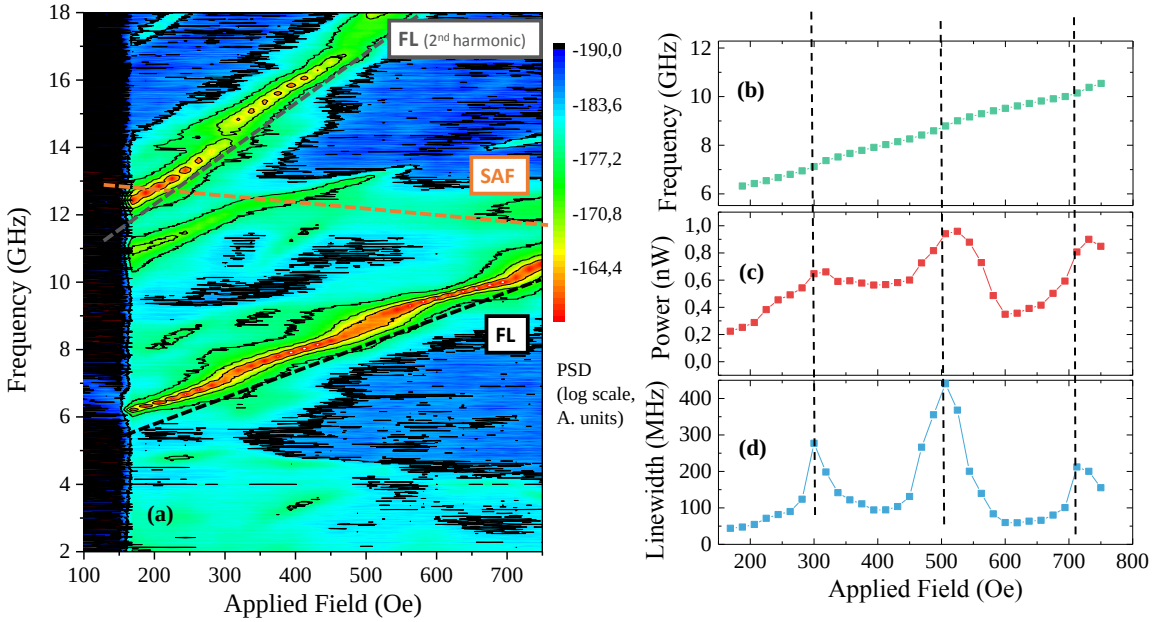

Figure V.2 – (a) PSD, (b) generation frequency, (c) integrated peak power, and (d) linewidth of the first harmonic FL as a function of the applied field for an elliptic 65×130 nm^2 nanopillar and a DC current $I_{DC} = 0.8$ mA. TMR = 38%, RA = 1.07 $\Omega\mu$m^2, $I_C \approx 0.6$mA and the field is applied in plane with a 15° angle with respect to the easy axis. The branching behavior for the FL (valleys of minimum linewidth and frequency jumps) is typical of LTMR samples and can be attributed to dynamical coupling between the SAF top layer and the FL.

nopillar, which corresponds to a "zoom" on the $0 - 1000$ Oe region of the previous PSD Fig. V.1 in the configuration of (d) where the applied current I_{DC} is above the threshold for self-sustained oscillations of the FL. The FL frequency ranges from 6 to 10 GHz while the SAF frequency (orange dotted line) goes from 13 to 12 GHz. The SAF mode is hardly visible for positive currents but its presence can be confirmed for negative currents (not shown here). At last, the second harmonic of the FL mode arising from m_x component of the magnetization oscillating at $2f$ is also noticeable in the PSD.

As we recall the sample studied here is a LTMR sample, meaning that its TMR and RA are reduced due to the presence of one or more pinholes in the junction. It turns out that a very valuable property LTMR samples is that compared to HTMR samples, their generation linewidth is reduced up to one order of magnitude [35] from 100 (HTMR) to a few tens (LTMR) of MHz [3].

In parallel, we also observe that the branching behavior is more pronounced in LTMR samples than in HTMR samples. It indicates that the linewidth reduction observed in LTMR goes along with a "branching behavior" with the applied field. Indeed, as one can witness in the Fig. V.2(d), the generated signal goes in our range of field through 3 successive intervals where the linewidth reaches a minimum, and then increases strongly at the transition. In Fig. V.2(b), the generation frequency also exhibits the branching behavior, with a frequency jump between branches and a relatively flat dependence with the field in the branches.

No definite explanation has been provided yet as to the reason why the branching behavior is much more pronounced in LTMR samples than in HTMR samples. However we can affirm that it is related to the presence of a pinhole in the junction. The indisputable effect of a pinhole in the junction is that it changes the current distribution within the junction. We can propose several explanations for the role of this peculiar current distribution due to the pinhole on the dynamic properties of the STO. First it leads to a spatially inhomogeneous magnetization profile of the FL close to the pinhole and hence modifies dynamic properties, second it enhances the *magnetic coupling* between the FL and the SAF : at the position of the pinhole the local current density is strongly enhanced, generating a important Oersted field [64], and finally at the pinhole location, the increased current density leads to an overall increase of the STT efficiency which enhances the *coupling via mutual STT* (or electrical coupling) between the FL and the SAF [28].

As we mentioned earlier, the effect of dynamical coupling between magnetic layers on excitation spectra remains an active subject of discussion on STOs. Hamadeh *et al.* [**?**] have recently observed in vortex STOs a very similar branching behavior with important variations of the linewidth (100 kHz to 1 MHz) on the perpendicular field taking the form of 3 consecutive valleys. They observe that the linewidth *increases* when the harmonics of the thick vortex layer (excited mode) cross with the harmonics of the thin vortex layer (overdamped mode). Linewidth broadening of the excited mode is attributed in the reference not to an increase of frequency tunability but rather to the creation of a new relaxation channel, i.e. when the harmonics cross the energy can be transferred from the self-sustained mode to the overdamped mode. It opens a new channel of relaxation, and decreases coherence times (see Fig. V.3) which translates into linewidth broadening.

3. When we say that the linewidth is LTMR samples is reduced compared to HTMR samples, we do not mean the *overall* linewidth, i.e. an a value of linewidth that would be an average of linewidth taken over the complete range of the applied field (for example 0 to 2000 Oe). We mean the best reachable linewidth, when the optimal working point (in applied magnetic field angle and amplitude) is selected

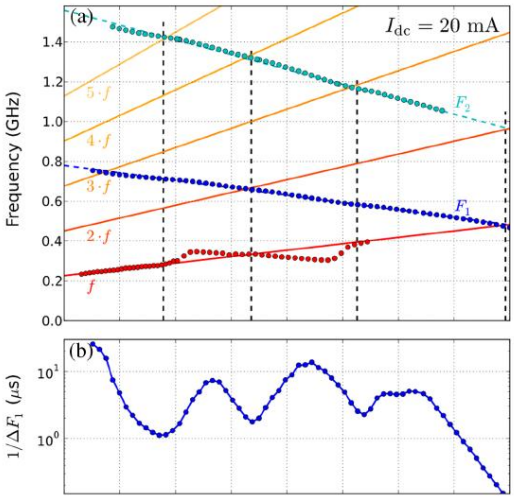

Figure V.3 – (a) Frequency of the first (blue), second (teal) harmonic of the self-sustained layer and frequency of the overdamped layer (red) as a function of the applied perpendicular field. (b) Inverse linewidth of F_1 as a function of the field. Similarly to our case in Fig. V.2, the linewidth goes through epochs of reduction and broadening with the applied field. Linewidth maxima are obtained when the harmonics of the two oscillations modes cross. From [**?**].

We can make a parallel between the case of Hamadeh *et al.* and our case. To do so, we make the simplifying assumption that the SAF excitations represent the overdamped mode, and the FL excitations represent the self-sustained mode. The dynamical dipolar coupling between the SAF and the FL is naturally present while the presence of the pinhole in our samples presumably leads to an increased STT coupling compared to intact junctions. In a very general manner, regardless of the effect on the coherence, coupling between oscillators leads to either a repulsive or attractive interaction. Now it has been shown in experiments and simulations that in our configuration the dipolar coupling induces a *repulsive interaction*, causing the frequencies of the two oscillators to be pushed away from each other at crossing points [49]. On the contrary the STT coupling creates an *attractive interaction* that causes the frequencies of the two oscillators to be drawn closer at crossing points [28, 29]. The balance between the two types of coupling can indicate whether we observe rather "frequency pulling" or "frequency jumps" at crossing points.

V.1.2.2 Proposition on the effect of dynamical coupling on frequency fluctuations

What follows in this segment of the manuscript is a very raw and phenomenological explanation of the effects of the linewidth broadening/reduction due to dynamical coupling in an attempt to present an intuitive (but very simplified) understanding of the situation. The underlying idea is to consider separately the frequency dependence of two interacting oscillators on the external control parameters, the applied field and the applied current which are the actual sources of frequency fluctuations in experiments. Then it is the sensitivity (the derivative) to the field (df/dH) and to the current (df/dI) at a given working point (H_0, I_0) which regulates frequency fluctuations for each oscillator. The idea is to incorporate in the sensitivity to the field and the current the frequency coupling between the two oscillators via $\partial f_1/\partial f_2$.

Evidently a much more refined approach is required in order to make quantitative predictions on the the effect of dynamical coupling on the generation linewidth and frequency.

In that respect we orient the reader to these publications [29, 30, 63] which address in better detail the effect of dynamical coupling on linewidth. Nevertheless, for we present here this simplified picture.

Let us suppose the closed system of two interacting oscillators or modes with respectively frequency f_1 and f_2, corresponding in our case to FL and SAF excitations. The two external control parameters are the DC current and the DC field which are sources of fluctuation respectively dI and dH. Using the chain rule, frequency fluctuations df_1 and df_2 can be decomposed as follows :

$$\begin{cases} df_1(I,H,f_2) &= \dfrac{\partial f_1}{\partial I}dI + \dfrac{\partial f_1}{\partial H}dH + \dfrac{\partial f_1}{\partial f_2}df_2 \\ df_2(I,H,f_1) &= \dfrac{\partial f_2}{\partial I}dI + \dfrac{\partial f_2}{\partial H}dH + \dfrac{\partial f_2}{\partial f_1}df_1 \end{cases} \tag{V.1}$$

In the above equation, frequency fluctuations in the first oscillator arise from : (i) current-induced fluctuations, i.e. how much current-induced noise is transferred to the first oscillator (when on its own), correspond to the *intrinsic* sensitivity with current $\partial f_1/\partial I$ (non-linearity) (ii) field-induced fluctuations. Likewise, $\partial f_1/\partial H$ measures the intrinsic sensitivity to field-induced fluctuations (iii) Fluctuations induced by the second oscillator. $\partial f_1/\partial f_2$ measures the frequency dependence of oscillator 1 on oscillator 2. This term is enhanced when the frequencies of the two oscillators cross, while it is almost zero far from crossing points.

We can rewrite the first line of Eq. V.1 by reinjecting the complete expression of frequency fluctuations df_2 from the second line. It yields :

$$df_1(I,H)\left[1-\frac{\partial f_1}{\partial f_2}\frac{\partial f_2}{\partial f_1}\right] = \left[\frac{\partial f_1}{\partial I}+\frac{\partial f_1}{\partial f_2}\frac{\partial f_2}{\partial I}\right]dI + \left[\frac{\partial f_1}{\partial H}+\frac{\partial f_1}{\partial f_2}\frac{\partial f_2}{\partial H}\right]dH \tag{V.2}$$

In this form frequency fluctuations of the first oscillator only come from current (dI) and field (dH) fluctuations. If we examine the fluctuations from the current, then we have isolated the two contributing factors : First the intrinsic current tunability of the first oscillator $\partial f_1/\partial I$ and second the contribution from the second oscillator which is the product of (i) $\partial f_1/\partial f_2$ (ii) $\partial f_2/\partial I$, the intrinsic current tunability from the second oscillator. The sensibility to field fluctuations can be decomposed in the same way.

The intrinsically strong non-linearity of STOs which gives them good tunability with current is also the factor that decreases coherence by increasing the influence of current fluctuations. Using expression V.2 then we see that by coupling oscillations one may actually tune the influence of current (and field) fluctuations for each oscillator. If we suppose that f_1 stands for the FL excitations, then according to KTS theory for an IPP mode the frequency redshift yields $\partial f_1/\partial I \leq 0$. Now at crossing points between the SAF and the FL frequency coupling causes the term $\partial f_1/\partial f_2$ to be important, and the contribution from the SAF mode to FL fluctuations becomes important as well. Then if $\partial f_1/\partial f_2.\partial f_2/\partial I$ is *positive*, it will *counterbalance* the frequency redshift, decrease the overall sensitivity with current and eventually lead to a decrease of frequency fluctuations. Otherwise if $\partial f_1/\partial f_2.\partial f_2/\partial I$ is *negative*, then it will *enhance* the frequency redshift and the overall sensitivity with current and as a consequence the opposite effect arises and frequency fluctuations are enhanced. Once again, the same reasoning applies to field fluctuations.

In Fig. V.4 are shown the experimental frequency, peak power and linewidth for the

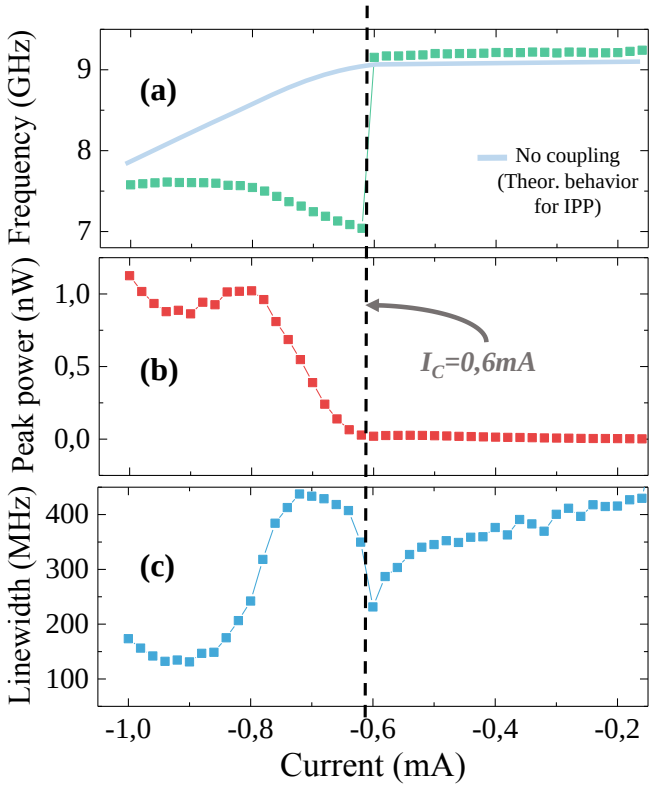

Figure V.4 – Experimental data for Generation frequency (a), peak power (b) and linewidth (c) of the first harmonic free layer function of the applied current. Same sample as in Fig. V.2 in a minimum linewidth valley for $H = 375$ Oe. Due to pinholes it exhibits a LTMR-like behavior with current as in [35], with : (i) a frequency discontinuity at the critical current value (ii) frequency blueshift over the critical current and then a almost flat df/dI current sensitivity. The sensitivity to current is inversely proportional to the linewidth over the critical current. (a) in solid line (light blue) the expected behavior for an uncoupled IPP mode according to the KTS model (HTMR samples).

same sample but as a function of the current instead of the field. The applied field of $H = 375$ Oe has been chosen in order to be in a valley of linewidth minimum. As we can see by comparing Fig. V.4(a) and (c), above the critical current the linewidth is directly correlated to the sensitivity with current df/dI.

The dependence with current is characteristic of LTMR samples (i.e. with a pinhole in the barrier) as in [35] : we observe an important frequency discontinuity at the critical current accompanied with frequency blueshift (increase with current) above the critical current. This type of dependence is not predicted by the KTS model : in this configuration, the excited precession is expected to be of IPP-type, and as it was confirmed by macrospin simulations in the third chapter (see Fig. III.1), increasing the DC current over the critical current leads to a frequency redshift with no discontinuity in frequency (theoretical behavior in blue line in Fig. V.4).

Here we have a presented an argument as to why this unexpected behavior of the linewidth and frequency with current can be attributed to the coupling between the top SAF layer and the FL. In its current version the KTS model does not take into account dynamical coupling between layers, and the presented macrospin simulations suppose that the FL is not coupled with the other magnetic layers. We also remark that predictions using the KTS model require the macrospin approximation, which may not be strictly respected experimentally, so that we have this particular type of behavior with current.

Using Eq. V.2, our analysis provides an approach to explain qualitatively what is the influence of the coupling on the frequency and linewidth vs current characteristics in LTMR. We decompose the current sensitivity df/dI in two parts, the intrinsic sensitivity of the FL $\partial f/\partial I$ and the "coupling-induced" sensitivity $\partial f/\partial f_2.\partial f_2/\partial I$. Following this decomposition, the blue line in Fig. V.4(a) indicates the intrinsic sensitivity (i.e. in the absence of dynamical coupling between the magnetic layers) as predicted by the KTS model while the experimental data in green df/dI is the combination of both intrinsic and "coupling-induced" sensitivity [4].

V.2 Characterization of synchronous dynamics at $2f$

We now examine the STO dynamics in the presence of an RF current source at $2f$. In the previous section we looked at the dynamics of a MTJ-based STO without RF current and we made a few observations :

• *Behavior with applied field.* We have seen that the linewidth goes through important variations with the field, and we observe frequency jumps as well. These variations are not expected from the KTS model.

• *Behavior with DC current.* At the critical current we observe a frequency discontinuity, and above the critical current we observe a frequency blueshift rather than the redshift for IPP predicted from the model and confirmed by simulations.

• *Linewidth.* The results as shown in Fig. V.4 show that the linewidth is naturally correlated to the current sensitivity df/dI and the field sensitivity df/dH as well. As we are looking for the minimum linewidth conditions to carry out injection-locking experiments,

4. The transition from redshift to blueshift with current in LTMR samples can be understood by decomposing the sensitivity with current. However the frequency discontinuity at the critical current is a particular issue. A possible explanation is that when the critical current is reached, an important frequency coupling sets up and the feedback term on the left hand side of Eq. V.2 goes close to 1. Then the overall frequency sensitivity df tends to infinity, which creates a frequency discontinuity.

the unusual branching behavior of LTMR samples will actually be beneficial if we pick the appropriate working point (I_0, H_0). In particular, the field H_0 is picked is that it corresponds to a center of a linewidth "valley" (limiting df/dH). The current I_0 is chosen so that $I_0 > I_C$, but also in conditions where $df/dI(I_0)$ is minimum.

Experimental measurements in the autonomous regime point towards the fact that the SAF and the FL are dynamically coupled but it remains difficult to give a definite conclusion as to the origin of the coupling. Both dipolar coupling and coupling via the STT are playing a role on the dynamics, but we have not evaluated their relative impact. Nevertheless, the presence of a pinhole in LTMR samples presumably leads to an increase of STT coupling due to the enhancement of the current density at the pinhole location. In contrast, the dipolar coupling may not be as much affected by the presence of the pinhole in the barrier - or in other terms, the dipolar coupling should be of similar magnitude in HMTR and LTMR samples.

Compared to HTMR samples (no pinholes) which exhibit an overall high generation linewidth, the increased coupling in LTMR is a double edged sword : by tuning the field and current sensitivities (see Eq. V.2), the coupling creates new conditions in (I, H) that, if fulfilled, will greatly reduce frequency fluctuations (and the linewidth as well). However the coupling renders the analysis and the comparison with the analytical model much more tedious because the KTS model does not take into account the interaction between several modes. The most striking discrepancy with the model is the observed frequency discontinuity at the critical current accompanied with a frequency blueshift, which does not correspond to the predicted continuous frequency redshift of the IPP.

V.2.1 Evolution with the source frequency f_e

Regardless of the effect of the coupling between the FL and the SAF, we report here the dynamical behavior of our LTMR samples under a RF current applied at twice the generation frequency. In practice synchronization is accompanied by important reduction of the linewidth in the locking-range and frequency entrainment of the STO frequency by the RF source.

We start by monitoring the effect of the external source on the STO with the particular working point of $I_{DC} = -2.3$ mA and $H = 650$Oe, above the critical current $I_C = -2.05$ mA. The sample used for measurements in this section is a LTMR sample of 135 nm in diameter, TMR = 48%, RA = 1.2 $\Omega/\mu m^2$. It exhibits a dynamical behavior above the critical current similar to the sample of Fig. V.4. At the operation point and without RF current, the signal exhibits a linewidth of $\Delta f = 75$ MHz, $P = 2$ nW and $f_0 = 8.0$ GHz.

Fig. V.5 shows the evolution of the PSD of a LTMR sample when the RF source frequency is swept close to $2f$ for three values of RF power. The PSD is acquired using a spectrum analyzer with a RBW of 100 kHz and a span of 1 GHz. Using the electrical model and the calculations introduced in Sec. IV.2 for the device impedance we can estimate with sufficient accuracy the RF current i_{RF} that is injected in the junction. From there the RF/DC current ratio ϵ is extracted. In this case the RF power of (a)-10.5 dB (b)-8.5 dB and (c)-6.5 dB correspond respectively to current ratios of $\epsilon = 0.33$, $\epsilon = 0.42$ and $\epsilon = 0.49$. Throughout injection-locking measurements, we have made sure that the condition of weak forcing is respected, i.e. $\epsilon < 1$. In addition the DC current is chosen so that the supercriticality $\zeta = I/I_C$ is below 1.3 (approximate domain of validity for the

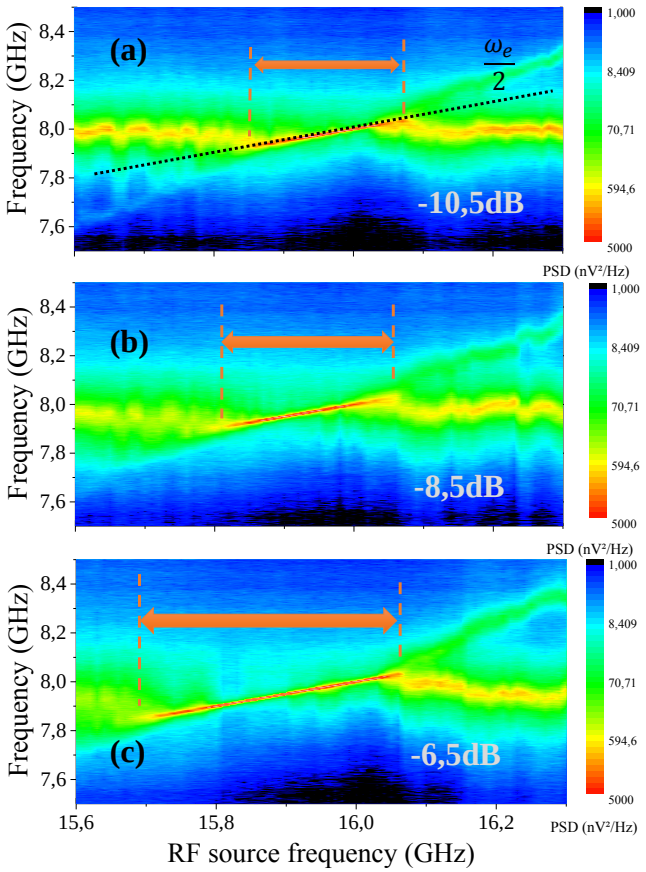

Figure V.5 – PSD of the STO signal as a function of the external source frequency f_e for various RF powers (a)-10.5dB (b)-8.5 dB (c)-6.5 dB. Applied field of $H = 650$ Oe and $I = -2,3$ mA, yielding $f_0 = 8$ GHz. In the synchronization region the spectral purity of the output signal is substantially enhanced and the STO frequency follows that of the external source as well. As predicted, the synchronization region increases alongside the RF power. Outside the synchronization region (orange arrow) the beat frequency is visible via the presence of sidebands.

KTS model [83]).

In the locking range the STO frequency follows half that of the external source (frequency-locking) as expected and frequency fluctuations are drastically reduced by the much more stable RF source. This behavior is typical of injection-locking experiments, and was experimentally reported several times in STOs of type spin-valve [75, 27] MTJ [72, 19] and vortex [57, 51].

Fig. V.5 also shows us the influence of the forcing strength (the RF power). The most immediate effect is that the synchronization region increases (orange arrow in Fig. V.5) as the forcing strength increases. Likewise, as the forcing strength increases, the effect on linewidth narrowing increases as well. This simultaneous effect of the forcing strength on the locking-range and linewidth narrowing was already discussed in [72].

To quantify the linewidth narrowing effect, Fig. V.6 shows the frequency and linewidth using a Lorentzian fitting function versus the detuning $f_e - 2f_0$. As we can see the linewidth is substantially reduced from 60 MHz outside the locking-range to 200 kHz in the middle of the synchronization region. It corresponds to a linewidth narrowing between two and three orders of magnitude, which is significant compared to the previous report of injection-locking using the same samples with a reduction from $df = 200$ MHz to $df = 20$ MHz in [72]. Recently Dürrenfeld *et al.* have observed a similar intensity in linewidth narrowing in MTJ STOs from $df = 30$ MHz to $df = 200$ kHz [19].

In the inset of Fig. V.6 is presented the evolution of the peak power in the synchronization region. The peak power decreases from 5 nW to 3 nW at the extremities of the locking-range and goes to 4 nW in the middle of the locking-range.

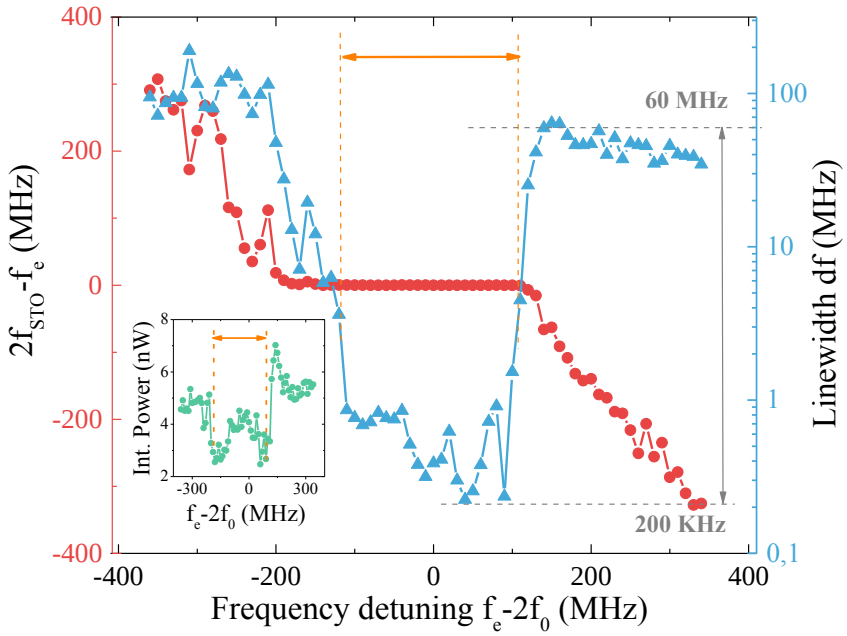

Figure V.6 – Forced frequency difference (red) $f_{STO} - f_e$ and linewidth (blue) df versus detuning $f_e - 2f_0$ for $f_e \approx 2f_0$, with $I = -2.3$ mA and $\epsilon = 0.52$. inset : Integrated peak power vs detuning. At zero detuning, the linewidth reaches a minimum of 200 kHz. Orange arrows indicate the synchronization region.

According to the analytical model developed in Chapter II, at $2f$ power variations δp_s in the locking-range are directly linked to frequency variations via the frequency-amplitude coupling, i.e. $\delta p_s = N/\delta\omega_s$. It results in a linear "power-locking" dependence with the RF source frequency (see Fig. III.2), in opposite fashion to the STO frequency in the locking-range.

However, having this linear dependence of the power with the source frequency relies on the assumption that the integrated peak power P is proportional to the normalized power $p = |c|^2$ utilized in the KTS model. In other words, that the integrated peak power corresponds to a measure of the precession amplitude.

In practice, the integrated peak power depends on the precession amplitude, but what we measure is an electrical signal, which includes other contributions. In the best case the power is directly proportional to the intensity of the magnetoresistive signal coming from the dynamic resistance variation due to precession, which is obtained by projection of the magnetization trajectory on the polarizer axis. In this situation the magnetoresistive signal depends on two factors, the precession amplitude of the FL and the projection of the symmetry axis of the precession trajectory on the polarizer axis.

From our analytical derivation we have come to the conclusion that the effect of the RF current at $2f$ is to slightly increase or decrease the oscillation amplitude in the synchronization region to adjust the precession frequency to that of the external source. We do not predict that the RF current tilts the symmetry axis of the precession trajectory. However recent studies on the spin-torque diode effect (i.e., the conversion of a RF current into a DC bias in a STO) conducted by Miwa *et al.* [58] concluded that the injection of a RF current at the FMR frequency actually lead to a tilting of the symmetry axis of the precession angle, and it is this tilting that is the essential contribution to the spin-torque

diode effect.

So, knowing that for our experiments we need to break the symmetry to observe an electrical signal on the first harmonic (i.e. the magnetic field is applied in-plane with a 15° angle with respect to the polarizer axis), we can expect that a similar tilting of the precession axis due to the injected RF current happens inside the synchronization region. As a consequence, the integrated peak power may be modified due to this effect, which leads to the unexpected power dependence in the inset of Fig. V.6. Finally, we also note that the integrated power is extracted using a Lorentzian fit of the peak in the PSD which presupposes that in the synchronization region the peak has still the attributes of a Lorentzian function. This is a strong hypothesis which is not necessarily fulfilled, explaining the discrepancies with the model.

V.2.2 Evolution of the locking-range with RF and DC current

V.2.2.1 Extraction of the locking-range with thermal noise

We recall that in Chap.II and III we analyzed synchronization to an RF current with the following thought in mind : what is the role played by frequency-amplitude coupling on the frequency locking process ? To do so we investigated amplitude changes in the synchronized regime, and using the KTS model we managed to obtain an expression for the locking-range at $2f$ which evidenced in an intuitive way the relation between the coupling sensitivity and the frequency shift $Np_0 = \omega_0 - \omega_r$ (see Eq. II.65). This expression was then verified and gave very satisfactory quantitative agreement with results from macrospin simulations (Fig. III.15(a)). In comparison, correction factors for the analytic expression of the coupling sensitivity at f were required to obtain an acceptable quantitative agreement (Fig. III.15(b)).

The locking-range is a quantity that has been often extracted from injection-locking experiments in STOs. In [75, 21, 72, 19], the locking-range is extracted as a function of the forcing amplitude, i.e. the RF current amplitude, i_{RF}. The results obtained are consistent with each other and the classical theory of synchronization, namely the locking-range increases with forcing amplitude i_{RF}. In the case of [75] and [19] a clear linear dependence with i_{RF} is evidenced.

Now it remains difficult to quantitatively compare the locking-range measured at room temperature with the locking-range from the model which is defined at 0K. Fig. V.7 represents schematically the effect of thermal noise on typical detuning plots. We see that in the absence of thermal noise (solid black line) the frequency-locking interval (locking-range) has clear boundaries. In this interval the frequency-locking is perfect, in the sense that the oscillator frequency *exactly* follows the frequency of the external source.

But when thermal noise comes into play, strictly speaking if the noise is unbounded [5] then frequency and phase locking is achieved only at zero detuning [67] and the locking-range is reduced to a point. Then how to delimit the locking-range in the presence of a strong noise ? We obviously want a value for the locking-range that does not depend on the intensity of the noise and that corresponds to the locking-range at 0K, i.e. $\Delta\Omega$ in Eq.II.3.2 or Eq.II.76. If the criterion for the locking-range is “apparent frequency-locking”, then it does not work in our case : looking at Fig. V.7 we see that for a strong thermal

5. A gaussian noise is unbounded

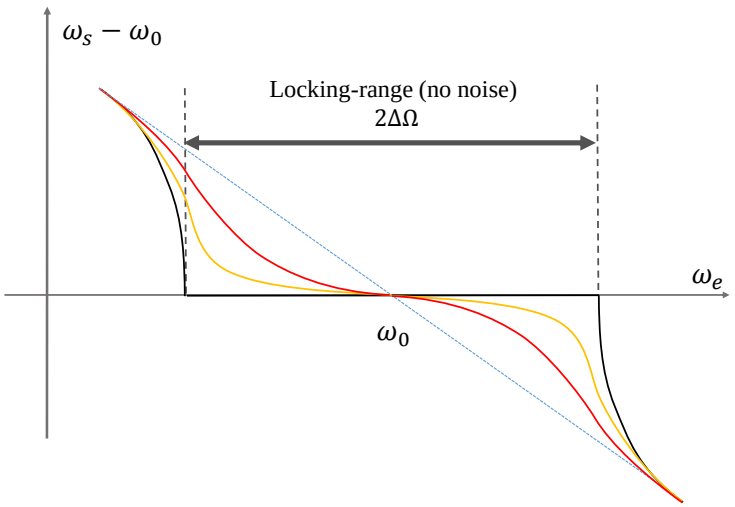

Figure V.7 – Schematic representation of the influence of thermal noise on the frequency-locking process. The dashed blue line corresponds to the STO frequency in the absence of forcing. At 0K (solid black line) the frequency-locking interval (locking-range) has clear boundaries and corresponds to $2\Delta\Omega$ as in the phase equation II.3.2 or II.76. (yellow) weak thermal noise (red) strong thermal noise. Due to noise, boundaries of the locking-range are blurred.

noise (red line) the interval of "apparent frequency-locking" is much reduced compared to the case of a weak thermal noise (yellow line). Evidently it will not correspond the value of the locking-range at 0 K.

In order to establish a more dependable criterion for the estimation of the locking-range, we will measure the variation of linewidth in this situation. Experimentally synchronization induces important linewidth narrowing and it is the most characteristic signature of efficient synchronization. Fig. V.8 presents the method used for the experimental extraction of the locking from df versus ω_e plots.

First (see Fig. V.8(1)), the raw data is plotted in linear scale in the y axis. Here the representation in linear scale makes it difficult to appreciate the linewidth narrowing effect, especially when the reduction is more than one order of magnitude.

This is why we compute the logarithm of the linewidth (2) : it limits linewidth fluctuations outside the locking-range and the effect of detuning on the linewidth within the locking-range is much easier to perceive. In addition, we are looking for a method to obtain the locking-range by fitting and not graphical reading. The idea is to obtain the locking-range by fitting a peak function to the linewidth vs detuning plots. Comparing (1) and (2), it is clear that it is in log scale that the linewidth vs detuning plots resemble most to a peak function.

In (3) we apply a two point FFT filter to smooth the data and limit signal instabilities, and finally in (4) we fit the result by a peak function (red line), an asymmetric double sigmoidal [6]. From there the locking-range is obtained by fitting, where it corresponds to the half-linewidth at half maximum of the function (shown in (4) of Fig. V.8).

We use the following criterion : the extremities of the locking-range are reached when, in log scale, half of the linewidth reduction has taken effect. Translated mathematically,

6. This peak function has the advantage to take into account peak asymmetry, which comes from the asymmetric behavior of the linewidth in the locking-range

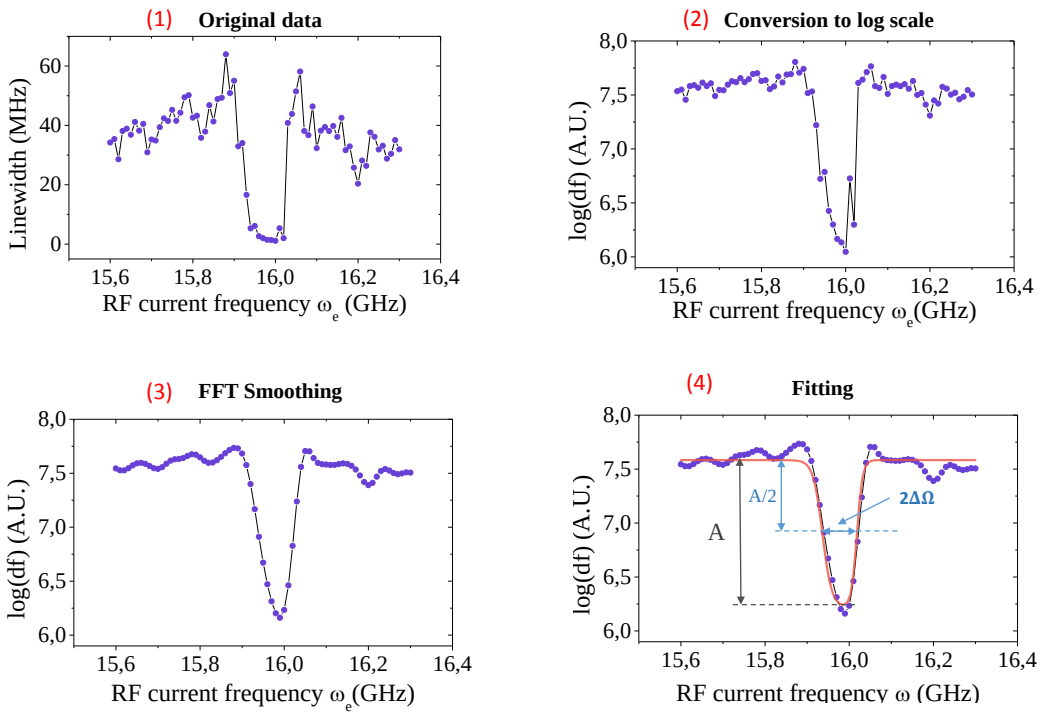

Figure V.8 – Extraction of the locking-range from experimental linewidth versus detuning plots. The data is transformed in log scale (2), then smoothed (3) and finally fitted (4) by a peak function (solid red line). The locking-range is obtained by fitting of the half-linewidth at half maximum.

this means :

$$\log\left(df(\Delta\Omega)\right) = \frac{\log\left(df_{max}\right) - \log\left(df_{min}\right)}{2}.$$

V.2.2.2 Evolution of the locking-range with ϵ and I_{DC}

Here we present the results of the experimental extraction of the locking-range in our MTJ samples for a RF current injected at $2f$. We start with verifying the dependence of the locking-range on the RF current amplitude. Measurements were performed on the LTMR sample used in this section (see Fig. V.5) in the same configuration. Here we will vary the DC and RF current amplitude, and the RF current frequency as well[7]. Ultimately we want to verify the $2f$ model by checking the equivalence between the coupling sensitivity and the frequency shift $\omega_0(I_{DC}) - \omega_r = Np_0$.

Fig. V.9(a) shows the frequency versus DC current dependence in the autonomous regime, and Fig. V.9(b) presents the dependence of the locking-range on ϵ for three values of DC current above the threshold. The critical current $I_C = -0.208$ mA is marked by a frequency discontinuity in the f vs I characteristic, yielding a shift in frequency of about 400 MHz. In Fig. V.9(b) we show the evolution for three values of the DC current only. However the sample was robust enough for dynamic measurements on eight values of the DC current, from -2.2 mA to -2.5 mA with a step of 0.05 mA. For each value of the DC current, the RF source power was set from -11 dBm to -6 dBm by eleven steps of 0.5 dBm, corresponding to current ratios $0.2 < \epsilon < 0.6$. Then the RF source frequency ω_e

7. The applied field direction and amplitude (650 Oe) remains constant throughout measurements of the locking-range

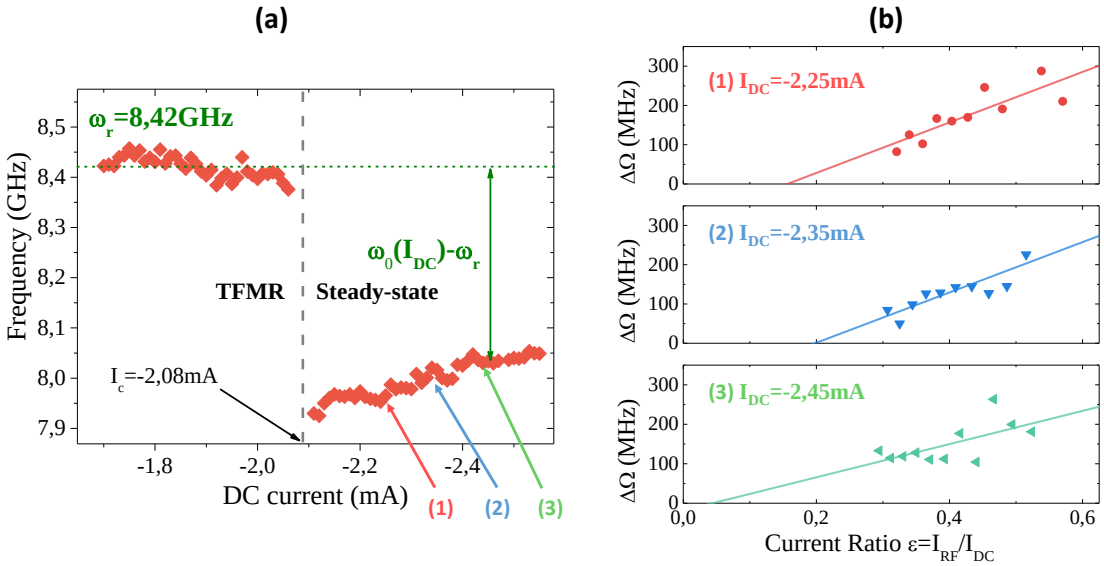

Figure V.9 – (a) Experimental STO frequency vs DC current in the absence of RF current. As in Fig. V.4, at the critical current $I_c = -0.208$ mA we observe a frequency discontinuity typical of LTMR samples. (b) Evolution of the locking-range with the forcing amplitude $0.2 < \epsilon < 0.6$ for several values of DC current (1),(2),(3) in (a). The locking-range follows a linear dependence with ϵ (solid lines : fit).

is swept close to $2f$ in steps of 10MHz to plot the generation linewidth with respect to ω_e and obtain the locking-range using the extraction method presented above.

Fig. V.9(b) confirms that the locking-range follows a linear dependence with the forcing amplitude ϵ as expected. We remark that the linear regression does not go through the origin, but crosses the x axis for $\epsilon > 0$. According to theory at 0K (Eq. II.65), there is no threshold effect, in the sense that there is no critical value ϵ_{min} above which synchronization is enabled. The threshold effect in Fig. V.9(b) cannot be explained with our model. However we possibly have a threshold coming from the fact that we do not have confirmation that the locking-range that we extract here in the presence of strong thermal fluctuations corresponds exactly to the locking-range at 0K.

Fig. V.10 shows the experimental results for the coupling sensitivity as a function of the DC current. We extracted the coupling sensitivity $\Delta\Omega/\epsilon$ for 7 values of the DC current using the linear fit of Fig. V.9(b). Then the coupling sensitivity is compared with the frequency shift $\omega_0(I_{DC}) - \omega_r$ of Fig. V.9(a).

We recall the prediction from the model : under strong ellipticity of the IPP trajectory the coupling sensitivity for synchronization to a RF at $2f$ is equal to the frequency-shift (Eq. II.65), and it has been verified by macrospin simulations. The underlying assumption leading to this statement is that the frequency shift is due exclusively to a change of precession amplitude (i.e. $\omega_0(I_{DC}) - \omega_r = Np_0$).

The experimental data for the coupling-sensitivity presented in Fig. V.10 indicate that indeed, in our range of currents $\Delta\Omega/\epsilon \approx \omega_0(I_{DC}) - \omega_r \approx 400$ MHz and we have a good quantitative agreement. Nevertheless, we cannot declare yet that our expression for the coupling sensitivity has been validated experimentally. The main reason why we must be cautious for the interpretation is that LTMR samples do not have the predicted f vs I_{DC} dependence for the IPP. According to macrospin simulations and the KTS model above the critical current we should observe a continuous frequency redshift with the current as

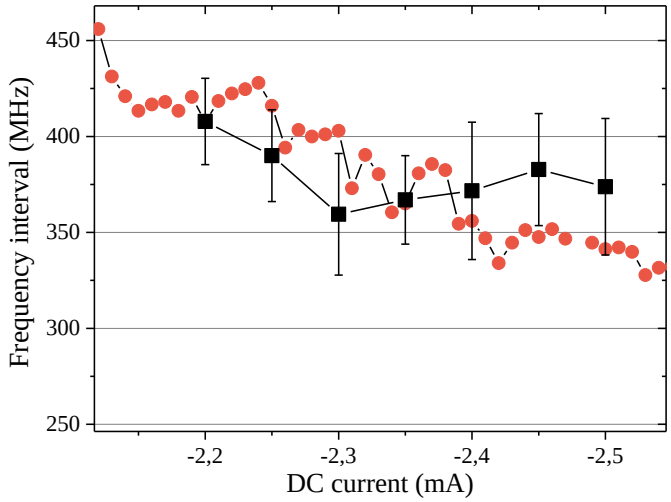

Figure V.10 – Comparison of the coupling sensitivity $\Delta\Omega/\epsilon$ (black dots) and the frequency-shift $\omega_0(I_{DC})-\omega_r$ (red circles) with respect to the DC current. The coupling sensitivity is obtained by linear fit of the data in Fig. V.9. In our range of currents, we have $\Delta\Omega/\epsilon \approx \omega_0 - \omega_r \approx 400$ MHz.

in Fig. III.1(a). Clearly the frequency discontinuity at the critical current accompanied with a slight frequency blueshift that we obtain experimentally cannot be explained by the KTS model nor macrospin simulations (at least without dynamical interlayer coupling).

This leads us to the blocking point. Experimentally, we verify one part of the equation, i.e. $\Delta\Omega/\epsilon = \omega_0(I_{DC})-\omega_r$. However, the second part $\omega_0(I_{DC})-\omega_r = Np_0$ remains a question in LTMR samples because we cannot affirm that the frequency discontinuity comes from a rapid increase of the precession amplitude. As a consequence, the theoretical prediction for the coupling sensitivity at $2f$ has not clearly been verified yet and we have a partial result here. Indeed the quantitative agreement in Fig. V.10 is worth noting but there is a missing link between the KTS model and the experimental f vs I_{DC} characteristic in LTMR samples which limits the validity of our interpretation.

V.3 Extended discussion : Phase relations and coherence in the synchronization region

V.3.1 Time dependence of the phase difference : Phase-slips

In the absence of noise, within the synchronization region by definition the phase-difference between the external force and the oscillator is constant. As shown in Fig. III.5(b), using macrospin simulations we have verified that it is the case in our configuration. However just outside of the synchronization region we have a quasiperiodic motion of the phase-difference : Indeed Fig. III.5(b) (points (1) and (3)) we observe alternate epochs of "almost constant" phase difference with rapid phase-slips.

Thermal noise induces fluctuations of the STO phase, and strictly speaking within the synchronization region the phase difference is not constant anymore. The behavior of the phase-difference under thermal noise in the synchronization region is comparable

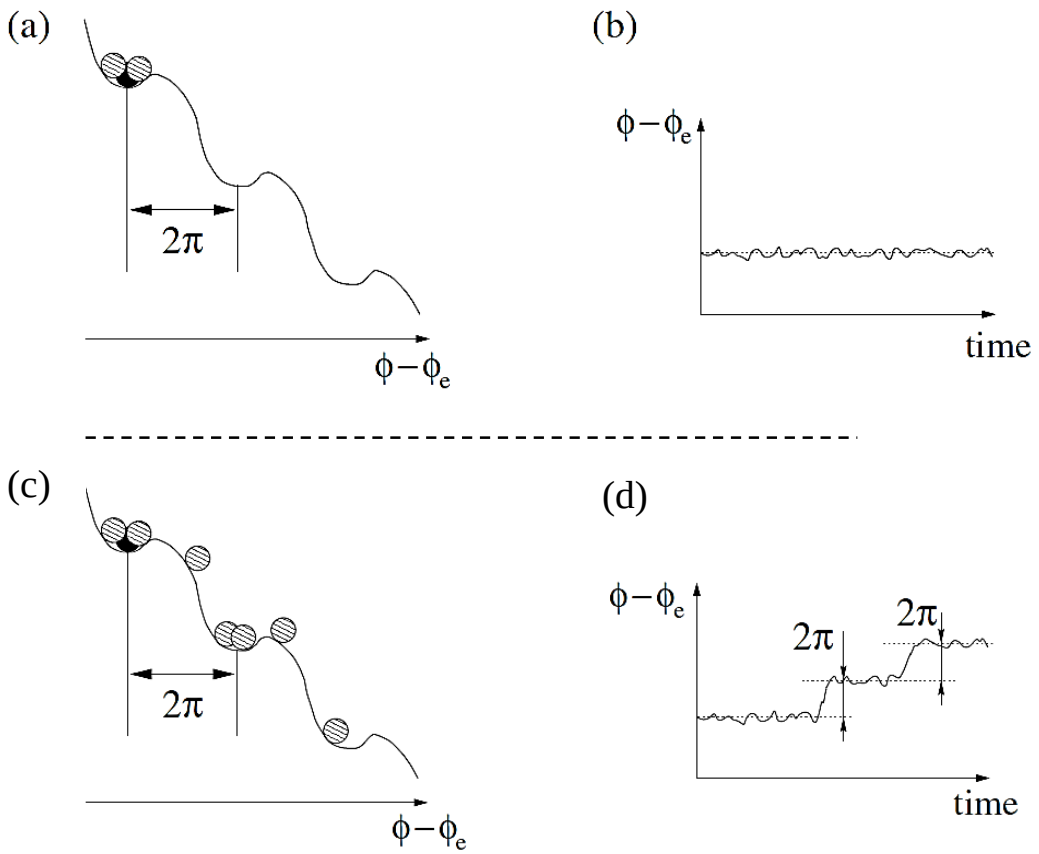

Figure V.11 – Influence of the noise on the forced phase dynamics. (a)(b) Case of a weak bounded noise. The phase-difference fluctuates close to the equilibrium position but does not escape the potential well. (c)(d) Case of an unbounded noise (thermal noise). The phase difference oscillates close to the equilibrium position ψ^0 as well but at moments the noise supplies enough energy to overcome the potential barrier. As a consequence, the phase difference jumps from ψ^0 to equivalent states $\psi^0 \pm 2k\pi$. The sign of the detuning will determine if the phase-difference more frequently jumps in the positive direction $+2k\pi$ (as in (c)) or negative direction $-2k\pi$. From [67], Sec. 3.4.2.

to that of the phase-difference outside the synchronization region without noise, i.e. the noise generates phase-slips as well.

To be more precise, the effect of an unbounded noise on the phase-difference can be decomposed in two parts, the fluctuations around the equilibrium position of the phase difference (as in the case of a weak bounded noise, see Fig. V.11(a)(b)) and the appearance of phase-slips when the noise is unbounded (see Fig. V.11(c)(d)). As a consequence, we can expect phase-slips in our system since measurements are performed at room temperature. In Fig. V.12 we report experimental measurements of the phase-difference $\psi = 2\phi - \phi_e$ and its evolution with time.

First we describe briefly how to experimentally acquire the phase-difference ψ. The RF source signal is split so that the most part is injected in the pillar and the remaining portion of the signal is plugged into the second channel of the oscilloscope. Then the RF signal from the pillar is amplified and injected in the first channel of the oscilloscope, and both signals are collected simultaneously and saved. Finally we apply the Hilbert

transform to each signal and we obtain the phase which is then "unwrapped" [8] and the difference $\psi = 2\phi - \phi_e$ is then computed.

Fig. V.12(a) shows the results of the extraction of the phase difference for various values of the RF current frequency inside the locking-range for a LTMR sample. We see the typical signatures of thermal noise on the phase-difference as in Fig. V.11, where the phase fluctuates close to a constant value ψ_0 (weak bounded noise) and eventually the phase slips to an equivalent value $\psi_0 \pm 2\pi$ (strong noise). Fig. V.12(b) shows the associated STO frequency and linewidth for the same sample indicating frequency-locking and linewidth reduction. The center of the synchronization region (maximum linewidth reduction) is reached for $\omega_e = 15.95$ GHz.

We note that in Fig. V.12(a), the phase-difference is plotted for *positive detunings* only, i.e. $\omega_e \geq 2\omega_0$. According to Fig. V.11, it means that the phase potential is tilted in one direction favoring downwards jumps of the phase difference, i.e. of -2π. Here we do not observe enough phase-slips to positively confirm which direction is favored for the phase-slips. There is approximately one phase slip every 100 ns, which is in the order of one phase-slip for 1000 periods of the STO. Moreover, we observe asymmetry in the phase-slip process, namely downward and upward jumps do not happen on the same time-scale. Downward phase jumps take about 10 ns while upwards jumps take effect within a much quicker time window, in the order of a tenth of a nanosecond [9].

Another way to characterize synchronization by analyzing relations between the phases is to use the *stroboscopic technique* (see 6.3.3. in ref. [67]). The principle works as such : rather than plotting the phase-difference ψ continuously with time, we acquire the phase ϕ (mod(2π)) of the driven oscillator with the period of the RF source, i.e. we record $\phi(t_k)$, where $t_k = k.T_{str}$ with $k = 1, 2, 3...n$ and where T_{str} is a multiple of the period of the external force T_e. In our case of synchronization at $2f$, we record the phase every 2 periods of the external force (or one period of the forced STO frequency ω_s), so that $T_{str} = 2T_e = \pi/\omega_e \approx= 0.125$ ns. If there is no synchronization, then the phase $\phi(t_k)$ will take random values. Otherwise in the synchronized state, $\phi(t_k) = \phi(t_{k+1}) = \phi(t_{k+2})$ and so on, so that we should observe a constant value with time. This is called a phase stroboscope, and this technique was used to characterize synchronization in very different contexts (spiking of electroreceptors of a paddlefish in ref. [99] or analyzing cardiorespiratory interactions in humans in ref. [79]).

Fig. V.13 shows an example of an experimental phase stroboscope for synchronization to a RF current at $2f$. According to expectations we see that the phase $\phi(t_k)$ converges to an equilibrium value ϕ_0 indicating phase locking. We make a few observations. First, the phase noticeably fluctuates around the equilibrium state, which indicates the effect of the noise is quite important. Second we see that there seem to be two equilibrium states, ϕ_0 and $\phi_0 \pm \pi$, which was not expected. Finally, the time required to switch from one state to the other is of about 8 ns. It means that the switch is performed within more than 100 periods of the STO, which is actually very slow for a slip of the phase.

8. After the Hilbert transform, we obtain a phase that is defined in the $[0, 2\pi]$ interval. In order to have a linearly growing phase, we add 2π after each complete rotation of the phase.

9. We note our extraction technique for the phase difference has limitations : the phase is numerically unwrapped so that it grows linearly and as a consequence the unwrapping process causes sometimes unwanted additions or subtractions of 2π to the phase. This may be at the origin of the rapid upwards phase-shifts that we observe.

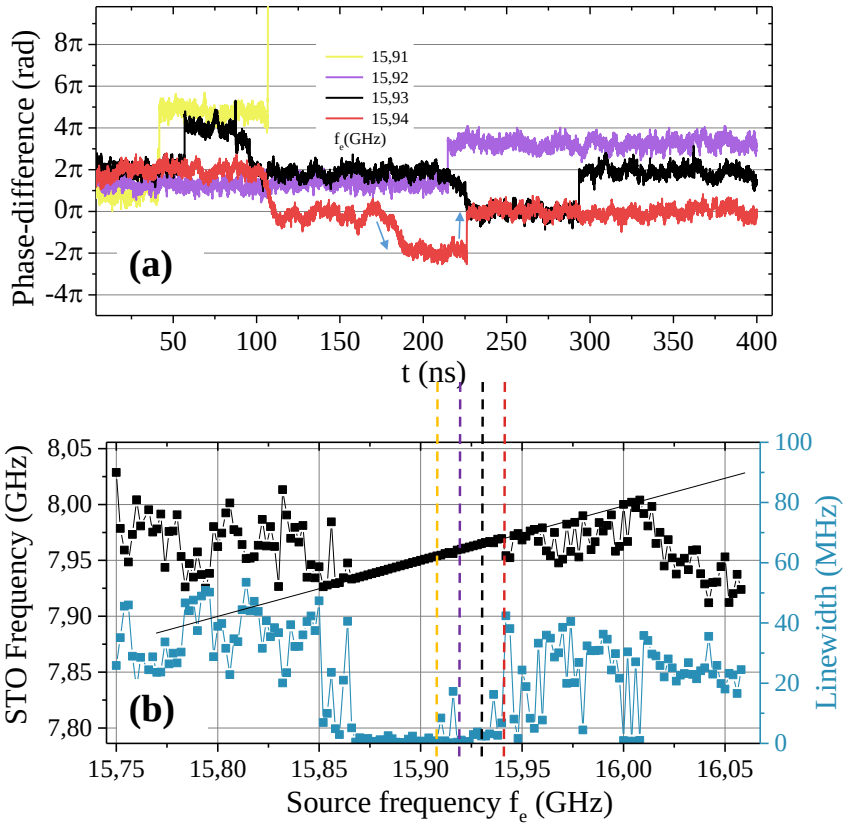

Figure V.12 – (a) 400ns time-trace of the phase-difference $\psi = 2\phi - \phi_e$ in the synchronization region for several ω_e. We observe plateaus with rapid phase jumps of $\pm 2\pi$. The RF source power is set at -8dBm and data were collected using the experimental setup represented in Fig. IV.7. (b) Evolution of the STO frequency (black) and linewidth (blue) as a function of the RF source frequency. Colored vertical lines indicate frequencies at which the phase-difference is plotted in (a).

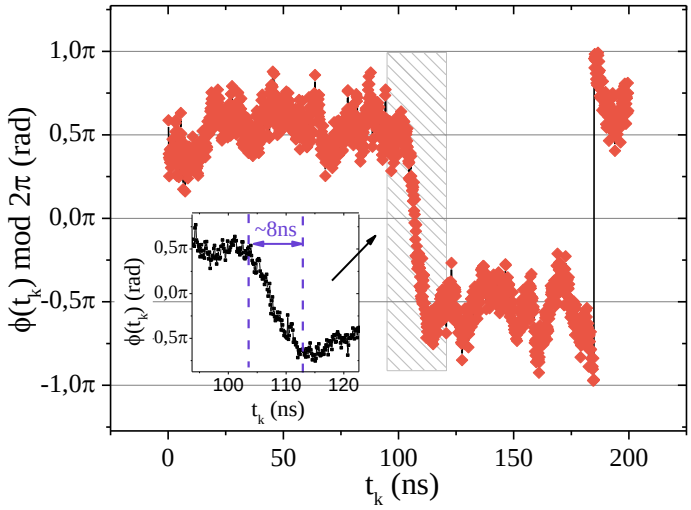

Figure V.13 – Example of experimental phase stroboscope using the data from Fig. V.12. The phase of the STO is observed with twice the period of the RF source. Here, $\omega_e/2\pi = 15.94$ GHz, yielding a time interval between two points of 0.125 ns. The phase fluctuates close to a constant value $\phi_0 = \pi/2$ and at 100ns drops to $\phi_0 - \pi = -\pi/2$. (Inset) zoom on the phase-slip. About 8 ns is required to adjust to the new value, accounting to more than a 100 periods of the STO.

V.3.2 Distribution of the phase-difference

Now that we have looked at the time evolution of the phase and shown that the relations between the phases evidence a synchronization, we can examine the distribution of the phase difference ψ mod(2π) in the synchronization region. We will try to link the coherence of the signal with the characteristics of the distribution of the phase difference.

We recall that, in the perspective of realizing STO devices for frequency generation, the synchronization approach was adopted because it yields the best promise to increase the signal properties, and in particular we have seen that for sufficient power of the RF source it dramatically decreases the linewidth of the signal. Now the analysis of the phase-difference can help us provide a deeper insight as to how this linewidth reduction takes effect.

If we go back to the time-evolution of the phase difference ψ, we saw that in the synchronization region the phase-difference fluctuates close to a constant value ψ_0 and occasionally jumps to an equivalent state $\psi_0 \pm 2\pi$. Then if ψ is wrapped around the trigonometric circle (i.e. we take ψ mod(2π)), all equivalent states $\psi_0 \pm 2n\pi$ merge together. As a consequence we can plot the *distribution* of ψ in the interval $]-\pi, \pi]$ by counting the number of occurrences.

Fig. V.14(a) shows an example of the distribution of ψ mod(2π) for several RF source frequencies, inside and outside the locking-range, obtained from plots such as Fig. V.12. The black curve corresponds to the distribution outside the locking-range (the locking-range is roughly marked in Fig. V.14(b) by blue area), where this distribution is almost flat, meaning that all the values of ψ are equally favored, which is is what we expect when there is no phase-locking.

If we enter the synchronization range (the red and green curves) then the distribution is much more narrow and we observe a marked peak that is the signature of phase-locking.

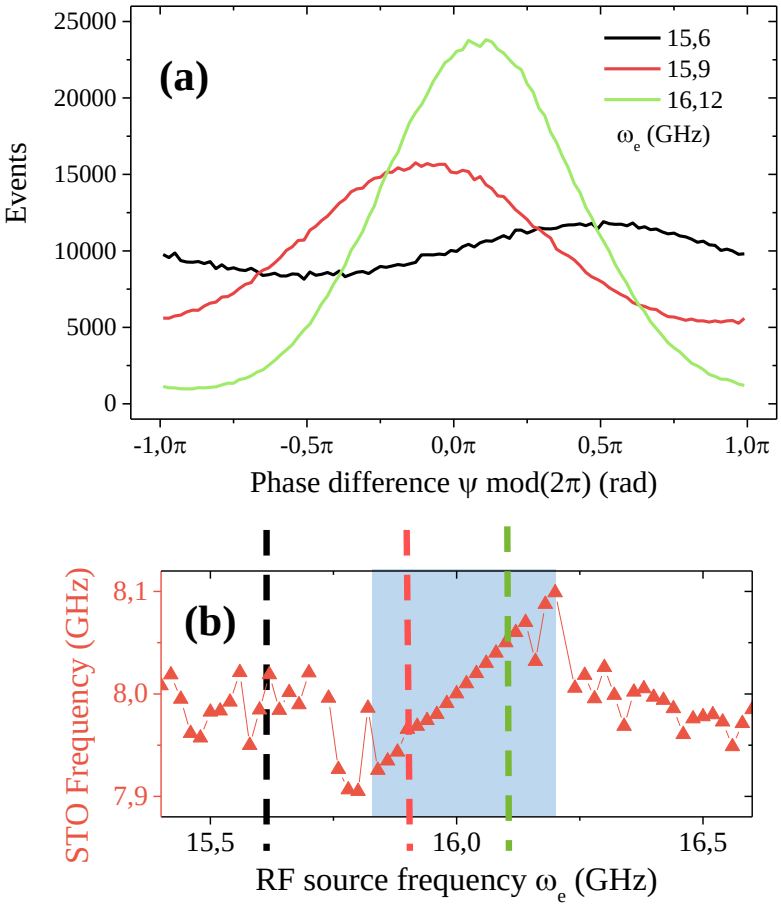

Figure V.14 – (a) Distribution of the phase-difference ψ mod(2π) for several RF source frequencies ($P_e = -7$ dBm). Outside the locking-range (black line) the distribution is almost flat, meaning that no value of the phase ψ is favored. Inside the locking-range the distribution narrows (green and red lines) and meaning one value ψ_0 of the phase is favored. (b) STO frequency versus RF source frequency identifying the synchronization region (clear blue area, $\Delta\Omega \approx 400$ MHz). Vertical lines indicate frequencies ω_e at which the distribution is plotted.

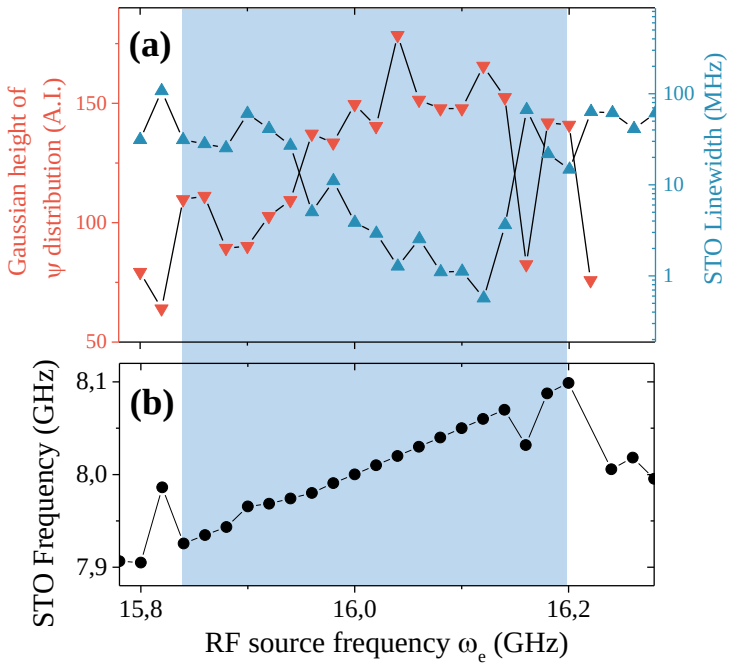

Figure V.15 – (a)Comparison of the Gaussian height ψ distribution (red triangles) with the STO linewidth (blue triangles) versus ω_e in the synchronization region (clear blue area). Distribution height and linewidth are inversely correlated, showing the link between stability of the phase difference and STO signal coherence. (b) STO frequency versus RF source frequency.

Here, due to the noise the distribution is not a δ function since the fluctuations of the phase-difference around its equilibrium value broaden the peak.

We can now fit the distribution of ψ by a Gaussian function. From the fit we can obtain, the center of the peak,i.e. the equilibrium value ψ_0 and the height / width of the peak.

We have extracted the equilibrium value ψ_0 from the gaussian fit. According to the analytical model of Chapter II, the equilibrium value is given by $\psi = \arcsin(\delta\omega_e/\Delta\Omega) + \pi/2$. So by plotting the distribution for different RF source frequencies and extracting the center of the peak, we should obtain a dependence of ψ as a function of the RF frequency ω_e in $\arcsin(\omega_e - \omega_0)$. So far (not shown here) the extraction of ψ as a function of ω_e has given inconsistent results, and the phase seems to take random values and does not follow the arcsin dependence.

On the other hand, we show results from extraction of the height of the ψ distribution as a function of the source frequency ω_e that we compare with the linewidth of the STO signal in Fig. V.15(a). The red curve represents the height of the distribution and the blue curve stands for the STO linewidth. The clear blue square designates the synchronization region. We can see that in this region the height of the distribution and the STO linewidth are inversely correlated - if we take $\omega_e = 16.12$ GHz which corresponds to the linewidth minimum, it coincides with a height maximum of the distribution.

This correlation shows the role played by the phase-locking process on the coherence of the signal. In particular, the height of the distribution represents how stable is the equilibrium state ψ_0, or in others term how small are the fluctuations of the phase difference. So, as the height increases, the fluctuations of the phase difference decrease and as a consequence the coherence of the signal increases, which diminishes the signal linewidth.

V.3.3 Phase and amplitude noise in the synchronized state

In the last subsection we established a link between stability of the phase-difference and the linewidth of the STO signal. We recall that at Spintec we applied the phase and

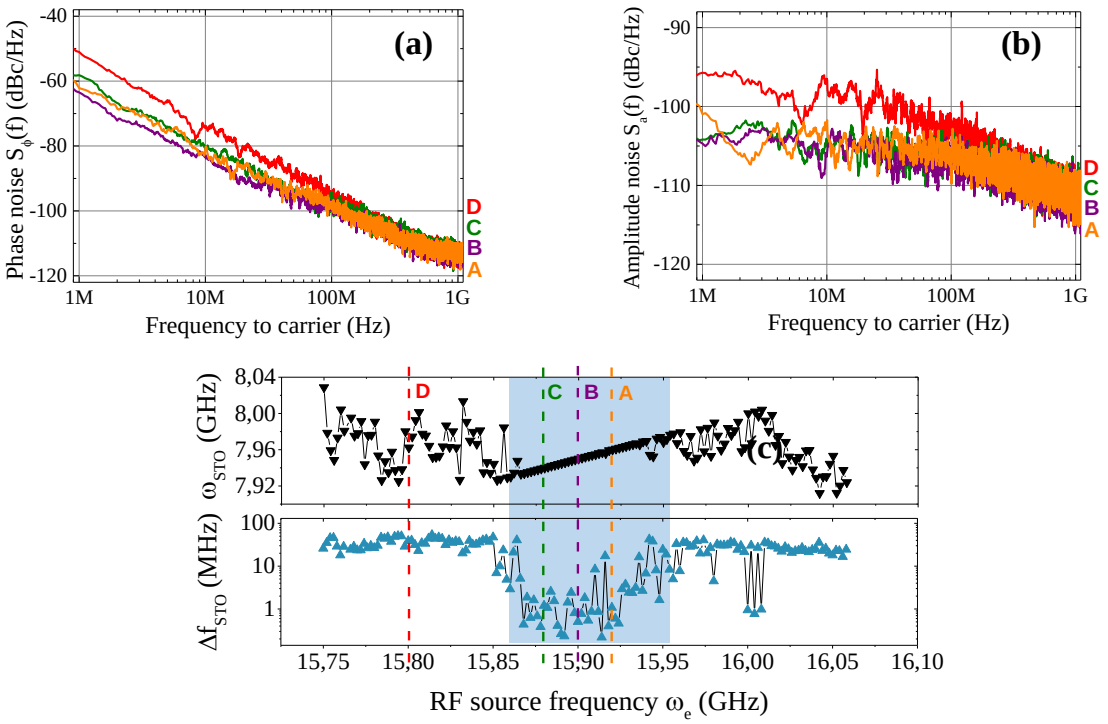

Figure V.16 – (a) Phase and (b) Amplitude noise measurements for a LTMR sample (used in this section) for several RF source frequencies with RF power $P_e = -7$ dBm.(c) Frequency and linewidth of the corresponding STO signal.

amplitude noise characterization techniques to STOs (these techniques are common for the characterization of noise in electronic oscillators). This technique was briefly introduced in the second part of the second chapter on experimental methods. Here in this final subsection we provide experimental measurements of the phase and amplitude noise inside and outside the synchronization region for two different samples, but we will limit the interpretation to a very basic level.

The first sample is the one that was examined in this section : a LTMR sample which has already a reduced linewidth at the working point in the free-running regime (about 30 MHz). Fig. V.16(a) and (b) show respectively phase and amplitude noise measurements for several source frequencies (see A,B,C,D in Fig. (b)). The first (red curve) corresponds to noise plots outside the synchronization region, while the other three correspond to noise plots inside the synchronization region.

We can see that inside the synchronization region, it is difficult to discriminate between the plots in both amplitude and phase noise. It can be explained because both plots correspond to zones inside the synchronization region (see Fig. (c)) where the linewidth is roughly the same. As a consequence, the effect of noise is comparable in the three cases which makes the three amplitude and phase noise plot look similar.

We present also another set of experimental phase and amplitude plots on an HTMR sample with Fig. V.17. This sample is a circular 115 × 115 nm diameter pillar with TMR= 61%, with a free-running linewidth of $\Delta f \approx 200$ MHz for $I_{DC} = -1.6$ mA. In the center of the synchronization region, for a source power $P_e = -5$ dBm, the linewidth is reduced to $\Delta f \approx 10$MHz (see Fig. V.17(c)).

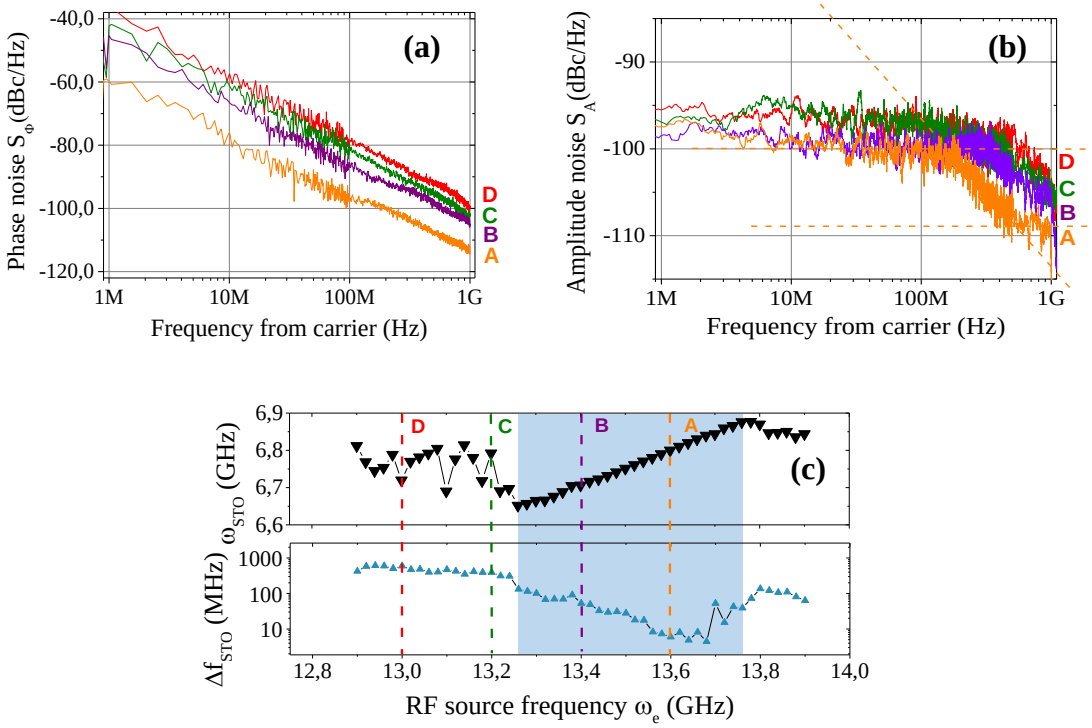

Figure V.17 – Phase (a) and Amplitude (b) noise measurements for a HTMR sample TMR = 61% (not used in this section) for several RF source frequencies. (c) Frequency and linewidth of the STO signal.

In contrast to the previous sample, here we see clearly that synchronization induces important changes in both phase and amplitude noise. Looking at the phase noise characteristics of Fig. V.17(a), as we move towards the center of the synchronization region (from D to A), there are no evident qualitative changes, but quantitatively speaking, synchronization manifests itself as a progressive downwards shift of the overall phase noise. In the end, the noise reduction in the phase from D (outside the synchronization region) to A (inside the synchronization region) accounts for a total of −20 dB.

As for the amplitude noise (Fig. V.17(b)), qualitative changes are visible. The most distinctive feature of the synchronization effect is (from D to A) the reduction of the roll-off frequency [10] from 600 MHz to 200 MHz. As we recall the roll-off frequency [71] is a measure of the amplitude relaxation rate Γ_p. It means that in this case synchronization decreases the amplitude relaxation rate, which in turn reduces linewidth and increases overall coherence. This decrease of the amplitude relaxation rate is not obvious, and goes in opposite direction with the theoretical predictions made in [104] [11] where the relaxation rate is said to increase instead.

10. The frequency at which the amplitude noise goes from a flat 0 dB/dec to a −20 dB/dec

11. See Fig. 2(b) in Ref. [104] for the the phase *and* amplitude relaxation rate in pre-oscillatory regime. We note that in our case, we sweep the source frequency f_e from the exterior to the center of the synchronization range while in the reference it is the RF amplitude that increases. Since in both cases it is accompanied with linewidth reduction, we make the assumption that the effect on the coherence is comparable.

Conclusion

Here we close this manuscript on synchronization of spin-torque oscillators and we summarize the main findings. But before we remember the context and the underlying motivations for this work. The first motivation was to fulfill a need in terms of understanding of synchronization mechanisms of a STO on a qualitative and quantitative level. Despite the theoretical ground provided by the KTS model in Ref. [81], there has not been a systematic verification by macrospin simulations of the domain of validity of the expressions advanced there, in particular for important quantities such as the locking-range, the phase-difference or the amplitude variations in synchronized regime. In addition, we explore in detail the link between synchronization properties and the characteristics of the IPP orbit. The second motivation is about developing other means of characterization and obtaining supplementary information of injection-locked STOs at room temperature. For example the majority of studies on injection-locked STOs concentrated on measurements in the frequency domain, and here we explored time-domain techniques for characterization of the synchronized regime.

Chapter II and III have been dedicated to the investigation on synchronization mechanisms in a STO. To do so, we took the particular configuration of a in-plane precession STO synchronized to a driving RF current, and using the KTS formalism we made a mathematical development which produced analytical expressions that put together with macrospin simulation results. From there, we have drawn the following conclusions :

1/ *Synchronization at f and $2f$ obey distinct mechanisms.* In the analytical development we saw that there are two different coupling factors at f and $2f$, and it changes the way the RF current interacts with the STO. In particular coupling with the RF current acts as a perturbation of non-linearity in the the anti-damping at $2f$, while at f the coupling acts as a perturbation of the whole equation. Macrospin simulations confirm the difference between f and $2f$, notably in the evolution with amplitude.

2/ *At $2f$, frequency and amplitude variations are directly linked via the non-linearity* i.e. $\delta\omega_s = N\delta p_s$. In a general context, synchronization to an external force requires that the oscillator adjusts its frequency to that of the external force. We show that synchronization at $2f$ follows this pattern : (i) Due to the external force the energy supply is modified by a factor proportional to the phase-difference and the forcing amplitude ; (ii) The balance between energy supply and damping is shifted so that the synchronous precession amplitude p_s is increased or decreased in comparison to the free-running amplitude p_0 ; (iii) via the non-linearity N, the oscillator adjusts its frequency to that of the external force. This mechanism, not reported yet, makes synchronization at $2f$ a original and representative feature of the effect of the non-linearity on the STO dynamics.

3/ *The geometry of the oscillation orbit plays an essential role on synchronization features.* The work of Urazhdin *et al.* [93] is an important step in this direction, where it was demonstrated that the relative orientation between the symmetry axis of the orbit

and the direction of the RF field determines the conditions for even or odd synchronization regimes. Here we make a similar observation, where it is the polarizer direction instead of the RF field direction that determines whether f or $2f$ synchronization is favored. In addition we looked at other aspects of the oscillation orbit in relation to synchronization properties : (i) the ellipticity of the orbit, where in particular the analytical development shows that only for a strong ellipticity of the IPP orbit synchronization at $2f$ is allowed ; (ii) the amplitude of the oscillations, where at $2f$ the coupling sensitivity equals the frequency shift due to amplitude Np_0. The analytical expression is verified quantitatively by macrospin simulations and gives excellent agreement.

The last part of the manuscript with Chapters IV and V examined the issues about characterization and reliability of injection-locking at $2f$ in MTJ-based STOs at room temperature.

From the standpoint of the STO device, the simultaneous application of a RF and DC current induces an important electrical stress on the tunnel junction. Interestingly the samples that exhibit the best dynamical properties seem to be the samples having one or more pinholes in the barrier (LTMR samples) but they are also less stable and one must be very careful not to deteriorate them during measurements. For practical applications the stability and the resistance on the long run of the device is an indispensable quality. Still, an important deal of engineering of the junction to be accomplished before reliable injection-locking of a MTJ-based STO can be realized.

Nevertheless, there are alternative routes to improve the reliability of injection-locked STOs. First by optimization of the microwave properties of the STO, indeed the impedance mismatch of a MTJ-STO with respect to the rest of the circuit at 50Ω creates RF losses, which are prejudicial to efficient signal transfer, but also to injection-locking. A well thought out design of the device electrodes and a high resistivity substrate also helps to limit RF losses. The second way has been proposed recently and involves using Spin-Hall oscillators [53, 12] or three-terminal MTJ devices [52]. In these devices the current used for excitation does not flow in the oscillating layer (the energy supply is provided by pure spin current), so that there is no risk of degradation due to the long term application of a high current density through the device.

As for the characterization of the injection-locked STO, we applied the techniques previously developed at Spintec for noise measurements, that is to say we quantified the amplitude and phase noise reduction in injection-locked regime. We also proposed a method to extract the locking-range in the presence of noise and we found a first hint of the link between precession amplitude and coupling sensitivity, and finally we obtained the distribution of the phase-difference that we compared with the linewidth reduction.

To conclude, the study and characterization of synchronization in spintronic oscillators will surely remain a very active subject of research in the coming years. Whether being a specialist on non-linear dynamics or spintronics, basic research on this systems is captivating and certainly holds many surprises for the future. In the meantime, developing a reliable and competitive STO device for frequency synthesis continues to be a challenging but exciting task. If it cannot be realized in the short term, there exist other perspectives for the practical application of a STO : frequency detection [58], frequency modulation [60] or, closer to our topic, injection-locked frequency dividers similarly to [74, 96] for electronic oscillators.

We wish that the reader of this manuscript finds here some appreciable material and

useful information, that going through it did not cause too serious headaches, and hopefully it will be a valuable step for the progress in the topic of synchronization in spintronic oscillators.

References

[1] Robert Adler. Locking Phenomena in Oscillators. 61(10) :1380–1385, 1973.

[2] M. N. Baibich, J. M. Broto, A. Fert, F. Nguyen Van Dau, F. Petroff, P. Etienne, G. Creuzet, A. Friederich, and J. Chazelas. Giant magnetoresistance of (001)fe/(001)cr magnetic superlattices. *Phys. Rev. Lett.*, 61 :2472–2475, Nov 1988.

[3] C. Baraduc, M. Chshiev, and U. Ebels. *INTRODUCTION TO SPIN TRANSFER TORQUE*, chapter 8, pages 173–192.

[4] L Baselgia, M Warden, F Waldner, Stuart L Hutton, and John E Drumheller. Derivation of the resonance frequency from the free energy of ferromagnets. *Physical Review B*, 38(4) :2237–2242, 1988.

[5] L Berger. Emission of spin waves by a magnetic multilayer traversed by a current. *Physical Review B*, 54(13) :9353–9358, 1996.

[6] P. Bortolotti, E. Grimaldi, a. Dussaux, J. Grollier, V. Cros, C. Serpico, K. Yakushiji, a. Fukushima, H. Kubota, R. Matsumoto, and S. Yuasa. Parametric excitation of magnetic vortex gyrations in spin-torque nano-oscillators. *Physical Review B*, 88(17) :174417, November 2013.

[7] P. Bruno and C. Chappert. Ruderman-Kittel theory of oscillatory interlayer exchange coupling. *Physical Review B*, 46(1) :261–270, 1992.

[8] W. Butler, X.-G. Zhang, T. Schulthess, and J. MacLaren. Spin-dependent tunneling conductance of Fe|MgO|Fe sandwiches. *Physical Review B*, 63(5) :1–12, January 2001.

[9] W H Butler, X Zhang, S Vutukuri, M Chshiev, and T C Schulthess. Theory of Tunneling Magnetoresistance for Epitaxial Systems. 41(10) :2645–2648, 2005.

[10] P.-Y. Clement, C. Ducruet, C. Baraduc, M. Chshiev, and B. Dieny. Diffusive model of current-in-plane-tunneling in double magnetic tunnel junctions. *Applied Physics Letters*, 100(26) :262404, 2012.

[11] Charles A. Czeisler, Jeanne F. Duffy, Theresa L. Shanahan, Emery N. Brown, Jude F. Mitchell, David W. Rimmer, Joseph M. Ronda, Edward J. Silva, James S. Allan, Jonathan S. Emens, Derk-Jan Dijk, and Richard E. Kronauer. Stability, precision, and near-24-hour period of the human circadian pacemaker. *Science*, 284(5423) :2177–2181, 1999.

[12] V E Demidov, H Ulrichs, S V Gurevich, S O Demokritov, V S Tiberkevich, a N Slavin, a Zholud, and S Urazhdin. Synchronization of spin Hall nano-oscillators to external microwave signals. *Nature communications*, 5 :3179, January 2014.

[13] T. Devolder, a. Meftah, K. Ito, J. a. Katine, P. Crozat, and C. Chappert. Spin transfer oscillators emitting microwave in zero applied magnetic field. *Journal of Applied Physics*, 101(6) :063916, 2007.

[14] B. Dieny, V. S. Speriosu, S. Metin, S. S. P. Parkin, B. a. Gurney, P. Baumgart, and D. R. Wilhoit. Magnetotransport properties of magnetically soft spin-valve structures (invited). *Journal of Applied Physics*, 69(8) :4774, 1991.

[15] B. Dieny, V. S. Speriosu, S. S. P. Parkin, B. A. Gurney, D. R. Wilhoit, and D. Mauri. Giant magnetoresistive in soft ferromagnetic multilayers. *Phys. Rev. B*, 43 :1297–1300, Jan 1991.

[16] B. Dieny, V.S. Speriosu, S.S.P. Parkin, B.A. Gurney, D. R. Wilhoit, and D. Mauri. Giant magnetoresistance in soft ferromagnetic multilayers. *Physical review B*, 43(1), 1991.

[17] David D. Djayaprawira, Koji Tsunekawa, Motonobu Nagai, Hiroki Maehara, Shinji Yamagata, Naoki Watanabe, Shinji Yuasa, Yoshishige Suzuki, and Koji Ando. 230magnetic tunnel junctions. *Applied Physics Letters*, 86(9) :–, 2005.

[18] Randy K. Dumas, E. Iacocca, S. Bonetti, S. R. Sani, S. M. Mohseni, a. Eklund, J. Persson, O. Heinonen, and Johan Å kerman. Spin-Wave-Mode Coexistence on the Nanoscale : A Consequence of the Oersted-Field-Induced Asymmetric Energy Landscape. *Physical Review Letters*, 110(25) :257202, June 2013.

[19] P. Dürrenfeld, E. Iacocca, J. Å kerman, and P. K. Muduli. Parametric excitation in a magnetic tunnel junction-based spin torque oscillator. *Applied Physics Letters*, 104(5) :052410, February 2014.

[20] a. Dussaux, a. V. Khvalkovskiy, J. Grollier, V. Cros, a. Fukushima, M. Konoto, H. Kubota, K. Yakushiji, S. Yuasa, K. Ando, and a. Fert. Phase locking of vortex based spin transfer oscillators to a microwave current. *Applied Physics Letters*, 98(13) :132506, 2011.

[21] B. Georges, J. Grollier, V. Cros, and a. Fert. Impact of the electrical connection of spin transfer nano-oscillators on their synchronization : an analytical study. *Applied Physics Letters*, 92(23) :232504, 2008.

[22] B. Georges, J. Grollier, M. Darques, V. Cros, C. Deranlot, B. Marcilhac, G. Faini, and a. Fert. Coupling Efficiency for Phase Locking of a Spin Transfer Nano-Oscillator to a Microwave Current. *Physical Review Letters*, 101(1) :4–7, July 2008.

[23] B. Georges, J. Grollier, M. Darques, V. Cros, C. Deranlot, B. Marcilhac, G. Faini, and a. Fert. Coupling Efficiency for Phase Locking of a Spin Transfer Nano-Oscillator to a Microwave Current. *Physical Review Letters*, 101(1) :017201, July 2008.

[24] A. Ghosh, S. Auffret, U. Ebels, and W. E. Bailey. Penetration depth of transverse spin current in ultrathin ferromagnets. *Phys. Rev. Lett.*, 109 :127202, Sep 2012.

[25] C. Graves, L Glass, D. Laporta, R Meloche, and A. Grassino. Respiratory phase locking during mechanical ventilation in anesthetized human subjects. *Am. J. Physiol.*, 1979.

[26] Eva Grimaldi, Antoine Dussaux, Paolo Bortolotti, Julie Grollier, Grégoire Pillet, Akio Fukushima, Hitoshi Kubota, Kay Yakushiji, Shinji Yuasa, and Vincent Cros. Response to noise of a vortex based spin transfer nano-oscillator. *Physical Review B*, 89(10) :104404, March 2014.

[27] J. Grollier, V. Cros, and a. Fert. Synchronization of spin-transfer oscillators driven by stimulated microwave currents. *Physical Review B*, 73(6) :060409, February 2006.

[28] D. Gusakova, D. Houssameddine, U. Ebels, B. Dieny, L. Buda-Prejbeanu, M. Cyrille, and B. Delaët. Spin-polarized current-induced excitations in a coupled magnetic layer system. *Physical Review B*, 79(10) :1–16, March 2009.

[29] D. Gusakova, M. Quinsat, J. F. Sierra, U. Ebels, B. Dieny, L. D. Buda-Prejbeanu, M.-C. Cyrille, V. Tiberkevich, and a. N. Slavin. Linewidth reduction in a spin-torque nano-oscillator caused by non-conservative current-induced coupling between magnetic layers. *Applied Physics Letters*, 99(5) :052501, 2011.

[30] a. Hamadeh, N. Locatelli, V. V. Naletov, R. Lebrun, G. de Loubens, J. Grollier, O. Klein, and V. Cros. Perfect and robust phase-locking of a spin transfer vortex nano-oscillator to an external microwave source. *Applied Physics Letters*, 104(2) :022408, 2014.

[31] Christian Heiliger and M. D. Stiles. *Ab Initio* studies of the spin-transfer torque in magnetic tunnel junctions. *Phys. Rev. Lett.*, 100 :186805, May 2008.

[32] O. Heinonen, S. Stokes, and J. Yi. Perpendicular Spin Torque in Magnetic Tunnel Junctions. *Physical Review Letters*, 105(6) :6–9, August 2010.

[33] D Houssameddine, U Ebels, B Delaët, B Rodmacq, I Firastrau, F Ponthenier, M Brunet, C Thirion, J-P Michel, L Prejbeanu-Buda, M-C Cyrille, O Redon, and B Dieny. Spin-torque oscillator using a perpendicular polarizer and a planar free layer. *Nature materials*, 6(6) :441–7, June 2007.

[34] D. Houssameddine, U. Ebels, B. Dieny, K. Garello, J.-P. Michel, B. Delaet, B. Viala, M.-C. Cyrille, J. Katine, and D. Mauri. Temporal Coherence of MgO Based Magnetic Tunnel Junction Spin Torque Oscillators. *Physical Review Letters*, 102(25), June 2009.

[35] D. Houssameddine, S. H. Florez, J. a. Katine, J.-P. Michel, U. Ebels, D. Mauri, O. Ozatay, B. Delaet, B. Viala, L. Folks, B. D. Terris, and M.-C. Cyrille. Spin transfer induced coherent microwave emission with large power from nanoscale MgO tunnel junctions. *Applied Physics Letters*, 93(2) :022505, 2008.

[36] Mark Johnson. Analysis of anomalous multilayer magnetoresistance within the thermomagnetoelectric system. *Phys. Rev. Lett.*, 67 :3594–3597, Dec 1991.

[37] Mark Johnson and R. H. Silsbee. Thermodynamic analysis of interfacial transport and of the thermomagnetoelectric system. *Phys. Rev. B*, 35 :4959–4972, Apr 1987.

[38] M Julliere. Tunneling between ferromagnetic films. *Physics Letters A*, 54(3) :225–226, 1975.

[39] Shehzaad Kaka, Matthew R Pufall, William H Rippard, Thomas J Silva, Stephen E Russek, and Jordan a Katine. Mutual phase-locking of microwave spin torque nano-oscillators. *Nature*, 437(7057) :389–92, September 2005.

[40] Joo-Von Kim, Q. Mistral, C. Chappert, V. Tiberkevich, and a. Slavin. Line Shape Distortion in a Nonlinear Auto-Oscillator Near Generation Threshold : Application to Spin-Torque Nano-Oscillators. *Physical Review Letters*, 100(16) :167201, April 2008.

[41] Joo-Von Kim, Vasil Tiberkevich, and Andrei Slavin. Generation Linewidth of an Auto-Oscillator with a Nonlinear Frequency Shift : Spin-Torque Nano-Oscillator. *Physical Review Letters*, 100(1) :1–4, January 2008.

[42] S I Kiselev, J C Sankey, I N Krivorotov, N C Emley, R J Schoelkopf, R a Buhrman, and D C Ralph. Microwave oscillations of a nanomagnet driven by a spin-polarized current. *Nature*, 425(6956) :380–3, September 2003.

[43] Charles Kittel. On the theory on Ferromagnetic Resonance Absorption. *Physical Review*, 73(2), 1948.

[44] K. Komagaki, M. Hattori, K. Noma, H. Kanai, K. Kobayashi, Y. Uehara, M. Tsunoda, and M. Takahashi. Influence of Diffused Boron Into MgO Barrier on Pinhole Creation in CoFeB/MgO/CoFeB Magnetic Tunnel Junctions. *IEEE Transactions on Magnetics*, 45(10) :3453–3456, October 2009.

[45] Makoto Konoto, Hiroshi Imamura, Tomohiro Taniguchi, Kay Yakushiji, Hitoshi Kubota, Akio Fukushima, Koji Ando, and Shinji Yuasa. Effect of MgO Cap Layer on Gilbert Damping of FeB Electrode Layer in MgO-Based Magnetic Tunnel Junctions. *Applied Physics Express*, 6(7) :073002, July 2013.

[46] Hitoshi Kubota, Kay Yakushiji, Akio Fukushima, Shingo Tamaru, Makoto Konoto, Takayuki Nozaki, Shota Ishibashi, Takeshi Saruya, Shinji Yuasa, Tomohiro Taniguchi, Hiroko Arai, and Hiroshi Imamura. Spin-Torque Oscillator Based on Magnetic Tunnel Junction with a Perpendicularly Magnetized Free Layer and In-Plane Magnetized Polarizer. *Applied Physics Express*, 6(10) :103003, October 2013.

[47] Kiwamu Kudo, Tazumi Nagasawa, Rie Sato, and Koichi Mizushima. Measurement of nonlinear frequency shift coefficient in spin-torque oscillators based on MgO tunnel junctions. *Applied Physics Letters*, 95(2) :022507, 2009.

[48] Raneyuri Kurorawa. Injection Locking of Microwave Solid-State Oscillators. *IEE Transactions on Microwave theory and Techniques*, 61(10), 1973.

[49] Sung Chul Lee, Ung Hwan Pi, Keewon Kim, Kwang Seok Kim, Jaikwang Shin, and U-In Chung. Current driven magnetic damping in dipolar-coupled spin system. *Scientific reports*, 2 :531, January 2012.

[50] Y. M. Lee, J. Hayakawa, S. Ikeda, F. Matsukura, and H. Ohno. Effect of electrode composition on the tunnel magnetoresistance of pseudo-spin-valve magnetic tunnel junction with a mgo tunnel barrier. *Applied Physics Letters*, 90(21) :–, 2007.

[51] R. Lehndorff, D. E. Burgler, C. M. Schneider, and Z. Celinski. Injection locking of the gyrotropic vortex motion in a nanopillar. *Applied Physics Letters*, 97(14) :142503, 2010.

[52] Luqiao Liu, Chi-Feng Pai, D. C. Ralph, and R. a. Buhrman. Magnetic Oscillations Driven by the Spin Hall Effect in 3-Terminal Magnetic Tunnel Junction Devices. *Physical Review Letters*, 109(18) :186602, October 2012.

[53] R. H. Liu, W. L. Lim, and S. Urazhdin. Spectral Characteristics of the Microwave Emission by the Spin Hall Nano-Oscillator. *Physical Review Letters*, 110(14) :147601, April 2013.

[54] V.S. L'vov. Wave Turbulence under Parametric Excitation. *New York : Springer-Verlag*, 1994.

[55] F B Mancoff, N D Rizzo, B N Engel, and S Tehrani. Phase-locking in double-point-contact spin-transfer devices. *Nature*, 437(7057) :393–5, September 2005.

[56] M. Manfrini, T. Devolder, Joo-Von Kim, P. Crozat, N. Zerounian, C. Chappert, W. Van Roy, L. Lagae, G. Hrkac, and T. Schrefl. Agility of vortex-based nanocontact spin torque oscillators. *Applied Physics Letters*, 95(19) :192507, 2009.

[57] S. Y. Martin, N. de Mestier, C. Thirion, C. Hoarau, Y. Conraux, C. Baraduc, and B. Diény. Parametric oscillator based on nonlinear vortex dynamics in low-resistance magnetic tunnel junctions. *Physical Review B*, 84(14) :144434, October 2011.

[58] S Miwa, S Ishibashi, H Tomita, T Nozaki, E Tamura, K Ando, N Mizuochi, T Saruya, H Kubota, K Yakushiji, T Taniguchi, H Imamura, a Fukushima, S Yuasa, and Y Suzuki. Highly sensitive nanoscale spin-torque diode. *Nature materials*, 13(1) :50–6, January 2014.

[59] T. Miyazaki and N. Tezuka. Giant magnetic tunneling effect in fe/al2o3/fe junction. *Journal of Magnetism and Magnetic Materials*, 139(3) :L231 – L234, 1995.

[60] K. Mizushima, K. Kudo, T. Nagasawa, and R. Sato. Signal-to-noise ratios in high-signal-transfer-rate read heads composed of spin-torque oscillators. *Journal of Applied Physics*, 107(6) :–, 2010.

[61] J. S. Moodera, Lisa R. Kinder, Terrilyn M. Wong, and R. Meservey. Large magnetoresistance at room temperature in ferromagnetic thin film tunnel junctions. *Phys. Rev. Lett.*, 74 :3273–3276, Apr 1995.

[62] Robert Y. Moore. A clock for the ages. *Science*, 284(5423) :2102–2103, 1999.

[63] P. Muduli, O. Heinonen, and Johan Å kerman. Decoherence and Mode Hopping in a Magnetic Tunnel Junction Based Spin Torque Oscillator. *Physical Review Letters*, 108(20) :1–5, May 2012.

[64] Bryan Oliver, Qing He, Xuefei Tang, and J. Nowak. Dielectric breakdown in magnetic tunnel junctions having an ultrathin barrier. *Journal of Applied Physics*, 91(7) :4348, 2002.

[65] Bryan Oliver, Qing He, Xuefei Tang, and Janusz Nowak. Tunneling criteria and breakdown for low resistive magnetic tunnel junctions. *Journal of Applied Physics*, 94(3) :1783, 2003.

[66] B. Picinbono. On instantaneous amplitude and phase of signals. *IEEE Transactions on Signal Processing*, 45(3) :552–560, March 1997.

[67] Arkady Pikovsky. Synchronization - A universal Concept in Nonlinear Sciences. *Cambridge University Press*, 2001.

[68] David M. Pozar. Microwave Engineering, 1998.

[69] M. R. Pufall, W. H. Rippard, S. Kaka, T. J. Silva, and S. E. Russek. Frequency modulation of spin-transfer oscillators. *Applied Physics Letters*, 86(8) :082506, 2005.

[70] M. Quinsat. Etude d un auto-oscillateur non-isochrone : Application à la dynamique non-linéaire de l aimantation induite par transfert de spin. 2012.

[71] M. Quinsat, D. Gusakova, J. F. Sierra, J. P. Michel, D. Houssameddine, B. Delaet, M.-C. Cyrille, U. Ebels, B. Dieny, L. D. Buda-Prejbeanu, J. a. Katine, D. Mauri, a. Zeltser, M. Prigent, J.-C. Nallatamby, and R. Sommet. Amplitude and phase noise of magnetic tunnel junction oscillators. *Applied Physics Letters*, 97(18) :182507, 2010.

[72] M. Quinsat, J. F. Sierra, I. Firastrau, V. Tiberkevich, a. Slavin, D. Gusakova, L. D. Buda-Prejbeanu, M. Zarudniev, J.-P. Michel, U. Ebels, B. Dieny, M.-C. Cyrille, J. a. Katine, D. Mauri, and a. Zeltser. Injection locking of tunnel junction oscillators to a microwave current. *Applied Physics Letters*, 98(18) :182503, 2011.

[73] M. Quinsat, V. Tiberkevich, D. Gusakova, a. Slavin, J. Sierra, U. Ebels, L. Buda-Prejbeanu, B. Dieny, M.-C. Cyrille, a. Zelster, and J. Katine. Linewidth of higher harmonics in a nonisochronous auto-oscillator : Application to spin-torque nano-oscillators. *Physical Review B*, 86(10) :104418, September 2012.

[74] Hamid R Rategh, Student Member, and Thomas H Lee. Superharmonic Injection-Locked Frequency Dividers. 34(6) :813–821, 1999.

[75] W. Rippard, M. Pufall, S. Kaka, T. Silva, S. Russek, and J. Katine. Injection Locking and Phase Control of Spin Transfer Nano-oscillators. *Physical Review Letters*, 95(6) :10–13, August 2005.

[76] J.-C. Rojas-Sánchez, N. Reyren, P. Laczkowski, W. Savero, J.-P. Attané, C. Deranlot, M. Jamet, J.-M. George, L. Vila, and H. Jaffrès. Spin pumping and inverse spin hall effect in platinum : The essential role of spin-memory loss at metallic interfaces. *Phys. Rev. Lett.*, 112 :106602, Mar 2014.

[77] a Ruotolo, V Cros, B Georges, a Dussaux, J Grollier, C Deranlot, R Guillemet, K Bouzehouane, S Fusil, and a Fert. Phase-locking of magnetic vortices mediated by antivortices. *Nature nanotechnology*, 4(8) :528–32, August 2009.

[78] J. Rutman. Characterization of phase and frequency instabilities in precision frequency sources : fifteen years of progress. *Proceedings of the IEEE*, 66(9) :1048–1075, 1979.

[79] C. Schafer. Synchronization in the human cardiorespiratory system. *Phys. Rev. E*, (60) :857–870, 1999.

[80] a. Slavin and V. Tiberkevich. Nonlinear self-phase-locking effect in an array of current-driven magnetic nanocontacts. *Physical Review B*, 72(9) :092407, September 2005.

[81] Andrei Slavin. Microwave sources : spin-torque oscillators get in phase. *Nature nanotechnology*, 4(8) :479–80, August 2009.

[82] Andrei Slavin and Vasil Tiberkevich. Excitation of Spin Waves by Spin-Polarized Current in Magnetic. 44(7) :1916–1927, 2008.

[83] Andrei Slavin and Vasil Tiberkevich. Advances in Magnetics Nonlinear Auto-Oscillator Theory of Microwave Generation by Spin-Polarized Current. 45(4) :1875–1918, 2009.

[84] Andrei N Slavin and Pavel Kabos. Approximate Theory of Microwave Generation in a Current-Driven Magnetic Nanocontact Magnetized in an Arbitrary Direction. 41(4) :1264–1273, 2005.

[85] J.C. Slonczewski. Current-driven excitation of magnetic multilayers. *Journal of Magnetism and Magnetic Materials*, 159(1-2) :L1–L7, June 1996.

[86] J. Smit. *Philips Res. Rep.*, 113(10), 2005.

[87] Phillip Tabor, Vasil Tiberkevich, Andrei Slavin, and Sergei Urazhdin. Hysteretic synchronization of nonlinear spin-torque oscillators. *Physical Review B*, 82(2) :020407, July 2010.

[88] Ioannis Theodonis, Nicholas Kioussis, Alan Kalitsov, Mairbek Chshiev, and W. Butler. Anomalous Bias Dependence of Spin Torque in Magnetic Tunnel Junctions. *Physical Review Letters*, 97(23) :2–5, December 2006.

[89] A.A. Thiele. Steady-State Motion of Magnetic Domains. *Physical Review Letters*, 30(6) :3–6, 1973.

[90] Vasil Tiberkevich, Andrei Slavin, Elena Bankowski, and Grant Gerhart. Phase-locking and frustration in an array of nonlinear spin-torque nano-oscillators. *Applied Physics Letters*, 95(26) :262505, 2009.

[91] Vasil Tiberkevich, Andrei Slavin, and Joo-Von Kim. Microwave power generated by a spin-torque oscillator in the presence of noise. *Applied Physics Letters*, 91(19) :192506, 2007.

[92] Sergei Urazhdin, Phillip Tabor, Vasil Tiberkevich, and Andrei Slavin. Fractional Synchronization of Spin-Torque Nano-Oscillators. *Physical Review Letters*, 105(10) :3–6, August 2010.

[93] Sergei Urazhdin, Vasil Tiberkevich, and Andrei Slavin. Parametric Excitation of a Magnetic Nanocontact by a Microwave Field. *Physical Review Letters*, 105(23) :1–4, December 2010.

[94] T Valet and a Fert. Theory of the perpendicular magnetoresistance in magnetic multilayers. *Physical review. B, Condensed matter*, 48(10) :7099–7113, September 1993.

[95] P.C. van Son, H. van Kempen, and P. Wyder. Boundary resistance of Ferromagnetic-nonferromagnetic Metal Interface. *Phys. Rev. Lett.*, 58(21) :2271–2273, 1987.

[96] Shwetabh Verma, Student Member, Hamid R Rategh, and Thomas H Lee. A Unified Model for Injection-Locked Frequency Dividers. 38(6) :1015–1027, 2003.

[97] François Vernotte. Stabilité temporelle et fréquentielle des oscillateurs : outils d'analyse. *Techniques de l'ingénieur. Mesures et contrôle*, TIB415DUO :r681, 2006.

[98] François Vernotte. Stabilité temporelle et fréquentielle des oscillateurs : modèles. *Techniques de l'ingénieur. Mesures et contrôle*, TIB415DUO :r680, 2014.

[99] L.A. Wilkens. The paddlefish rostrum functions as an electrosensory antenna in plankton feeding. *Proc. Roy. Soc. Lond.*, (264) :1723–1729, 1997.

[100] Mykhailo Zarudniev. Synthèse de fréquence par couplage d'oscillateurs spintroniques.

[101] Zhongming Zeng, Pedram Khalili Amiri, Ilya N Krivorotov, Hui Zhao, Giovanni Finocchio, Jian-Ping Wang, Jordan a Katine, Yiming Huai, Juergen Langer, Kosmas Galatsis, Kang L Wang, and Hongwen Jiang. High-power coherent microwave emission from magnetic tunnel junction nano-oscillators with perpendicular anisotropy. *ACS nano*, 6(7) :6115–21, July 2012.

[102] S. Zhang, P. M. Levy, and A. Fert. Mechanisms of spin-polarized current-driven magnetization switching. *Phys. Rev. Lett.*, 88 :236601, May 2002.

[103] Yan Zhou and Johan AÌkerman. Perpendicular spin torque promotes synchronization of magnetic tunnel junction based spin torque oscillators. *Applied Physics Letters*, 94(11) :112503, 2009.

[104] Yan Zhou, Vasil Tiberkevich, Giancarlo Consolo, Ezio Iacocca, Bruno Azzerboni, Andrei Slavin, and Johan Å kerman. Oscillatory transient regime in the forced dynamics of a nonlinear auto oscillator. *Physical Review B*, 82(1) :4–7, July 2010.